

University of Warwick institutional repository: <http://go.warwick.ac.uk/wrap>

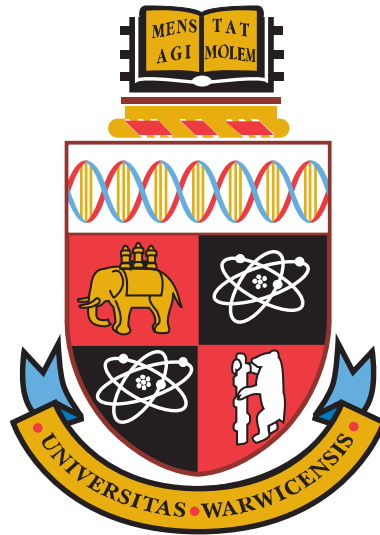
**A Thesis Submitted for the Degree of PhD at the University of Warwick**

<http://go.warwick.ac.uk/wrap/74159>

This thesis is made available online and is protected by original copyright.

Please scroll down to view the document itself.

Please refer to the repository record for this item for information to help you to cite it. Our policy information is available from the repository home page.



**Fast Magnetoacoustic Waves in Non-Equilibrium  
Solar Wind and Coronal Plasmas**

by

**Luke Albert Selzer**

**Thesis**

Submitted to the University of Warwick

for the degree of

**Doctor of Philosophy**

**Department of Physics**

March 2015

THE UNIVERSITY OF  
**WARWICK**

# Contents

<b>List of Tables</b>	<b>v</b>
<b>List of Figures</b>	<b>vii</b>
<b>Acknowledgments</b>	<b>xviii</b>
<b>Declarations</b>	<b>xix</b>
<b>Abstract</b>	<b>xx</b>
<b>Chapter 1 Introduction</b>	<b>1</b>
1.1 Basic Plasma Physics . . . . .	1
1.1.1 Definition of a Plasma . . . . .	1
1.1.2 Characteristic scales of plasma dynamics . . . . .	1
1.2 Kinetic Plasma Theory . . . . .	2
1.2.1 Phase Space Description . . . . .	3
1.2.2 Macroscopic Variables . . . . .	5
1.2.3 Adiabatic Invariants . . . . .	7
1.3 Magnetohydrodynamics (MHD) . . . . .	8
1.3.1 Multi-Fluid Theory . . . . .	8
1.3.2 One-Fluid Theory . . . . .	9
1.3.3 Plasma $\beta$ . . . . .	12
1.3.4 MHD Approximations . . . . .	13
1.4 Plasma Wave Theory . . . . .	14
1.4.1 General Dispersion Relation . . . . .	15
1.5 Magnetohydrodynamic Waves . . . . .	16
1.6 Low Frequency Plasma Waves . . . . .	18
1.6.1 Linear MHD Waves . . . . .	18
1.6.2 Waves Modes of a Plasma Cylinder . . . . .	19

1.7	High Frequency Plasma waves . . . . .	22
1.7.1	Waves in unmagnetised plasmas . . . . .	23
1.7.2	High Frequency Waves in a Magnetised Plasma . . . . .	24
1.7.3	Summary of Plasma Wave Modes . . . . .	25
1.8	Non-Thermal Distribution Functions . . . . .	25
1.8.1	Growth Rate . . . . .	26
1.8.2	Landau Damping . . . . .	27
1.8.3	Instabilities and Resonances. . . . .	30
<b>Chapter 2 Space Plasmas</b>		<b>37</b>
2.1	Introduction . . . . .	37
2.2	The Solar Wind . . . . .	37
2.3	Collisionless Shocks . . . . .	39
2.3.1	What is a Shock Wave? . . . . .	39
2.3.2	Interplanetary Shocks . . . . .	40
2.3.3	Parallel and Perpendicular Shocks . . . . .	41
2.3.4	The Terrestrial Foreshock . . . . .	42
2.4	Solar Atmosphere . . . . .	45
2.4.1	The Sun . . . . .	45
2.4.2	The Photosphere and Chromosphere . . . . .	46
2.4.3	The Solar Corona . . . . .	48
2.4.4	Coronal Structures and Phenomena . . . . .	50
2.5	A Solar Flare . . . . .	51
2.5.1	The Standard 2D Model . . . . .	52
2.5.2	Quasi-Periodic Pulsations (QPP) . . . . .	53
2.5.3	Radio Emission from Flaring Regions . . . . .	53
2.5.4	The Zebra Pattern (ZP) . . . . .	56
<b>Chapter 3 Instrumentation</b>		<b>63</b>
3.1	Introduction . . . . .	63
3.2	Space Mission Cluster . . . . .	63
3.2.1	Geocentric Solar Elliptical Co-ordinate System . . . . .	64
3.2.2	Flux Gate Magnetometer (FGM) . . . . .	65
3.2.3	Cluster Ion Spectrometer (CIS) . . . . .	65
3.3	Wind . . . . .	68
3.4	Ground Based Radio Telescopes . . . . .	69
3.4.1	Solar Broadband Radio Spectrometer (SBRs/Huairou) . . . . .	70
3.4.2	Nobeyama Radioheliograph (NoRH) . . . . .	70



<b>Chapter 4</b>	<b>Temperature Anisotropy in the Terrestrial Foreshock</b>	<b>72</b>
4.1	Introduction . . . . .	72
4.1.1	Wave Modes of the Terrestrial Foreshock . . . . .	73
4.2	Data Intervals . . . . .	74
4.2.1	Data Interval Selection . . . . .	74
4.3	Signal Analysis . . . . .	76
4.3.1	Field Aligned Projection . . . . .	76
4.3.2	Correlation . . . . .	78
4.3.3	The Taylor Hypothesis and Advection . . . . .	80
4.3.4	Periodicity Analysis . . . . .	81
4.4	Polarisation and Propagation Direction . . . . .	85
4.4.1	Hodogram . . . . .	85
4.4.2	Time Delay Analysis . . . . .	87
4.5	Differential Analysis . . . . .	89
4.6	Temperature Anisotropy . . . . .	93
4.6.1	The $(\beta_{\parallel}, T_{\perp}/T_{\parallel})$ Parameter Space . . . . .	93
4.6.2	Visualisation . . . . .	94
4.6.3	Time Evolution . . . . .	101
4.7	Discussion . . . . .	102
<b>Chapter 5</b>	<b>Zebra Patterns I: Simulation and Analytics</b>	<b>105</b>
5.1	Introduction . . . . .	105
5.2	Analytical Description of Zebra Pattern Fine Structure. . . . .	106
5.2.1	Deriving the Density Field . . . . .	106
5.2.2	Deriving the Magnetic Field Perturbations . . . . .	112
5.2.3	Zebra Pattern Formation . . . . .	113
5.3	Numerical Simulations . . . . .	114
5.3.1	Static Simulations . . . . .	115
5.3.2	2D Dynamic Coronal Loop Model . . . . .	123
5.3.3	Zebra Pattern Simulation . . . . .	129
5.4	Conclusion . . . . .	132
<b>Chapter 6</b>	<b>Zebra Patterns II: Observational Work</b>	<b>136</b>
6.1	Introduction . . . . .	136
6.2	Radio Data . . . . .	137
6.3	Zebra Pattern Wiggles . . . . .	138
6.3.1	ZP Image Processing . . . . .	139
6.3.2	Large Scale Trend Removal . . . . .	139

6.3.3	Low Pass Filter . . . . .	140
6.3.4	Threshold Filter . . . . .	140
6.4	Data Series Extraction . . . . .	141
6.5	Periodicity Analysis . . . . .	142
6.5.1	Auto-Correlation . . . . .	142
6.5.2	Periodogram . . . . .	143
6.6	Discussion . . . . .	146
<b>Chapter 7 Summary and Discussion</b>		<b>148</b>

# List of Tables

1.1	A summary of plasma wave modes classified by magnetic field dependency and propagation direction. <i>Key symbols:</i> $\omega$ - wave frequency, $k$ - wave number, $c$ - speed of light, $\omega_{pe}$ - electron plasma frequency (1.1), $\omega_{pi}$ - ion plasma frequency (1.1), $\omega_{ce}$ - electron cyclotron frequency (1.2), $\omega_{ci}$ - ion cyclotron frequency (1.2), $\omega_{UH}$ - upper hybrid frequency, $c_s$ - sound speed (1.70) and $v_A$ is the Alfvén speed (1.72). Table adapted from [Swanson, 2003]. . . . .	27
2.1	Key physical parameters within the solar wind, Baumjohann and Treumann [2012]. . . . .	38
2.2	Table of radio burst parameters taken from [IPS, 2014]. . . . .	57
2.3	Characteristic fine structure parameters of solar radio bursts, from [Kuijpers, 1980, Yu et al., 2013] . . . . .	60
3.1	The complete instrument list for each Cluster spacecraft, [Escoubet and Goldstein, 2001] . . . . .	66
3.2	CIS Operational Modes, taken from [Dandouras and Barthe, 2012]. . . . .	66
3.3	Overview of the operating parameters of NoRH. . . . .	71
4.1	Experimentally measured parameters of the solar wind at a distance of approximately $10R_E$ from Earth along the Earth-Sun line. Values were averaged over the interval: 27/01/2004, 03:50-04:35. . . . .	72
4.2	Cluster data intervals used in this chapter. Intervals were selected from the much larger dataset presented in [Narita et al., 2004]. . . . .	75
4.3	Correlation coefficients for the correlation analysis between magnetic field magnitude and proton density for the intervals listed. A 2000 s sample was taken for each interval. . . . .	80

4.4	Table of peak frequency values found in the power spectra of the corresponding data intervals, the average solar wind speed for that interval and the corresponding wavelength found using the Taylor hypothesis (section 4.3.3). . . . .	83
4.5	Table of circular polarisation directions found for the highest spectral power ULF wave observed in each interval. The polarisation was calculated in the spacecraft reference frame using the hodogram technique. . . . .	87
4.6	Table of results for delay analysis. The wave vector co-ordinate system was orientated to the field aligned system outlined in section 4.3.1. . . . .	89
4.7	Instability thresholds used to bound the $(\beta_{\parallel}, R)$ parameter space. These values are the parametric fit values used in equation 4.12 to calculate the maximum growth rate of $\gamma/\omega_{ci} = 10^{-3}$ . Values have been taken from [Hellinger et al., 2006, Marsch et al., 2004]. . . . .	94
5.1	Results for the 1D static ZP model. A value of 1.2 MK was taken for the coronal temperature while the coronal magnetic field was assumed to take a value of 1 mT (10 gauss). The coronal plasma frequency was estimated at 3 GHz. . . . .	118
5.2	A comparison of frequency and height results from the reproduction of ZPs using several techniques. All heights are normalised to the height of the loop apex of 75 Mm which corresponds to a loop of length 235 Mm, [Chen et al., 2011]. All simulations were carried out for the $s = 1 - 50$ harmonics. . . . .	132

# List of Figures

1.1	Wave velocity diagram for the three MHD wave modes. The left diagram, (a), displays group velocity, (b), shows the wave mode phase velocities for the low $\beta$ case. The length of the radius from the origin to a point on the associated closed curve is proportional to the wave vector. . . . .	19
1.2	Model of a straight magnetic cylinder of radius $a$ , with the parameters of the internal and external plasma labelled. . . . .	20
1.3	The profiles of plasma cylinder perturbations for different modes. Left: Symmetric (sausage) and Right: Antisymmetric (kink) perturbations of a straight cylinder. . . . .	22
1.4	Schematic diagram showing electron oscillations around the ion background, (image from [Tesla, 2013]). . . . .	23
1.5	Dispersion relations for electromagnetic waves, Langmuir waves, and ion-acoustic waves in an unmagnetised plasma. In the dotted regions the waves are strongly damped, according to kinetic theory, figure from [Baumjohann and Treumann, 2012]. . . . .	24
1.6	Relative electron and ion gyration directions and radii (not to scale). . . . .	25
1.7	Top: The dispersion curves for parallel propagation are shown on the $\omega k$ -plane. Bottom: The dispersion curves for perpendicular propagation are shown on the $\omega k$ -plane, from [Baumjohann and Treumann, 2012]. . . . .	26
1.8	Maxwellian distribution for a one dimensional plasma. Particles slower than the $v_{ph}$ absorb energy from the waves. Particles faster lose energy to the wave. . . . .	29

1.9	Schematic diagram to illustrate the direction of diffusion for a cold ion beam. Blue denotes the proton bulk while red the energetic alpha beam which has been used as a proxy for a proton beam. The diffusion paths are shown around the position of the parallel phase speed $v_{ph}$ . The beam speed of a particle in the proton frame $U_i$ is shown by the green dash iso-contours. a) $U_i < v_{ph}$ and b) $U_i > v_{ph}$ . Similarly (c-e) show the diffusion of particles in velocity space for the cyclotron-resonance due to the presence of an alpha particle beam. c) $U_i < v_{ph}$ , d) $U_i > v_{ph}$ , e) $v_{ph} < 0$ . (Image from [Verscharen and Chandran, 2013]). . . . .	31
1.10	A bi-Maxwellian distribution is used to describe a plasma with a beam or a two stream plasma system. The positive gradient in the distribution gives rise to the beam instability. The red region contains particles with $v < v_{ph}$ which stand to gain energy from the wave while the blue region contains particles with $v > v_{ph}$ which stand to lose energy. . . . .	33
1.11	The image shows the effect of the ion-cyclotron and firehose instabilities on a long element of plasma. Colour contours encode the background magnetic fluctuations generated by ion-cyclotron (left) and fire-hose (right) instabilities. The density of protons at the current sheet at the same simulation time is reported on the superimposed black solid line contour. The arrows show the local direction of the resulting contribution to the electric field component $E_x$ generated by the magnetic fluctuations in the figure. Adapted from [Matteini et al., 2013]. . . . .	34
1.12	The left shows magnetic field and plasma density within mirror mode waves. The right shows the satellite measurements across the mirror-unstable relation region, from [Treumann and Baumjohann, 1997]. . . . .	36
2.1	The variability of solar wind speed with inclination from the ecliptic plane, [NASA, 2014a]. . . . .	38

2.2	The Parker solar wind model solutions, values are normalised to the critical radius $r_c$ and sound speed $c_s$ . Types I and II are double valued proving to be non-physical. Types III has supersonic speeds at the Sun which are not observed. Types IV is excluded due to the infinite densities predicted in the heliosphere. Hence we are left with the unique solution of type V which passes through the critical point ( $r = r_c, v = c_s$ ) and is given by $C = -3$ . This is known as the ‘solar wind’ solution [Parker, 1958]. . . . .	39
2.3	Left: A small scale X-15 missile placed in supersonic flow to produce an oblique shock wave at the nose of the model, shown by the straight lines directed at an angle to the nose. (Image from [NASA, 2014g]). Right: photograph of bow shock waves around a blunt object, displayed as the black curve ahead of the object. (Image from [NASA, 2014f]). . . . .	41
2.4	Schematic diagram of the interaction between the high speed solar wind and the Earth’s magnetic field. The white arrows indicate the direction of plasma flow while the grey arrows show the movement of charges along the plasma boundary layer. Finally the red arrows indicate the direction of charged particles along the plasma sheet boundary layer, [Reiff, 1999]. . . . .	42
2.5	Schematic view of the terrestrial foreshock system. The solar wind direction is shown from left to right. The bow shock is represented by the curved purple line. Representative 2D particle velocity distributions are shown to give an understanding of the large variation in distributions across the foreshock, [Eastwood et al., 2005]. . . . .	43
2.6	A kinetic simulation of the foreshock region where $d_i$ refers to the cell number in the $X$ and $Y$ directions. The magnetic field lines structure is overlaid in white. The colour range is prescribed by the total ion temperature. Although bow shock and foreshock temperatures are not negative in this simulation the scale was shifted to provide improved contrast in the image, from [Karimabadi et al., 2014]. . . .	44
2.7	Unstable ion beam effects in the foreshock region (left). Electron and ion foreshock geometries (right). (Image from [Treumann and Baumjohann, 1997]). . . . .	45
2.8	The solar structure. (Image from [Infactcollaborative, 2014]). . . .	46

2.9	Top: Image of the photosphere with a few sunspots present. Bottom: An image of the chromosphere. These images were taken by the Solar Dynamics Observatory (SDO) on the 16/11/2014. The numbers identify different active regions according to the NOAA classification scheme. . . . .	47
2.10	Large structured loop arcades demonstrate the inhomogeneity of the solar corona. (Image from [NASA, 2014e]). . . . .	48
2.11	Variation of the temperature versus the height above the photosphere. (Image from [Yang et al., 2009]). . . . .	49
2.12	A image showing the plethora of phenomena found in the solar corona, including coronal loops, flares, coronal mass ejections, sunspots and prominences, from [NASA, 2014b]. . . . .	50
2.13	The standard model according of a flare, initially a prominence rises (a), this triggers magnetic reconnection beneath a prominence (b), shown in side view (b'), and ends with the draining of chromospheric plasma from the flare loops (c). 'LPS' refers to $H_\alpha$ loops which tend to be the most dense regions, from [Hirayama, 1974]. . . . .	52
2.14	a) Integrated flux time profile of microwave emission at 17 GHz for the solar flare of 08/05/1998, as recorded by NoRH. The dashed line is the background emission profile obtained from the integrated flux signal which was smooth using a 20s window. b) The background subtracted signal. c) Microwave emission profiles at 9.4 GHz (dot-dashed line), 17 GHz (solid line) and 3.75 GHz (dotted line), acquired by the Nobeyama Radiopolarimeters, from [Inglis et al., 2008]. . . .	54
2.15	An example of a typical radio spectrogram of a solar flare. At low frequencies the radio emission is predominantly type III bursts. The brightest feature is a type V event. At high frequencies, synchrotron emission of mildly relativistic electrons dominates. In the mid-frequency range from 800–2000 MHz, narrowband spikes of the decimetric type can be seen, from [Benz, 2008, Figure 28]. . . . .	55
2.16	A sample dynamic spectrogram exhibiting a ZP structure from the event of 21/04/2002 at 02:00:43-02:01:03 UT, from [Chernov et al., 2005]. . . . .	58
2.17	An example of a large stripe number ZP radio emission. The highly polarised ZP was observed by the Huairou radio observatory near Beijing. . . . .	59



2.18	Proposed extended source of the double plasma resonance emission mechanism, from [Winglee and Dulk, 1986]. . . . .	59
2.19	Energy flow for the production of ZP using the DPR emission mechanism. This is an adaptation of the plasma emission theory from [Ginzburg and Zhelezniakov, 1958], with the inclusion of the DPR mechanism (red). The radio emission mechanisms are highlighted in green. . . . .	61
3.1	Artist’s impression of the four satellites of Cluster in orbit, (Image from [ESA, 2014b]). . . . .	64
3.2	Cluster Orbit plot for the 27/01/2004, the left, displays the tetrahedral formation, the right, demonstrates Cluster’s elliptical orbit. The orbit plots also presents lines to show the average positions of the bow shock and magnetopause, from [ESA, 2014a]. . . . .	65
3.3	Schematic diagram of the geocentric solar elliptical coordinate system used by the Cluster satellite group. . . . .	67
3.4	Schematic diagram of Hot Ion Analyser (HIA) high and low sensitivity sections. (Image from [Rème et al., 2001]). . . . .	68
3.5	Left: schematic diagram of the Wind satellite, image from [NASA, 2014c]. Right: six month orbit given in GSE coordinates, starting in July 2009, image from [NASA, 2014d]. . . . .	69
3.6	Photograph of the array of dishes at the Nobeyama Radioheliograph, Japan. (Image from [NOAJ, 2014]). . . . .	70
4.1	Cluster overview showing key parameters, for the 27/01/2004 with a plot of the constellation position in relation to the bowshock displayed in the upper right panel. This interval exhibits a clear increase in electric field wave power at discrete frequencies, seen to occur at 2:00 am. The higher resolution magnetic field data was needed to observe fluctuations clearly. . . . .	75
4.2	Example of structured fluctuations found in the foreshock region. A 70 s snapshot taken from the 27/01/04 interval. . . . .	77

4.3	Upper panel: The normalised magnetic field magnitude and proton density used in the correlation analysis. Lower panel: A representative cross correlation analysis for the interval: 27/01/2004, time: 03:50-04:35 for magnetic field magnitude and proton density. Magnetic field strength and density were found to be strongly correlated with a coefficient of 0.9907. All other intervals exhibit a similar form and correlation value. . . . .	79
4.4	The power spectra were calculated for the representative interval 27/01/2004 and an interval where the Cluster satellite group was upstream of the foreshock region, a data sample considered to be free of the foreshock interaction. The black curve denotes the power as a function of frequency for the upstream solar wind region. The red curve displays the power as a function of frequency for the 27/01/2004 interval. Two distinct peaks above the solar wind spectrum were found at frequencies of $\sim 0.04$ Hz and $\sim 1$ Hz. This was in agreement with the frequency ranges for ULF waves 5 mHz to 0.1 Hz and the whistler wave which is found at $\sim 1$ Hz as outlined in section 4.1.1. .	82
4.5	Dynamical spectrum of the solar wind interval (upper panel) shows that background turbulence has the majority of its power in the lower frequency modes. With the presence of fluctuations (lower panel) a sudden increase in density at a higher frequency range was observed. Some higher frequencies are seen intermittently in the solar wind panel (left) however we define wave activity as a sustained increase in power, these could be intermittent bursts of waves or just background turbulence being advected past the satellite. . . . .	84
4.6	A sample of hodograms of Cluster magnetic field data taken from the canonical sample 27/01/2004 from 04 : 03 : 20 onwards. Nine samples were taken, each five seconds in length. The magnetic field was projected on the plane perpendicular to the sample average magnetic field which is directed out of the page in all figures. Some panels show distinct left handed polarisation while others show a more noisy fluctuation. . . . .	86

4.7	A sample of Cluster magnetic field data taken from the canonical sample 27/01/2004 at 03:48:35 for 15 s projected onto the plane perpendicular to the sample average magnetic field. The hodogram clearly shows the two periodicities observed in the power spectrum shown in section 4.3.4. The lower frequency ULF wave underwent half a period of rotation while the ‘1 Hz’ whistler was seen to last for about six cycles of the oscillation during the same time interval. . . . .	88
4.8	Auto correlation analysis for high resolution Cluster magnetic field data for the canonical sample 27/01/2004. A peak was found at 19 s corresponding to a frequency of 0.05 Hz which was in close agreement with the result derived by the power spectrum of 0.04 Hz, section 4.3.4. . . . .	88
4.9	A flow chart to demonstrate how the collected information was used to identify the intrinsic polarisation of the ULF waves found in the data samples. The flow chart was based on a left-handed spacecraft polarisation input. If the input was right-handed in the spacecraft reference frame the chart is simply inverted. . . . .	90
4.10	A study into compressibility using magnetic field data as a proxy. Differential analysis was carried out on the pre-foreshock solar wind (dotted black) and both IR (solid black) and IL (solid red) data samples. An increase, above the turbulence level, in compressibility was observed in both IL and IR with distinct peaks found in both. . . .	92
4.11	A contour plot is presented for the grouping of $(\beta, R)$ in the Wind/SWE data for the period of (1995-2001), the p subscript denotes that these have been plotted for protons. The curves show the contours of the maximum growth rate (normalised to $\omega_{ci}$ ) in the plasma (left) for the proton cyclotron instability (solid curves) and the parallel fire hose (dashed curves) and (right) for the mirror instability (dotted curves) and the oblique fire hose (dash-dotted curves), [Hellinger et al., 2006, Figure 1]. . . . .	95
4.12	Anisotropy plots for the intrinsically right-hand polarised intervals for both Cluster 1 and Cluster 3. The curves show the maximum growth rates for the proton cyclotron instability (solid black curve), mirror instability (dashed black curve), oblique fire hose instability (green dashed curve) and the parallel fire hose instability (solid green curve). The growth rates were plotted for $\gamma_{max}=10^{-3}\omega_{ci}$ . The colour was assigned using the Cluster HIA ion temperature data. . . . .	96

4.13	Anisotropy plots for the intrinsically left-hand polarised intervals for both Cluster 1 and Cluster 3. The curves show the maximum growth rates for the proton cyclotron instability (solid black curve), mirror instability (dashed black curve), oblique fire hose instability (green dashed curve) and the parallel fire hose instability (solid green curve). The growth rates were plotted for $\gamma_{max}=10^{-3}\omega_{ci}$ . The colour was assigned using the Cluster HIA ion temperature data. . . . .	97
4.14	(a) Ensemble averaged distribution of counts for all intervals with left-hand polarisation. (b) Same as (a) for the ensemble of right-hand polarisation. (c) Pixelised plot of the ensemble averaged, normalised proton temperature at $(\beta_{\parallel}, R)$ for the left-handed intervals. Only bins with counts larger than 3 are considered. (d) same as (c) for the right-hand intervals. The curves show the maximum growth rates for proton cyclotron instability (solid black curve), mirror instability (dashed black curve), oblique fire hose instability (green dashed curve) and the parallel fire hose instability (solid green curve). The growth rates were plotted for $\gamma_{max}=10^{-3}\omega_{ci}$ , from [Selzer et al., 2014].	99
4.15	(a) A Comparison of the upstream solar wind anisotropy, as seen by Wind spacecraft (black solid line) with that observed by Cluster spacecraft (red solid line) is presented. The dashed blue curve shows the integrated wavelet coefficient power in the ULF frequencies of 0.02 – 0.06 Hz. (b, c) Distribution of counts for Cluster and Wind spacecraft, from [Selzer et al., 2014]. . . . .	100
4.16	Magnetic field strength down-sampled to 4 sec. resolution (black line) and HIA proton density (blue line) (a), ion temperature (b), temperature anisotropy ratio $R$ (c), normalised first adiabatic invariant (d) and normalised second adiabatic invariant (e) for the interval: 27/01/2004 4:07-04:26. Solid symbols (circles) in panel (c) indicate temporal position of 30 highest temperature measurements. Dashed vertical lines indicate examples of drops in the anisotropy trace, which are not coinciding with a significant magnetic field strength change, from [Selzer et al., 2014]. . . . .	104
5.1	The symmetric Epstein profile representing the plasma density across a coronal loop, normalised to the width parameter $\delta$ and the maximum density, $\rho_{max}$ (see [Adams, 1981, Nakariakov and Roberts, 1995]). . .	107

5.2	The dispersion relation plotted for equation 5.9. The solution is confined between the region of $v_{A0} < a < v_{A\infty}$ in phase speed ( $v_{A0}$ is chosen at 0.3). A cutoff wavelength $k_c$ also prescribes the domain in $k$ space to insure a real phase speed defined as $k_c$ . . . . .	109
5.3	The normalised transverse profile of plasma velocity perturbations in a sausage mode was plotted for various values of normalised longitudinal wave number $k$ as a function of the transverse spatial variable $x$ . . . . .	110
5.4	The normalised density perturbations were plotted for the loop apex ( $x = 0$ ) (solid line) and the loop edge ( $x = \delta$ ) (dotted line). A clear regular oscillation was seen in both regions with the greatest amplitude shown in the loop apex. . . . .	111
5.5	The analytically derived zebra pattern in radio emission is recreated. The zebra pattern clearly exhibits the ‘wiggle’ result shown in [Yu et al., 2013, figure 1, section 1]. . . . .	114
5.6	The $s$ harmonics of $f_{ce}$ are plotted (solid black) against $f_{uh}$ (dashed). Intersections are where the DPR condition was satisfied. . . . .	116
5.7	The following are plotted for the one dimensional zebra pattern emission system for both high and low altitude solutions: The stripe spacing is plotted against the double resonance harmonic number; the stripe spacing is plotted against stripe frequency; the stripe spacing is plotted against stripe emission height and finally the frequency is plotted against stripe emission height. . . . .	117
5.8	Normalised transverse and longitudinal electron density (dashed) and absolute magnetic field (solid) profiles for the static 2D loop model. The loop’s density structure was used to solve for the magnetic field under equilibrium conditions according to [van Hoven et al., 1977]. . . . .	119
5.9	The 2D static loop model for ZP emission using the DPR mechanism. Magnetic field, electron density, upperhybird frequency and ZP locations are plotted onto the 2D loop. . . . .	120
5.10	A 2D static loop model for ZP emission using the DPR mechanism zoomed in the vicinity of one of the footpoints. Magnetic field, electron density, upperhybird frequency and ZP locations are plotted onto the 2D loop. . . . .	121

5.11	Schematic diagram outlining the observations of [Chen et al., 2011]. The ZP sources are located at a height of 60 – 80 Mm in a post flare/post-CME loop system. The ZP source region was observed to be extended across a height range of $\approx 20$ Mm. Within the zebra source, individual stripes correspond to emissions near the local plasma frequencies at the DPR levels (horizontal dashed lines, of which the lowest one corresponds to the $s = f_{pe}/f_{ce} = 8$ layer). . . .	124
5.12	The numerical grid used in the Lare2D numerical software. . . . .	126
5.13	Illustration of the straight slab geometry. $L$ is the loop length with $2a$ representing the cross-sectional width. A uniform magnetic field is shown as $B_0$ with internal and external density values given by $\rho_0$ and $\rho_e$ respectively. The colour denotes the scaling of the density structure. . . . .	128
5.14	The transverse velocity is measured across the loop performing a sausage oscillation and plotted. It shows identical form as that demonstrated in figure 5.3 produced from an analytical investigation. . . .	130
5.15	Snapshots of the evolutions of the pulses in the slab and the simulated spectrum with ZP structures of the fast-propagating mode (first row) and the fast-standing mode (second row). The $x$ -component of velocity $V_x$ is shown at times of 0, $\frac{1}{4}$ , $\frac{1}{2}$ , 1 of the simulation runtimes. The simulation runtimes $\tau_1$ and $\tau_2$ for each wave were 20 s and 5 s respectively. The grey contours in the snapshots show the position of the resonance levels. . . . .	131
6.1	Full disk <i>SOHO/EIT</i> 195 Å at 03:00:01 UT and NoRH 17 GHz intensity images at 02:47:09 UT on 13/12/2006. Insets show the <i>TRACE</i> 195 Å image and the enlarged NoRH 17 GHz image of AR 10930, from [Yu et al., 2013]. . . . .	138
6.2	The various image processing techniques used in the extraction of ZP stripe data. In image: a) the original image is displayed; b) the trend has been removed; c) a low pass filter was applied; d) a threshold filter was applied; e) the image was thinned to stripes and f) the final stripe locations are plotted over b). . . . .	139

6.3	Zebra pattern structures on 13 December 2006 02:43:00-02:43:25 UT and 03:03:00-03:03:20 UT observed by <i>SBR/Suairou</i> at 2.6-3.8 GHz, and the illustration of the processes of extracting the zebra pattern stripes. a,b) The raw spectrograms at 2.6-3.8GHz on LHCP; c,d) high contrast images; e,f) the rescaled images with the extracted stripes superimposed; (g, h) the de-trended stripes frequency $f_N$ , from [Yu et al., 2013]. . . . .	141
6.4	Periodograms and auto-correlation functions of QPP components of a,b) stripe frequency $f_N$ and c,d) frequency separation $\Delta f_N$ in the ZP structure (ZP1) recorded on 13 December 2006, 02:43:00-02:43:25 UT: red line for $f_1$ , yellow line for $f_2$ , green line for $f_3$ , blue line for $f_4$ . The horizontal line in periodograms indicates the 99.99% confidence level for the highest spectral peak, calculated using the Fisher randomisation test detailed in section 6.5.2. The confidence levels for each trace were tightly packed in the power range therefore a representative level was plotted. Figure taken from [Yu et al., 2013].	144
6.5	Periodograms and auto-correlation functions of QPP components of a,b) stripe frequency $f_N$ and c,d) frequency separation $\Delta f_N$ in the ZP structure (ZP2) recorded on 13 December 2006, 03:03:00-03:03:20 UT: red line for $f_1$ , yellow line for $f_2$ , green line for $f_3$ , blue line for $f_4$ . The horizontal line in periodograms indicates the 99.99% confidence level calculated using the Fisher randomisation test detailed in section 6.5.2. Figure taken from [Yu et al., 2013]. . . . .	145

# Acknowledgments

First and foremost I would like to thank my family, Albert, Ronéll and brother Sean who have always been nothing but supportive and encouraging throughout my time at the University of Warwick. I would like to thank my supervisors Dr. Bogdan Hnat and Prof. Valery Nakariakov for their support, guidance and endless enthusiasm which has made my PhD a challenging yet satisfying experience.

Thanks also to members of the CFSA and other postgraduate students in the physics department, for insightful discussions and distractions, both work related and otherwise. I am also grateful to the STFC for financial assistance through the STFC studentship. Finally, I would like to thank the University of Warwick American Football club for making my time as a PhD student that much more enjoyable.



# Declarations

This thesis is submitted to the University of Warwick in support of my application for the degree of Doctor of Philosophy. It has been composed by myself and has not been submitted in any previous application for any degree or at any other university.

The work presented here was carried out by the author except in the cases outlined below: Figure 6.1 and Figure 6.4 which were made by Sijie Yu. Figures from Chapter 6 were made by Sijie Yu during collaboration work at the University of Warwick which resulted in the paper detailed below. Figure 4.14, 4.15 and 4.16 were reproductions produced by Dr Bogdan Hnat for the paper detailed below.

The work presented in this thesis is based on the following peer-review journal articles:

- S. Yu, V. M. Nakariakov, L. A. Selzer, B. Tan, and Y. Yan. Quasi-periodic Wiggles of Microwave Zebra Structures in a Solar Flare. *ApJ*, 777:159, November 2013.
- L. A. Selzer, B. Hnat, K. T. Osman, V. M. Nakariakov, J. P. Eastwood, and D. Burgess. Temperature Anisotropy in the Presence of Ultra Low Frequency Waves in the Terrestrial Foreshock. *ApJ*, 788:L5, June 2014.

# Abstract

In this thesis the effect of collective particle behaviour within a plasma was explored using kinetic plasma theory in conjunction with magnetohydrodynamics (MHD). Collisionless or quasi-collisionless space plasmas were used as test laboratories in an attempt to understand the evolution of space plasmas. In a collisionless plasma, forces and fields are mediated through collective behaviour such as instabilities and plasma waves, thus the plasma parameters evolve due to modification by collective effects. In this work we implemented analytical and numerical techniques to predict the effect of collective behaviour. These hypotheses were then tested against experimental data as a validation process.

The region near the Earth's bow shock where incoming solar wind interacts with plasma emanating from the bow shock is known as the foreshock. This region is an abundant source of complex particle distributions with associated collective phenomena. We report the first observation of correlation between elevated solar wind core plasma temperatures and temperature anisotropy in the terrestrial foreshock. Direct comparison of contemporaneous anisotropic temperatures in the upstream solar wind and the foreshock suggests that the net heating of plasma is mediated via a increase of the parallel temperature in the foreshock region where ultra low frequency (ULF) plasma waves have been observed. We consider the possibility that a mechanism based on Landau damping, where solar wind plasma temperature parallel to the background magnetic field is increased by interaction with oblique compressible fast magneto-acoustic ULF waves, influences temperature anisotropy.

Next the impact of wave phenomena on the radio emission fine structure in flaring loops of the solar corona was investigated. In particular, the impact of MHD oscillations on zebra pattern (ZP) radio emission. Initially static analytical studies were carried in one and two dimensions to show it was possible to derive a ZP using MHD techniques. The dynamics of ZP formation in the presence of MHD oscillations were then analytically studied to show the presence of 'wiggles' in the ZP. These results were then repeated using numerical simulations using the Lare2D MHD code. The catalogue of results suggests that the detected ZP wiggles were caused by a standing sausage oscillation. We affirm this conclusion using the observation that both instant frequencies of individual stripes and their spectral separation oscillate with the same periods. Thus it is consistent with a sausage oscillation that perturb both the plasma density and magnetic field. These results

are further underpinned by comparison to experimentally obtained ZP wiggles which exhibit similar periodicities. This new result could lead to a method for the direct measurement of coronal magnetic fields in flaring loops.

# Chapter 1

## Introduction

### 1.1 Basic Plasma Physics

#### 1.1.1 Definition of a Plasma

A plasma is defined as a state of matter consisting of a fully or partially ionised gas which exhibits electric charge *quasi-neutrality*, [Sturrock, 1994]. An ideal plasma consists of equal numbers of free positive and negative charges usually ions and electrons. The relative concentration of free charges should exceed a threshold for the medium to be considered as a plasma. Also, in a plasma above a certain spatial scale the average number of electrons within a volume almost equals the electric charge of the ions thus producing an overall neutral state or quasi-neutrality.

#### 1.1.2 Characteristic scales of plasma dynamics

##### Temporal Scales

If a disturbance is introduced to the quasi-neutrality of the plasma, the electrons, in contrast to the much more inertial ions, will move to reinstate the equilibrium condition. In the process of doing this the electrons oscillate around the equilibrium at the electron plasma frequency, [Davies and of Electrical Engineers, 1990]:

$$\omega_{pe} = \left( \frac{n_e e^2}{m_e \varepsilon_0} \right)^{\frac{1}{2}}, \quad (1.1)$$

with  $n_e$  the electron number density,  $e$  is the elementary charge,  $m_e$  is the electron mass and  $\varepsilon_0$  the permittivity of free space. The electron plasma frequency is an important parameter as it defines the time scales in which the effects of electric field disturbances are important. Another important timescale that must be addressed

is the gyro-frequencies of the electrons and ions. As seen in the theory of electrodynamics, [Griffiths, 1999], electrons and ions gyrate around magnetic field lines at specific frequencies. The gyro-frequency for the  $s$ -species in a plasma is defined as, [Chen, 1984]:

$$\omega_{cs} = \frac{q_s B}{m_s}, \quad (1.2)$$

where  $B$  is the magnetic field strength,  $q_s$  and  $m_s$  is the respective charge carrier mass and charge. This frequency is also referred to as the *cyclotron frequency* or *Larmour frequency*.

### Spatial scales

The *gyroradius* is an important quantity to define spatial scales of the plasma, for the  $s$  species it is defined as:

$$r_{cs} = \frac{v_{\perp s}}{|\omega_{cs}|} = \frac{m_s v_{\perp s}}{|q_s| B}, \quad (1.3)$$

where  $v_{\perp s}$  is the particle velocity in the plane perpendicular to the magnetic field. The *Debye sphere* is a sphere with radius equal to the ‘Debye length’,  $\lambda_D$  defined as, [Clemmow and Dougherty, 1969]:

$$\lambda_D = \left( \frac{\varepsilon_0 k_B T_e}{n_e e^2} \right)^{\frac{1}{2}}, \quad (1.4)$$

with  $k_B$  the Boltzmann constant and  $T_e$  electron temperature. Outside of this volume charges are electrically screened such that larger volumes can be considered as quasi-neutral.

## 1.2 Kinetic Plasma Theory

The starting point of modelling a plasma is to consider the collective behaviour of the electrons and ions within the quasi-neutral fluid. This approach is encompassed by kinetic plasma theory. The basis of using this method is anchored in the existence of long range electromagnetic interaction between charged particle components via the generation of electric  $\mathbf{E}(\mathbf{x}, t)$  and magnetic  $\mathbf{B}(\mathbf{x}, t)$  fields. The other charge carriers then respond to these fields and undergo energy and momentum exchange.

In order to consider a macroscopic plasma, the contribution to  $\mathbf{E}(\mathbf{x}, t)$  and  $\mathbf{B}(\mathbf{x}, t)$  from each particle would need to be incorporated, which creates an extremely complicated spatial structure for a many bodied system. This can quickly become

a highly complex and thus untreatable task. Hence using a statistical description reduces the size of the task while retaining the underlying physics of the system.

### 1.2.1 Phase Space Description

The plasma as a medium and its evolution can be described fully by a six dimensional *phase space*. This method is a well established approach for plasma modelling, the overlying theory and derivations can be found in a number of texts [Mandl, 2013, Baumjohann and Treumann, 2012, Krall and Trivelpiece, 1986, Montgomery and Tidman, 1964, Vlasov, 1961]. Each particle is tracked through this parameter space by its position  $\mathbf{x}_i(t)$  and velocity  $\mathbf{v}_i(t)$  as a function of time, where  $i$  denotes individual particles. The plasma can then be modelled by its particle density function as a summation over every particle contained therein:

$$\mathcal{F}(\mathbf{x}, \mathbf{v}, t) = \sum_i \delta(\mathbf{x} - \mathbf{x}_i(t)) \delta(\mathbf{v} - \mathbf{v}_i(t)), \quad (1.5)$$

where the  $\delta$  represents the three dimensional Dirac delta functions.

Further equations are required to adequately understand the evolution of particles within the plasma and as a result the medium in it's entirety. The equation of motion for a charged particle in the presence of electric and magnetic fields is given by the Lorentz force, [Griffiths, 1999]:

$$m_i \frac{d\mathbf{v}_i}{dt} = q_i(\mathbf{E} + \mathbf{v}_i \wedge \mathbf{B}). \quad (1.6)$$

To understand the impact of particles on one another a coupling is required between their respective equations of motion. This is sufficiently described through Maxwell's equations, [Maxwell, 1865]:

$$\nabla \wedge \mathbf{B}(\mathbf{x}, t) = \mu_0 \mathbf{j}(\mathbf{x}, t) + \varepsilon_0 \mu_0 \frac{\partial}{\partial t} \mathbf{E}(\mathbf{x}, t), \quad (1.7)$$

$$\nabla \wedge \mathbf{E}(\mathbf{x}, t) = -\frac{\partial}{\partial t} \mathbf{B}(\mathbf{x}, t), \quad (1.8)$$

$$\nabla \cdot \mathbf{E}(\mathbf{x}, t) = \frac{1}{\varepsilon_0} \rho(\mathbf{x}, t), \quad (1.9)$$

$$\nabla \cdot \mathbf{B}(\mathbf{x}, t) = 0, \quad (1.10)$$

where  $\mu_0$  and  $\varepsilon_0$  are the permeability and permittivity of free space, respectively. The coupling between particles is contained within the definition of the electric charge  $\rho$  and current density  $j$ . We define these as:

$$\rho(\mathbf{x}, t) = \sum_i q_i \int \mathcal{F}(\mathbf{x}, \mathbf{v}, t) d\mathbf{v}, \quad (1.11)$$

$$\mathbf{j}(\mathbf{x}, t) = \sum_i q_i \int \mathbf{v} \mathcal{F}(\mathbf{x}, \mathbf{v}, t) d\mathbf{v}, \quad (1.12)$$

where we have summed over all particles within the medium and integrated over the velocity parameter space to produce a spatial distribution of charge and current respectively.

In a macroscopic system such as a space plasma, the number of particles is very large and usually impossible to accurately evaluate. Therefore it is not possible to describe the motion of every particle, thus some form of averaging is required. Statistical kinetic theory smooths out the microscopic information of individual particles but still retains the observable phenomena. This is done by defining the particle distribution function:

$$f(\mathbf{x}, \mathbf{v}, t) = \langle \mathcal{F}(\mathbf{x}, \mathbf{v}, t) \rangle \quad (1.13)$$

The particle distribution function is averaged in one of two ways, the first is the mathematically rigorous method of producing an ensemble average over an infinite number of realizations which leads into statistical mechanics. However, for the purpose of this thesis the second method is sufficient, we consider the distribution function as a discrete distribution whereby particles are counted in definite boxes with size  $\Delta\mathbf{x}$  and  $\Delta\mathbf{v}$  respectively and binned correspondingly. This is an adequate approach as most instruments use this method when reproducing distribution functions from experimental data, these are often subsequently fitted to a Gaussian or Maxwell-Boltzmann distribution, [Mandl, 2013].

The distribution function  $f$  describes the plasma and its evolution, thus it is subject to manipulation through forces and external fields just as the particles it describes. The exact governing equation of the distribution function is very dependent on the environment it is applied to, predominantly based on the assumptions that can be made. As an estimate, the *Boltzmann equation* is generally used and can be derived using a variety of methods such as the ‘Klimontovich equation approach’ or the ‘Louiville equation approach’. The Boltzmann equation in this form neglects correlations between fields assuming the evolution can be modelled through particle interactions only. The derivations also assume the total number of particles are conserved by constraining the total derivative of the density function such that:

$$\frac{d\mathcal{F}}{dt} = 0 \quad (1.14)$$

The exact details of the derivation and the situational applicability of the terms in the Boltzmann equation encompass a large field of discussion but for simplicity the equation will be stated here without explicit derivation, however examples can be found in, [Vlasov, 1961]:

$$\frac{\partial}{\partial t}f + \mathbf{v} \cdot \nabla_{\mathbf{x}}f + \frac{q}{m}(\mathbf{E} + \mathbf{v} \wedge \mathbf{B}) \cdot \nabla_{\mathbf{v}}f = \left(\frac{\partial f}{\partial t}\right)_c. \quad (1.15)$$

The term on the right denotes the rate of change of the distribution function due to collisions of particles within the plasma. Again the exact nature of this term is dependent on the assumptions made however in this ideal case we assume the plasma to be collisionless and thus it tends to 0. This results in the well known *Vlasov equation*, [Vlasov, 1961, Krall and Trivelpiece, 1986]:

$$\boxed{\frac{\partial}{\partial t}f + \mathbf{v} \cdot \nabla_{\mathbf{x}}f + \frac{q}{m}(\mathbf{E} + \mathbf{v} \wedge \mathbf{B}) \cdot \nabla_{\mathbf{v}}f = 0}. \quad (1.16)$$

The Vlasov equation, supplemented by the Maxwell equations (1.7-1.10) forms the basis of all kinetic theory in all collisionless plasmas such as those found in the solar corona and solar wind. Although simplified, (1.16) still remains a highly non-linear equation in time and a six-dimensional phase space. This complexity requires further approximations to be made to find solutions under special conditions.

### 1.2.2 Macroscopic Variables

The fact that the distribution function represents the velocity, space and time of the particles within the system allows macroscopic quantities to be extracted. Physical quantities such as density  $n$ , bulk velocity  $\mathbf{V}$ , temperature  $T$  do not explicitly depend on the particle velocities. Hence to obtain these one would naturally integrate over the velocity space. These integration operations are known as ‘taking moments’. The  $i$ -th moment is defined as, [Montgomery and Tidman, 1964]:

$$\mathcal{M}_i(\mathbf{x}, t) = \int f(\mathbf{v}, \mathbf{x}, t) \mathbf{v}^i d\mathbf{v}, \quad (1.17)$$

where  $\mathbf{v}^i$  denotes the  $i$ -fold dyadic product. The result of this equation is a set of macroscopic variables:

$$n = \int f(\mathbf{v}) d\mathbf{v}, \quad (1.18)$$



$$\mathbf{V} = \frac{1}{n} \int \mathbf{v} f(\mathbf{v}) d\mathbf{v}, \quad (1.19)$$

$$\mathbf{P} = m \int (\mathbf{v} - \mathbf{V})(\mathbf{v} - \mathbf{V}) f(\mathbf{v}) d\mathbf{v}, \quad (1.20)$$

where  $m$  represents the particle species mass and  $\mathbf{P}$  is defined as the plasma pressure tensor. The  $(\mathbf{v} - \mathbf{V})(\mathbf{v} - \mathbf{V})$  term breaks down into several dyadic products:  $\mathbf{v}\mathbf{v} - 2\mathbf{v}\mathbf{V} + \mathbf{V}\mathbf{V}$ . The dyadic product results in a second order dyadic tensor from two vectors. If we let:

$$\begin{aligned} \mathbf{a} &= a_1 \mathbf{i} + a_2 \mathbf{j} + a_3 \mathbf{k}, \\ \mathbf{b} &= b_1 \mathbf{i} + b_2 \mathbf{j} + b_3 \mathbf{k}, \end{aligned} \quad (1.21)$$

such that:

$$\mathbf{ab} = \begin{pmatrix} a_1 b_1 & a_1 b_2 & a_1 b_3 \\ a_2 b_1 & a_2 b_2 & a_2 b_3 \\ a_3 b_1 & a_3 b_2 & a_3 b_3 \end{pmatrix}, \quad (1.22)$$

we form the dyadic tensor from two vectors. Here  $\mathbf{i}$ ,  $\mathbf{j}$  and  $\mathbf{k}$  are the Cartesian unit vectors.

### Understanding Temperature

The macroscopic temperature can be derived from kinetic theory using the definition of the pressure tensor (1.20) which is then substituted into the ideal gas equation, [Moran and Shapiro, 2006]:

$$p = nk_b T, \quad (1.23)$$

to produce the temperature tensor:

$$T = \frac{m}{k_b n} \int (\mathbf{v} - \mathbf{V}) \cdot (\mathbf{v} - \mathbf{V}) f(\mathbf{v}) d\mathbf{v}. \quad (1.24)$$

This temperature is the *kinetic temperature* which can be calculated for any distribution. Importantly though, it is not a true thermodynamic temperature but an estimate of the velocity distribution. In an anisotropic distribution this can be used to estimate the parallel and perpendicular temperatures independently, however non thermal distributions such as a bi-Maxwellian will result in an artificially high kinetic temperature, thus it is important to isolate the particle population of interest, a common occurrence in space plasmas.

This is helpful if we obtain an expression for the distribution function. However in experimental work this is rarely known. Instead the temperature can be derived using the plasma pressure. We can split the pressure tensor  $\mathbf{P}$  into components parallel and perpendicular to the field:

$$\mathbf{P} = p_{\perp} \mathbf{I} + (p_{\parallel} - p_{\perp}) \frac{\mathbf{B}\mathbf{B}}{B^2}, \quad (1.25)$$

which, in a coordinate system where the z-coordinate is field aligned, the tensor becomes:

$$\mathbf{P} = \begin{pmatrix} p_{\perp} & 0 & 0 \\ 0 & p_{\perp} & 0 \\ 0 & 0 & p_{\parallel} \end{pmatrix}. \quad (1.26)$$

such that:

$$\mathbf{T} = \frac{1}{nk_b} \begin{pmatrix} p_{\perp} & 0 & 0 \\ 0 & p_{\perp} & 0 \\ 0 & 0 & p_{\parallel} \end{pmatrix}, \quad (1.27)$$

which taking  $p_{\parallel} = p_{\perp} = p$  recovers the ideal gas equation for an isotropic plasma.

### 1.2.3 Adiabatic Invariants

Adiabatic invariants are physical quantities that change very slowly compared to typical periodicities of the particle motion. For particles in electromagnetic fields adiabatic invariants are associated with each type of motion the particle can perform. The magnetic moment  $\mu$  is associated with gyration around the magnetic field. The magnetic moment can be defined by the ratio between the perpendicular kinetic energy of the particle and the absolute value of the magnetic field, which for an isotropic medium is defined as:

$$\mu = \frac{mv_{\perp}^2}{2B}, \quad (1.28)$$

where  $v_{\perp}$  is the total perpendicular speed in an isotropic medium. When  $\mu$  is expressed in average quantities such as those derived in section 1.2.2 it can be expressed as:

$$\langle \mu \rangle = \frac{k_B T_{\perp}}{B} = \frac{p_{\perp}}{nB}, \quad (1.29)$$

because  $\langle \mu \rangle$  is an ensemble average it must be conserved, thus the right hand side is a constant.

### 1.3 Magnetohydrodynamics (MHD)

In many situations it is not necessary to know the exact evolution of the distribution function as outlined in section 1.2. In these cases it pays to consider only the macroscopic moments such as densities, velocities and temperatures as defined in section 1.2.2. The resulting theory falls under the category of fluid theories due to its hydrodynamic nature. Hence the name *magnetohydrodynamics* (MHD), the study of electrically conducting fluids which interact with external electric and magnetic fields.

#### 1.3.1 Multi-Fluid Theory

The MHD used in solar physics is usually a single fluid approximation of the more general *multi-fluid MHD theory* for plasmas, which is derived from the Vlasov equation (1.16). It is then natural to start by stating the full multi-fluid theory and then applying the one-fluid approximations.

The aim of multi-fluid theory is to describe the evolution of macroscopic quantities such as number density  $n_s(\mathbf{x}, t)$ , bulk flow velocity  $\mathbf{V}_s(\mathbf{x}, t)$ , pressure tensor  $\mathbf{P}_s(\mathbf{x}, t)$  and the kinetic temperature  $T_s(\mathbf{x}, t)$  for each particle species  $s$  within the plasma, in the first order case only electrons and ions are considered. Moments can be derived by integration over velocity space of the Vlasov equation (1.16) according to the method detailed in section 1.2.2. The results of this procedure are stated here, for a full derivation consult the work of [Baumjohann and Treumann, 2012, Davidson, 2001, Krall and Trivelpiece, 1986], one of many works on the topic. The zero-order moment produces what is known as the *continuity equation*:

$$\frac{\partial n_s}{\partial t} + \nabla \cdot (n_s \mathbf{V}_s) = 0. \quad (1.30)$$

The physical interpenetration of this equation is mass and charge density conservation in a plasma system where particles of species  $s$  are neither created nor destroyed.

The continuity equation is the first of the multi-fluid plasma equations as it forms an equation where velocity is coupled with density. Another equation is required for velocity to solve for the density field of the plasma. This naturally follows by repeating the procedure but this time using the first moment treatment of the Vlasov equation to produce the *Navier-Stokes* equation, [Landau and Lifshitz, 1989]:

$$\frac{\partial}{\partial t}(n_s \mathbf{V}_s) + \nabla \cdot (n_s \mathbf{V}_s \mathbf{V}_s) + \frac{1}{m_s} \nabla \cdot \mathbf{P}_s - \frac{q_s}{m_s} n_s (\mathbf{E} + \mathbf{V}_s \wedge \mathbf{B}) = 0. \quad (1.31)$$

This equation is responsible for momentum density conservation and force consideration in the plasma fluid.

With each iteration of the moment procedure, the previous quantity i.e. number density is fully described by involving a higher order variable such as velocity in this case. Thus the system is never closed. The last equation we will consider will describe the evolution of the pressure tensor  $\mathbf{P}_s$ . The resulting equation is known as the *energy density conservation equation*:

$$\frac{3}{2} n_s k_B \left( \frac{\partial T_s}{\partial t} + \mathbf{V}_s \cdot \nabla T_s \right) + p_s \nabla \cdot \mathbf{V}_s = -\nabla \cdot \mathbf{q}_s - (\mathbf{P}'_s \cdot \nabla) \cdot \mathbf{V}_s, \quad (1.32)$$

where  $T_s$  is the temperature defined by (1.24),  $p_s$  is the scalar plasma pressure and  $\mathbf{q}_s$  is the heat flux vector. The values  $p_s$  is found by assuming isotropy in the pressure tensor (1.26) such that  $p_\perp = p_\parallel = p_s$ .  $\mathbf{P}'_s$  denotes the stress tensor part of the full pressure tensor,  $\mathbf{P}_s$ , which describes the shear stress. In some cases the heat flux can be neglected and thus a closed system is formed. This approximation is not always valid however it is useful to derive a closed set of equations for MHD theory and the further simplified one-fluid theory.

### 1.3.2 One-Fluid Theory

A useful starting point is to consider the previously multi-species plasma as a singular charged fluid carrying magnetic and electric fields. As a result we can define some generalised average quantities, which have assumed no heavier species than the protons:

$$n = \frac{m_e n_e + m_i n_i}{m_e + m_i}, \quad (1.33)$$

$$m = m_i \left( 1 + \frac{m_e}{m_i} \right), \quad (1.34)$$

$$\mathbf{v} = \frac{m_i n_i \mathbf{V}_i + m_e n_e \mathbf{V}_e}{m_e n_e + m_i n_i}, \quad (1.35)$$

where  $n$  as the number density of charge carriers,  $m$  the fluid mass and  $v$  the velocity of each species. The charge and current densities are defined as:

$$\rho_c = e(n_i - n_e), \quad (1.36)$$

$$\mathbf{j} = e(n_i \mathbf{v}_i - n_e \mathbf{v}_e). \quad (1.37)$$

As  $m_e \ll m_i$  and the quasi-neutrality condition states  $n_i \simeq n_e$ , (1.33) - (1.35) approximate to  $n \simeq n_i \simeq n_e$ ,  $m \simeq m_i$  and  $\mathbf{v} \simeq \mathbf{v}_i$  respectively, the  $i$  subscript will be dropped. This assumption states that the global dynamics tend to be dominated by the ions and their inertia. This condition is only held under a slowly varying (on the order of the ion cyclotron frequency (1.2)) regime.

The MHD equations outlined in section 1.3 can be extracted from the multi-fluid theory.

### Continuity Equation

Again the starting point is the continuity equation, (1.30). If the equation for each species (electron and ion) is multiplied by the mass of the other and subsequently summed, the one-fluid version can be reached using the definition (1.33):

$$\frac{\partial n}{\partial t} + \nabla \cdot (n\mathbf{v}) = 0. \quad (1.38)$$

Which in keeping with the multi-fluid version maintains mass conservation in the non-relativistic plasma.

### Equation of Motion

Constructing the momentum density conservation equation for the total fluid is more difficult due to the non-linear  $n_s \mathbf{v}_s \mathbf{v}_s$  terms of (1.31). The detailed derivation can be found in [Baumjohann and Treumann, 2012, Chen, 1984] however for brevity it will just be quoted as:

$$\frac{\partial(nm\mathbf{v})}{\partial t} + \nabla \cdot (nm\mathbf{v}\mathbf{v}) = -\nabla \cdot \mathbf{P} + \rho_c \mathbf{E} + \mathbf{j} \wedge \mathbf{B}, \quad (1.39)$$

where  $\rho_c$  and  $j$  have come from the definitions (1.36 - 1.37). This equation ensures momentum conservation in the MHD system of equations.

### Generalised Ohm's Law

The momentum conservation equation (1.39) contains the electric current density,  $\mathbf{j}$  as a new variable. To close the set of equations one requires an expression for

the evolution of  $\mathbf{j}$ . This equation is the *generalised Ohm's law* of a plasma, [Somov, 2007]:

$$\frac{\partial \mathbf{j}}{\partial t} = -\frac{e}{m_e} \nabla \cdot \mathbf{P}_e + \frac{ne^2}{m_e} (\mathbf{E} + \mathbf{v}_e \wedge \mathbf{B}) + \frac{e}{m_e} (\mathbf{j} \wedge \mathbf{B}) - \frac{ne^2}{m_e} \hat{\boldsymbol{\eta}} \cdot \mathbf{j}, \quad (1.40)$$

where  $\hat{\boldsymbol{\eta}}$  is the resistivity tensor,  $e^2$  arises from Coulombic collisions between particles. The generalised Ohm's law can be explained through consideration of the individual terms. The term on the left hand side considers the electron inertia analogous to  $F = ma$ ; the first term on the right considers the force due to gradients in the electron pressure; the second considers the Lorentz force; the third on the right is considered as the hall term which accounts for the fact that electrons and ions decouple and move separately and the final term incorporates the electron drag on the ions (called the resistive term).

This equation implicitly implies that plasma resistivity,  $\mathbf{R}_{ei}$  can be modelled as as a collisional term between electrons and ions:

$$\mathbf{R}_{ei} = \eta e^2 n_e^2 (\mathbf{v}_i - \mathbf{v}_e) \quad (1.41)$$

where  $\eta$  is the specific resistivity.

### One Fluid MHD

Concluding the full set of equations, including the appropriate Maxwell equations (1.7 - 1.10), are listed:

$$\begin{aligned} \frac{\partial n}{\partial t} + \nabla \cdot (n\mathbf{v}) &= 0, \\ \frac{\partial(nm\mathbf{v})}{\partial t} + \nabla \cdot (nm\mathbf{v}\mathbf{v}) &= -\nabla \cdot \mathbf{P} + \rho_c \mathbf{E} + \mathbf{j} \wedge \mathbf{B}, \\ \frac{\partial \mathbf{j}}{\partial t} &= -\frac{e}{m_e} \nabla \cdot \mathbf{P}_e + \frac{ne^2}{m_e} (\mathbf{E} + \mathbf{v}_e \wedge \mathbf{B}) + \frac{e}{m_e} (\mathbf{j} \wedge \mathbf{B}) - \frac{ne^2}{m_e} \hat{\boldsymbol{\eta}} \cdot \mathbf{j}, \\ \nabla \wedge \mathbf{B} &= \mu_0 \mathbf{j} + \varepsilon_0 \mu_0 \frac{\partial \mathbf{E}}{\partial t}, \\ \nabla \wedge \mathbf{E} &= -\frac{\partial \mathbf{B}}{\partial t}, \\ \nabla \cdot \mathbf{B} &= 0. \end{aligned} \quad (1.42)$$

This system is also usually accompanied with an energy equation which depends on the nature of the pressure tensor. To simplify further the pressure tensor can

be taken to be isotropic such that it becomes a scalar quantity  $p$  for a uniform medium. In an MHD context the pressure can be expressed using (1.39) under the full electric neutrality, which cancels the  $\rho_c \mathbf{E}$ . It is then useful to eliminate the electric field using Faraday's law, (1.8):

$$\frac{\partial \mathbf{B}}{\partial t} = -\nabla \wedge \mathbf{E} = \nabla \wedge (\mathbf{v} \wedge \mathbf{B} - \eta \mathbf{j}). \quad (1.43)$$

Such that:

$$\boxed{\begin{aligned} \frac{\partial \rho}{\partial t} + \nabla \cdot (\rho \mathbf{v}) &= 0, \\ \frac{\partial(\rho \mathbf{v})}{\partial t} + \rho(\mathbf{v} \cdot \nabla) \mathbf{v} &= -\nabla p + \frac{1}{\mu_0} (\nabla \wedge \mathbf{B}) \wedge \mathbf{B}, \\ \frac{\partial \mathbf{B}}{\partial t} &= \nabla \wedge (\mathbf{v} \wedge \mathbf{B} - \eta \mathbf{j}), \\ \frac{\partial p}{\partial t} &= -(\mathbf{v} \cdot \nabla) p - \gamma p \nabla \cdot \mathbf{v}. \end{aligned}} \quad (1.44)$$

Which now contains an energy equation to close the isotropic uniform system. It is important to note that  $\rho = mn$  here is defined as the mass density not  $\rho_c$  which is the charge density described in (1.36). The full MHD energy equation can be derived by considering energy conservation. An expression can be found by multiplying the momentum conservation equation (1.39) by  $\mathbf{v}$  and manipulating the resulting expression with the implementation of the continuity equation to produce:

$$\frac{\partial}{\partial t} \left[ nm \left( \frac{1}{2} v^2 + w \right) + \frac{B^2}{2\mu_0} \right] = -\nabla \cdot \mathbf{q}, \quad (1.45)$$

where  $\mathbf{q}$  is the heat flux density vector and  $w$  is the free internal energy density also known as fluid enthalpy. The energy equation's derivation and its integration into the full set of MHD equations is beyond the scope of this work.

This set of equations provides a construct for modelling a plasma which doesn't require knowledge of the distribution function as outlined in section 1.2.1. This proves useful in the context of space plasmas as often in-situ observations of plasmas are not possible, therefore information must be extracted in the form of bulk parameters such as density,  $n$  or velocity  $v$ .

### 1.3.3 Plasma $\beta$

The interaction between the plasma and an external magnetic field induces a  $\mathbf{j} \wedge \mathbf{B}$  Lorentz force, defined in (1.6). This interaction carries the effect of the magnetic

field on a conducting MHD fluid. Using Maxwell's equation (1.7) we can write:

$$\mathbf{j} \wedge \mathbf{B} = -\nabla \left( \frac{B^2}{2\mu_0} \right) + \frac{1}{\mu_0} \nabla \cdot (\mathbf{B}\mathbf{B}). \quad (1.46)$$

The first term on the right corresponds to the magnetic pressure,  $p_B = B^2/2\mu_0$ , this ultimately adds to the thermal pressure to form the total pressure of the plasma. The second forms the magnetic stress tensor,  $\mathbf{B}\mathbf{B}/\mu_0$  which describes the magnetic stress in the plasma. This contributes to tension and torsion of the fluid. If we also assume equilibrium conditions such that  $\partial_t \rightarrow 0$  and  $v = 0$ :

$$\nabla \cdot \mathbf{P} = -\nabla \left( \frac{B^2}{2\mu_0} \right) + \frac{1}{\mu_0} \nabla \cdot (\mathbf{B}\mathbf{B}), \quad (1.47)$$

$\mathbf{P}$  is the gas pressure. If we take the isotropic pressure tensor such that  $\mathbf{P} = p\mathbf{I}$  and neglect off diagonal terms in the magnetic stress tensor, a homogeneous and straight field approximation we arrive at:

$$\nabla \left( p + \frac{B^2}{2\mu_0} \right) = 0. \quad (1.48)$$

Under these conditions we can define a plasma  $\beta$  parameter. The value  $\beta$  is used as a gauge whether a plasma is thermally or magnetically dominant, defined as, [Wesson and Campbell, 1997]:

$$\beta = \frac{2\mu_0 p}{B^2} = \frac{2}{\gamma} \frac{c_s^2}{v_A^2}, \quad (1.49)$$

where  $c_s$  is the plasma sound speed (defined in section 1.5 , equation 1.70) and  $v_A$  is the Alfvén speed (defined in section 1.5 , equation 1.72). Plasmas can be categorised by their  $\beta$  value i.e. A ‘hot plasma’ typically has  $\beta \gg 1$  and a ‘cold’  $\beta \ll 1$ . In anisotropic plasmas where the pressure tensor is split into parallel and perpendicular forms, as in section 1.2.2,  $\beta$  itself can be split accordingly:

$$\begin{aligned} \beta_{\parallel} &= \frac{2\mu_0 p_{\parallel}}{B^2}, \\ \beta_{\perp} &= \frac{2\mu_0 p_{\perp}}{B^2}. \end{aligned} \quad (1.50)$$

### 1.3.4 MHD Approximations

The use of MHD is only applicable under certain conditions, if these are not met more involved constructs such as resistive MHD or Chew-Goldberger-Low (CGL) (see [Chew et al., 1956]) are required. In certain cases a full kinetic approach is



needed, using techniques outlined in section 1.2.

MHD is a fluid theory and thus by definition certain restrictions are applied to the time and spatial scales. This approximation requires that the characteristic time scale of variation of the fluids and fields must be longer than the time scale of the heaviest particle, usually the ion (sometimes the alpha particle). Hence time scales should be larger than the ion cyclotron periods, (1.2). The assumption that electron dynamics will negate any fields produced enforces the restriction that time-scales are larger than those associated with plasma oscillations, (1.1):

$$\omega \ll \omega_{ci}, \omega_{pe}. \quad (1.51)$$

The same logic is applied to the spatial domain such that spatial scales should extend the ion gyroradius (1.3):

$$L \gg r_{gi}. \quad (1.52)$$

Magnetohydrodynamics is therefore restricted to very low frequencies and large spatial scales. We also state that all flows must be non-relativistic to avoid all relativistic terms, even so MHD proves very useful in space plasmas.

## 1.4 Plasma Wave Theory

A plasma, a charged fluid permeated by magnetic and electric fields provides the perfect environment for the appearance of a plethora of wave modes. In fact due to the high temperatures required for plasmas to exist and thus their high particle velocities it is impossible for a collision-less plasma to exist without collective motions. Microscopic charge separations produce restoring electric and magnetic forces. This background level of fluctuation is known as the *thermal fluctuation level*.

In addition to these unavoidable thermal fluctuations any plasma will react violently to external actions. Waves are the means in which these distortions are transported across the medium to communicate the energy and information to the entire plasma. These waves are not generated at random. In order for them to exist, first the wave must belong to one of the discrete modes as defined by the governing equations and secondly it can only be said to exist when its amplitude grows above the background fluctuation level. In line with this the linear growth rates must exceed non-linear such that the linear dispersion relation is defined. These waves are the linear eigenmodes of the plasma.

### 1.4.1 General Dispersion Relation

To thoroughly derive all possible wave modes a general dispersion relation is needed for a plasma. It is difficult to encompass the entirety of wave phenomena as non-linear effects can come into play in large amplitude waves, therefore in this section we restrict our analysis to linear waves which can be considered as small amplitude perturbations. This assumption holds for the remit of this thesis as our investigations only explore waves in the linear regime. As for most plasma properties the starting point is Maxwell's equations, (1.7-1.10) which can be written, [Maxwell, 1865]:

$$\nabla \wedge \mathbf{B} = \mu_0 \mathbf{j} + \varepsilon_0 \mu_0 \frac{\partial}{\partial t} \mathbf{E}, \quad (1.53)$$

$$\nabla \wedge \mathbf{E} = -\frac{\partial}{\partial t} \mathbf{B}, \quad (1.54)$$

$$\nabla \cdot \mathbf{B} = 0, \quad (1.55)$$

$$\nabla \cdot \mathbf{E} = \frac{1}{\varepsilon_0} \rho_c. \quad (1.56)$$

This derivation assumes the plasma is infinite to allow Fourier analysis in space and time. We assume variables can be described by planar perturbations to equilibrium fields in the form:

$$\exp i(\mathbf{k} \cdot \mathbf{x} - \omega t), \quad (1.57)$$

where the quantities  $\mathbf{B}$ ,  $\mathbf{E}$  and  $\mathbf{j}$  follow this form. Thus through this assumption we can write (1.53) as:

$$i\mathbf{k} \wedge \mathbf{B} = \mu_0 \mathbf{j} + \frac{-i\omega}{c^2} \mathbf{E}, \quad (1.58)$$

where the definition  $c^2 = 1/\varepsilon_0 \mu_0$  has been invoked, similarly (1.54) can be written:

$$i\mathbf{k} \wedge \mathbf{E} = i\omega \mathbf{B}. \quad (1.59)$$

The dependency on the magnetic field can be eliminated to produce:

$$\mathbf{k} \wedge (\mathbf{k} \wedge \mathbf{E}) + \frac{\omega^2}{c^2} \mathbf{E} + i\omega \mu_0 \mathbf{j} = 0. \quad (1.60)$$

To progress to a general wave solution we require a relationship between the electric field and the current density, this is supplied by Kirchhoff's reformulation of Ohm's Law, [Darrigol, 2000]:

$$\mathbf{j} = \boldsymbol{\sigma} \cdot \mathbf{E}, \quad (1.61)$$

where  $\boldsymbol{\sigma}$  is the plasma wave conductivity tensor which can be shown to only depend on relative position and time. Thus using a vector identity for the first term and substituting Ohm's law:

$$\mathbf{k}\mathbf{k} \cdot \mathbf{E} - k^2\mathbf{E} + \frac{\omega^2}{c^2}\mathbf{E} + i\omega\mu_0\boldsymbol{\sigma} \cdot \mathbf{E} = 0. \quad (1.62)$$

As a simplification the definition of the dielectric tensor which contains the physical response properties of a given dielectric medium, [Ichimaru, 2008]. :

$$\boldsymbol{\epsilon}(\omega, \mathbf{k}) = \mathbf{I} + \frac{i\mu_0 c^2}{\omega}\boldsymbol{\sigma} \quad (1.63)$$

which then reduces the overall equation to:

$$\hat{\mathbf{D}} \cdot \mathbf{E} = 0 \quad (1.64)$$

with:

$$\hat{\mathbf{D}} = \{\mathbf{k}\mathbf{k} - k^2\mathbf{I} + \frac{\omega^2}{c^2}\boldsymbol{\epsilon}\} \quad (1.65)$$

The medium's dispersion relation is then derived from the only non trivial solution to (1.64) whereby the determinant of  $\hat{\mathbf{D}}$  is zero. Thus if the dielectric tensor is known the above relation produces the solutions for every linear wave mode that is viable in the specific plasma environment. The specifics of the medium define the terms of the dielectric tensor, for example an isotropic unmagnetised plasma reduces  $\boldsymbol{\epsilon}$  and  $\boldsymbol{\sigma}$  to diagonal matrices.

## 1.5 Magnetohydrodynamic Waves

MHD waves can be derived using the general dispersion relation, (1.64) however it is easier to derive them using the idealised form of the MHD equations (1.44). As stated in section 1.3, MHD involves slow varying large spatial scale phenomena. In this section we apply this theoretical construct to derive a set of plasma waves which can be expressed in the MHD framework. Thus they themselves adhere to the assumptions made when deriving MHD theory.

We begin with the one fluid MHD equations outlined in 1.42 in the idealised regime. The system is referred to as idealised as the resistivity  $\eta = 0$  and the energy equation is written in its adiabatic form. The electric field has also been substituted

for the magnetic field and  $nm$  is set to  $\rho$  to simplify the derivation. Thus we use the following equation set, [Freidberg, 1987]:

$$\begin{aligned}
\frac{\partial \rho}{\partial t} + \nabla \cdot (\rho \mathbf{v}) &= 0, \\
\frac{\partial(\rho \mathbf{v})}{\partial t} + (\mathbf{v} \cdot \nabla) \rho \mathbf{v} &= -\nabla \cdot \mathbf{P} - \frac{1}{\mu_0} \mathbf{B} \wedge (\nabla \wedge \mathbf{B}), \\
\frac{\partial \mathbf{B}}{\partial t} &= \nabla \wedge (\mathbf{v} \wedge \mathbf{B}), \\
\frac{d}{dt} \left( \frac{P}{\rho^\gamma} \right) &= 0.
\end{aligned} \tag{1.66}$$

If we then consider a plasma in equilibrium and apply perturbation analysis such that:

$$\begin{aligned}
n &= n_0 + \delta n(\mathbf{r}, t), \\
\mathbf{v} &= \delta \mathbf{v}(\mathbf{r}, t), \\
\mathbf{B} &= \mathbf{B}_0 + \delta \mathbf{B}(\mathbf{r}, t), \\
P &= P_0 + \delta P(\mathbf{r}, t).
\end{aligned} \tag{1.68}$$

in this regime it is assumed that the background flow  $\mathbf{v}_0 = 0$  and the time derivative of equilibrium values is zero such that they are constants. The substitution of these values into (1.66), neglecting terms which contain powers of perturbed quantities greater than one yields:

$$\begin{aligned}
\frac{\partial \delta \rho}{\partial t} + \nabla \cdot (\rho \delta \mathbf{v}) &= 0, \\
\rho_0 \frac{\partial \delta \mathbf{v}}{\partial t} &= -\nabla \delta P - \frac{1}{\mu_0} \mathbf{B}_0 \wedge (\nabla \wedge \delta \mathbf{B}), \\
\frac{\partial \delta P}{\partial t} - c_s^2 \frac{\partial \delta \rho}{\partial t} &= 0, \\
\frac{\partial \delta \mathbf{B}}{\partial t} &= \nabla \wedge (\delta \mathbf{v} \wedge \mathbf{B}_0).
\end{aligned} \tag{1.69}$$

where the quantity  $c_s$  is the sound speed, defined by:

$$c_s^2 = \gamma P_0 / \rho_0 = \gamma P_0 / m_i n_0 \tag{1.70}$$

Projection of these equations into a coordinate system with careful consideration of the magnetic field direction yields a set of partial equations. A planar wave solution with wave number  $\mathbf{k} = k_{\parallel} \hat{\mathbf{e}}_{\parallel} + k_{\perp 1} \hat{\mathbf{e}}_{\perp 1} + k_{\perp 2} \hat{\mathbf{e}}_{\perp 2}$  can then be applied following the process outlined in section 1.4.1 to find the consistency conditions which result in the MHD wave dispersion relation. The equation is stated here without derivation

but the full work can be found in many plasma physics texts i.e. [Baumjohann and Treumann, 2012, Freidberg, 1987, Davidson, 2001] amongst many others:

$$[(\omega^2 - k_{\parallel}^2 v_A^2) \mathbf{I} - c_{ms}^2 \mathbf{k} \mathbf{k} + (\mathbf{k} \hat{\mathbf{e}}_{\parallel} + \hat{\mathbf{e}}_{\parallel} \mathbf{k}) k_{\parallel} v_A^2] \cdot \delta \mathbf{v}_0 = 0, \quad (1.71)$$

where  $v_A$  is a new quantity defined as:

$$v_A^2 = \frac{B^2}{\mu_0 n_0 m_i}. \quad (1.72)$$

This is known as the *Alfvén speed* which can be thought of as the ‘magnetic sound’ speed. It is also useful to define  $c_{ms}$ , known as the fast magnetosonic speed:

$$c_{ms}^2 = v_A^2 + c_s^2 \quad (1.73)$$

The solutions to (1.71) form the basis of linear MHD waves and will be discussed in section 1.6.1.

## 1.6 Low Frequency Plasma Waves

We define low frequency waves as oscillations with  $\omega \ll (\omega_{pi}, \omega_{gi})$ . One fluid MHD as that outlined in section 1.3.2 is valid only at these low frequencies. This is well below the ion cyclotron and plasma frequencies where electron inertia can be safely neglected and dynamics depends purely on ion motion.

### 1.6.1 Linear MHD Waves

If the system is orientated such that the perpendicular wave component is parallel to the  $x$  axis so that  $\mathbf{k} = k_{\parallel} \hat{\mathbf{e}}_{\parallel} + k_{\perp} \hat{\mathbf{e}}_x$  the wave mode solutions to (1.71) can be separated into two forms of linear waves.

#### The Alfvén Wave

The first solution of (1.71) is the shear wave. The above system allows a solution in which  $\delta \mathbf{v}$  decouples in the  $y$  direction. Such that:

$$\boxed{\omega = \pm k_{\parallel} v_A}. \quad (1.74)$$

This wave propagates parallel to the ambient field and is purely transverse and incompressible. It is an electromagnetic wave called a *shear Alfvén wave*. It represents simple string like oscillations of the magnetic field lines.

## The Magnetosonic Wave

The remaining solutions couple the parallel velocity components to the other transverse component  $\delta v_x$ . Thus the determinant of (1.71) reduces to the dispersion relation:

$$\omega^4 - \omega^2 c_{ms}^2 k^2 + c_s^2 v_A^2 k^2 k_{\parallel}^2 = 0, \quad (1.75)$$

which formally has two pairs of roots:

$$\omega^2 = \frac{k^2}{2} \left\{ c_{ms}^2 \pm \left[ (v_A^2 - c_s^2)^2 + 4v_A^2 c_s^2 \frac{k_{\perp}^2}{k^2} \right]^{\frac{1}{2}} \right\}. \quad (1.76)$$

The argument of square root is always positive resulting in real solutions. The root with the positive sign is called the *fast magnetosonic wave* and the negative the *slow magnetosonic wave*. They are both compressive modes. The phase difference between the thermal and magnetic field pressures dictate which mode the wave becomes. Given as  $p_{tot} = p + B^2/2\mu_0$  when  $\delta B$  and  $\delta p$  are in phase they amplify the force on the plasma and thus enter the fast branch, while if anti-phase they retard the magnetosonic wave and force it onto the slow branch. The relative phase and group velocities depend on the wave-vector as shown in figure 1.6.1.

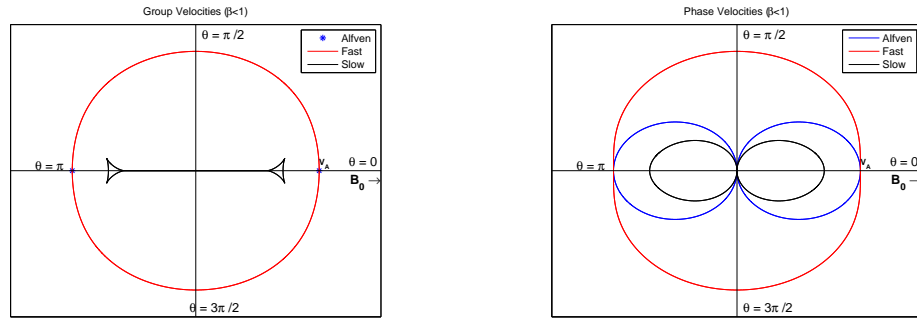


Figure 1.1: Wave velocity diagram for the three MHD wave modes. The left diagram, (a), displays group velocity, (b), shows the wave mode phase velocities for the low  $\beta$  case. The length of the radius from the origin to a point on the associated closed curve is proportional to the wave vector.

### 1.6.2 Waves Modes of a Plasma Cylinder

In the previous section the ideal MHD wave modes in a uniform magnetised plasma were introduced, namely the Alfvén wave and the slow and fast magnetoacoustic

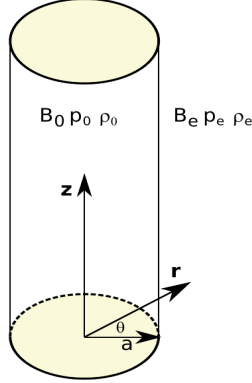


Figure 1.2: Model of a straight magnetic cylinder of radius  $a$ , with the parameters of the internal and external plasma labelled.

waves. It is useful to model a more structured plasma such as the solar corona which contains plasma that is filamented along the magnetic field, with characteristic transverse spatial scales comparable to the wavelength of the waves of interest. These structures can be modelled as a cylinder of plasma stretched along the magnetic field, which is denser than its surroundings. Wave modes of a straight magnetic cylinder have been investigated analytically by [Zaitsev and Stepanov, 1982, Edwin and Roberts, 1983] and this discussion follows their work. A simple model for a straight cylinder with a radius of  $a$  is shown in figure 1.3. To start with a stationary state is taken with a total pressure balance across the boundary, using the penultimate equation of (1.44) it is assumed that across the tube the internal (subscript 0) pressures balance the external (subscript  $e$ ). Such that:

$$p_0 + \frac{B_0^2}{2\mu_0} = p_e + \frac{B_e^2}{2\mu_0}. \quad (1.77)$$

It is useful at this stage to define two characteristic speeds, the *tube speed*,  $c_T$ :

$$c_T = \frac{c_s v_{A0}}{(c_s^2 + v_{A0}^2)^{\frac{1}{2}}}, \quad (1.78)$$

and the *kink mode speed*,  $c_k$ :

$$c_k = \left( \frac{\rho_0 v_{A0}^2 + \rho_e v_{Ae}^2}{\rho_0 + \rho_e} \right)^{\frac{1}{2}}. \quad (1.79)$$

Linear perturbations about this equilibrium lead to two equations in cylindrical co-ordinates  $(x, y, z) \rightarrow (r, \theta, z)$ , [Edwin and Roberts, 1983]:

$$\frac{\partial^2}{\partial t^2} \left( \frac{\partial^2}{\partial t^2} - (c_{s0}^2 + v_{A0}^2) \nabla^2 \right) \Delta + c_{s0}^2 v_{A0}^2 \frac{\partial^2}{\partial z^2} \nabla^2 \Delta = 0, \quad (1.80)$$

$$\left( \frac{\partial^2}{\partial t^2} - v_{A0}^2 \frac{\partial^2}{\partial z^2} \right) \Gamma = 0, \quad (1.81)$$

with

$$\nabla^2 = \frac{\partial^2}{\partial r^2} + \frac{1}{r} \frac{\partial}{\partial r} + \frac{1}{r^2} \frac{\partial^2}{\partial \theta^2} + \frac{\partial^2}{\partial z^2}, \quad (1.82)$$

and

$$\Delta = \nabla \cdot \mathbf{v}, \quad (1.83)$$

$$\Gamma = \hat{\mathbf{z}} \cdot (\nabla \wedge \mathbf{v}), \quad (1.84)$$

Following [Edwin and Roberts, 1983] we take a perturbation  $\Delta$  such that:

$$\Delta = \tilde{p}_T(r) \exp(i\omega t + im\theta + kz). \quad (1.85)$$

Then equations (1.80) and (1.81) imply that  $\tilde{p}_T(r)$  satisfies the Bessel equation:

$$\frac{d^2 \tilde{p}_T}{dr^2} + \frac{1}{r} \frac{d\tilde{p}_T}{dr} - \left( m_0^2 + \frac{m^2}{r^2} \right) \tilde{p}_T = 0, \quad (1.86)$$

where

$$m_0^2 = \frac{(k^2 c_{s0}^2 - \omega^2)(k^2 v_{A0}^2 - \omega^2)}{(c_{s0}^2 + v_{A0}^2)(k^2 c_T^2 - \omega^2)}, \quad (1.87)$$

where  $am_0$  is the radial wavenumber which depends on the frequency of the wave. Equation (1.86) is a Bessel equation. For a solution bounded on the axis of the cylinder ( $r = 0$ ):

$$\tilde{p}_T = A_0 \begin{cases} I_m(m_0 r) & m_0^2 > 0 \\ J_m(n_0 r) & n_0^2 = -m_0^2 > 0 \end{cases} \quad (1.88)$$

for  $r < a$ , the solutions of interest are those trapped by the wave guide, so:

$$\tilde{p}_T = A_1 K_m(m_e r), \quad (1.89)$$

where  $A_0$  is a constant and  $J_m$  is the Bessel function of the first kind. The functions  $I_m$  and  $K_m$  are the modified Bessel functions of the first and second kind respectively, see [Abramowitz and Stegun, 1967]. The expression  $m_e$  is the same as  $m_0$  but with external quantities. The dispersion relations follow from the continuity of the radial



displacement component and the total pressure across the cylinder boundary:

$$\rho_0(k^2 v_{A0}^2 - \omega^2) m_e \frac{K'_m(m_e a)}{K_m(m_e a)} = \rho_e(k^2 v_{Ae}^2 - \omega^2) m_0 \frac{I'_m(m_0 a)}{I_m(m_0 a)}, \quad (1.90)$$

for surface waves ( $m_0^2 > 0$ ), and

$$\rho_0(k^2 v_{A0}^2 - \omega^2) m_e \frac{K'_m(m_e a)}{K_m(m_e a)} = \rho_e(k^2 v_{Ae}^2 - \omega^2) n_0 \frac{J'_m(n_0 a)}{J_m(n_0 a)}, \quad (1.91)$$

for body waves. A surface wave propagates along the interface between the internal and external plasmas while the body wave exists throughout the plasma cylinder structure. The dash denotes a derivative of a Bessel function. For coronal conditions,  $v_{Ae}, v_{A0} > c_{se}, c_{s0}$  and there are no surface modes, only body modes. Modes with  $m = 0$  are cylindrically symmetric modes called sausage modes, modes with  $m = 1$  are called kink modes (see Figure 1.3) and modes with  $m > 1$  are called fluting or ballooning modes.

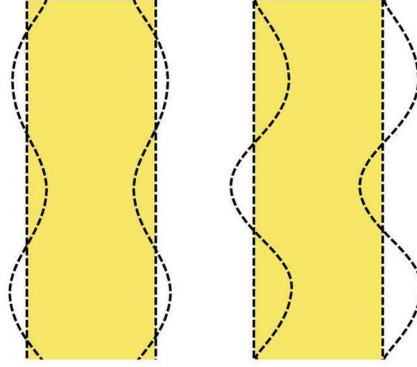


Figure 1.3: The profiles of plasma cylinder perturbations for different modes. Left: Symmetric (sausage) and Right: Antisymmetric (kink) perturbations of a straight cylinder.

## 1.7 High Frequency Plasma waves

In the region where wave frequencies approach the values ( $\omega_{pe}, \omega_{ce}, \omega_{pi}, \omega_{ci}$ ) the combination of electron and ion dynamics become important for wave propagation. One possibility is to relax the one-fluid model and analyse waves in a two component plasma. First we consider a cold unmagnetised electron plasma where the ions form a neutralising background. The derivations and equations used in this section can be found in any plasma waves text book, i.e. [Stix, 1992, Swanson, 2012, Baumjohann and Treumann, 2012] and many others.

### 1.7.1 Waves in unmagnetised plasmas

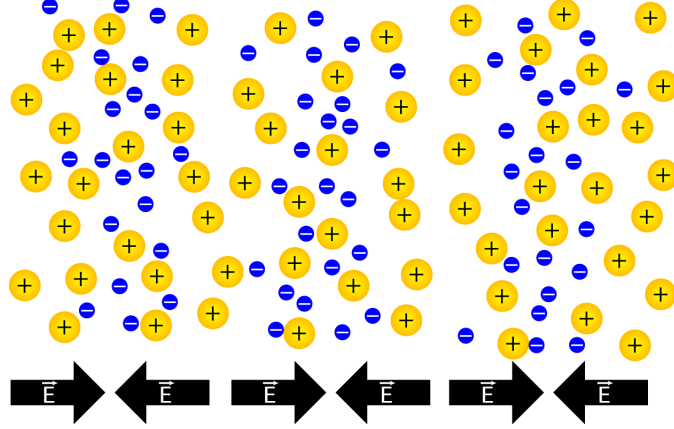


Figure 1.4: Schematic diagram showing electron oscillations around the ion background, (image from [Tesla, 2013]).

Waves in this regime are easy to understand when the motion of electrons is compared to that of the ions. The far less massive electrons will move fast enough to neutralise any fields produced, thus the ions can be neglected to the background and the electrons can be seen to oscillate around this neutral equilibrium with a frequency  $\omega_{pe}$  from (1.1), demonstrated in figure 1.4. This is somewhat artificially represented since the electron distribution is smeared in velocity space. Thus thermal effects need to be accounted with the introduction of the adiabatic variation of the electron thermal pressure  $\delta p_e = \gamma_e k_B T_e \delta n_e$ , such that the new wave frequency resides at:

$$\omega_l^2 = \omega_{pe}^2 + k^2 \gamma_e v_{the}^2, \quad (1.92)$$

with  $v_{the}$  being the electron thermal velocity defined as  $v_{the} = (k_B T_e / m_e)^{1/2}$ . This is the so-called *Bohm-Gross Dispersion Relation*, [Bittencourt, 2013] which describes the propagation of waves that are commonly known as *Langmuir waves*.

At lower frequencies the ion behaviour comes into play, a similar oscillation occurs for the ion species. These are known as *ion acoustic waves* and will not be discussed here. The dispersion plot for this plasma system is shown in figure 1.5.

### Electromagnetic Waves

The general dispersion relation (1.64) also includes a description of purely electrostatic disturbances which propagate as wave modes in the absence of an external magnetic field. A large number of these waves can propagate in a magnetised plasma

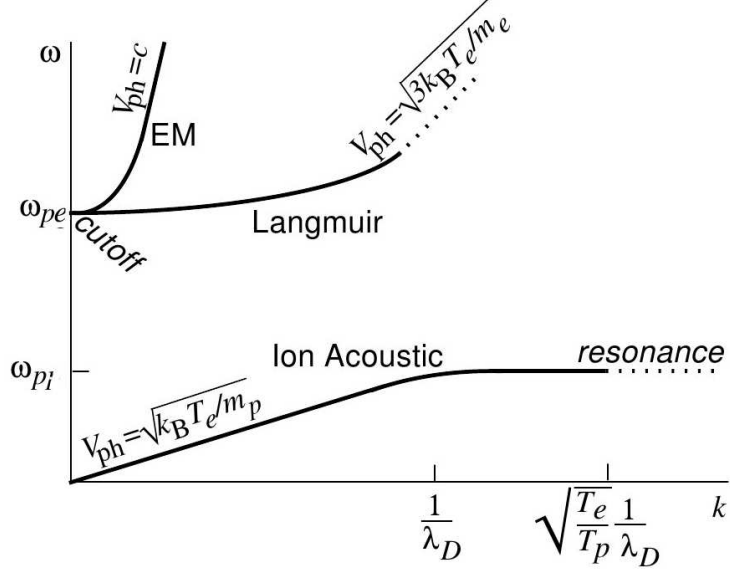


Figure 1.5: Dispersion relations for electromagnetic waves, Langmuir waves, and ion-acoustic waves in an unmagnetised plasma. In the dotted regions the waves are strongly damped, according to kinetic theory, figure from [Baumjohann and Treumann, 2012].

which are described in the subsequent sections. Here we consider the simple case of a electromagnetic wave propagating through an isotropic unmagnetised plasma. The dispersion relation for these waves is given without derivation:

$$\omega^2 = \omega_{pe}^2 + c^2 k^2. \quad (1.93)$$

The key difference to free space waves shows itself at frequencies below the electron plasma wave frequency as no real solutions exist for  $k$ . The electron plasma frequency acts as a cut-off frequency for the ordinary electromagnetic mode.

### 1.7.2 High Frequency Waves in a Magnetised Plasma

The addition of a magnetic field introduces a directionality to the system which interacts with the two species in opposing directions, see figure 1.6. This anisotropy affects wave propagation and modifies dispersion relations.

The dispersion relations in this case can be obtained from the general dispersion relation (1.64). The results of these calculations will be shown without derivation. Full calculations can be found in [Stix, 1992, Swanson, 2012, Baumjohann and Treumann, 2012]. Here we restrict ourselves to the consideration of waves propagating along and across the field only.

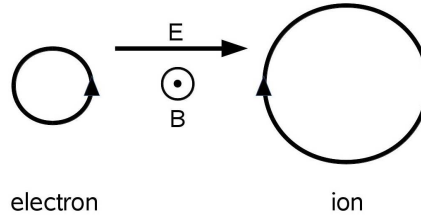


Figure 1.6: Relative electron and ion gyration directions and radii (not to scale).

### Parallel Propagation

The presence of the magnetic field introduces new modes and the modification of waves known to exist in a vacuum. In particular, in the case of parallel propagation the right-hand (R) and left-hand (L) circularly polarised electromagnetic wave modes exhibit different dispersion. Thus they have different cut-off frequencies and group and phase velocities. Accompanying these there is also the more dispersive *whistler* wave branch that does not exist in a vacuum. The full dispersion relation is shown in figure 1.7.

### Perpendicular Propagation

Following a similar path to that for parallel propagation the dispersion relation can be found for perpendicular propagation. The first mode to be introduced is the *ordinary* mode (O) already described for an unmagnetised plasma in section 1.7.1. It is called the ordinary mode because it has the same dispersion relation as an electromagnetic wave in a plasma without the magnetic field. The second branch of the dispersion relation is called the extraordinary mode (X). See figure 1.7.

#### 1.7.3 Summary of Plasma Wave Modes

Wave modes can be categorised by whether they are electromagnetic (magnetic field perturbations present) or electrostatic (no perturbations of the magnetic field). The modes can then be further classified by their oscillation species such as ions or electrons. The summary is shown in Table 1.1.

## 1.8 Non-Thermal Distribution Functions

In a collisionless plasma the equilibrium particle distribution is usually taken to be a Maxwellian (as shown below) as this is an exact, time independent solution to

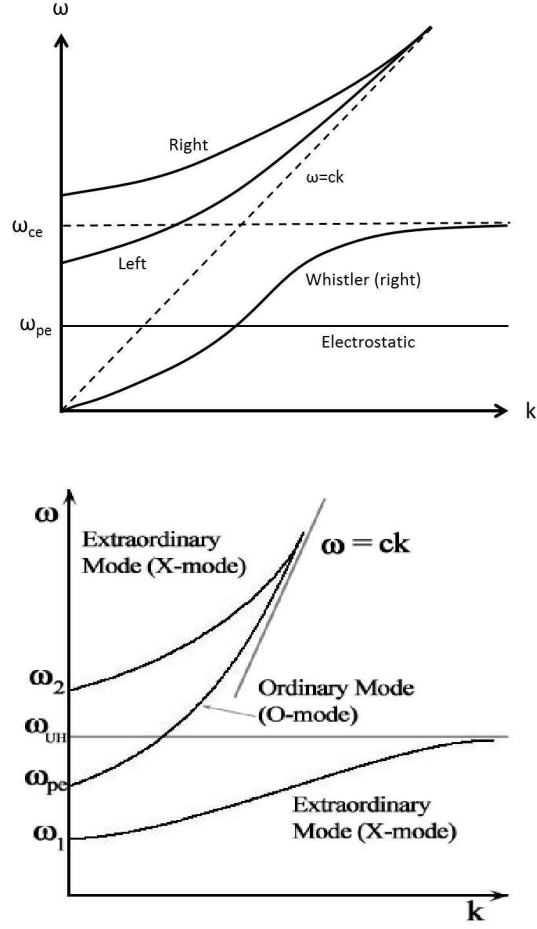


Figure 1.7: Top: The dispersion curves for parallel propagation are shown on the  $\omega k$ -plane. Bottom: The dispersion curves for perpendicular propagation are shown on the  $\omega k$ -plane, from [Baumjohann and Treumann, 2012].

the Vlasov equation, (1.16). When a distribution deviates from this the plasma reacts to produce instabilities and generate waves as an attempt to stabilise the distribution back to the thermal equilibrium. The study of this evolution can reveal details about the plasma medium and the wave modes that can exist within it.

### 1.8.1 Growth Rate

The solution to a wave's dispersion relation, as those listed in table 1.1, can carry an imaginary component, such that  $\omega(\mathbf{k}) = \omega_r(\mathbf{k}) + i\gamma(\omega_r, \mathbf{k})$ . It is clear that the real part of the solution  $\omega_r$  forms the oscillatory part of the wave function. The

Plasma Waves				
EM character	Species	Conditions	Dispersion Relation	Wave Name
Electrostatic	Electrons	$\mathbf{B}_0 = 0$ or $\mathbf{k} \parallel \mathbf{B}_0$ $\mathbf{k} \perp \mathbf{B}_0$	$\omega^2 = \omega_{pe}^2 + 3k^2 v_{th}^2$ $\omega^2 = \omega_{pe}^2 + \omega_{ce}^2 = \omega_{uh}^2$	Langmuir Upper Hybrid
	Ions	$\mathbf{B}_0 = 0$ or $\mathbf{k} \parallel \mathbf{B}_0$ $\mathbf{k} \perp \mathbf{B}_0$ (nearly) $\mathbf{k} \perp \mathbf{B}_0$ (exactly)	$\omega^2 = k^2 c_s^2$ $\omega^2 = \omega_{ci}^2 + k^2 c_s^2$ $\omega^2 = [(\omega_{ci}\omega_{ce})^{-1} + \omega_{pi}^{-2}]^{-1}$	Ion Acoustic Ion Cyclotron Lower Hybrid
Electromagnetic	Electrons	$\mathbf{B}_0 = 0$ $\mathbf{k} \perp \mathbf{B}_0, \mathbf{E}_1 \parallel \mathbf{B}_0$ $\mathbf{k} \perp \mathbf{B}_0, \mathbf{E}_1 \perp \mathbf{B}_0$ $\mathbf{k} \parallel \mathbf{B}_0$ (right circ. pol.) $\mathbf{k} \parallel \mathbf{B}_0$ (left circ. pol.)	$\omega^2 = \omega_{pe}^2 + k^2 c^2$ $\frac{c^2 k^2}{\omega^2} = 1 - \frac{\omega_{pe}^2}{\omega^2}$ $\frac{c^2 k^2}{\omega^2} = 1 - \frac{\omega_{pe}^2}{\omega^2} \frac{\omega^2 - \omega_{pe}^2}{\omega^2 - \omega_{uh}^2}$ $\frac{c^2 k^2}{\omega^2} = 1 \frac{\omega_{pe}^2/\omega^2}{1 - (\omega_{ce}/\omega)}$ $\frac{c^2 k^2}{\omega^2} = 1 \frac{\omega_{pe}^2/\omega^2}{1 + (\omega_{ce}/\omega)}$	Electromagnetic Ordinary (O) Extraordinary (X) Right (R) (Whistler) Left (L)
	Ions	$\mathbf{B}_0 = 0$ $\mathbf{k} \parallel \mathbf{B}_0$ $\mathbf{k}$ oblique to $\mathbf{B}_0$	$\omega^2 = k^2 v_A^2$ $\frac{\omega^2}{k^2} = c^2 \frac{c_s^2 + v_A^2}{c^2 + v_A^2}$	None Alfvén Magnetosonic

Table 1.1: A summary of plasma wave modes classified by magnetic field dependency and propagation direction. *Key symbols:*  $\omega$  - wave frequency,  $k$  - wave number,  $c$  - speed of light,  $\omega_{pe}$  - electron plasma frequency (1.1),  $\omega_{pi}$  - ion plasma frequency (1.1),  $\omega_{ce}$  - electron cyclotron frequency (1.2),  $\omega_{ci}$  - ion cyclotron frequency (1.2),  $\omega_{UH}$  - upper hybrid frequency,  $c_s$  - sound speed (1.70) and  $v_A$  is the Alfvén speed (1.72). Table adapted from [Swanson, 2003].

parameter  $\gamma$  defines whether the wave's amplitude will grow or decay:

$$A = \exp(i\mathbf{k} \cdot \mathbf{x} - i\omega t) = \exp(i\mathbf{k} \cdot \mathbf{x} - i\omega_r t) \exp(\gamma t). \quad (1.94)$$

Thus if  $\gamma < 0$  the wave amplitude decreases with time and the wave is said to be 'damped', while for  $\gamma > 0$  the amplitude grows exponentially in time and we encounter a linear instability. In this case  $\gamma$  is called the growth rate for the corresponding eigenmode. Note the instability can only arise if there is a source of free energy which can feed the growing waves, if not it is considered a spurious solution which violates energy conservation.

When the growth rate becomes greater than the wave frequency,  $\gamma > \omega$  the perturbations have no time to preform a single oscillation during one wave period. In doing so the wave concept becomes obsolete.

### 1.8.2 Landau Damping

Consider a one dimensional perturbation in a plasma with  $\mathbf{B} = 0$ . The unperturbed distribution function  $f = f_0(\mathbf{v})$  where  $f_0$  is the equilibrium distribution usually the

Maxwellian distribution, a solution to the Vlasov equation (1.16):

$$f_0(v) = n_0 \left( \frac{m_e}{2\pi k_B T_e} \right) \exp \left\{ -\frac{mv^2}{2k_B T_e} \right\}, \quad (1.95)$$

there is no time or spatial dependency for the background solution. If a perturbation is then applied such that:

$$f(\mathbf{r}, \mathbf{v}, t) = f_0(\mathbf{v}) + f_1(\mathbf{r}, \mathbf{v}, t), \quad (1.96)$$

then, under the assumption that  $f_1 \ll f_0$ , substitution into the Vlasov equation (1.16) yields:

$$\frac{\partial f_1}{\partial t} + v_x \frac{\partial f_1}{\partial x} - \frac{e}{m} E_1 \frac{\partial f_0}{\partial v_x} = 0, \quad (1.97)$$

for the one dimensional case, with  $E_1$  being the electric field induced by the perturbation. If we let the perturbation take the harmonic form of Langmuir waves outlined in section 1.7.1 then  $f_1 \propto \exp(ikx - i\omega t)$  then (1.97) becomes:

$$-i\omega f_1 + ikv_x f_1 = \frac{e}{m} E_1 \frac{\partial f_0}{\partial v_x}, \quad (1.98)$$

which rearranged gives an expression for  $f_1$ :

$$f_1 = \frac{ieE_1}{m} \frac{\partial f_0}{\partial v_x} \frac{1}{\omega - kv_x}. \quad (1.99)$$

Using Maxwell's equations (1.7-1.10),  $\varepsilon_0 \nabla \cdot \mathbf{E}_1 = -en_1$ , where  $n_1$  is the perturbed electric charge density which is dependent on the distribution function:

$$n_1 = \iiint f_1 d\mathbf{v}, \quad (1.100)$$

such that combined:

$$\varepsilon_0 \nabla \cdot \mathbf{E}_1 = -e \iiint f_1 d\mathbf{v}, \quad (1.101)$$

we can eliminate  $f_1$  using (1.99) and assuming  $E_1$  is also harmonic such that  $\nabla \cdot \mathbf{E}_1 \rightarrow ikE_1$ :

$$1 = -\frac{e^2}{km\varepsilon_0} \iiint \frac{\partial f_0 / \partial v_x}{\omega - kv_x} d\mathbf{v}, \quad (1.102)$$

for simplicity we now replace  $f_0$  with a normalised distribution  $F = f_0/n_0$  such that:

$$1 = -\frac{\omega_{pe}^2}{k} \int_{-\infty}^{+\infty} \frac{\partial F / \partial v_x}{\omega - kv_x} dv_x, \quad (1.103)$$

with the definition of  $\omega_{pe}$  being used, (1.1). The triple integral becomes a single integral if we constrain the system to one dimension. If we now take  $F$  to be the Maxwellian:

$$F = \frac{1}{\sqrt{\pi} v_{Te}} \exp\left(-\frac{v_x^2}{v_{Te}^2}\right), \quad (1.104)$$

with  $v_{Te}$  as the thermal electron speed, then without derivation, [Baumjohann and Treumann, 2012]:

$$1 - \frac{\omega_{pe}^2}{\omega^2} - \frac{3k^2 v_{Te}^2 \omega_{pe}^2}{2\omega^4} - i\pi \frac{\omega_{pe}^2}{k^2} \frac{\partial F}{\partial v_x} \approx 0. \quad (1.105)$$

This equation forms the dispersion relation for *Langmuir waves* (see discussion in

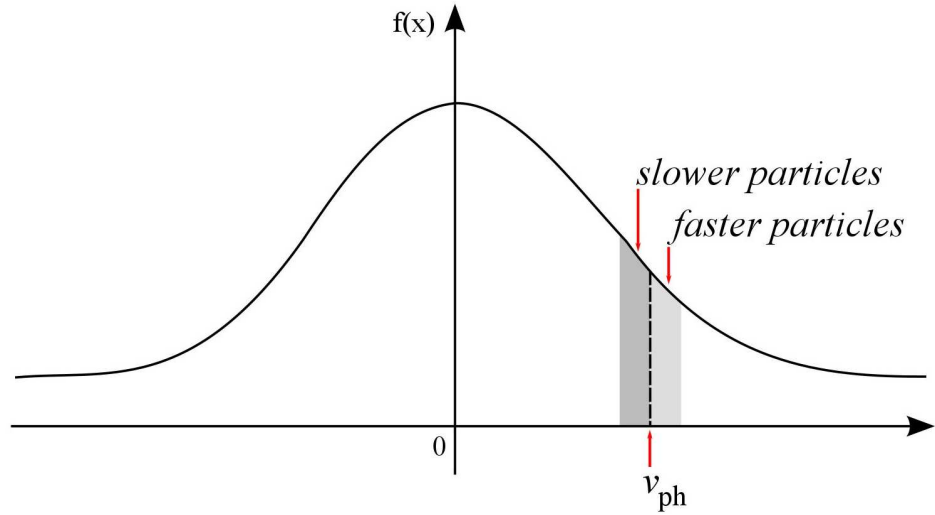


Figure 1.8: Maxwellian distribution for a one dimensional plasma. Particles slower than the  $v_{ph}$  absorb energy from the waves. Particles faster lose energy to the wave.

section 1.7.1). The first two terms describe plasma oscillations at frequency  $\omega_{pe}$ . The second, propagation of waves at around the sound speed. The third term describes the kinetic processes, as an imaginary component it can either define growth (if positive) or absorption (if negative) in the system. In general,  $\omega = Re(\omega) + iIm(\omega)$ . According to (1.105) the plasma waves either experience a decay or an undergo an instability around the wave phase speed in the velocity space. The sign of the imaginary part is defined by the sign of the derivative as:



$$\text{Im}(\omega) \propto \frac{\partial F}{\partial v_x}, \quad (1.106)$$

as all other parameters are either positive or squares. In the case of the Maxwellian the derivative is always negative, as shown in figure 1.8, such that the Langmuir waves are always damped. This is known as *Landau damping*. The plasma waves experience decay due to the presence of “resonant particles” with velocities near the phase speed of the wave. Particles with  $v < \omega/k$  gain energy from the wave whereas particles with  $v > \omega/k$  transmit energy to the wave as shown in figure 1.8. Due to the nature of the Maxwellian there are always more particles with  $v < \omega/k$  thus the net energy transfer is from the wave to the particles, thus the wave is damped.

### 1.8.3 Instabilities and Resonances.

Generation of instability or resonances is a general way of redistributing energy which has accumulated in a non-equilibrium state. In general when a particle distribution function is driven to a non-thermal (i.e. non-Maxwellian) then the system will endeavour to re-stabilise using these mechanisms. In plasma physics, sources of free energy interact with the eigenmodes of the plasma to grow or damp waves.

### Quasilinear Theory and the Resonance Instabilities

So far we have outlined the existence of a variety of wave modes within the plasma medium. The work carried out in this thesis also requires an understanding of the phenomena involved in wave particle interaction. Quasilinear theory provides an analytical description of the interaction between waves and particles in a collisionless plasma, a outline of quasilinear theory can be found in [Kennel and Engelmann, 1966, Stix, 1992] and the references therein. The common key assumptions held in these texts are outlined as:

- Fluctuation amplitudes are sufficiently small that they can be described as the superposition of linear waves.
- A particles orbit can be approximated as an unperturbed helix aligned with the background field.
- Growth or damp rates of the waves are much smaller than the linear frequencies.
- The plasma is treated as infinite and homogeneous.

This theoretical construct allows the interaction between waves and particles to be explicitly derived in a plasma with a constant homogeneous background magnetic field. These interactions have been shown to manipulate the distribution function through an energy exchange between particles and the plasma wave. In particular it has been shown that a distribution function containing a non thermal beam can in fact disrupt particular wave modes. These non-linear distributions have been shown to modify dispersion relations while simultaneously existing as a source of free energy which in turn can grow electromagnetic instabilities, [Montgomery et al., 1976, Gary, 1993]. Non-linear wave-wave coupling is disregarded in this work as it is essentially encompassed in assumptions made of the wave spectrum present, however it has been shown to be very important in the evolution of a plasma, [Galeev et al., 1965]. As we use quasi-linear theory in a qualitative sense it is less important to include these non-linear effects but more understand their impact if further analysis was required.

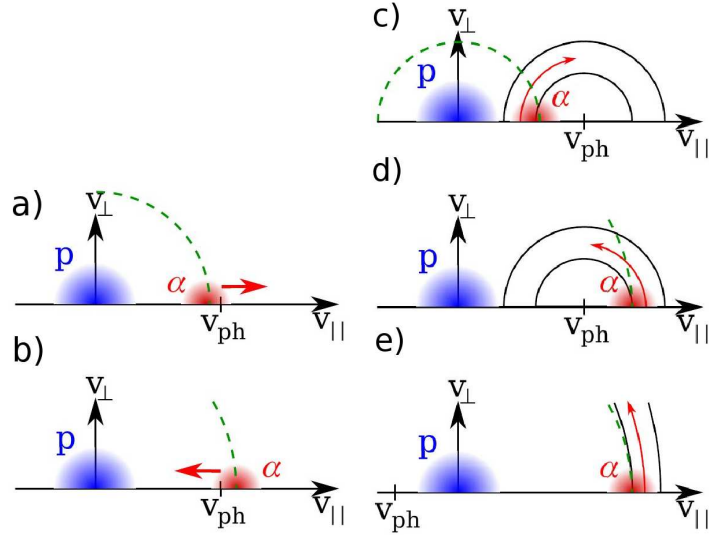


Figure 1.9: Schematic diagram to illustrate the direction of diffusion for a cold ion beam. Blue denotes the proton bulk while red the energetic alpha beam which has been used as a proxy for a proton beam. The diffusion paths are shown around the position of the parallel phase speed  $v_{ph}$ . The beam speed of a particle in the proton frame  $U_i$  is shown by the green dash iso-contours. a)  $U_i < v_{ph}$  and b)  $U_i > v_{ph}$ . Similarly (c-e) show the diffusion of particles in velocity space for the cyclotron-resonance due to the presence of an alpha particle beam. c)  $U_i < v_{ph}$ , d)  $U_i > v_{ph}$ , e)  $v_{ph} < 0$ . (Image from [Verscharen and Chandran, 2013]).

Quasi-linear theory is built upon the Vlasov equation, (1.16) which describes the evolution of the distribution function. Thus, under the right assumptions, it is

able to model the interaction between waves and particle distributions in a useful manner. The analytical process used to describe quasilinear theory is beyond the scope of this text as we will only present the relevant results, however detailed derivations can be found in [Verscharen and Chandran, 2013, Kennel and Engelmann, 1966] and the references contained therein. In a very qualitative sense quasi-linear theory separates the variables  $f$ ,  $\mathbf{E}$  and  $\mathbf{B}$  into two parts: the space independent components and small, rapidly fluctuating parts due to waves. A Fourier analysis approach is then used on the components separately, the resulting equations predict that waves cause particles to diffuse in velocity space. The second consequence of the analysis manifests itself as a resonance condition due to the presence of a delta function within the quasi-linear diffusion equation of the particle distribution function:

$$\omega_{kr} - k_{\parallel} v_{\parallel} = n\omega_{cs}, \quad (1.107)$$

where  $n$  is any integer. This is called the *Landau resonance* condition when  $n = 0$  and the *cyclotron-resonance* condition when  $n \neq 0$ . Note, because the Landau resonance only occurs when  $v_{ph} = v_{\parallel}$ , diffusion of particles in velocity space only occurs in  $v_{\parallel}$ , not  $v_{\perp}$ .

We can demonstrate the impact of the resonance condition using the very simplistic case a particle within a non thermal beam and its projection onto the  $(v_{\parallel}, v_{\perp})$  plane. In the situation we assume the interaction with the wave involves no energy exchange and the kinetic energy of the particle is conserved. Its position therefore sits on a circular curve with a radius proportional to its kinetic energy in the  $(v_{\parallel}, v_{\perp})$  plane. Thus changes to the particle's parallel velocity through the resonance condition will move it along this curve towards the perpendicular axis, this is represented by the green dashed curve in figure 1.9. This in essence models a transfer of energy from the parallel to perpendicular direction. It is important to note that [Verscharen and Chandran, 2013] was tailored to alpha particle beams, shown by 1.9. In our research we do not consider alpha beams, however the analysis presented is transferable to proton beams.

If we now relax the assumption of conserved kinetic energy and allow particles to gain or lose energy to the interacting wave mode then these circular curves will no longer exhibit constant radii. Their trajectory is now defined by:

$$(v_{\parallel} - v_{ph})^2 + v_{\perp}^2 = \text{constant}, \quad (1.108)$$

where  $v_{ph} = \omega_{kr}/k_{\parallel}$  is the parallel phase velocity of the waves. Some particle diffusion paths are shown in figure 1.9 for various values of  $v_{ph}$ . The consideration of one particle can be extended to a section of the distribution function which interacts with a range of frequencies contained within a broad peak in the wave spectrum. The result, shown in figure 1.9 c,d,e is that the cyclotron resonant wave-particle interactions cause the beam particles to lose energy if  $0 < v_{ph} < U_i$ .

### The Beam Instability

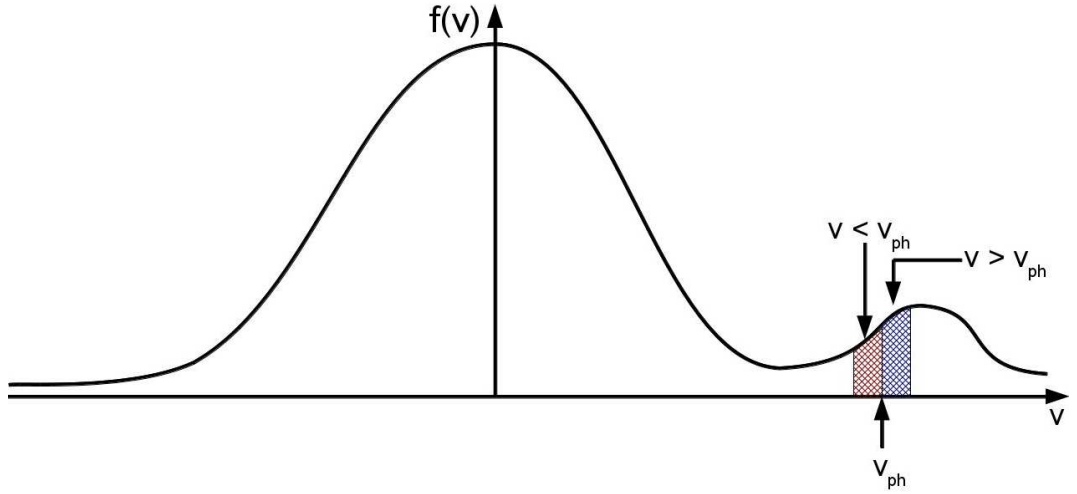


Figure 1.10: A bi-Maxwellian distribution is used to describe a plasma with a beam or a two stream plasma system. The positive gradient in the distribution gives rise to the beam instability. The red region contains particles with  $v < v_{ph}$  which stand to gain energy from the wave while the blue region contains particles with  $v > v_{ph}$  which stand to lose energy.

Following Section 1.8.2 we consider the introduction of a ‘beam’ into the distribution function. This can be considered as a secondary Maxwellian peak centred on the average beam velocity, figure 1.10. The positive gradient produced by the second peak in figure 1.10 leads to  $Im(\omega)$  becoming positive locally. Therefore the Langmuir waves with the associated values of  $\mathbf{k}$  are grown at a rate,  $t_0 = [Im(\omega)]^{-1}$ .

The dispersion relation of the beam system can be constructed using the fact that the dielectric tensor, (1.63), can be found as the sum of the contributions of the plasma components [Treumann and Baumjohann, 1997]. Seeing as the system can be thought of as two isotropic plasmas coexisting we get:

$$\epsilon(\omega, \mathbf{k}) = 1 - \frac{\omega_{p0}^2}{\omega^2} - \frac{\omega_{pb}^2}{(\omega - \mathbf{k} \cdot \mathbf{v}_b)^2} = 0. \quad (1.109)$$

The first term on the right hand side is the background plasma which in the absence of the beam would yield Langmuir oscillations. The second term is the same structure except the background plasma frequency is replaced with the Doppler-shifted beam frequency  $(\omega - \mathbf{k} \cdot \mathbf{v}_b)$ , and the plasma frequency is replaced with the beam plasma frequency  $\omega_{pb}^2 = n_b e^2 / \varepsilon_0 m_e$  from (1.1). If we neglect the background plasma by setting  $\omega_{p0} = 0$  the dispersion relation can be solved yielding, [Treumann and Baumjohann, 1997]:

$$\omega = \mathbf{k} \cdot \mathbf{v}_b \pm \omega_{pb}. \quad (1.110)$$

The two waves described by this relation are known as *beam modes*. They exist only in the presence of a beam.

### The Firehose Instability

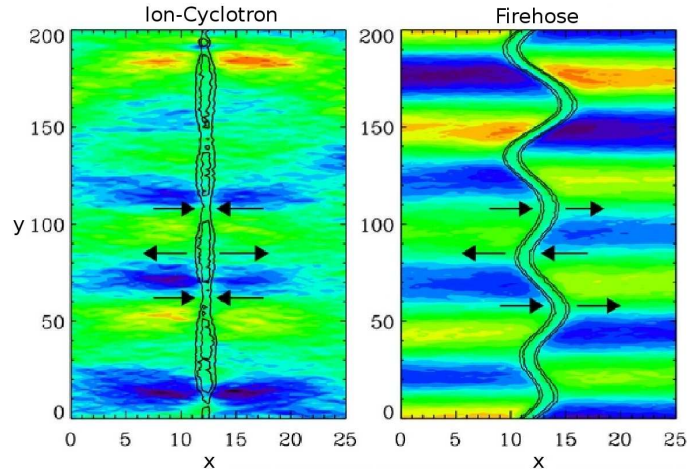


Figure 1.11: The image shows the effect of the ion-cyclotron and firehose instabilities on a long element of plasma. Colour contours encode the background magnetic fluctuations generated by ion-cyclotron (left) and fire-hose (right) instabilities. The density of protons at the current sheet at the same simulation time is reported on the superimposed black solid line contour. The arrows show the local direction of the resulting contribution to the electric field component  $E_x$  generated by the magnetic fluctuations in the figure. Adapted from [Matteini et al., 2013].

In section 1.6 we showed that plasmas can support a variety of low frequency/ large scale Alfvén and magnetosonic waves. We now focus on a mechanism which can be used to produce these wave modes, the *firehose instability*. It can arise in a plasma when the plasma pressure becomes anisotropic:

$$\mathbf{P} = p_{\perp} \mathbf{I} + (p_{\parallel} - p_{\perp}) \frac{\mathbf{B}\mathbf{B}}{B^2} \quad (\text{with } p_{\parallel} \neq p_{\perp}). \quad (1.111)$$

Under certain conditions a magnetic flux tube containing the anisotropic plasma can be stimulated to preform global transverse oscillations such as the oscillations seen in a firehose when the water is turned on and allowed to move freely. The nature of the firehose instability is shown in figure 1.11.

The physical mechanism of the firehose instability can be understood as follows, from the derivation in [Treumann and Baumjohann, 1997]. Imagine a magnetic flux tube and let the plasma flow along the magnetic field at a parallel velocity,  $v_{\parallel}$ . If the flux tube is slightly bent the plasma flow will exert a centrifugal force,  $F_R = m_i n_0 v_{th\parallel}^2 / R$ , on the flux tube of curvature radius,  $R$ .

The centrifugal force is directed outwards and tends to increase the amplitude of the initial bending. The thermal pressure force in the plane perpendicular to the tube as well as the magnetic tension forces resist a full kink. Requiring force equilibrium in the tube implies:

$$\frac{m_i n_0 v_{th\parallel}^2}{R} = \frac{p_{\perp}}{R} + \frac{B_0^2}{\mu_0 R}. \quad (1.112)$$

The term on the left hand side is simply the thermal pressure  $p_{\parallel}$  over the radius of curvature  $R$ . So the condition for the firehose instability simplifies to:

$$\boxed{p_{\parallel} > p_{\perp} + B_0^2 / \mu_0.} \quad (1.113)$$

The instability excites or amplifies waves in the parallel direction, a oblique firehose mode does exist for waves travelling in the oblique direction however for the purposes of this thesis the parallel mode will sufficiently represent both. For parallel propagation there are two solutions, one is the parallel propagating ion acoustic wave detailed in section 1.7.3. The other solution induces instability in the flux tubes creating transverse oscillations resulting in parallel propagating Alfvén waves. The firehose threshold is correctly described in CGL theory.

### The Mirror Instability

The *mirror instability* evolves at nearly perpendicular propagation of waves. Though it is a macroscopic instability it involves the motion on the particle level, therefore it is difficult to treat using MHD. One therefore requires kinetic methods in the very low frequency limit. The mirror mode works to excite or amplify obliquely propagating slow magnetosonic waves in the low frequency limit. The mirror mode grows

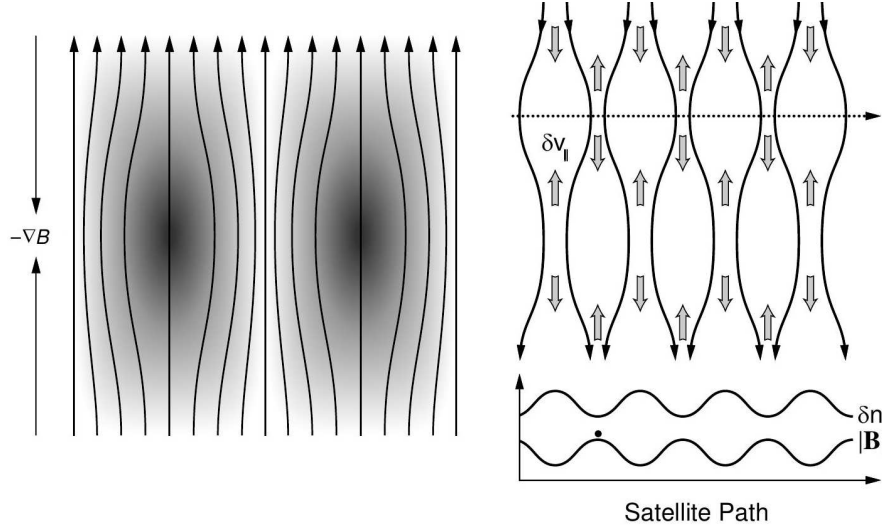


Figure 1.12: The left shows magnetic field and plasma density within mirror mode waves. The right shows the satellite measurements across the mirror-unstable relation region, from [Treumann and Baumjohann, 1997].

if the free energy of the pressure anisotropy is sufficiently large. For this growth the instability requires that the perpendicular pressure is larger than the parallel pressure. Phenomenologically it can be understood as particles stuck in magnetic configurations. In this bottle the particles perform a mirror motion between the knots of the wave. If then a whole region consists of these particle streams then to an observing spacecraft pulsations can be seen, see figure 1.12. The instability condition, [Treumann and Baumjohann, 1997] is given as a function of plasma  $\beta$  defined in section 1.3.3:

$$\sum_s \beta_{s||} > 2 + \sum_s \beta_{s\perp}. \quad (1.114)$$

If this condition is fulfilled the mirror instability sets engages in an anisotropic plasma. The mirror instability condition cannot be satisfied simultaneously with the firehose therefore the two instabilities are mutually exclusive.

## Chapter 2

# Space Plasmas

### 2.1 Introduction

In this chapter we introduce several space plasma environments. We intend to provide the reader with a background understanding of the different environments we have explored in our research. We also aim to exhibit some average parameters for each arena to give a quantitative feel for the strongly contrasting natural plasma laboratories.

### 2.2 The Solar Wind

The solar wind is a continuous flow of plasma emitted by the Sun at speeds of  $\approx 300 - 1400 \text{ km s}^{-1}$ . This outflow is due to the supersonic expansion of open magnetic field configurations within the solar corona, [Meyer-Vernet, 2007].

The solar wind interacts with the Earth's magnetic field to produce the bow shock and magnetopause shown in figure 2.1 discussed in more detail in section 2.3.2. The plasma parameters change drastically as the observer progresses from the solar wind through the bow shock and into the magneto-sheath. The composition of the solar wind plasma is predominantly electrons and protons but does contain 5 % fully ionised Helium. Its key properties are given in table 2.1, [Baumjohann and Treumann, 2012, Chashei et al., 2005, Mullan and Smith, 2006]:

In [Parker, 1958], Parker proposes the ingenious idea that the open corona (see section 2.4.3) could not be in a hydrostatic equilibrium and as a result derived a dynamic solution that includes the continuous expansion of the solar wind, with a vanishing pressure at large distances. The solution for the solar radial velocity,  $v(r)$  is stated without derivation, which can be found in [Aschwanden, 2006]:



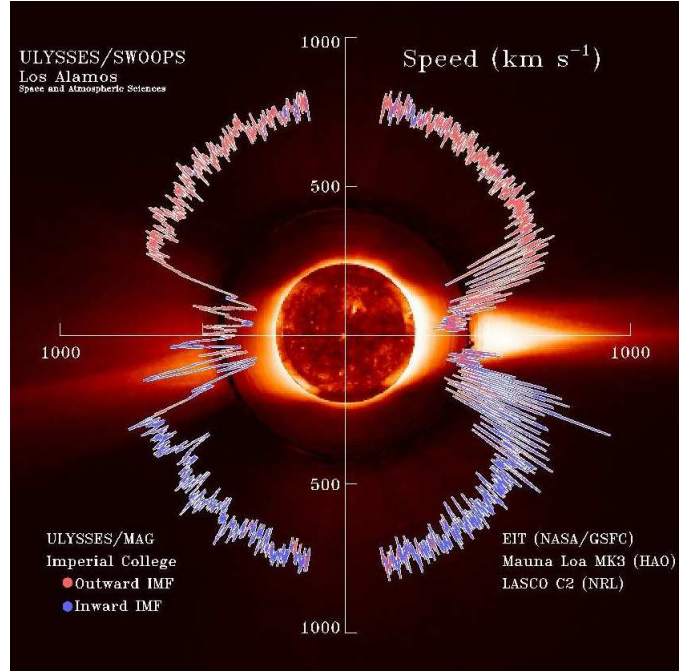


Figure 2.1: The variability of solar wind speed with inclination from the ecliptic plane, [NASA, 2014a].

Parameter	Value
Electron or ion number density $n$	$\approx 5 \text{ cm}^{-3}$
Debye wavelength $\lambda_D$	$\approx 10 \text{ m}$
Plasma electron frequency $\omega_{pe}$	$10^4 < \omega_{pe} < 10^5 \text{ Hz}$
Plasma $\beta$	$0.1 < \beta < 10$
Electron temperature $T_e$	$\approx 10^5 \text{ }^\circ\text{K}$
Acoustic ion sound speed $c_s$	$\approx 100 \text{ kms}^{-1}$
Alfvén wave speed at 1 AU $v_A$	$\geq 100 \text{ kms}^{-1}$

Table 2.1: Key physical parameters within the solar wind, Baumjohann and Treumann [2012].

$$\frac{v^2}{c_s^2} - \ln \left( \frac{v^2}{c_s^2} \right) = 4 \ln \left( \frac{r}{r_c} \right) + 4 \frac{r_c}{r} + C \quad (2.1)$$

where  $C$  is a constant and  $r_c = g_\odot R_\odot^2 / 2c_s^2$  which is the radius at which the wind speed equals the sound speed,  $v = c_s$ . Acceptable solar wind solutions are that which are subsonic at the sun and pass through the critical point ( $v = c_s$  thus requiring  $C = -3$ ), although these characterise the observed solar wind approximately not exactly. The solutions have been shown in figure 2.2 with type V solution as the

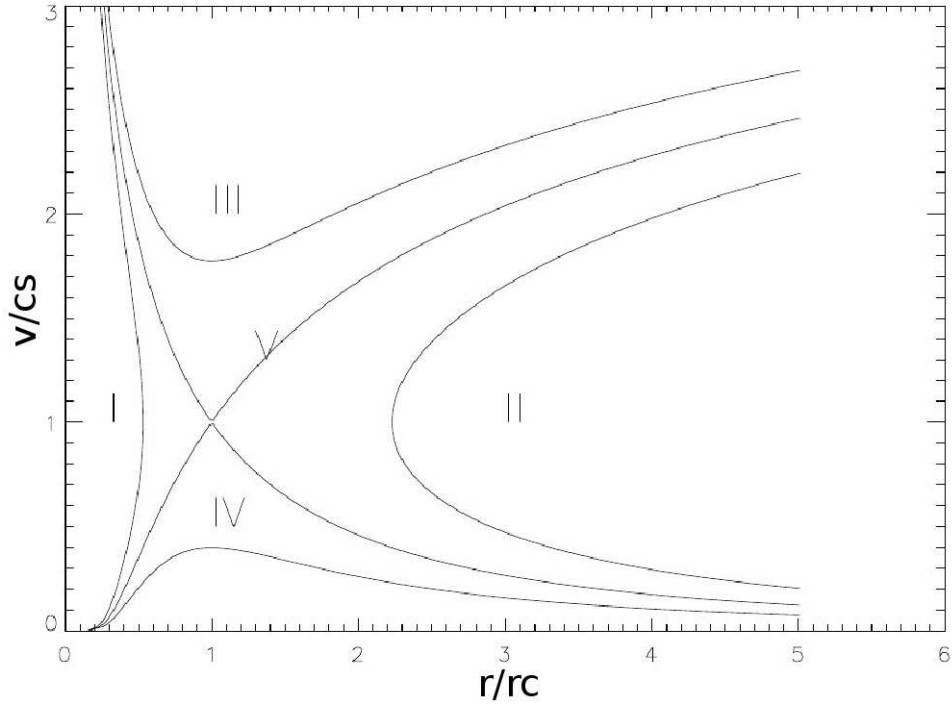


Figure 2.2: The Parker solar wind model solutions, values are normalised to the critical radius  $r_c$  and sound speed  $c_s$ . Types I and II are double valued proving to be non-physical. Types III has supersonic speeds at the Sun which are not observed. Types IV is excluded due to the infinite densities predicted in the heliosphere. Hence we are left with the unique solution of type V which passes through the critical point ( $r = r_c$ ,  $v = c_s$ ) and is given by  $C = -3$ . This is known as the ‘solar wind’ solution [Parker, 1958].

accepted simplest solar wind model.

## 2.3 Collisionless Shocks

### 2.3.1 What is a Shock Wave?

A shock wave has similar properties to any other wave, a propagating disturbance that carries energy. It differs from a regular wave, which has a smooth variation in physical quantities, as a shock is characterised by an abrupt, nearly discontinuous change in the medium parameters before and after the wave front [Anderson, 2010]. Critically, a shock wave can travel much faster than a regular travelling wave, which propagates at the sound speed (or magnetosonic speed for a magnetoacoustic wave). The speeds of shock waves are characterised by their respective Mach

number, defined as:

$$M_{s,ms} = \frac{v}{c_{s,ms}} \quad (2.2)$$

where  $c_s$  and  $c_{ms}$  are the sound and fast magnetosonic speeds defined by (1.70) and (1.73) respectively.

Shocks are a thin layer, approximately the size of the mean free path of the medium. Thus shocks, locally, can be thought of as a two dimensional plane in a three dimensional system. In the case of acoustic perturbation, if an object or disturbance moves faster than the respective sound speed in the medium then there is no transfer of information between the wave front and the upstream fluid. This results in the thin layer transition between the upstream and downstream regions of the shock.

### Oblique and Bow Shocks

An *oblique shock* wave is a shock wave which forms at an angle to the incident flow direction. It occurs for example, when a supersonic flow encounters an object which deflects the flow into itself as shown in the left of figure 2.3, [Anderson, 2010]

A *bow shock* wave forms when a blunt object is in a supersonic or super-magnetosonic flow or is moving supersonically in a fluid. A stationary shock wave (relative to the object) is formed at the front surface. Unlike an *oblique shock* the bow shock is not necessarily attached to the body. When the deflection needed exceeds the maximum achievable deflection for an oblique attached shock, the shock detaches from the body (see the right of figure 2.3). This usually occurs in high Mach numbers shocks.

#### 2.3.2 Interplanetary Shocks

One of the most prevalent phenomena in interplanetary space plasmas are collisionless shock waves. The most famous being the Earth's *bow shock*. A shock like this forms due to its high magnetosonic Mach number,  $M_{ms} \approx 8$  that characterises the relative speed of the Earth and solar wind. The bow shock is a fast magnetosonic shock, i.e. it falls in the fast magnetosonic family. The incoming solar wind impacts the Earth's magnetic field faster than the information can be conveyed through magnetosonic waves. Therefore a discontinuity forms between the two regions. The shock exists only over a limited region of space in front of the Earth, the size of this region depends on the angle between the normal of the bow shock,  $\mathbf{n}$ , the interplanetary magnetic field direction,  $\mathbf{B}$  and the wind velocity component normal to the

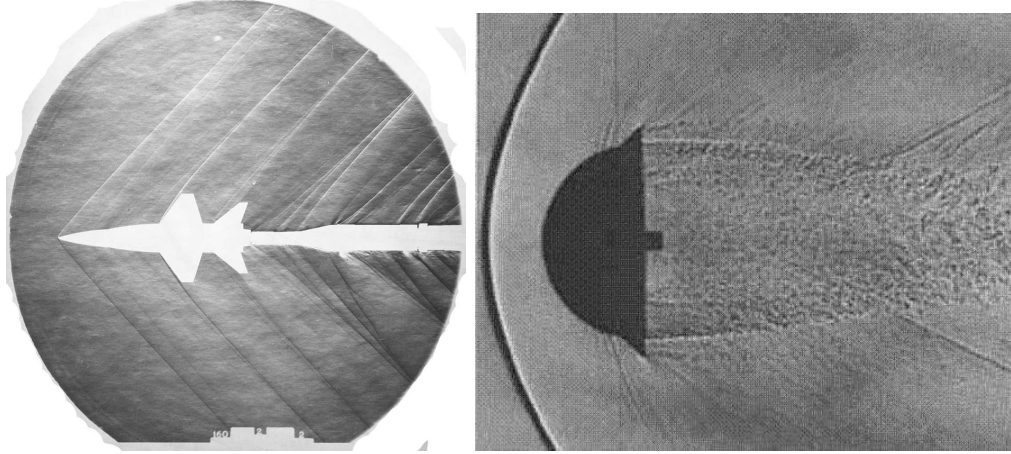


Figure 2.3: Left: A small scale X-15 missile placed in supersonic flow to produce an oblique shock wave at the nose of the model, shown by the straight lines directed at an angle to the nose. (Image from [NASA, 2014g]). Right: photograph of bow shock waves around a blunt object, displayed as the black curve ahead of the object. (Image from [NASA, 2014f]).

shock. The plasma is slowed at the shock and a substantial portion of its kinetic energy is converted to thermal energy. The geometry of the bow shock is shown in figure 2.4.

### 2.3.3 Parallel and Perpendicular Shocks

Plasma shocks can take many forms, however for the purpose of this thesis we will restrict to parallel and perpendicular collisionless shocks. First to address what is meant by collisionless: when a shock wave transitions from pre to post shock on a length scale smaller than the average particle collisional mean free path, usually the ion gyroradius (1.3) it can be considered as collisionless. The reason such structures exist is because particles interact with each other through the emission and absorption of collective excitations of plasma waves, as detailed in section 1.7.3, not through Coulomb collisions.

Another differentiation between regions of the bow shock can be realised from figures 2.5 and 2.6. Regions where the angle,  $\theta_{Bn}$ , between the shock normal and magnetic field is zero are classified as *parallel shocks*. Similarly if  $\theta_{Bn} = 90^\circ$  then the shock is known as a *perpendicular shock*. The prefix *quasi* is usually applied to a shock if the shock angle does not deviate too far from these specified geometries.

The physics of these two categories varies drastically. In a truly perpendicular shock the wind and shock regions are only connected by a small diffuse region

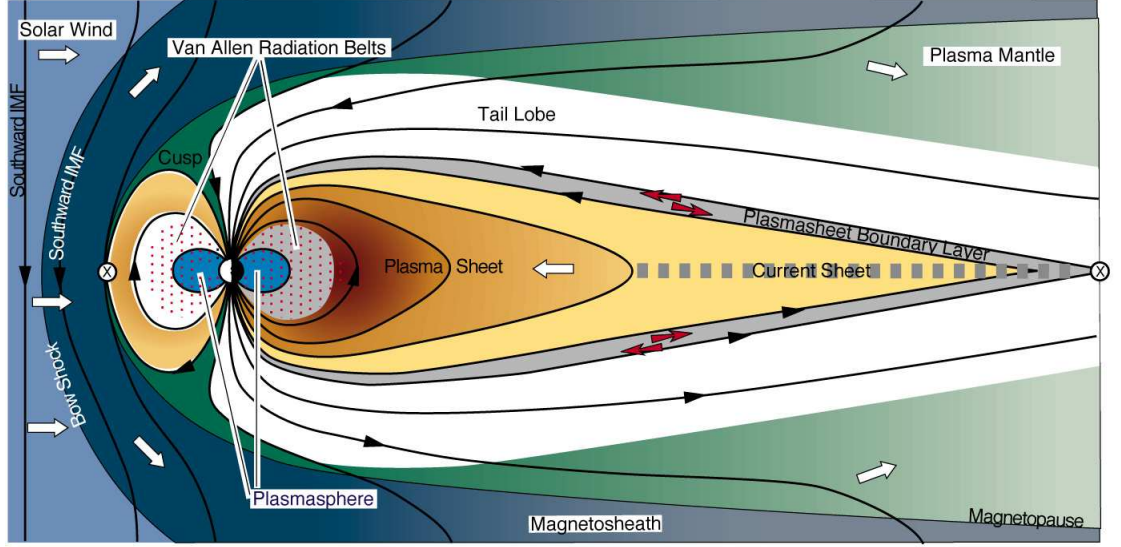


Figure 2.4: Schematic diagram of the interaction between the high speed solar wind and the Earth's magnetic field. The white arrows indicate the direction of plasma flow while the grey arrows show the movement of charges along the plasma boundary layer. Finally the red arrows indicate the direction of charged particles along the plasma sheet boundary layer, [Reiff, 1999].

between field lines on the gyro-scale. On the other hand the pre-shock and post-shock regions in a parallel shock are magnetically connected. This allows a reflection of charge carriers upstream. These newly formed beams can induce instabilities to grow wave activity such as that defined in section 1.8.3. This region of reflected particles is known as a *foreshock* which proves to be a useful laboratory in studying wave activity in space plasmas.

### 2.3.4 The Terrestrial Foreshock

The region of quasi parallel shock upstream of the *bow shock* is known as the *fore-shock*. It is magnetically connected to the bow shock and permeated with upstreaming particles. The two dominant regions in the foreshock are the electron and ion foreshocks where the respective species constitutes the majority of upstreaming particles. The electron foreshock is a narrow region which extends further into the solar wind bounded by the field line tangential to the bow shock, see figure 2.7. The most energetic electrons appear at the tangential point.

In this thesis our attention is solely restricted to the ion foreshock. In the ion foreshock region ions are reflected from the shock front and propagate upstream.



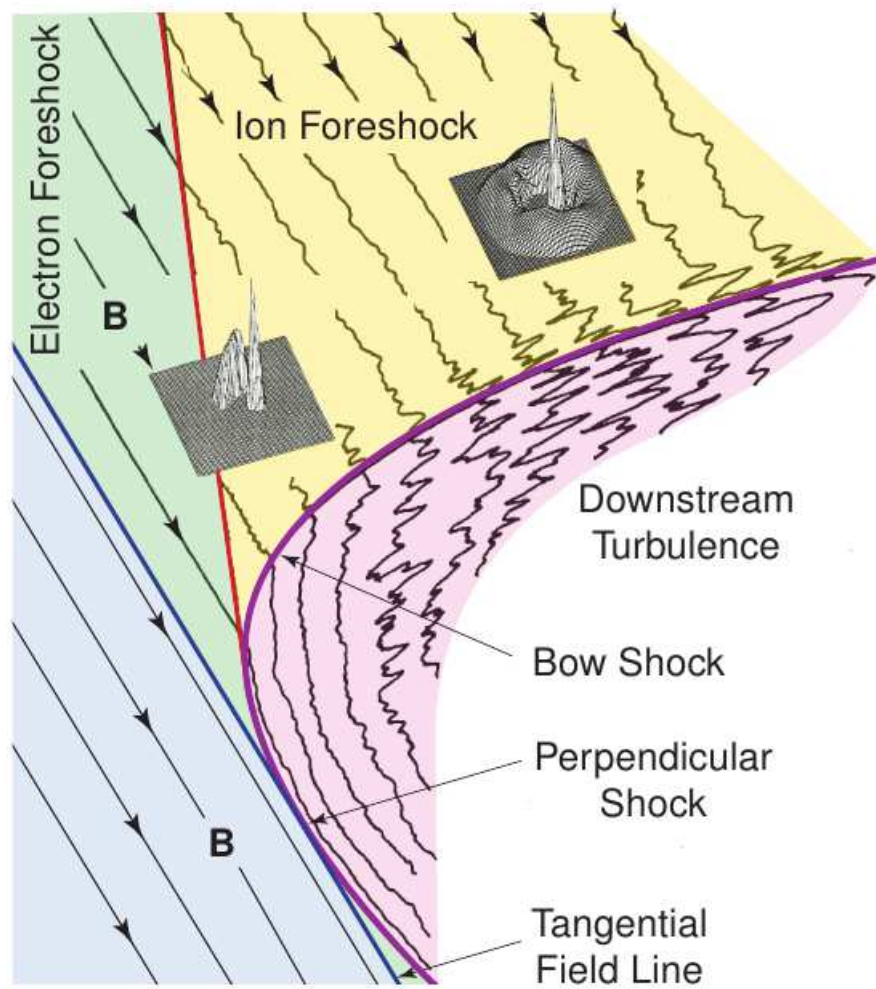


Figure 2.5: Schematic view of the terrestrial foreshock system. The solar wind direction is shown from left to right. The bow shock is represented by the curved purple line. Representative 2D particle velocity distributions are shown to give an understanding of the large variation in distributions across the foreshock, [Eastwood et al., 2005].

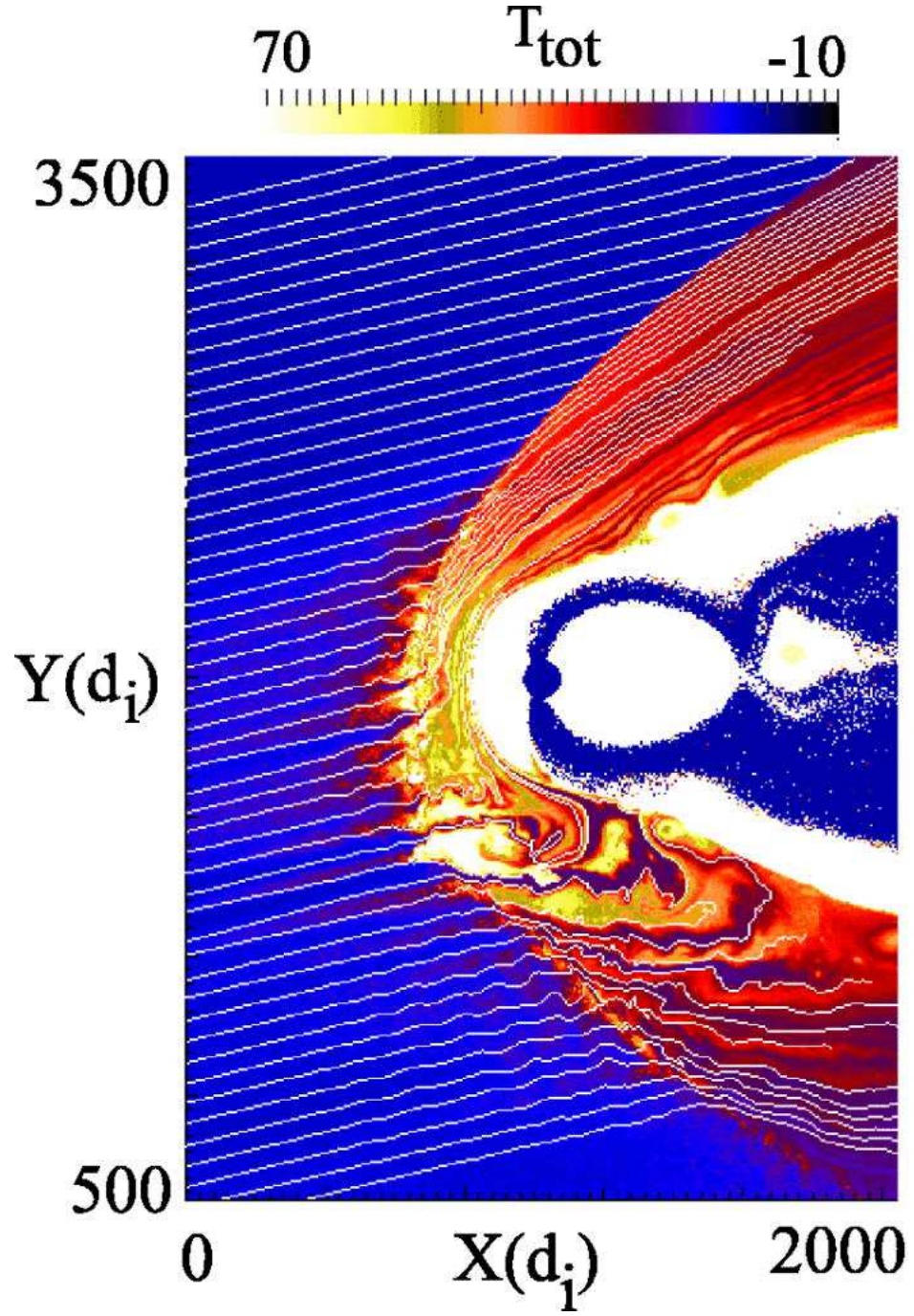


Figure 2.6: A kinetic simulation of the foreshock region where  $d_i$  refers to the cell number in the  $X$  and  $Y$  directions. The magnetic field lines structure is overlaid in white. The colour range is prescribed by the total ion temperature. Although bow shock and foreshock temperatures are not negative in this simulation the scale was shifted to provide improved contrast in the image, from [Karimabadi et al., 2014].

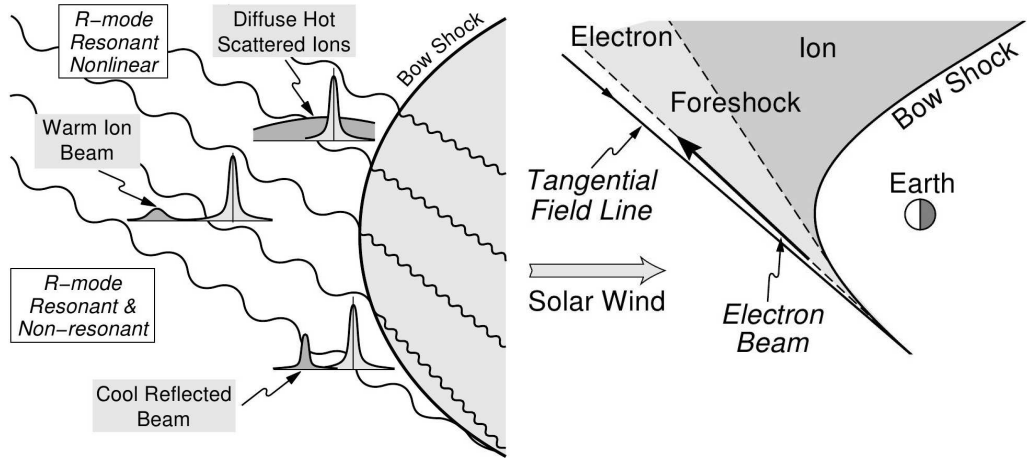


Figure 2.7: Unstable ion beam effects in the foreshock region (left). Electron and ion foreshock geometries (right). (Image from [Treumann and Baumjohann, 1997]).

This sets up conditions for the classic beam instability outlined in 1.8.3. The beam is less dense than the solar wind  $\approx 1\%$  of the background. The right hand circularly polarised wave also known as the R-mode (detailed in section 1.7.3) is the fastest growing wave mode due to the nature of ion rotation. It causes large fluctuations in the foreshock solar wind magnetic field. Figure 2.7 shows schematically what may happen in the Earth's ion foreshock.

## 2.4 Solar Atmosphere

### 2.4.1 The Sun

The Sun is our closest star and thus is the best starting point in plasma observations in our Solar system. It hosts some of the most energetic and spectacular plasma phenomena in our vicinity. Its proximity allows detailed observations to be carried out while simultaneously gauging the impact of these events on the Earth. Solar flares are some of the most powerful of these phenomena, they will be discussed in more detail in section 2.5. The Sun is a main sequence star with spectral classification G2, it has a mass of  $2 \times 10^{30}$  kg, radius of  $6.96 \times 10^8$  m and a luminosity of  $3.83 \times 10^{26}$  W. The radial structure the Sun and its atmosphere is shown in figure 2.8.

The Sun's interior consists of a central core where the Sun's energy is generated, radiation and convection zones where this energy is transported from the core towards the upper layers, the photosphere and the atmosphere comprising of the chromosphere, transition region and corona. Probing the solar interior is possible



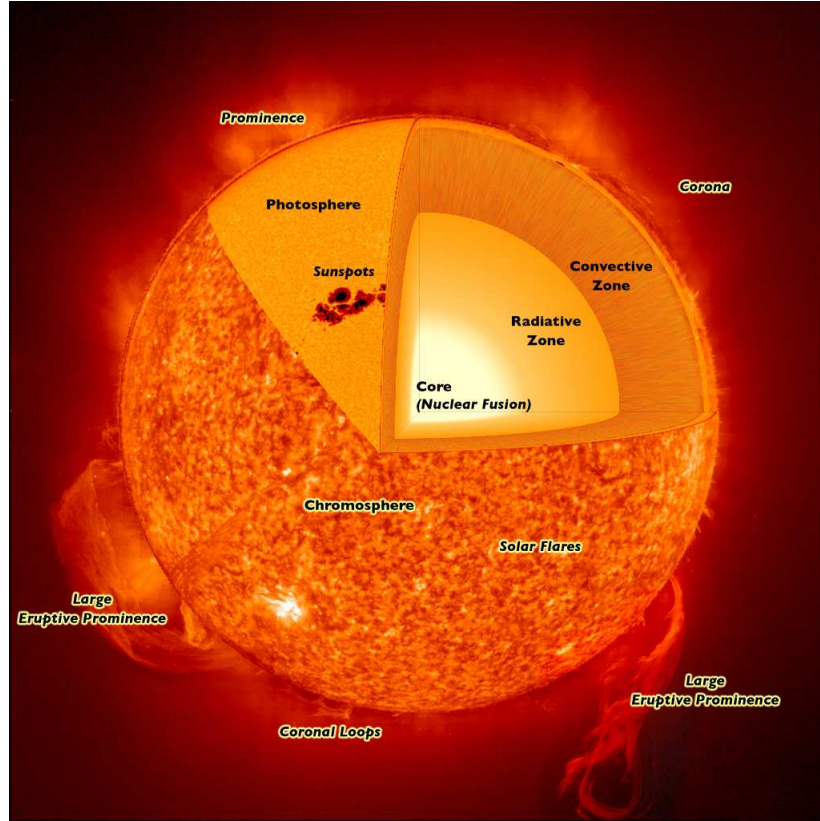


Figure 2.8: The solar structure. (Image from [Infactcollaborative, 2014]).

using helioseismology a technique outline in detail in [Gizon and Birch, 2005]. This analysis is not necessary for our research domain we will instead focus on the solar atmosphere.

### 2.4.2 The Photosphere and Chromosphere

The *photosphere* is a narrow layer that separates the convective zone of the solar interior and the solar atmosphere. Between an average temperature of 4500 K and 6000 K it can be seen in the optical spectrum as the recognisable ‘yellow smooth sun’ that we are accustomed to, see figure 2.9. It marks the point at which the plasma becomes opaque in the white light band to observations. The photosphere is composed of convection cells called *granules* each approximately 1000 km in diameter. Hot plasma rises in regions which are in the centre of a granulation cell while cooler plasma returns to the depths at the edges of each granule. A typical granule has a lifespan of only about eight minutes, resulting in a continually shifting boiling pattern. Super-granulation is observed in the chromosphere. Super granules grow

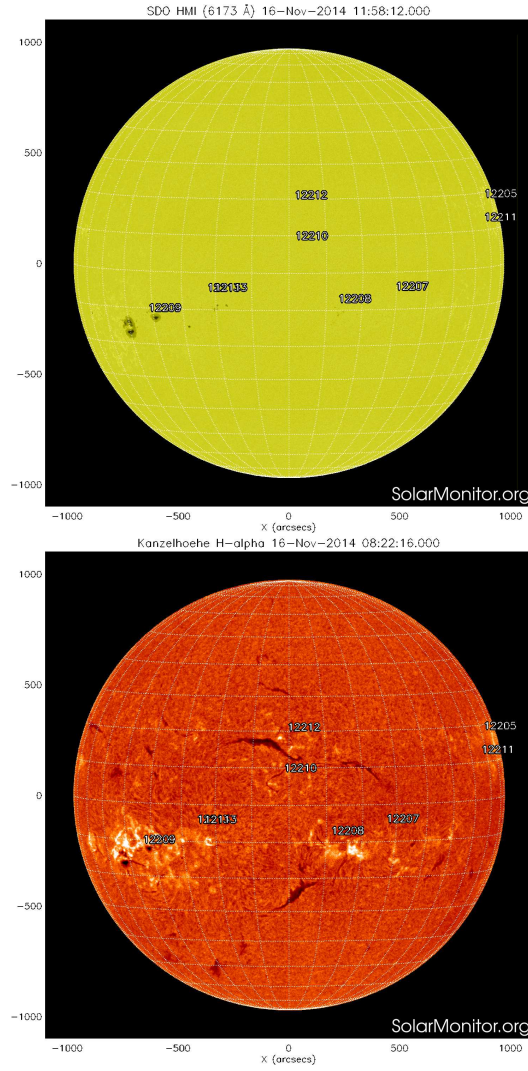


Figure 2.9: Top: Image of the photosphere with a few sunspots present. Bottom: An image of the chromosphere. These images were taken by the Solar Dynamics Observatory (SDO) on the 16/11/2014. The numbers identify different active regions according to the NOAA classification scheme.

up to 30,000 km in diameter with lifespans of up to 24 hours. These details are too fine to see on other stars.

The *chromosphere* is the base of the solar atmosphere extending to 2000 km. Using spectral analysis it was found that temperatures in the chromosphere grow with height from photospheric temperatures at its base up to 10,000 - 20,000 K at its boundary with the corona, [Golub and Pasachoff, 2010]. Densities are seen to decrease rapidly from  $10^{15} \text{ cm}^{-3}$  near the photosphere to  $10^{11} \text{ cm}^{-3}$ . At these higher temperatures hydrogen emits light that gives off a reddish colour (H- $\alpha$  emission) see figure 2.9.

### 2.4.3 The Solar Corona

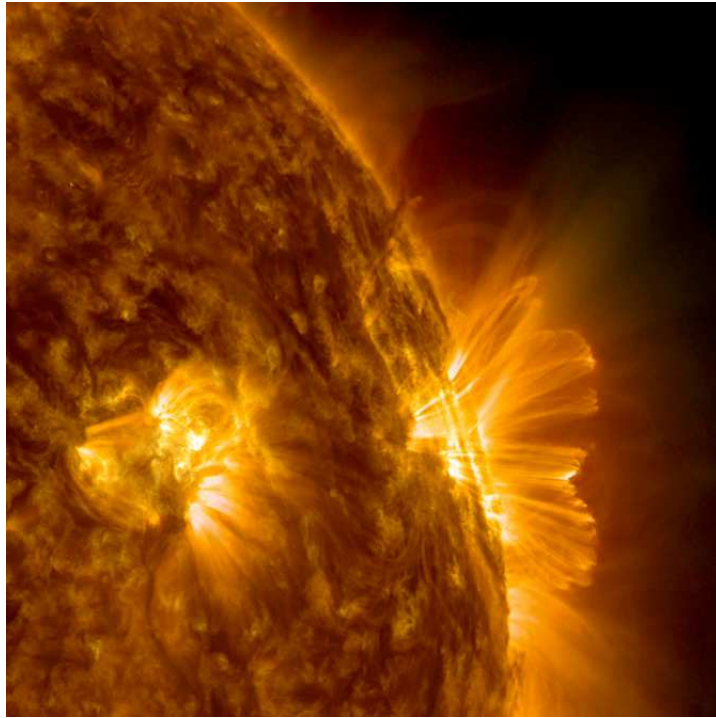


Figure 2.10: Large structured loop arcades demonstrate the inhomogeneity of the solar corona. (Image from [NASA, 2014e]).

The *solar corona* is the high-temperature layer of the Sun's outer atmosphere. It is difficult to define, a simple stratified atmospheric model doesn't capture the prevalent inhomogeneous structures scattered throughout. The extent in which these structures deviate the corona from a spherically symmetric model is shown in figure 2.10. These loop like structures are believed to be magnetic flux tubes filled with hot dense plasma that can be seen anchored in the photosphere and stretching

out to the outer solar atmosphere. Therefore they too, in turn fail to provide a distinct way of categorizing the corona. As it proves difficult to define using height alone another parameter is involved, namely temperature. The photosphere is at a temperature  $\approx 5800$  K. Using basic equations of state it can be shown that the atmosphere is expected to drop in temperature with height however we observe a sharp rise in temperature at  $\approx 2000$  km above the photosphere, see figure 2.11. This small region is labelled the *transition region*. A rough definition of the corona is taken as the domain above the transition region where the temperature has grown to exceed  $10^5$  K. The physical mechanisms for this unexpected heating are unknown, which constitute the coronal heating problem - one of the most popular directions of the solar research, [Marsch, 2006]. This topic although intriguing will not be covered in this work.

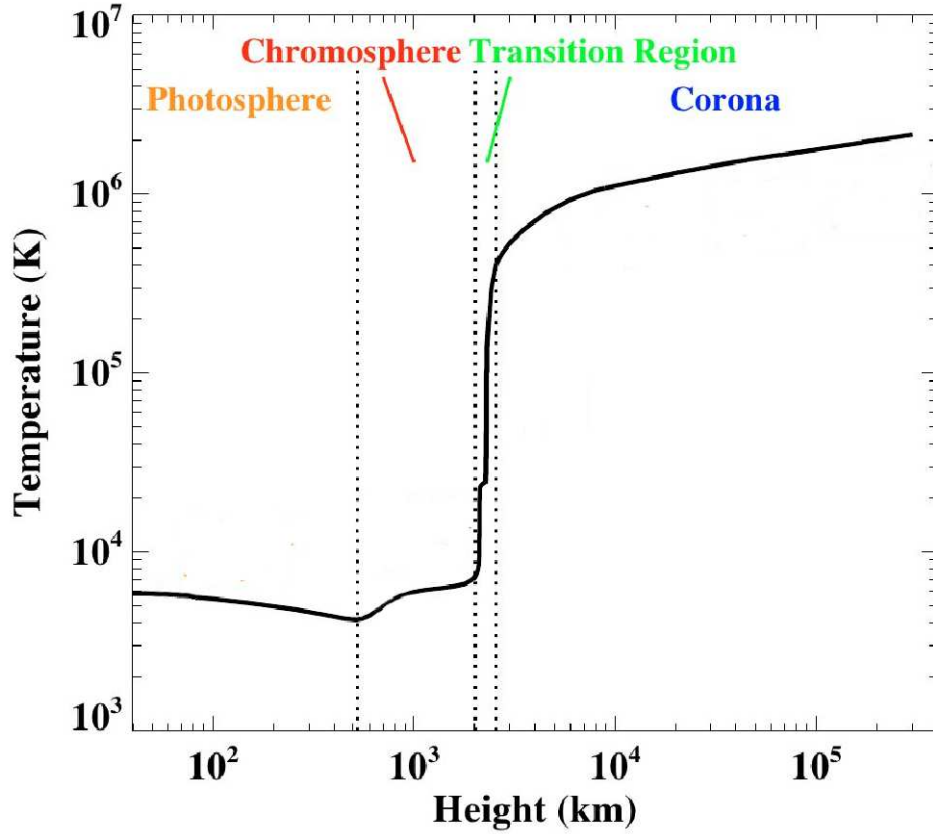


Figure 2.11: Variation of the temperature versus the height above the photosphere. (Image from [Yang et al., 2009]).

The highly structured corona is a magnetically dominated, fully ionised plasma which provides an ideal ground for wave generation and propagation studies.

The observed coronal radiation is characterised by three components: the K-corona where photospheric light is scattered by free electrons; the L-corona which is the spectral line emission from highly ionised atoms or heavy elements and the F-corona exists due to absorption lines of photospheric Fraunhofer spectrum caused by scattering from dust, [Aschwanden, 2006].

#### 2.4.4 Coronal Structures and Phenomena

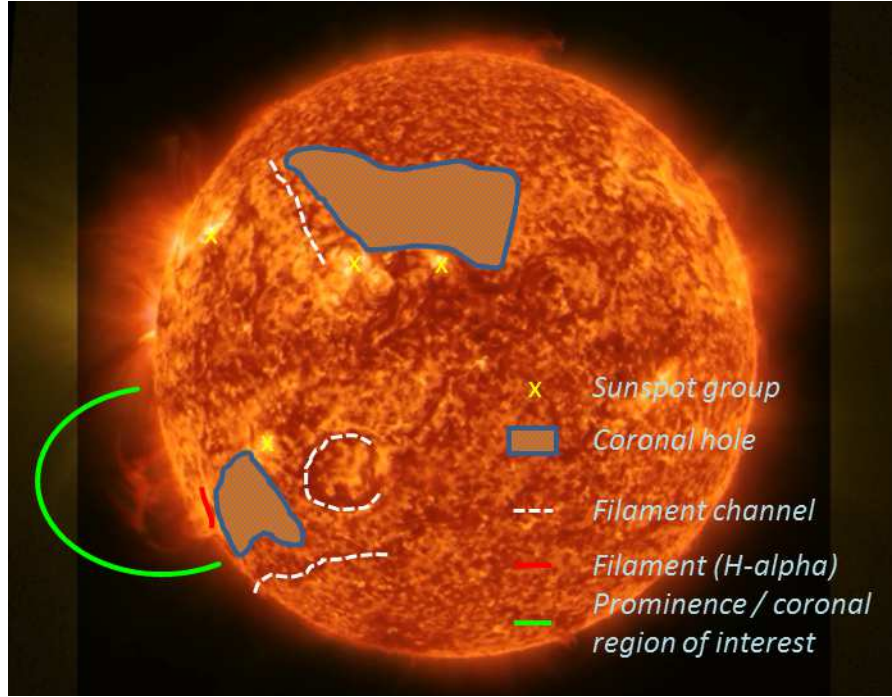


Figure 2.12: A image showing the plethora of phenomena found in the solar corona, including coronal loops, flares, coronal mass ejections, sunspots and prominences, from [NASA, 2014b].

Regions of the corona can be categorised into three main phenotypes, the first are *active regions*, closed magnetic field concentrations which are visible at the photospheric level in optical wavelengths such as *sunspots* or other large-scale magnetic concentrations, see figure 2.9. These regions are normally associated with dynamic processes such as solar flares, see section 2.5. The second domain are *coronal holes*, predominantly located in polar regions and usually consisting of open field lines. They can appear darker due to their reduced density, as a result of efficient plasma transport into the solar wind. The third and final category is the *quiet sun*, regions of closed field lines that are not active regions or coronal holes.



Coronal phenomena tend to be categorised by their morphological appearance in observed images. Analogous to the variety of clouds the Earth’s atmosphere can support, the solar corona exhibits an equally rich menagerie of structures presented in figure 2.12. Reviews of observations and models for all the phenomena discussed can be found in [Reale, 2010, Benz, 2008, Borrero and Ichimoto, 2011, Parenti, 2014].

**Coronal Loops:** The most basic and prevalent structure is the coronal loop. It can be thought of as a magnetic flux tube which has both ends anchored in the photosphere. A closed field line does not constitute a coronal loop, the closed flux tube must be filled with plasma before it can be called a coronal loop. The mechanism behind plasma filling and the stability of such structures remains an active research area, [Aschwanden, 2006, Reale, 2010]. Loops can be seen forming a loop arcade in figure 2.10. Regions of opposite magnetic polarity can sometimes extend to large enough regions to form loop arcades, so that the dipoles can be found aligned perpendicularly to a *neutral line*.

**Flares:** A flare process is associated with a rapid conversion of non-potential magnetic energy into a rapid energy cascade. Such a release results in an acceleration of non-thermal particles, heating of chromosphere/coronal plasmas and a vast quantity of electromagnetic radiation. These processes release radiation on almost all wavelengths: radio, white light, extreme ultra violet (EUV), soft X-rays, hard X-rays and sometimes  $\gamma$  rays for very high energy flares. A more detailed summary of solar flares is outlined in section 2.5.

**Coronal Mass Ejections (CME’s):** Large flares are generally accompanied by eruptions of mass into interplanetary space. Flares and CME’s are two aspects of a large scale magnetic energy release. The two terms have evolved historically from different observational manifestations.

**Filaments and Prominences:** A filament is a region of plasma above a magnetic neutral line that builds up gradually over a few days and may erupt during a flare or CME process. Filaments and prominences are the same structures just observed from different view points. Filaments are observed across the solar disk whereas prominences are observed off limb.

## 2.5 A Solar Flare

In this section we discuss the most eminent physical model, in 2D, for flare excitation and the associated electromagnetic energy releases mechanisms in the radio spectrum. There are a variety of flare models which can describe different phenomena seen in flares. What distinguishes them are mainly the initial magnetic topologies.

A comprehensive review on flare/CME models can be found in [Shibata and Magara \[2011\]](#). Although not all flares can be explained by a single model, it is constructive to start with a standard model that fits most observations and has a well understood theoretical foundation. The most widely accepted model for flares is the 2D magnetic reconnection model that evolved from the concepts of [[Carmichael, 1964](#), [Sturrock, 1966](#), [Hirayama, 1974](#), [Kopp and Pneuman, 1976](#)], called the CSHKP model according to the author initials as described in [[Aschwanden, 2006](#)].

### 2.5.1 The Standard 2D Model

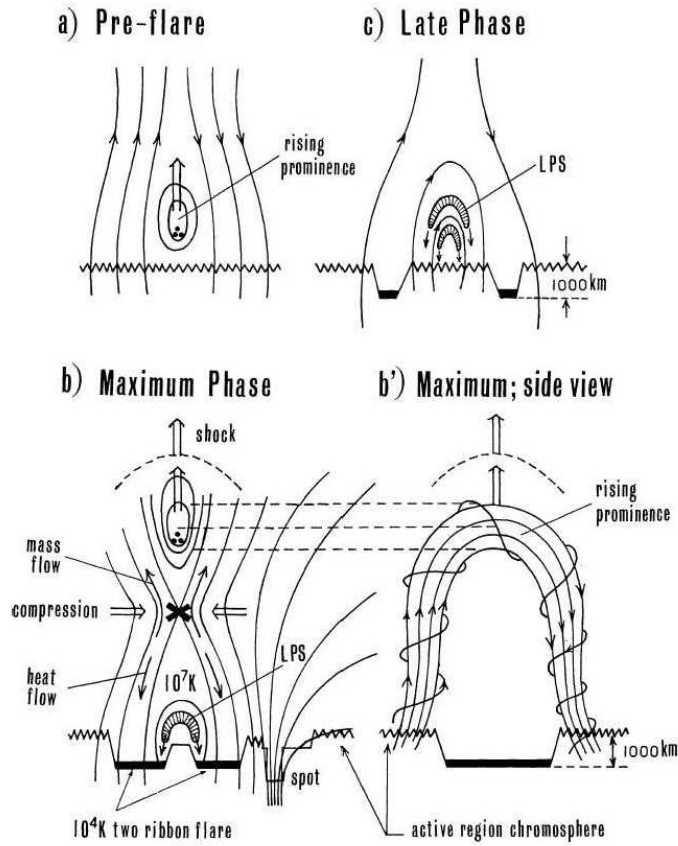


Figure 2.13: The standard model according of a flare, initially a prominence rises (a), this triggers magnetic reconnection beneath a prominence (b), shown in side view (b'), and ends with the draining of chromospheric plasma from the flare loops (c). 'LPS' refers to  $H_\alpha$  loops which tend to be the most dense regions, from [[Hirayama, 1974](#)].

[[Hirayama, 1974](#)] explains the preflare process as a rising prominence above the neutral line in an active region. The prominence carries electric current parallel to the

neutral line which induces a magnetic collapse on both sides of the current sheet after the eruption of the prominence as seen in figure 2.13. The reconfiguration of the magnetic topology converts the liberated magnetic energy into thermal. The local coronal plasma is heated and non-thermal particles follow the magnetic field lines and approach the denser layers of the solar atmosphere at the footpoints of the guiding field lines. As a result of this impulsive heating, chromospheric plasma evaporates and fills the newly reconnected field lines with over dense heated plasma, which produce soft X-ray emitting flare loops. Fast shocks produced in the reconnection outflows collide with previously connected field lines to produce hot thermal hard X-ray sources above the flare loop tops.

### 2.5.2 Quasi-Periodic Pulsations (QPP)

QPP are the quasi-periodic variation in time of flare generated emission in a variety of different bands. Oscillatory variations in the radio and microwave emission from flaring loops have been investigated for several decades, [Aschwanden, 1987]. They are not truly harmonic in nature therefore they have been coined as *quasi-periodic pulsations* (QPP). The periodicities range from a fraction of a second to several minutes. Similar periodicities are often seen in hard X-rays, see [Nakariakov and Melnikov, 2009b]. There is growing evidence that QPP are an intrinsic feature of solar flares. A recent analysis of microwave emission generated in 12 similar single-loop flares showed that 10 events (83%) had at least one or more significant spectral peaks with periods from 5 to 60 s, [Kupriyanova et al., 2010]. Figure 2.14 shows a typical QPP event in microwave emission. MHD coronal seismology uses MHD disturbances as a diagnostic tool to investigate the solar corona. Hence flaring QPPs are a very interesting subject in the coronal seismology community. The observed periods of QPP coincide with the periods of coronal waves and oscillations that are confidently interpreted in terms of the MHD wave theory. Thus, QPP may well be the manifestation of coronal MHD oscillations.

### 2.5.3 Radio Emission from Flaring Regions

In parallel to QPP investigations there are renewed efforts into the radio emission in solar flares mainly due to advances in radio observation instrumentation. According to [Benz, 2008] most radio emission emanating from flare regions do not come from the acceleration region itself but more the non-thermal electrons produced in the acceleration processes which then travel along field lines. This radiation is categorised into two subsets, *coherent* and *incoherent*.



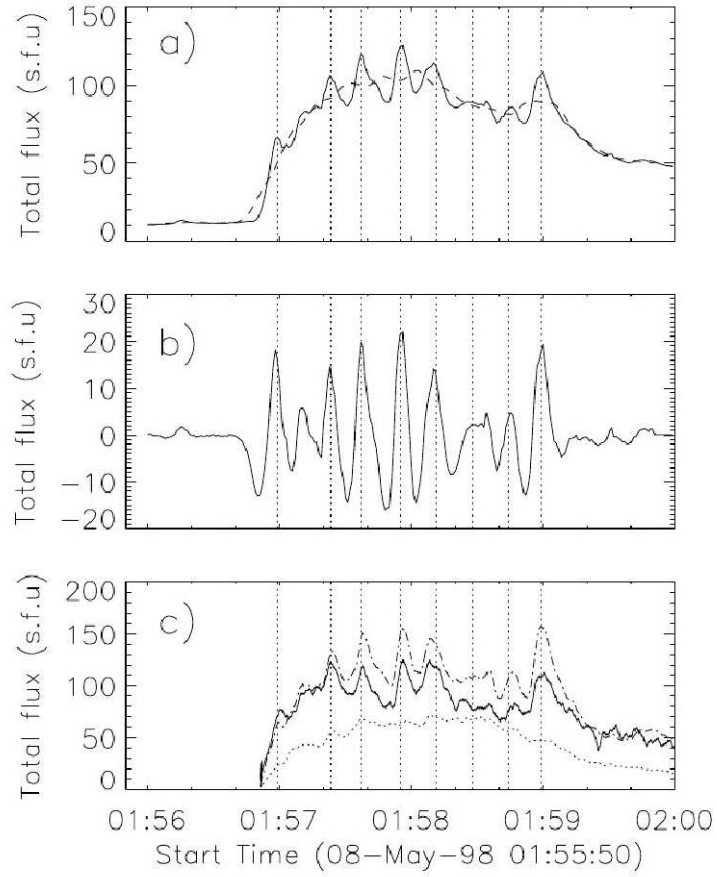


Figure 2.14: a) Integrated flux time profile of microwave emission at 17 GHz for the solar flare of 08/05/1998, as recorded by NoRH. The dashed line is the background emission profile obtained from the integrated flux signal which was smooth using a 20s window. b) The background subtracted signal. c) Microwave emission profiles at 9.4 GHz (dot-dashed line), 17 GHz (solid line) and 3.75 GHz (dotted line), acquired by the Nobeyama Radiopolarimeters, from [Inglis et al., 2008].

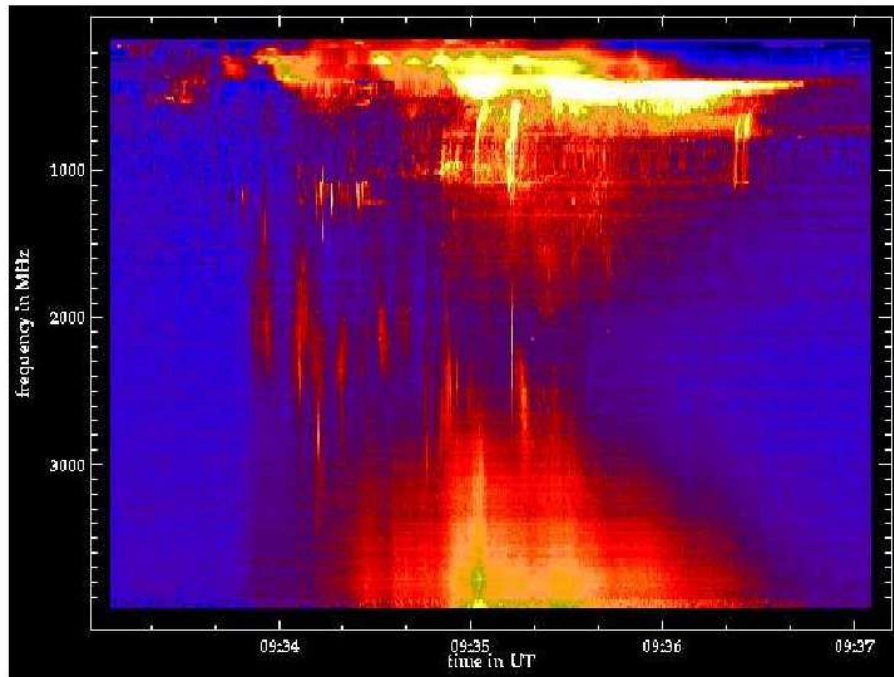


Figure 2.15: An example of a typical radio spectrogram of a solar flare. At low frequencies the radio emission is predominantly type III bursts. The brightest feature is a type V event. At high frequencies, synchrotron emission of mildly relativistic electrons dominates. In the mid-frequency range from 800 – 2000 MHz, narrowband spikes of the decimetric type can be seen, from [Benz, 2008, Figure 28].

In incoherent emission, such as synchrotron emission, non-thermal electrons radiate individually. When a wave organises electrons to emit in phase, the emission becomes coherent. In particular, in some cases radio emission can result from the coalescence of two plasma waves. Coherent emissions are typically produced at the local plasma frequency, (1.1), electron gyrofrequency, (1.2), upper hybrid frequency, ( $\omega_{uh}^2 = \omega_{pe}^2 + \omega_{ce}^2$ ) and their higher harmonics. The plasma frequency, being the cut-off frequency, is the lowest frequency observable directly from outside the solar atmosphere. It is common for these phenomena to produce emission to frequencies high enough to be categorised as microwave. The large variety of flare related radio emissions may be grasped from figure 2.15. It is important to distinguish the emission processes as they refer to widely different physical mechanisms. A brief overview of some of the radio emissions are outlined in table 2.2, however we will not go into detailed explanations in this thesis. Instead we focus more on the impact of MHD perturbations on the radio emission mechanisms.

## Radio Burst Fine Structure

Radio bursts are short lived radio emission usually accompanied with flare activity. The first spectral observations of the large type IV radio bursts revealed a rich variety of fine structures within the radio emission, in particular, a modulation of the continuum emission in the form of narrow stripes in emission and absorption.

Stripes in emission and absorption against the continuum background of solar type IV radio bursts in the meter and decimeter wave ranges are traditionally subdivided into two kinds: zebra pattern (ZP) and fiber bursts (FB), [Kuijpers, 1980, Slottje, 1980]. Their respective parameters are outlined in table 2.5.3. In this thesis we will solely focus on ZP structures.

### 2.5.4 The Zebra Pattern (ZP)

Zebra pattern structures, see figures 2.16 & 2.17, have been observed since the early seventies [Slottje, 1971] yet we are still undecided on their generation mechanism. What is clear is that they are becoming an increasingly revealing tool in the study of flaring loops in the corona. Advances in radio telescopes such as the new Chinese Spectral Radio-Heliograph (CSRH) will allow not only high temporal but also some spatial resolution. If ZP structure can be fully understood then it may become a viable probe into the coronal magnetic field.

TYPE	CHARACTERISTICS	DURATION	FREQUENCY RANGE	ASSOCIATED PHENOMENA
I	Short, narrow-bandwidth bursts. Usually occur in large numbers with underlying continuum.	Single burst: ~ 1 second Storm: hours - days	80 – 200 MHz	Active regions, flares, eruptive prominences.
II	Slow frequency drift bursts. Usually accompanied by a (usually stronger intensity) second harmonic.	3- 30 minutes	Fundamental: 20 – 150 MHz	Flares, proton emission, magnetohydrodynamic shockwaves.
III	Fast frequency drift bursts. Can occur singularly, in groups, or storms (often with underlying continuum). Can be accompanied by a second harmonic	Single burst: 1 - 3 seconds Group: 1 -5 minutes Storm: minutes - hours	10 kHz – 1 GHz	Active regions, flares.
IV	Stationary Type IV: Broadband continuum with fine structure Moving Type IV: Broadband, slow frequency drift, smooth continuum.	Hours - days  30 – 2 hours	20 MHz – 2 GHz  20 – 400 MHz	Flares, proton emission.  Eruptive prominences, magnetohydrodynamic shockwaves.
	Flare Continua: Broadband, smooth continuum.	3 – 45 minutes	25 – 200 MHz	Flares, proton emission.
V	Smooth, short-lived continuum. Follows some type III bursts. Never occur in isolation.	1-3 minutes	10 - 200 MHz	Same as type III bursts.

Table 2.2: Table of radio burst parameters taken from [IPS, 2014].

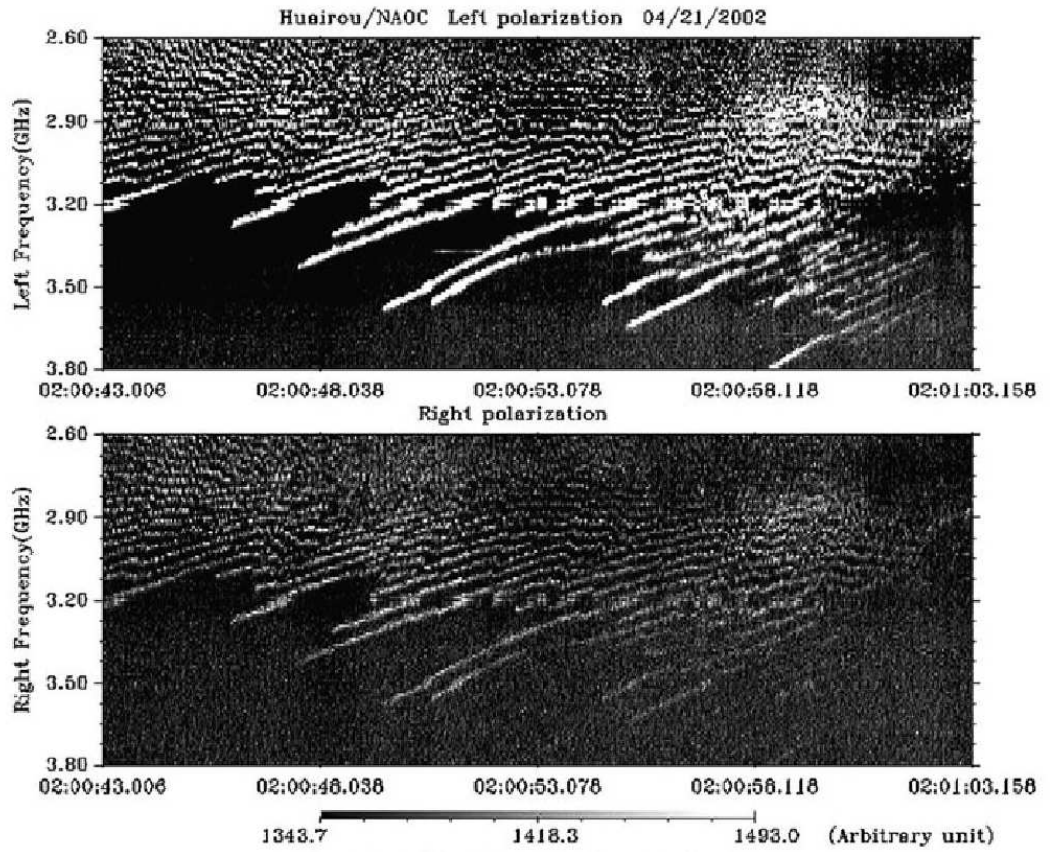


Figure 2.16: A sample dynamic spectrogram exhibiting a ZP structure from the event of 21/04/2002 at 02:00:43-02:01:03 UT, from [Chernov et al., 2005].



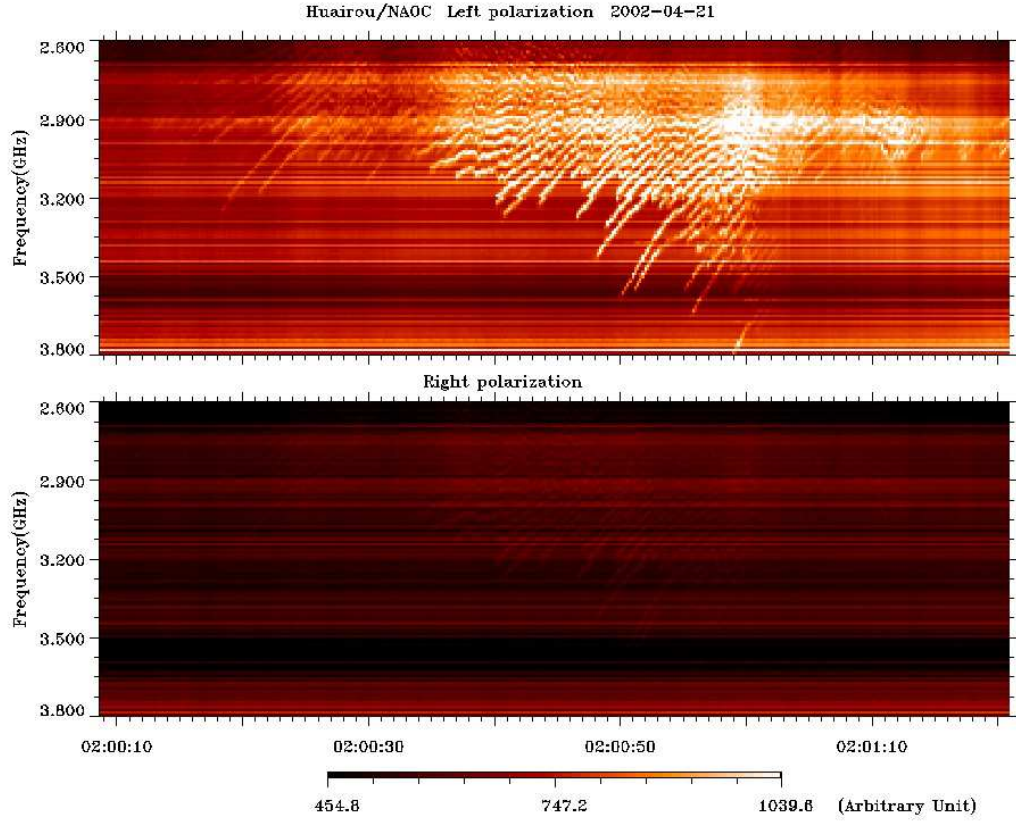


Figure 2.17: An example of a large stripe number ZP radio emission. The highly polarised ZP was observed by the Huairou radio observatory near Beijing.

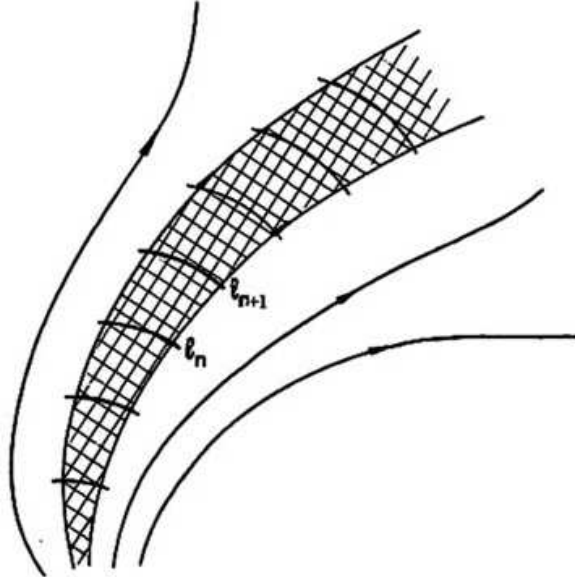


Figure 2.18: Proposed extended source of the double plasma resonance emission mechanism, from [Winglee and Dulk, 1986].

Observed characteristics of ZP and FB	
<b>Zebra patterns:</b>	
Frequency extent	$\leq 3.8$ GHz
Number of consecutive stripes	5-20 (up to 70)
Stripe spacing at 160 - 200 MHz	2-3 MHz
at 800 - 900 MHz	20 MHz
<b>Fiber bursts:</b>	
Frequency extent	30 MHz (up to 120 MHz)
Duration	5-10 s
Single frequency duration	0.2-0.4 s
Instantaneous bandwidth	$\leq 1$ MHz
Drift rate, $-\frac{df}{dt}$	$10^{-2}f + 6 \times 10^5 f^2$
Number in one group	10-30 (up to 300)
Flux	
At 160 - 320 MHz	200 sfu
At 50 - 600 MHz	500 sfu

Table 2.3: Characteristic fine structure parameters of solar radio bursts, from [Kuijpers, 1980, Yu et al., 2013]

### The Double Plasma Resonance Model

The Double Plasma Resonance model, (DPR) is the most widely accepted model to describe the peculiar ZP emission, [Zheleznyakov and Zlotnik, 1975, Kuznetsov and Tsap, 2007]. It relies on electrostatic wave emission when Langmuir waves (see section 1.7.1) self-interact at frequencies near the upper hybrid:

$$f_{uh} = \sqrt{f_{ce}^2 + f_{pe}^2} = s f_{ce}, \quad (2.3)$$

where  $f_{ce}^2 \ll f_{pe}^2$  and  $s$  is any integer. DPR leads to the amplification of plasma fluctuations which following their the conversion to electromagnetic waves significantly increases the associated radio emission in frequencies near the upper hybrid harmonics. This is shown in more detail in figure 2.19.

If the plasma density and the absolute value of the magnetic field, and hence the electron plasma and cyclotron frequencies, vary with height, there are several spatially-separated levels where the DPR condition is satisfied, figure 2.18. Radio emission from different DPR levels come at the local upper hybrid frequencies. The emission from DPR levels form different individual stripes within the ZP structure. Taking into account that  $f_{pe} \gg f_{ce}$  in coronal plasmas, i.e. the upper hybrid frequency  $f_{uh} \simeq f_{pe}$ , the emission frequency,  $f_s$  of a ZP stripe at the harmonics  $s$  equals the plasma frequency  $f_{pe}$  or its harmonic. In a horizontally uniform plasma, the frequency separation between the neighbouring ZP stripes at the harmonics  $s$

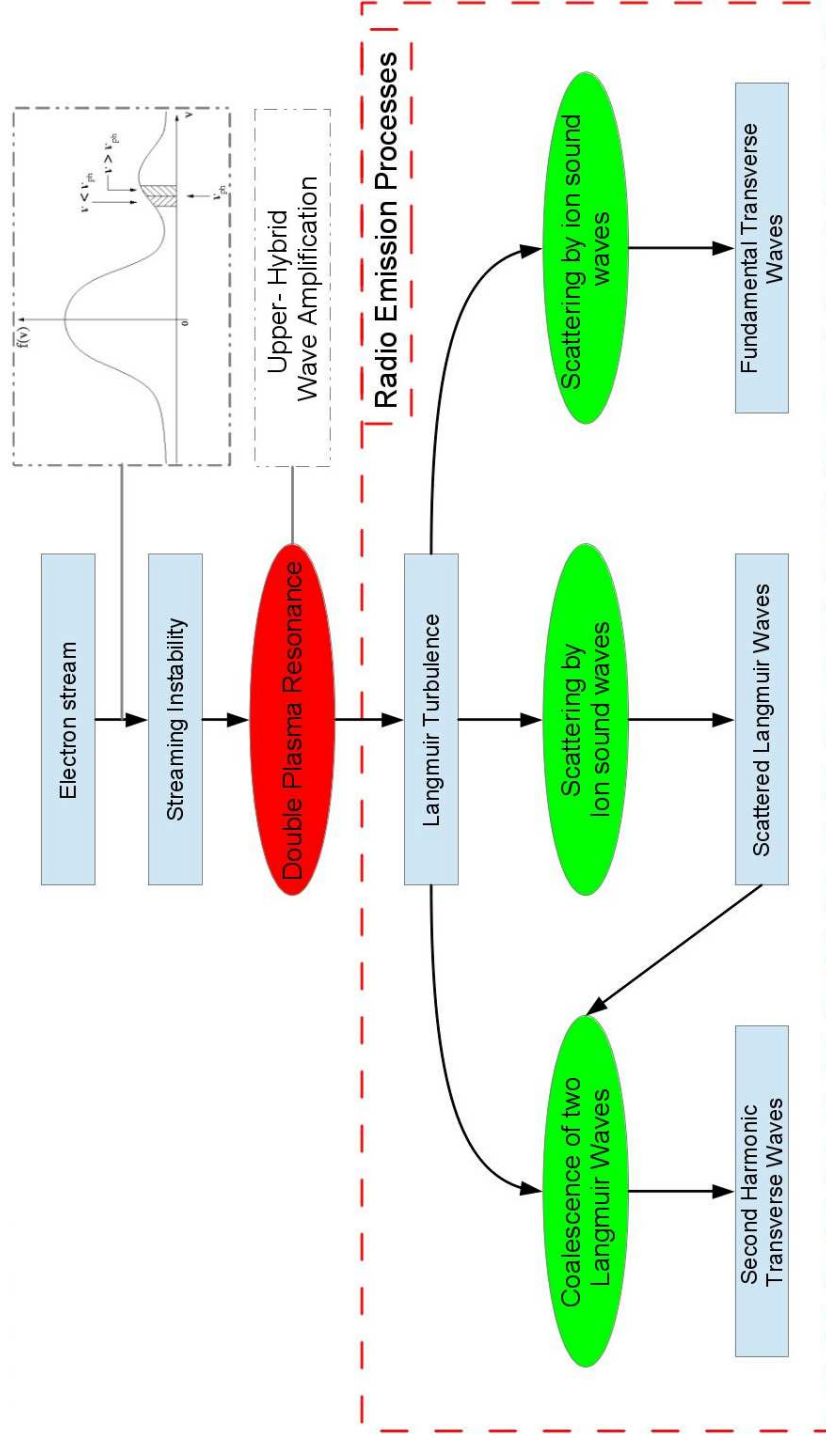


Figure 2.19: Energy flow for the production of ZP using the DPR emission mechanism. This is an adaptation of the plasma emission theory from [Ginzburg and Zhelezniakov, 1958], with the inclusion of the DPR mechanism (red). The radio emission mechanisms are highlighted in green.



and  $s + 1$  is given by:

$$\Delta f_s = f_{s+1} - f_s \simeq \frac{m}{1 - (2L_n/L_B)} f_{ce}, \quad (2.4)$$

where  $L_n = n_e(\partial n_e/\partial h)^{-1}$  and  $L_B = B(\partial B/\partial h)^{-1}$  are the density and magnetic field scale heights as a function of height above the photosphere  $h$  and the coefficient  $\xi$  describes the mechanism of wave coalescence. In DPR  $\xi = 1$  when the emission engages from the coalescence of two excited plasma waves, resulting in weakly polarised radio emission.  $\xi = 2$  when the emission generates from the coalescence of an excited plasma wave with a low frequency electrostatic wave, conversely producing strongly polarised radio emission shown in figure 2.17. The concluding relations:

$$f_s \simeq \xi f_{pe} \propto n_e^{1/2}, \quad (2.5)$$

$$\Delta f_s \propto \xi f_{ce} \propto B, \quad (2.6)$$

implicate time variation of magnetic and density fields with the dynamics of ZPs. This link can be exploited to gain new information on the plasma regions in which ZP production occurs. By this argument the movement of MHD fluctuations through ZP emission regions should result in periodic fluctuations in ZP emission and structure.

There are several other ZP emission models in literature, the most advanced model is that proposed by [Winglee and Dulk, 1986], based on cyclotron non-saturated maser emission of electrostatic waves by a loss-cone electron distribution. However the DPR mechanism is the most widely accepted although it and most other emission mechanisms cannot account for all the features found in ZP fine structure.

## Chapter 3

# Instrumentation

### 3.1 Introduction

In this chapter we present an overview of the satellite and ground based observational systems used throughout this thesis. The purpose is to provide the reader with a base understanding of the observational tools used in this thesis as well as detailed description of data available from each instrument.

### 3.2 Space Mission Cluster

The Cluster mission was launched in the year 2000 to study the magnetosphere and interplanetary plasmas in three dimensions. The mission consists of four satellites flying in a tetrahedral formation. Cluster was set up in a polar orbit with apogee and perigee at  $19.6 R_E$  and  $4.0 R_E$  respectively. The separation of the individual Cluster spacecraft has changed throughout the mission and was approximately  $\approx 1000$  km for the periods studied in this thesis.

Its elliptical orbit takes it through the magnetosphere and out into the foreshock region (as discussed in 2.3.2) and eventually the solar wind, see figure 3.2. During certain intervals of time the satellite group can be used to study the solar wind and the terrestrial foreshock in situ. Cluster continuously takes measurements of electromagnetic fields, plasma velocity and charge carrier densities at a sampling frequency of  $\approx 0.25$  Hz. The FGM measurement system (see section 3.2.2) has an enhanced resolution capacity for magnetic field readings, sampling at a frequency of  $\approx 22$  Hz. It is for this reason that studies on the solar wind will be carried out predominately using magnetic field data when available.

Cluster satellites spin with a period of 4 s to produce three dimensional

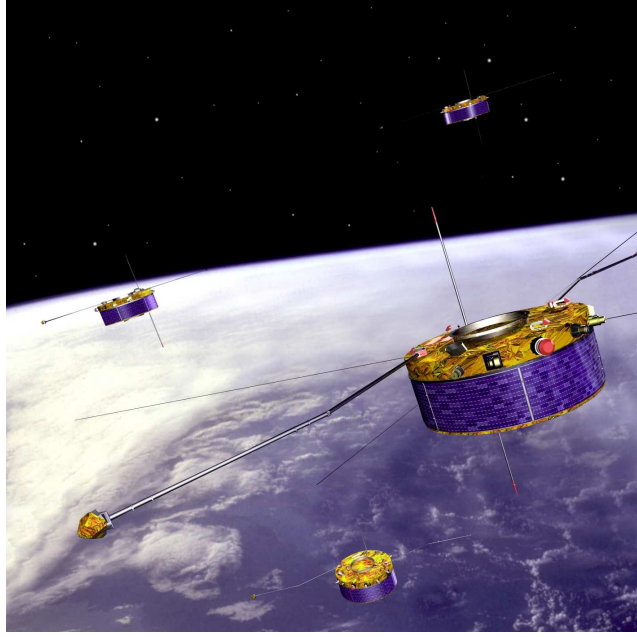


Figure 3.1: Artist's impression of the four satellites of Cluster in orbit, (Image from [ESA, 2014b]).

distributions. Data on particle distribution functions is obtained with the Cluster Ion Spectrometer (CIS). The instrument produces spectra which are averaged over the 4-second window, as a result the resolution of plasma parameters is much lower than magnetic field. This thesis utilises data from both FGM and CIS instruments, see sections 3.2.2 and 3.2.3. To account for the difference in sampling rates the magnetic field data can be re-sampled at the lower rate of 0.25 Hz when being compared with plasma parameters. A full list of the instruments on the Cluster spacecraft is shown in table 3.1.

### 3.2.1 Geocentric Solar Elliptical Co-ordinate System

All three dimensional Cluster data is presented in a Cartesian format with  $(x, y, z)$  components. The Cluster group uses the *geocentric solar elliptical* co-ordinate system (GSE). With the origin at the centre of the Earth it aligns the x-axis with the central line between the Earth and Sun centres. The z-axis is aligned with the ecliptic north pole which is defined as the normal to the plane of the Earth's orbit. The y-axis is simply oriented such that the system forms a orthonormal axis set that points in the direction motion through the orbit, this is shown schematically in figure 3.3. It is useful for magnetospheric and bow shock studies as all motion is relative to the Earth not to the Sun.

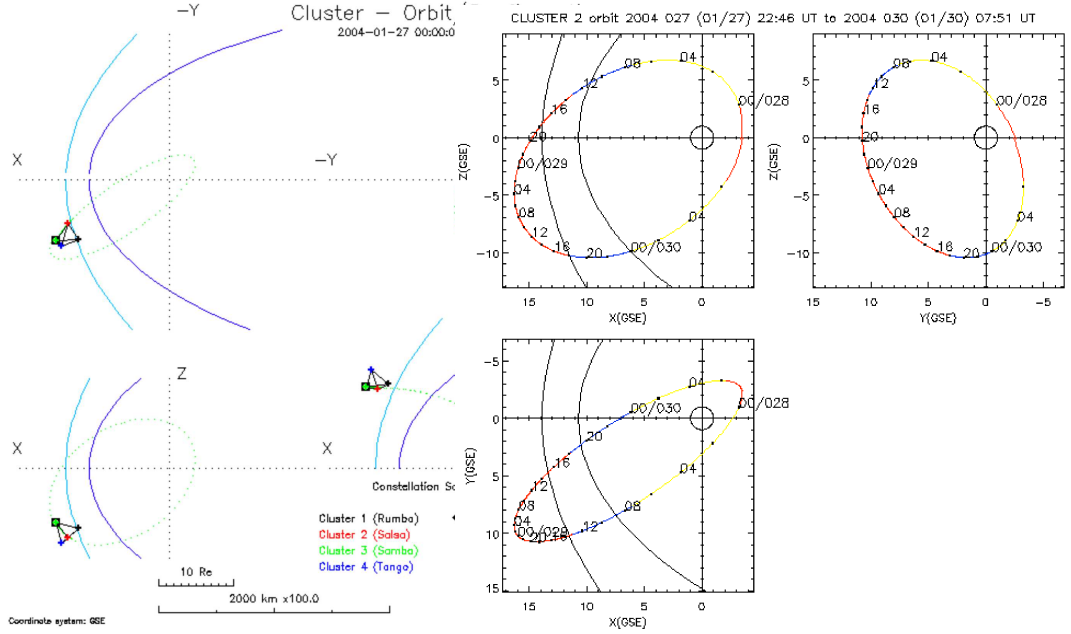


Figure 3.2: Cluster Orbit plot for the 27/01/2004, the left, displays the tetrahedral formation, the right, demonstrates Cluster’s elliptical orbit. The orbit plots also presents lines to show the average positions of the bow shock and magnetopause, from [ESA, 2014a].

### 3.2.2 Flux Gate Magnetometer (FGM)

Each Cluster spacecraft carries an identical FGM instrument, [Balogh et al., 2001]. The instrument consists of two tri-axial fluxgate magnetic field sensors located on one of the two radial booms of the spacecraft. The primary sensor samples the magnetic field vector at 201.793 vectors  $s^{-1}$  however this cannot be streamed to the ground due to the small bandwidth. This rate is therefore re-sampled at a lower rate for streaming. The sample rate used in this thesis is at a rate of 22.417 vectors  $s^{-1}$ . The magnetic field vectors are converted from Cluster’s spinning reference frame to the de-spun frame in GSE coordinates and into the scientific units nT.

### 3.2.3 Cluster Ion Spectrometer (CIS)

CIS is capable of measuring three dimensional ion distributions at a resolution which coincides with the spacecraft rotation time (spin resolution), [Rème et al., 2001]. It is made up of two detectors, the Hot Ion Analyser (HIA) and the Composition and Distribution Function Analyser (CODIF). The data used in this thesis comes from HIA thus the CODIF instrument will not be discussed further.

Instrument	Purpose
ASPOC	Spacecraft potential control
CIS	Ion velocity distributions
EDI	Electric field drift velocity
FGM	Magnetometer
PEACE	Electron velocity distributions
RAPID	High energy electron and ion velocity distributions
DWP	Wave processor
EFW	Electric field and waves
STAFF	Magnetic and electric fluctuations
WBD	Electric field and wave forms
WHISPER	Electron density and waves

Table 3.1: The complete instrument list for each Cluster spacecraft, [[Escoubet and Goldstein, 2001](#)]

CIS Mode	Mode Name
0 SW-1	Solar Wind / SW tracking - Mode 1
1 SW-2	Solar Wind / 3D upstreaming ions - Mode 2
2 SW-3	Solar Wind / SW tracking - Mode 3
3 SW-4	Solar Wind / 3D upstreaming ions - Mode 4
4 SW-C1	Solar Wind / SW tracking - Data Compression - Mode 1
5 SW-C2	Solar Wind / 3D upstreaming ions - Data Compression-Mode 2
6 RPA	RPA Mode
7 PROM	PROM Operation
8 MAG-1	Magnetosphere - Mode 1
9 MAG-2	Magnetosphere - Mode 2
10 MAG-3	Magnetosphere - Mode 3
11 MAG-4	Magnetosphere / Magnetosheath - Mode 1
12 MAG-5	Magnetosheath - Mode 2
13 MAG-C1	Magnetosphere - Data Compression - Mode 1
14 MAG-C2	Magnetosheath - Data Compression - Mode 2
15 CAL	Calibration / Test Mode

Table 3.2: CIS Operational Modes, taken from [[Dandouras and Barthe, 2012](#)].

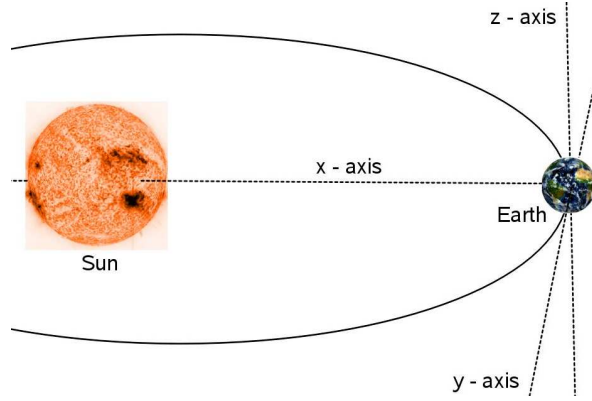


Figure 3.3: Schematic diagram of the geocentric solar elliptical coordinate system used by the Cluster satellite group.

The CIS instruments possess a large degree of flexibility in the selection of operational mode. CIS can maintain one of sixteen operational modes listed in table 3.2. Our data was sampled while CIS was in mode 5 exclusively to insure that the solar wind and the upstream ions were the sole contribution to the HIA moments. In this mode the solar wind beam is tracked by HIA only once every 16 spins. In the remaining 15/16 spins a broader energy sweep is used for the solar wind detection by the ‘*’*’ section (discussed below). At the same time upstreaming ions are observed by the ‘high G’ section, which is then looking in the anti-sunward direction.

### Hot Ion Analyser (HIA)

The Hot Ion Analyser (HIA) instrument combines the selection of incoming ions according to the ion energy per charge by electrostatic deflection in a symmetrical, quadrispherical analyser which has a uniform angle-energy response with a fast imaging particle detection system. HIA has two  $180^\circ$  sections which look in a plane parallel to the spin axis as shown in figure 3.6. They are known as high and low sensitivity, *high G* and *low G*, respectively. They provide different resolution in the polar angle yet have the same azimuthal resolution of  $5.625^\circ$ . The azimuthal resolution arises because of the two dimensional resolution is recorded every 62.5 ms as the spacecraft spins. In this way a full three dimensional distribution can be measured every spin. The high G section’s polar range is divided into 16 equal sections, whereas the low g is divided into 8. High G is specified for hot plasmas and is dedicated to studying the magnetosphere while low g is meant for the solar wind. The plasma data from HIA presented in this work is made up solely from data taken in the low g mode.

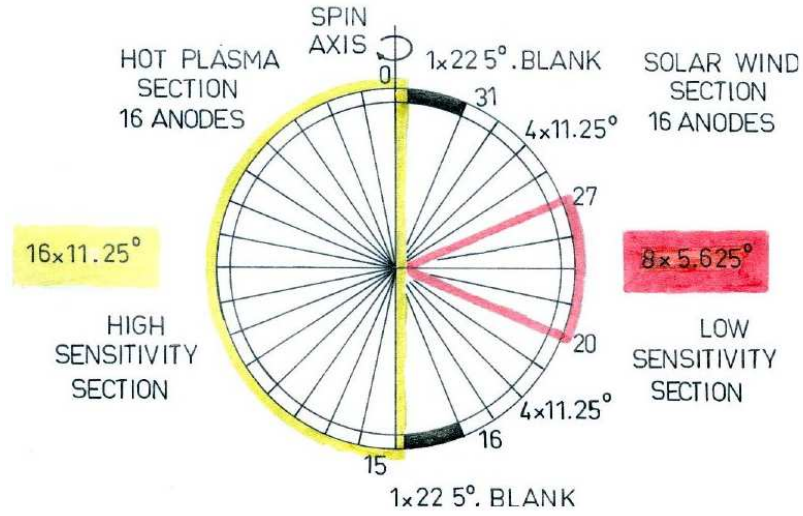


Figure 3.4: Schematic diagram of Hot Ion Analyser (HIA) high and low sensitivity sections. (Image from [Rème et al., 2001]).

### 3.3 Wind

Wind was launched on November 1, 1994 and was the first of two NASA spacecraft in the Global Geospace Science initiative and part of the International Solar Terrestrial Physics (ISTP) Project. A schematic diagram is shown in figure 3.5. Objectives of the Wind mission were to provide complete plasma and magnetic field data for magnetospheric and ionospheric studies. It also aimed to study basic plasma processes in the near Earth solar wind. Since its launch it has spent time orbiting near Earth studying the ionosphere and then the magnetosphere. In the more recent years it has shifted to an orbit around the L1 Lagrange point between the Earth and the Sun, allowing studies of the solar wind before its interaction with the Earth's bow shock, see section 2.3.2. We have used data from times when it was in the deep solar wind and thus not influenced by the terrestrial foreshock.

We used the Solar Wind Experiment (SWE) as a comparison to Cluster data taking advantage of the fact Wind was situated upstream of the Cluster mission. The SWE measures ions and electrons in the solar wind to deduce the solar wind velocity, density, temperature and heat flux. SWE consists of five integrated sensor boxes and a data processing unit. Three dimensional velocity distributions of the ion component in the solar wind are made by a pair of Faraday Cup analysers, [Lazarus et al., 2007]. These provide a wide field of view while being able to measure velocity distributions in plasmas with Mach numbers greater than one. In this thesis we

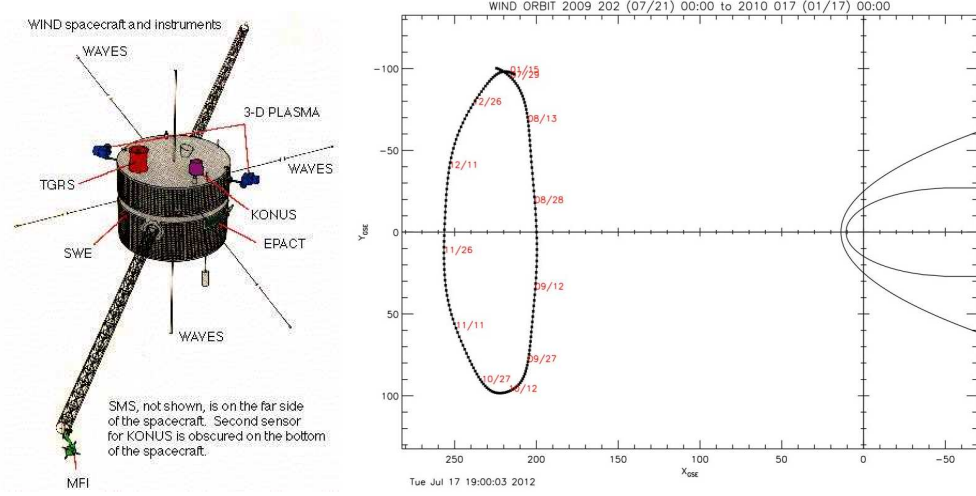


Figure 3.5: Left: schematic diagram of the Wind satellite, image from [NASA, 2014c]. Right: six month orbit given in GSE coordinates, starting in July 2009, image from [NASA, 2014d].

implement Wind SWE ion anisotropy data with a cadence of 92 s. This data is used as a control comparison to Cluster data.

### 3.4 Ground Based Radio Telescopes

Ground based radio telescopes are used to investigate flare processes in the solar corona in the radio and microwave wavebands. There is little absorption of high frequency ( $> 50$  MHz) radio waves in the Earth's atmosphere. Radio telescopes require very large antenna in comparison to shorter wavelength observatories to achieve the same spatial resolution. Tangentially to this radio observatories possess shortened time cadences in comparison to space-borne instruments such as on-board SOHO or SDO. This allows observers to probe temporal scales approaching and beyond the MHD limit.

It is often useful to compare events using two or more radio telescopes to ensure that they are not acquiring terrestrial or artificial signals. Thus this thesis has utilised data from both Nobeyama Radioheliograph and the Solar Broadband Radio Spectrometer. They are situated far enough apart to de-tangle respective local interference yet close enough to ensure they are able to simultaneously observe the full solar disc for extended periods of time.



### 3.4.1 Solar Broadband Radio Spectrometer (SBRS/Huairou)

The Solar Broadband Radio Spectrometer (SBRS/Huairou) is a robust solar radio spectrometer based near Beijing, China. It consists of one dish and is built to measure radio waves emitted by the Sun, [Fu et al., 1995]. The total flux density of solar microwave emission is observed in both left- and right-handed circular polarization (LHCP and RHCP) at three frequency bands:

- 1.10-2.06 GHz (time resolution: 5 ms, frequency resolution: 4 MHz).
- 2.60-3.80 GHz (time resolution: 8 ms, frequency resolution: 10 MHz).
- 5.20-7.60 GHz (time resolution: 5 ms, frequency resolution: 20 MHz).

Typical data is presented as a dynamic spectra, see figure 2.17, which has already undergone calibration. Each one of the 240 channels records intensity of emission against time. These are then stacked to form an image of frequency against time with the artificial colour specified by the intensity.

### 3.4.2 Nobeyama Radioheliograph (NoRH)



Figure 3.6: Photograph of the array of dishes at the Nobeyama Radioheliograph, Japan. (Image from [NOAJ, 2014]).

Nobeyama Radioheliograph (NoRH) is a ground based radio-interferometer situated in Nagano, Japan, [Nakajima et al., 1994]. The instrument consists of 84 parabolic antennas, 80 cm in diameter. It was built in a T-shape base line

Frequency	17 GHz (Right and left circular polarization), 34 GHz (only intensity)
Field of view	Full solar disk
Spatial resolution	10 arcsec (17 GHz), 5 arcsec ( 34GHz)
Temporal resolution	0.1 s (Event), 1 s (Steady)

Table 3.3: Overview of the operating parameters of NoRH.

configuration and has been observing since April 1992 at an observation frequency of 17 GHz in both left- and right-handed circular polarisation. Later an observational band of 34 GHz was added however it is unable to distinguish between polarisations. An overview of the operational parameters is shown in table [3.3](#).

## Chapter 4

# Temperature Anisotropy in the Terrestrial Foreshock

### 4.1 Introduction

In this chapter we aim to explore the effect of non equilibrium particle distributions on waves and turbulence in the foreshock region, already discussed in 2.3.4. Typical plasma parameters for this region are shown in Table 4.1. A portion of the solar wind plasma is returned to the upstream region after a collisionless interaction with the Earth’s magnetosphere to produce an observable ion beam, see section 2.3.4. The combination of inflowing and counterstreaming plasma upstream of the shock is subject to a variety of instabilities leading to wave generation described in more detail in section 1.8.

Parameter	Interval: 27/01/2004
Average Magnetic Field $\langle B \rangle$	$8.3 \pm 0.8$ nT
Average Number Density $\langle n \rangle$	$7.052 \pm 0.050$ cm <sup>-3</sup>
Plasma $\beta$	$0.488 \pm 0.405$
Alfvén Wave Speed $v_A$	$513 \pm 110$ kms <sup>-1</sup>
Solar Wind Speed $v_{sw}$	$483 \pm 139$ kms <sup>-1</sup>

Table 4.1: Experimentally measured parameters of the solar wind at a distance of approximately  $10R_E$  from Earth along the Earth-Sun line. Values were averaged over the interval: 27/01/2004, 03:50-04:35.

The terrestrial foreshock is an ideal laboratory for the in-situ study of the interaction between a quasi-stationary shock and a collisionless plasma. In particular, the region upstream of the quasi-parallel shock supports a plethora of dispersive

plasma waves as discussed in section 1.7.3. Wave modes can interact with particles in both a resonant and non-resonant manner as described in section 1.8.3. These interactions may lead to particle acceleration and plasma heating. An understanding of heating mechanisms in collisionless quasi-parallel shocks is crucially important to many outstanding space plasma problems, such as coronal heating and the non-adiabatic expansion of the solar wind. This work presents observational evidence for foreshock dissipation mediated by the fire hose instability.

Early foreshock studies identified multiple wave generation mechanisms for both left and right hand circularly polarised waves in the plasma frame [Heppner et al., 1967, Fairfield, 1969, Russell et al., 1971, Barnes, 1970].

The beam instability (see section 1.8.3) is the primary mechanism producing right-hand polarised transverse waves, propagating parallel and anti-parallel to the interplanetary magnetic field (IMF). Waves travelling along the beam are resonant with the ion beam population, while waves propagating anti-parallel to the beam may become unstable to the non-resonant fire hose instability.

#### 4.1.1 Wave Modes of the Terrestrial Foreshock

Recent studies in this region explore a number of distinct wave modes which have previously been identified in the Earth’s foreshock. Burgess [1997], Eastwood et al. [2005] provide comprehensive reviews of this topic. The foreshock displays a large variance in particle distributions. This complex morphology leads to an associated multitude of upstream waves. Eastwood et al. [2005] outlines how wave species are categorised by observed frequency and key characteristics. A first step in understanding the evolution of the terrestrial foreshock plasma is to understand which of these wave modes are present. We can then assess their impact on the particle distributions and thus the plasma parameters.

The first mode of importance to this work was identified as the ultra low frequency (ULF) fast magnetoacoustic wave mode. This mode typically spans 5 mHz to 0.1 Hz with a peak frequency  $\approx 0.1 w_{pi}$ . These fast magneto-acoustic waves are seen travelling radially outward from the Earth. They are distinct due to their large amplitude,  $\delta B/B \approx 0.2$ , compared to other wave modes. It is believed that they are generated via the ion resonant beam instability, section 1.8.3.

The second, higher frequency mode, was identified as the ‘1 Hz whistler’ wave mode. Eastwood et al. [2005] and Burgess [1997] describe it by its small amplitude and intrinsic right hand polarisation. Burgess [1997] provides evidence for their production via oscillations of the bow shock, not an energised particle population, however this is still not proven conclusively.

Several data analysis techniques have been used to identify these modes in our data intervals. We pay particular attention to the ULF magnetoacoustic modes.

## 4.2 Data Intervals

The data analysed in this chapter consists of Cluster high resolution ( $\approx 22$  Hz) magnetic field data from the FGM instrument (see section 3.2) and the lower resolution spin data (0.25 Hz) from CIS-HIA onboard calculated solar wind moments. They contain measurements of core population properties such as proton temperature, density and velocity in GSE coordinates as discussed in section 3.2.1). All CIS-HIA samples were collected in mode 5, which measures the core population of the solar wind beam, see section 3.2.3.

In principle, a small fraction of a field-aligned beam may contribute to these measurements. Here, we assume that such effects would lead to small variations in the on-board computed moments, but would not result in the large and systematic changes. Also, the HIA instrument cannot differentiate between different ion species, thus the effects of  $\alpha$ -particles are folded into these measurements. The field of view of the instrument in this mode is approximately  $\pm 22$  degrees as discussed in section 3.2. The visual inspection of the velocity distributions, using [CLWeb, 2014] ground computed product, confirmed that this field of view was sufficient to capture the majority of the distribution functions for selected intervals. We consider a ‘core’ proton velocity distribution that is defined as a distribution which can be approximated by a single temperature Maxwellian, [Kasper et al., 2002, Hellinger et al., 2006]. While HIA was in mode 5 it excluded any particles outside of the core distribution of the reflected ions, i.e. the bulk solar wind distribution. All intervals had core plasma thermal velocities much lower than the average solar wind velocity.

### 4.2.1 Data Interval Selection

We began by searching for intervals where Cluster passed through the foreshock while showing a strong increase in fluctuation strength, shown by the example figure 4.1. A comprehensive list of these intervals was found in [Narita et al., 2004]. Unfortunately not all of these suited our study due to missing data or Cluster taking observations in an unsuitable mode. However we isolated the intervals which were found to match all the necessary criteria, listed in Table 4.2.

In this chapter we use the interval 27/01/2004 as a canonical sample to represent all intervals highlighted in table 4.2 as the results found are in agreement. If results differ the full dataset will be presented with variations highlighted. When

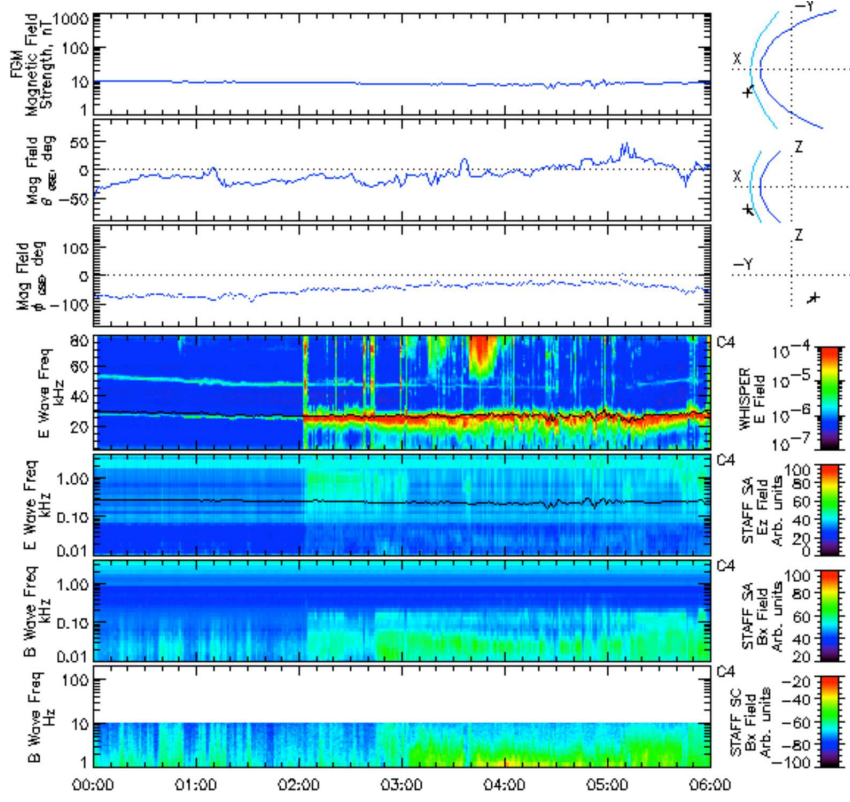


Figure 4.1: Cluster overview showing key parameters, for the 27/01/2004 with a plot of the constellation position in relation to the bowshock displayed in the upper right panel. This interval exhibits a clear increase in electric field wave power at discrete frequencies, seen to occur at 2:00 am. The higher resolution magnetic field data was needed to observe fluctuations clearly.

Date	Times	Spacecraft
27/01/2004	03:50-04:35	C1
16/02/2002	06:19-06:29	C1, C3
20/02/2002	22:00-22:06	C1 C3
19/02/2010	00:16-01:10	C1
21/02/2002	22:19-22:29	C1, C3
11/02/2002	22:04-22:14	C1, C3
27/03/2002	07:15-07:25	C1, C3

Table 4.2: Cluster data intervals used in this chapter. Intervals were selected from the much larger dataset presented in [Narita et al., 2004].

available, measurements from spacecraft *C1* and *C3* were treated as independent measurements. Separation between these spacecraft was  $\approx 10000$  km, except for interval 4, when spacecraft *C1* and *C3* were considerably closer. In order to compare foreshock data with that of the ambient solar wind upstream, we have identified one interval of Wind spacecraft data, for which Wind magnetic field vector data was correlated to Cluster data. This is Cluster interval of 19/02/2010 which resides in the foreshock from 00:16-01:10. We examined Wind SWE ion anisotropy data with time cadence of 92 seconds. Time shift of 3200 s was obtained from cross correlation of Wind (3 sec cadence) and Cluster (4 sec cadence) magnetic field data.

### 4.3 Signal Analysis

This section outlines the various data analysis techniques deployed to exploit the datasets as an attempt to identify wave activity. Several different techniques have been used to derive the same result in order to underpin the observations made.

Inspection of Cluster quick view data panels indicated fluctuations in all of the intervals chosen as shown by our example figure 4.1. The nature of these fluctuations needed to be identified to find regions of strong wave activity to compare to established observations as those shown in [Eastwood et al., 2003, 2005, Burgess, 1997]. The fluctuations have strong, regular periodicity as shown by figure 4.2. Strong periodicity doesn't provide evidence for the presence of waves as there are several wave-free mechanisms which can induce periodicity into a signal. If we consider a situation where Cluster is moving obliquely to the field and thus experiencing varying particle densities, then there could exist a situation where a periodic signal would be observed by the instrumentation due to periodic regions of concentrated particle densities. This could not be considered a wave but would still manifest as a strongly periodic signal, hence other data analysis techniques were required to investigate their existence.

#### 4.3.1 Field Aligned Projection

The individual Cluster spacecraft are spread over a large region in space. This results in each spacecraft feeling the IMF at a slightly different orientation in the GSE coordinate system (see section 3.2.1). So to compare datasets between satellites it was important to rotate into an invariant coordinate system, for simplicity a field aligned Cartesian system was chosen. The unit vectors were chosen to be:

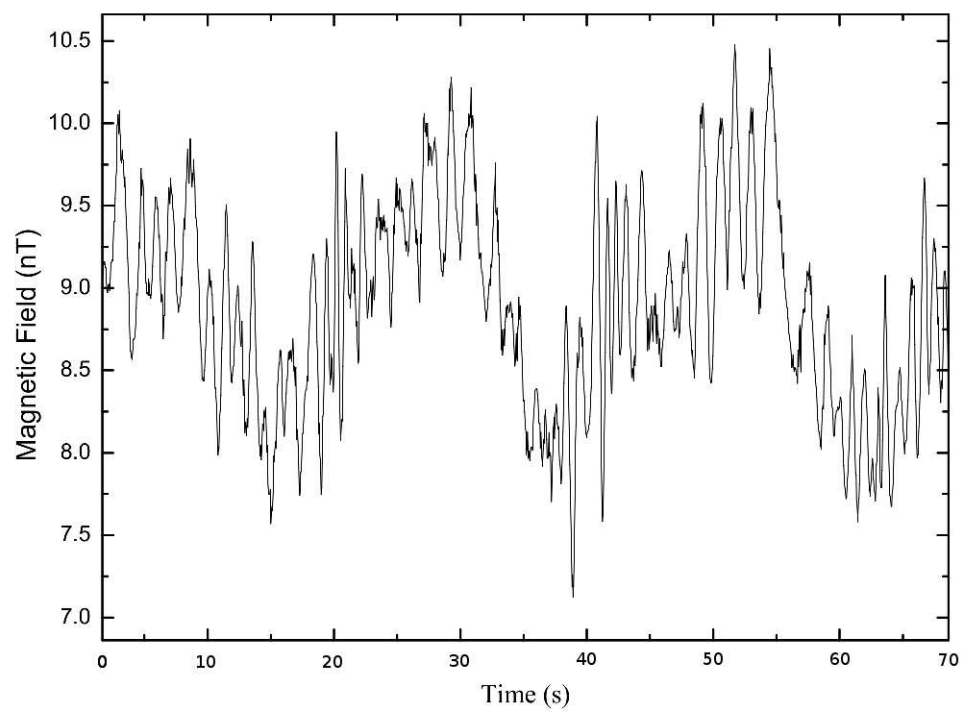


Figure 4.2: Example of structured fluctuations found in the foreshock region. A 70 s snapshot taken from the 27/01/04 interval.



$$\begin{aligned}
\hat{e}_1 &= \hat{\mathbf{b}}, \\
\hat{e}_{\perp 1} &= \mathbf{B} - (\mathbf{B} \cdot \hat{\mathbf{b}})\hat{\mathbf{b}}, \\
\hat{e}_{\perp 2} &= (\hat{e}_1 \times \hat{e}_{\perp 1}),
\end{aligned} \tag{4.1}$$

where  $\hat{\mathbf{b}} = \mathbf{B}/B$ . The magnetic field vector  $\mathbf{B}$  was taken to be the interval average. The data sets used span a few hours at most, therefore it was assumed that the IMF varies slowly enough in this time to be considered as constant in direction. The benefit of this set up was that it allowed the observer to disentangle fluctuation motion parallel and perpendicular to the magnetic field. This aids the identification of fluctuations and their growth mechanisms.

### 4.3.2 Correlation

As shown in section 1.6.1 the phase shift between thermal and magnetic pressure oscillations has a succinct impact on the nature of the fluctuations. It was possible to use proton density for the determination of the thermal pressure, through the ideal gas law (1.23). Hence we were able to observe correlations between magnetic and thermal pressures using Cluster’s CIS proton densities directly. This analysis allowed a quick preliminary check to identify correlated fluctuations and the phase between density and magnetic field. Magnetoacoustic perturbations will show in both variables and can present themselves as inphase ‘fast’ oscillations or antiphase ‘slow’ oscillations as outlined in section 1.6.1.

Both magnetic field strength  $|\mathbf{B}|$  and individual magnetic field components were used in the correlation analysis. Analysis showed that density and magnetic field strength were correlated with the cross correlation coefficient exceeding 0.97 for all intervals in Table 4.2, see example figure 4.3 and values are shown in Table 4.3. This provided some evidence for the presence of MHD oscillations in the foreshock as found in [Eastwood et al., 2005]. The fact that density and magnetic field fluctuations were correlated indicates that the fluctuations could be waves which exist on the fast branch of the magnetosonic dispersion relation such as the ULF waves outlined in section 4.1.1. It must be stressed that correlation between density and magnetic field strength is not conclusive proof of the presence of MHD fluctuations. However, if it can be shown that the fluctuation period is well below the gyro-periods (see section 4.3.4) then we can present a strong argument for the presence of MHD oscillations, given the many examples in literature.

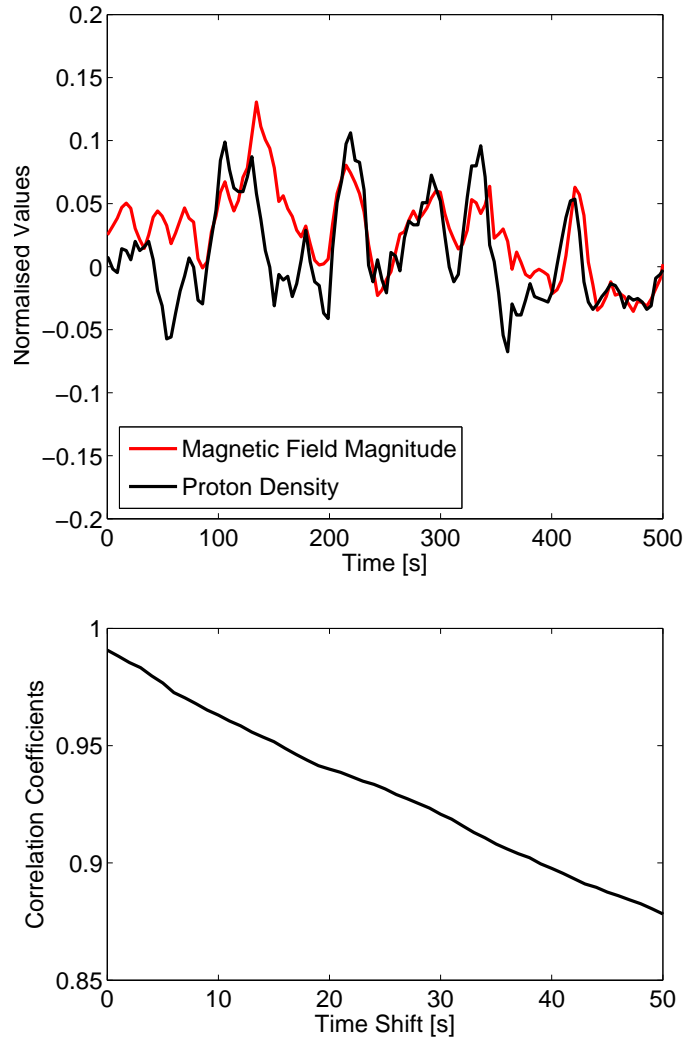


Figure 4.3: Upper panel: The normalised magnetic field magnitude and proton density used in the correlation analysis. Lower panel: A representative cross correlation analysis for the interval: 27/01/2004, time: 03:50-04:35 for magnetic field magnitude and proton density. Magnetic field strength and density were found to be strongly correlated with a coefficient of 0.9907. All other intervals exhibit a similar form and correlation value.

Date	Times	Correlation Coefficients
27/01/2004	03:50-04:35	0.99
16/02/2002	06:19-06:29	0.98
20/02/2002	22:00-22:06	0.98
19/02/2010	00:16-01:10	0.97
21/02/2002	22:19-22:29	0.99
11/02/2002	22:04-22:14	0.99
27/03/2002	07:15-07:25	0.97

Table 4.3: Correlation coefficients for the correlation analysis between magnetic field magnitude and proton density for the intervals listed. A 2000 s sample was taken for each interval.

### 4.3.3 The Taylor Hypothesis and Advection

The Taylor hypothesis was first described in [Taylor, 1938], it attempts to tackle the problem of advection in high speed flows. In this section we derive the hypothesis in a solar wind context due to the solar wind's high speed. Taylor's original derivation was developed for the application to a general high flow plasma.

The IMF and the fluctuations that exist within the solar wind plasma described in as a function of space and time,  $\mathbf{B}(\mathbf{x}, t)$  can be expressed as a sum of Fourier components in wavevector,  $\mathbf{k}$  and frequency  $\omega$  by the expression:

$$\mathbf{B}(\mathbf{x}, t) = \sum_{\mathbf{k}} \sum_{\omega} \hat{\mathbf{B}}(\mathbf{k}, \omega) e^{i(\mathbf{k} \cdot \mathbf{x} - \omega t)}. \quad (4.2)$$

The solar wind data is collected by a spacecraft moving at velocity  $-\mathbf{v}_{sw}$  which is equivalent to the spacecraft's measurement of the solar wind velocity as it streams past. The position of the spacecraft as a function of time is given by  $\mathbf{x} = -\mathbf{v}_{sw}t$ . So the magnetic field time series is simply given by  $\mathbf{B}(t) = \mathbf{B}(\mathbf{x}, t)|_{\mathbf{x}=-\mathbf{v}_{sw}t}$  yielding:

$$\mathbf{B}(t) = \sum_{\mathbf{k}} \sum_{\omega} \hat{\mathbf{B}}(\mathbf{k}, \omega) e^{-i(\mathbf{k} \cdot \mathbf{v}_{sw} + \omega)t}. \quad (4.3)$$

Finally, we Fourier transform the spacecraft frame magnetic field time series via  $\mathbf{B}_{sc} = \int dt \mathbf{B}(t) e^{i\omega_{sc}t}$  to obtain the signal in terms of the spacecraft frame frequency  $\omega_{sc}$  given by:

$$\mathbf{B}(\omega_{sc}) = \sum_{\mathbf{k}} \sum_{\omega} \hat{\mathbf{B}}(\mathbf{k}, \omega) \delta[\omega_{sc} - \mathbf{k} \cdot \mathbf{v}_{sw} - \omega]. \quad (4.4)$$

Thus we find that the spacecraft-frame frequency is given by the argument of the delta function:

$$\omega_{sc} = \mathbf{v}_{sw} \cdot \mathbf{k} + \omega. \quad (4.5)$$

The Taylor hypothesis follows from this and takes advantage of the fact that the plasma flow is predominantly super Alfvénic,  $v_A \ll v_{sw}$ . Allowing observers to adopt the Taylor hypothesis which assumes that  $|\omega| \ll |\mathbf{v}_{sw} \cdot \mathbf{k}|$ . Thus we can approximate (4.5) to:

$$\omega_{sc} \approx \mathbf{v}_{sw} \cdot \mathbf{k}, \quad (4.6)$$

which allows the conversion between frequency and wavenumber under certain conditions.

We should mention that more recently observers have begun to question the validity of the Taylor hypothesis, [Howes et al., 2014]. This will not be explored within this thesis. The hypothesis will be used to estimate the wave numbers using frequency values from section 4.3.4 in order to understand the size of spacial scales involved. These are not required to derive the results for this chapter.

#### 4.3.4 Periodicity Analysis

After the identification of fluctuations in the data it was imperative to establish if they were indeed periodic in nature as those outlined in section 1.7.3, providing confirmation that the fluctuations in the data were the same as those observed in [Eastwood et al., 2003, 2005, Burgess, 1997]. There are various techniques used to understand the periodicity of fluctuations. This section will implement some of these processes to identify periodicity and structure within the observed perturbations of the foreshock region such as that shown in figure 4.2.

#### Power Spectrum

The power spectrum technique implements the fast Fourier transform (FFT) to convert the time series into the frequency domain. The resulting dataset consists of the spectral amplitude or power versus the frequency, phase information was also available from the complex plane if required. The frequency domain is bounded by the Nyquist frequency which is just simply half the sample rate, [Oppenheim and Schaffer, 2010]. The FFT converts a time series  $f(t)$  into the frequency domain,  $F(\omega)$  [Fourier, 1822, Cooley and Tukey, 1965]:

$$F(\omega) = \int f(t)e^{i\omega t} dt. \quad (4.7)$$

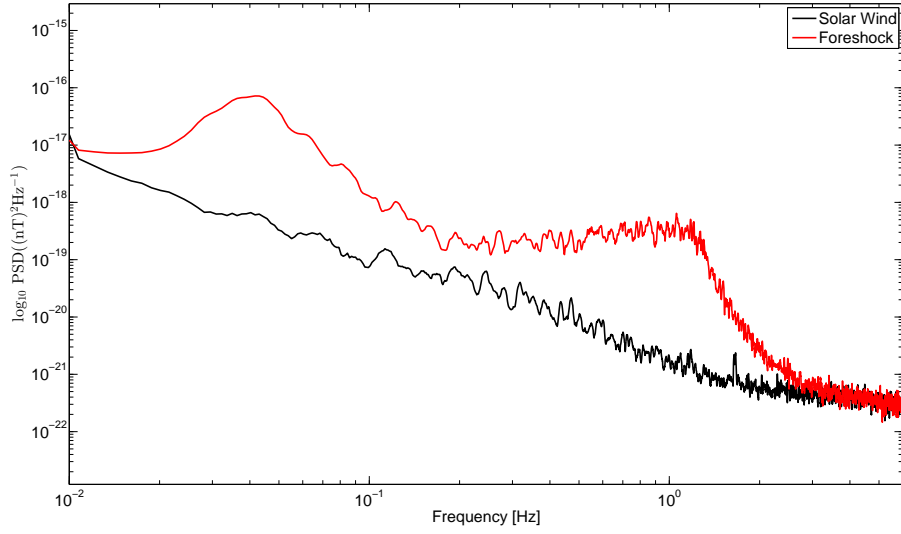


Figure 4.4: The power spectra were calculated for the representative interval 27/01/2004 and an interval where the Cluster satellite group was upstream of the foreshock region, a data sample considered to be free of the foreshock interaction. The black curve denotes the power as a function of frequency for the upstream solar wind region. The red curve displays the power as a function of frequency for the 27/01/2004 interval. Two distinct peaks above the solar wind spectrum were found at frequencies of  $\sim 0.04$  Hz and  $\sim 1$  Hz. This was in agreement with the frequency ranges for ULF waves 5 mHz to 0.1 Hz and the whistler wave which is found at  $\sim 1$  Hz as outlined in section 4.1.1.

This technique was carried out on all of the intervals outlined in Table 4.2. The power spectra were then compared with the spectra of signals obtained in the solar wind intervals considered to be free of the foreshock interaction region. This was used as a control background turbulence level due to its lack of noticeable spectral peaks. Increases in the fluctuation power above the solar wind turbulence level were found at discrete frequencies for all intervals, see Table 4.4. The presence of peaks above the solar wind background turbulence power spectrum indicated quasi-monochromatic fluctuations which are usually associated with wave activity. The results shown in Table 4.4 strongly agree with the values found in [Narita et al., 2004]. This identifies them to be within the ULF classification outlined in section 4.1.1 which is in agreement with Burgess [1997], Narita et al. [2004], Eastwood et al. [2005].

Date	Times	Peak Frequencies [Hz]	$v_{sw}$ [kms <sup>-1</sup> ]	Wavelength [Mm]
27/01/2004	03:50-04:35	0.04	385	6.40
16/02/2002	06:19-06:29	0.04	311	7.80
20/02/2002	22:00-22:06	0.05	445	8.90
19/02/2010	00:16-01:10	0.03	442	14.70
21/02/2002	22:19-22:29	0.06	437	7.30
11/02/2002	22:04-22:14	0.05	521	10.40
27/03/2002	07:15-07:25	0.04	440	11.00

Table 4.4: Table of peak frequency values found in the power spectra of the corresponding data intervals, the average solar wind speed for that interval and the corresponding wavelength found using the Taylor hypothesis (section 4.3.3).

### Dynamical Spectra

The disadvantage of using the power spectrum as described above was the lack of time resolution in the power measurement of distinct frequency modes. So it was not possible to observe how long they last or if there was any periodicity in their growth. The dynamical approach sacrifices spectral resolution to allow the observation of the time variation in a spectrum.

The dynamical spectrum is constructed with the FFT algorithm but instead of carrying out the analysis on the entire time series it applies the Fourier transform to a short time window which can be altered at the users discretion. A Hanning window was applied to the data to allow analysis to be carried out on a segment of the time series. The Hanning window is given by, [Oppenheim and Schaffer, 1989]:

$$W(t) = \alpha - \beta \cos\left(\frac{2\pi t}{N-1}\right), \quad (4.8)$$

where  $\alpha$  and  $\beta$  are control parameters specified by the program. The power spectra procedure was carried out on the windowed dataset and the result was logged. This was then repeated after shifting the Hanning window along the time series to produce a dynamical spectrum image, see figure 4.5.

Figure 4.5 has shown that the waves are not continuous in nature but are produced in a more intermittent manner. This was to be expected by a system of waves driven by the beam instability, as the non thermal particles are produced from the turbulent solar wind.

The dynamical spectrum was limited by its shorter windowed data series. This meant that it was not able to observe the time variation of the lower ULF frequencies. However, attempts yielded a consistently increased power in the observable ULF frequency range. The rest of this chapter will focus on the ULF waves

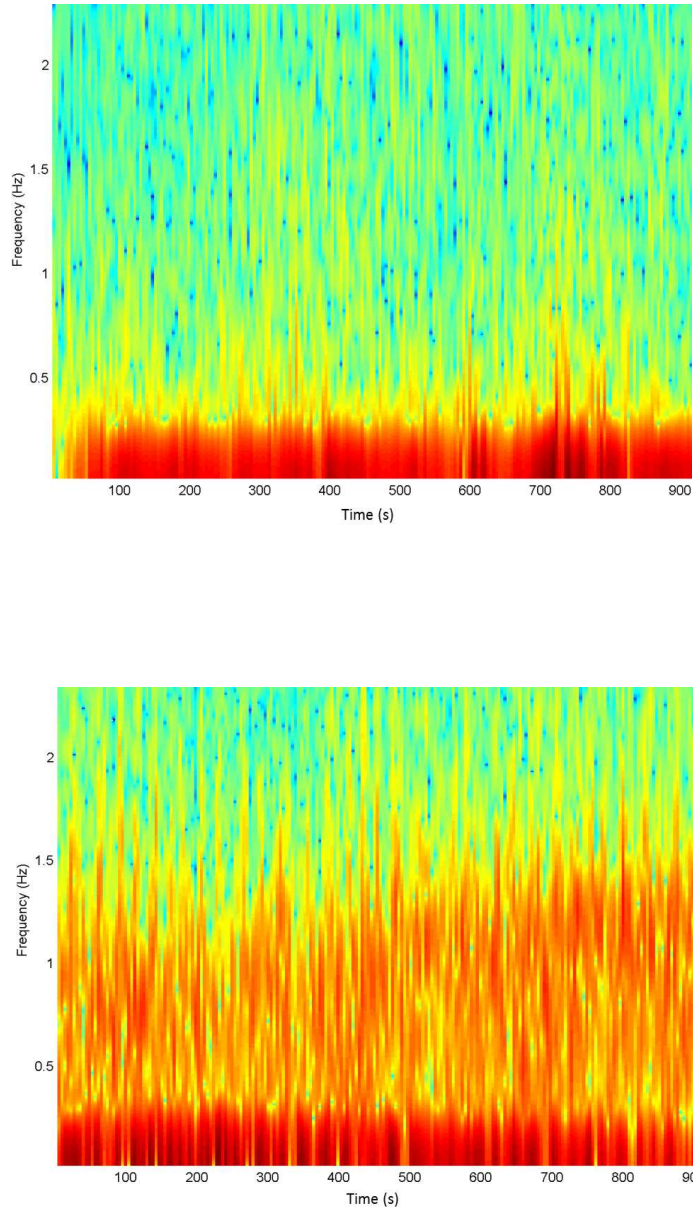


Figure 4.5: Dynamical spectrum of the solar wind interval (upper panel) shows that background turbulence has the majority of its power in the lower frequency modes. With the presence of fluctuations (lower panel) a sudden increase in density at a higher frequency range was observed. Some higher frequencies are seen intermittently in the solar wind panel (left) however we define wave activity as a sustained increase in power, these could be intermittent bursts of waves or just background turbulence being advected past the satellite.

only, due to their large amplitudes. Further analysis will allow the separation of left-handed and right handed ULF waves.

## 4.4 Polarisation and Propagation Direction

After the identification of ULF waves in the foreshock, the next step was to estimate their propagation direction and polarisation in the plasma frame of reference. This information allowed us to understand what excitation and amplification mechanisms were being activated. It also allowed us to narrow down the possible instability mechanisms that were engaged by the ULF waves.

A problem arose when we considered the super Alfvénic speed of the solar wind and its advection of structures past the spacecraft. This meant it was not possible to measure intrinsic wave speed or direction using a single spacecraft. As a consequence it was important to cross-reference data from multiple spacecraft to look at propagation times and directions. The advection further complicated the situation by altering polarisation measurement. Waves travelling upstream in the plasma stream with speed lower than the stream velocity,  $|\mathbf{v}_{wv}| < |\mathbf{v}_{sw}|$  would see a polarisation reversal as they were advected past Cluster. This holds as a good assumption as  $v_A < v_{sw}$  for all of our intervals, see table 4.4 for exact values. Hence both polarisation and propagation direction were required to isolate the wave’s intrinsic polarisation.

### 4.4.1 Hodogram

The hodogram technique takes advantage of the high resolution magnetic field data to estimate the sense of wave polarisation in the spacecraft reference frame. First the magnetic field data was rotated into the field aligned co-ordinate system as outlined in section 4.3.1. This system aligns the magnetic field to the average of the time series magnetic field. The two perpendicular components were then plotted against each other to observe the rotation of the magnetic field vector around the sample average magnetic field. This method only works for small sections of the dataset with lengths on the order of the wave period for the ULF waves, as it is very sensitive to noise. In a longer sample, the noise would clutter the graph, any shorter and a complete rotation would not be observed. Longer intervals will also experience a greater drift in the average magnetic field. This prevents the hodogram from itself and thus observation of polarisation helices will become increasingly difficult.

Again 27/01/2004 was used as the representative interval for the ensemble as similar results were observed in all of the samples. The hodogram analysis showed



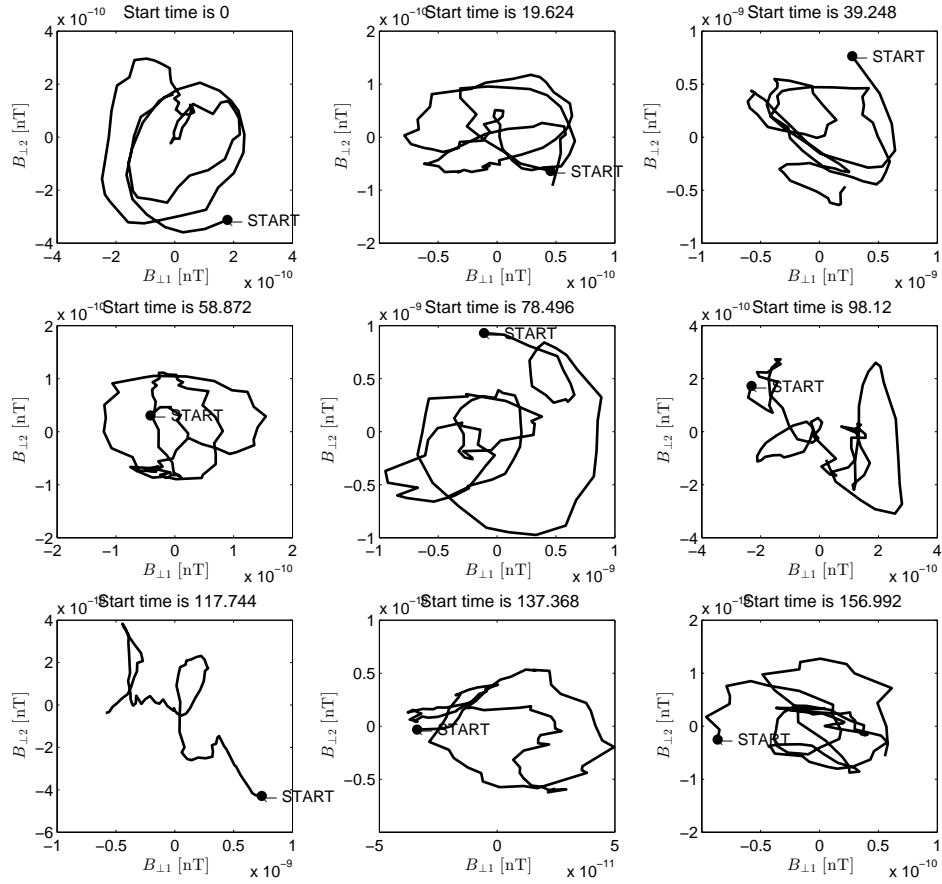


Figure 4.6: A sample of hodograms of Cluster magnetic field data taken from the canonical sample 27/01/2004 from 04 : 03 : 20 onwards. Nine samples were taken, each five seconds in length. The magnetic field was projected on the plane perpendicular to the sample average magnetic field which is directed out of the page in all figures. Some panels show distinct left handed polarisation while others show a more noisy fluctuation.

Date	Times	Spacecraft Polarisation
27/01/2004	03:50-04:35	Left-hand
16/02/2002	06:19-06:29	Left-hand
20/02/2002	22:00-22:06	Left-hand
19/02/2010	00:16-01:10	Left-hand
21/02/2002	22:19-22:29	Left-hand
11/02/2002	22:04-22:14	Left-hand
27/03/2002	07:15-07:25	Left-hand

Table 4.5: Table of circular polarisation directions found for the highest spectral power ULF wave observed in each interval. The polarisation was calculated in the spacecraft reference frame using the hodogram technique.

that the waves found in the power spectra, section 4.3.4, were in fact circularly polarised for some periods of time shown by figure 4.6. However their existence was fleeting which was to be expected in a regime driven by the turbulent solar wind. Table 4.5 shows the relevant polarisations observed in the spacecraft frame of reference. At times they also exhibited the reverse of the polarisations shown in table 4.5, however the spacecraft polarisation was taken to be the most common and prevalent polarisation observed for the respective interval.

After a more detailed inspection of the 27/01/2004 sample we were able to observe both periodicities within the hodogram, as shown in figure 4.7. The retrograde motion observed indicates both wave modes exhibit left-hand polarisation in the spacecraft frame of reference.

It is important to highlight that the polarisation observed in the spacecraft reference frame is not necessarily the intrinsic polarisation of the wave. This also depends on the propagation direction. Waves travelling upstream will experience a polarisation reversal due to the advection of the super Alfvénic solar wind. These will display the reverse polarisation in the spacecraft frame. Hence further information is needed to isolate the wave propagation direction and hence the intrinsic polarisation.

#### 4.4.2 Time Delay Analysis

In order to determine the intrinsic polarisation of the ULF waves, a multi-spacecraft time delay analysis [Paschmann and Daly, 1998] was performed. This allowed the direct determination of the propagation direction.

Autocorrelation of each signal highlights its periodicity which can be compared to the power spectra of section 4.3.4. The results are shown for our canonical sample 27/01/2004, figure 4.8. A peak was found at 19 s corresponding to a frequency of 0.05 Hz which closely matches the 0.04 Hz seen in the power spectrum,

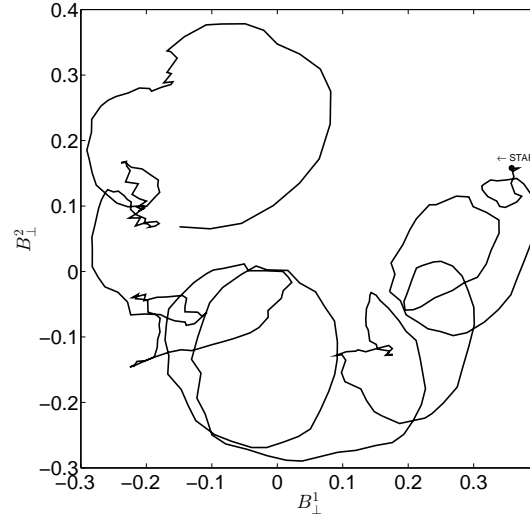


Figure 4.7: A sample of Cluster magnetic field data taken from the canonical sample 27/01/2004 at 03:48:35 for 15 s projected onto the plane perpendicular to the sample average magnetic field. The hodogram clearly shows the two periodicities observed in the power spectrum shown in section 4.3.4. The lower frequency ULF wave underwent half a period of rotation while the ‘1 Hz’ whistler was seen to last for about six cycles of the oscillation during the same time interval.

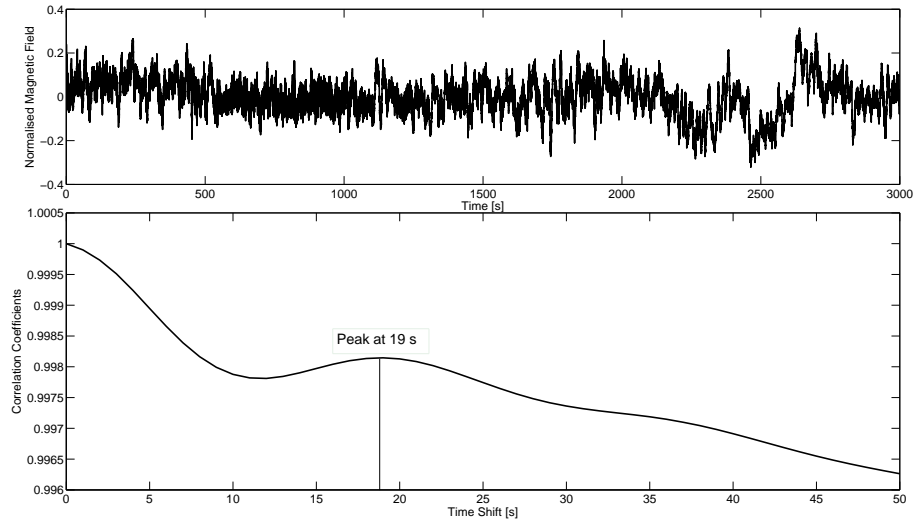


Figure 4.8: Auto correlation analysis for high resolution Cluster magnetic field data for the canonical sample 27/01/2004. A peak was found at 19 s corresponding to a frequency of 0.05 Hz which was in close agreement with the result derived by the power spectrum of 0.04 Hz, section 4.3.4.

Date	Times	<b>B</b> Field Direction	Wave Vector	Intrinsic Polarisation
27/01/2004	03:50-04:35	Sunward	(0.99, 0.16, -0.04)	Right-hand
16/02/2002	06:19-06:29	Anti-sunward	(-0.81, 0.58, 0.74)	Right-hand
20/02/2002	22:00-22:06	Sunward	(0.83, 0.55, -0.01)	Right-hand
19/02/2010	00:16-01:10	Anti-Sunward	(-0.84, -0.29, -0.45)	Right-hand
21/02/2002	22:19-22:29	Sunward	(-0.98, -0.14, -0.14)	Left-hand
11/02/2002	22:04-22:14	Anti-sunward	(0.86, -0.39, -0.31)	Left-hand
27/03/2002	07:15-07:25	Anti-sunward	(0.86, -0.51, 0.03)	Left-hand

Table 4.6: Table of results for delay analysis. The wave vector co-ordinate system was orientated to the field aligned system outlined in section 4.3.1.

figure 4.4. Thus the ULF frequency observations were further underpinned.

A cross-correlation between the signals recorded by different Cluster spacecraft provided the time of travel information of the ULF waves between the satellites. An optimisation procedure was used to obtain the direction of the wave vector. The wave vector was found using the field aligned co-ordinate system outlined in section 4.3.1. The first component of the wave vector identifies if the wave was travelling along (positive) or against (negative) the magnetic field direction. This information was filtered through the flow chart in figure 4.9 to establish the intrinsic polarisation of the sample, IL or IR for the intrinsically left and right handed polarisation, respectively. The results are displayed in Table 4.6.

Table 4.6 shows that the dataset has bifurcated into two distinct subsets, those with waves that are intrinsically left-handed, IL and those that are right-handed IR. Due to this we have used the 11/02/2002 as the second representative sample to contrast to the 27/01/2004 sample. These two will now represent the intrinsically left and right handed intervals of ULF waves. They are labelled IL and IR respectively.

## 4.5 Differential Analysis

ULF waves are fast magnetoacoustic waves, detailed in section 1.7.3, therefore they exhibit compressibility. A study into the compressibility of the dataset was therefore required as further proof of the presence of magnetoacoustic waves. Unfortunately Cluster does not possess high enough resolution proton density data to view this directly, hence the magnetic field data was used as a proxy.

Using high resolution magnetic field data in the projected form, outlined in Section 4.3.1, fluctuations in the magnetic field data were directly related to number density fluctuations as shown in [Hollweg, 1999]:

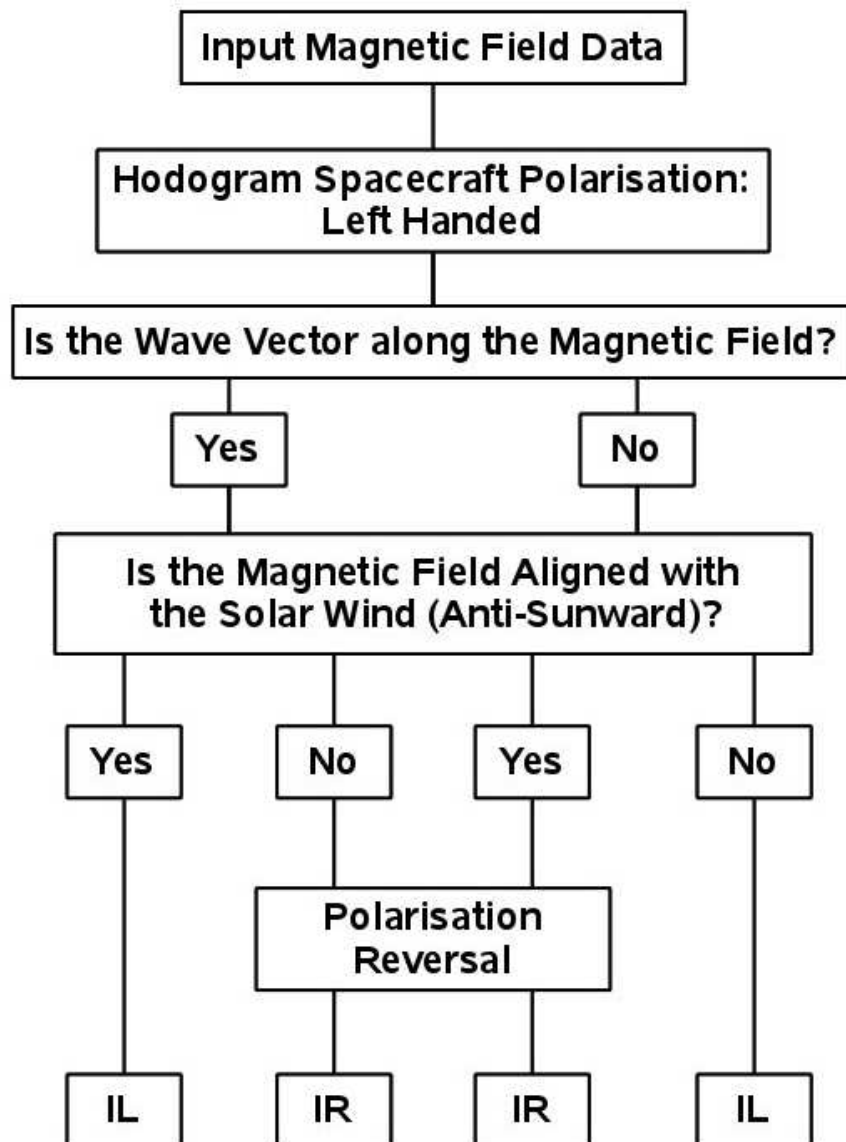


Figure 4.9: A flow chart to demonstrate how the collected information was used to identify the intrinsic polarisation of the ULF waves found in the data samples. The flow chart was based on a left-handed spacecraft polarisation input. If the input was right-handed in the spacecraft reference frame the chart is simply inverted.

$$\frac{\delta B_{\parallel}}{\delta B_0} \sim \frac{\delta n}{n_0}. \quad (4.9)$$

In order to obtain  $\delta B_{\parallel}$  the magnetic field data was processed using a differential algorithm at a range of time-scales,  $\tau$ :

$$\delta B_{\parallel}(t) = B_{\parallel}(t + \tau) - B_{\parallel}(t), \quad (4.10)$$

$$\delta B_0(t) = |\mathbf{B}(t + \tau)| - |\mathbf{B}(t)|. \quad (4.11)$$

In order to attain a dataset for various time-scales the algorithm was simply run in a loop with the value of the time-scale growing with each iteration.

In the solar wind a pure Alfvén mode will exhibit perpendicular wave vector components even if initially it is only parallel propagating, see section 1.7.3. The effect of turbulence on the parallel wave components is to naturally transfer a fraction of the energy into the perpendicular direction. Therefore there will always be a background level of compressibility observed. Figure 4.10 shows that the solar wind (dotted black line) does exhibit a base level of compressibility. However, the IR and IL intervals presented a significantly higher level of compressibility in the ULF frequency range. The solar wind compressibility also tended to smaller values with larger time-scales as one would expect for turbulence.

In the IR compressibility analysis two distinct peaks were found at 1.6 s and 25 s, these correspond to the frequency modes outlined in Section 4.3.4 for this interval. These correspond to frequencies 0.8 Hz and 0.04 Hz respectively which was slightly lower than established in previous sections for the 1 Hz ‘whistler’ mode.

Although the peaks in the IL are less defined it was still possible to make out a peak at 5.8 s which corresponds to a 0.17 Hz frequency. Unfortunately the longer period peak appears to be lost to an overall increase in compressibility. Alternatively it may be possible that this peak has shifted beyond the time-scale maximum. It was not possible to extend the time-scale range due to the computing power required.

These observations agree with the frequencies outlined in Table 4.4, however all frequencies seem to be slightly underestimated which could be due to an unidentified systematic error in the algorithm.

Nevertheless we have observed that at distinct time-scales, in the vicinity of the wave periodicities, we detect an increase in  $\delta B_{\parallel}/\delta B_0$ . This demonstrates an enhanced compressibility via (4.9) due to the presence of the ULF waves.

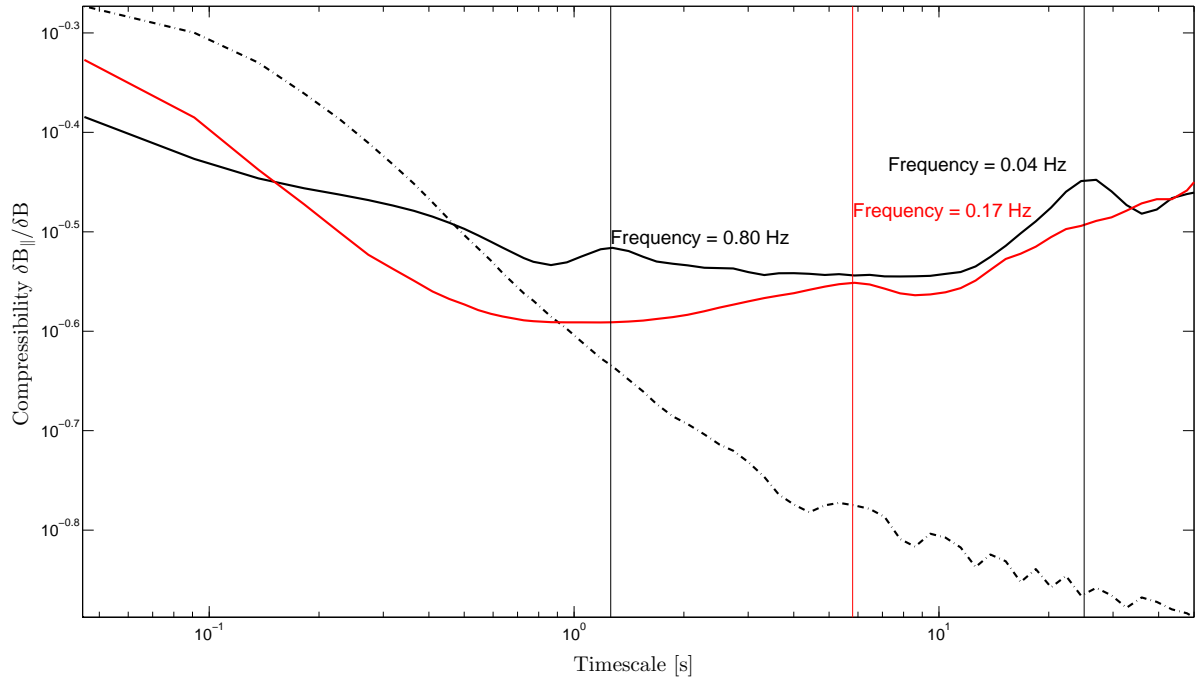


Figure 4.10: A study into compressibility using magnetic field data as a proxy. Differential analysis was carried out on the pre-foreshock solar wind (dotted black) and both IR (solid black) and IL (solid red) data samples. An increase, above the turbulence level, in compressibility was observed in both IL and IR with distinct peaks found in both.

## 4.6 Temperature Anisotropy

Through sections 4.3 to 4.5 we have conclusively demonstrated the existence of ULF waves in the foreshock dataset shown in Table 4.2. We now move on to follow [Selzer et al., 2014] and explore the growth and impact of the ULF waves in the foreshock.

The beam instability (see section 1.8.3) is the primary mechanism for producing right-hand polarised transverse waves, propagating parallel and anti-parallel to the interplanetary magnetic field (IMF). Waves travelling along the beam are resonant with the ion beam population, while waves propagating anti-parallel to the beam may become unstable to the non-resonant fire hose instability (see section 1.8.3), in the presence of temperature anisotropy [Sentman et al., 1981, Gary et al., 1998]. The plasma becomes unstable to fire hose when  $P_{\parallel} - P_{\perp} > B^2/2\mu_0$ , the plasma pressure parallel to the magnetic field direction is greater than that perpendicular by an amount exceeding the local magnetic pressure, explained in more detail in section 1.8.3.

The linear phase of the beam instability is well understood: long wavelength transverse electromagnetic fluctuations are produced and these scatter and isotropise the beam particles reducing the source of the instability, discussed in detail in section 1.8.3. The interaction of these waves with the unstable population may, however, be diminished due to advection of waves by the solar wind as well as their refraction [Scholer et al., 2003]. The non-linear phase of this process is less understood, but it is known that the generated fluctuations can interact with the bulk ion population and affect global plasma properties.

Two general mechanisms may then be considered. If an isolated mode becomes unstable and nonlinear temporal scale exceeds the linear one, coherent waves may lead to the wave particle interactions. If the broad-band spectrum is generated and nonlinearity is strong, the energy may cascade to large scales modifying plasma parameters in order to suppress the instability [Rosin et al., 2011, Quest and Shapiro, 1996].

Here, we consider a hypothesis that, in the nonlinear phase of the beam instability, the ULF waves influence the temperature anisotropy of the core ion population, which may lead to a “secondary instability” of the fire hose or proton cyclotron (PC) type.

### 4.6.1 The $(\beta_{\parallel}, T_{\perp}/T_{\parallel})$ Parameter Space

A parameter space given by proton temperature anisotropy  $R = T_{\perp}/T_{\parallel}$  and parallel plasma  $\beta$ ,  $\beta_{\parallel} = 2\mu_0 nk_B T_{\parallel}/B^2$  [Hellinger et al., 2006, Bale et al., 2009, Osman et al.,



Instability Threshold	$a$	$b$	$\beta_0$
Proton Cyclotron	0.43	0.42	-0.0004
Mirror	0.77	0.76	-0.0016
Parallel Firehose	-0.47	0.53	0.5900
Perpendicular Firehose	-1.4	1.0	-0.1100

Table 4.7: Instability thresholds used to bound the  $(\beta_{\parallel}, R)$  parameter space. These values are the parametric fit values used in equation 4.12 to calculate the maximum growth rate of  $\gamma/\omega_{ci} = 10^{-3}$ . Values have been taken from [Hellinger et al., 2006, Marsch et al., 2004].

2012] was used to visualise a possible link between temperature anisotropy and core proton temperatures (defined in section 4.2).

This parameter space is bounded by the theoretical marginal stability thresholds [Hellinger et al., 2006, Marsch et al., 2004] of the proton cyclotron resonance (PC) instability, mirror instability, oblique and parallel fire hose instabilities. These are discussed in more detail in section 1.8.3. When the plasma parameters cross these instability thresholds the plasma engages the corresponding instability, thus bringing the parameters back into the stable domain. The position of the threshold lines is somewhat arbitrary, since the exact position requires the ratio of growth rate and ion cyclotron frequency,  $\gamma/\omega_{ci} = 0$ . In practice this limit is approximated, similarly to other studies, by a small value  $\gamma/\omega_{ci} = 10^{-3}$ . The thresholds follow the form:

$$R = 1 + \frac{a}{(\beta_{\parallel} - \beta_0)^b}, \quad (4.12)$$

where  $a$ ,  $b$  and  $\beta_0$  are adjustable parameters. The parameter values for each instability threshold can be found in Table 4.7.

#### 4.6.2 Visualisation

We follow the method used by [Hellinger et al., 2006, Bale et al., 2009, Osman et al., 2012] to visualise the  $(\beta_{\parallel}, R)$  plane, see figure 4.11. Each data point was mapped onto the plane, colour values were then assigned to it using HIA ion temperature values. All the data points were then used to extrapolate a two dimensional mesh which was then displayed as a colour image on the  $(\beta_{\parallel}, R)$  axis, see figures 4.12 and 4.13. The instability thresholds (section 4.6.1) were then plotted over the image to bound the parametric space.

Cluster HIA temperature data has been smoothed over a window of four neighbouring points in order to construct these quantities. A anisotropy plot was

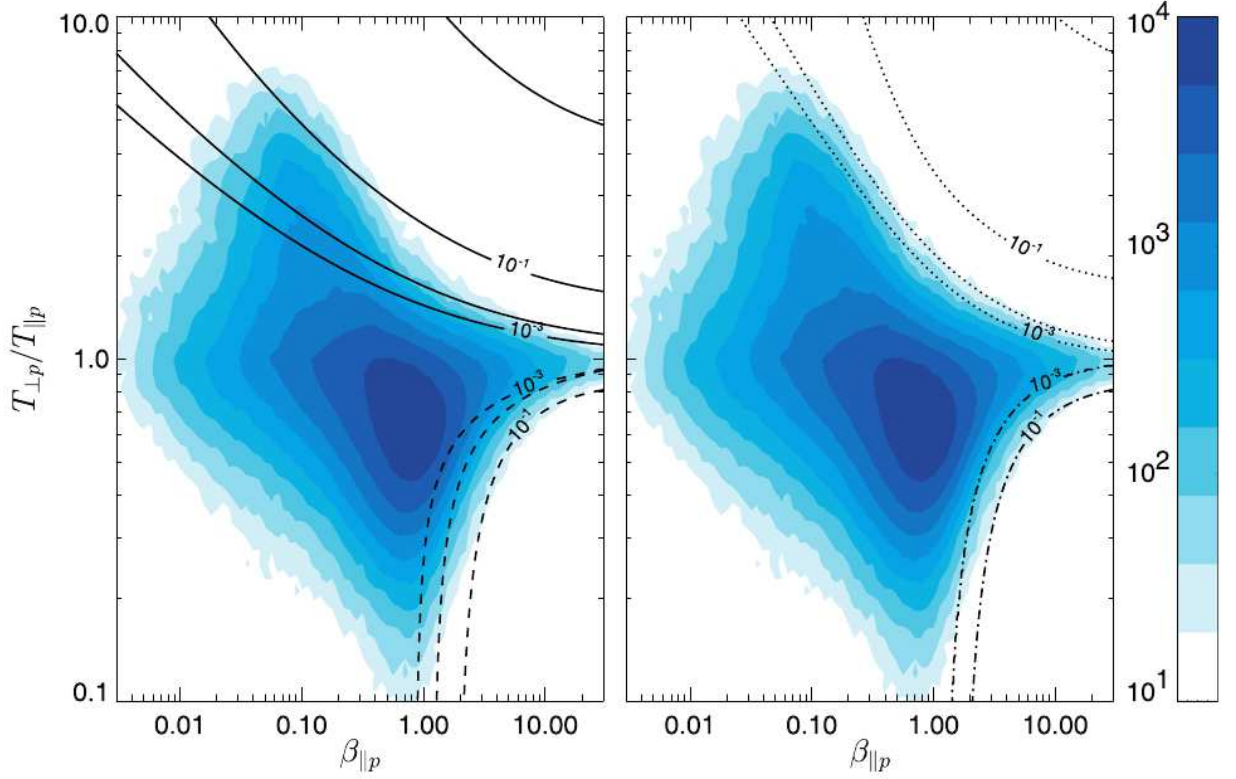


Figure 4.11: A contour plot is presented for the grouping of  $(\beta, R)$  in the Wind/SWE data for the period of (1995-2001), the p subscript denotes that these have been plotted for protons. The curves show the contours of the maximum growth rate (normalised to  $\omega_{ci}$ ) in the plasma (left) for the proton cyclotron instability (solid curves) and the parallel fire hose (dashed curves) and (right) for the mirror instability (dotted curves) and the oblique fire hose (dash-dotted curves), [Hellinger et al., 2006, Figure 1].

made for each interval of Table 4.2. The plots have been grouped according to intrinsic polarisation, see figures 4.12 and 4.13.

Figure 4.12 shows the temperature anisotropy plots for the IR intervals of table 4.2. With the exception of the 20/02/2002 C3 interval all plots show an increase in proton temperature when the distribution approaches the firehose instability thresholds. The temperature for the points located near the fire hose marginal stability curves were usually a factor of 2 – 3 times higher than compared to those located near the  $R = 1$  line. The fact that 20/02/2002 C3 interval lacks the corresponding increase in temperature could be down to a number of reasons. Most

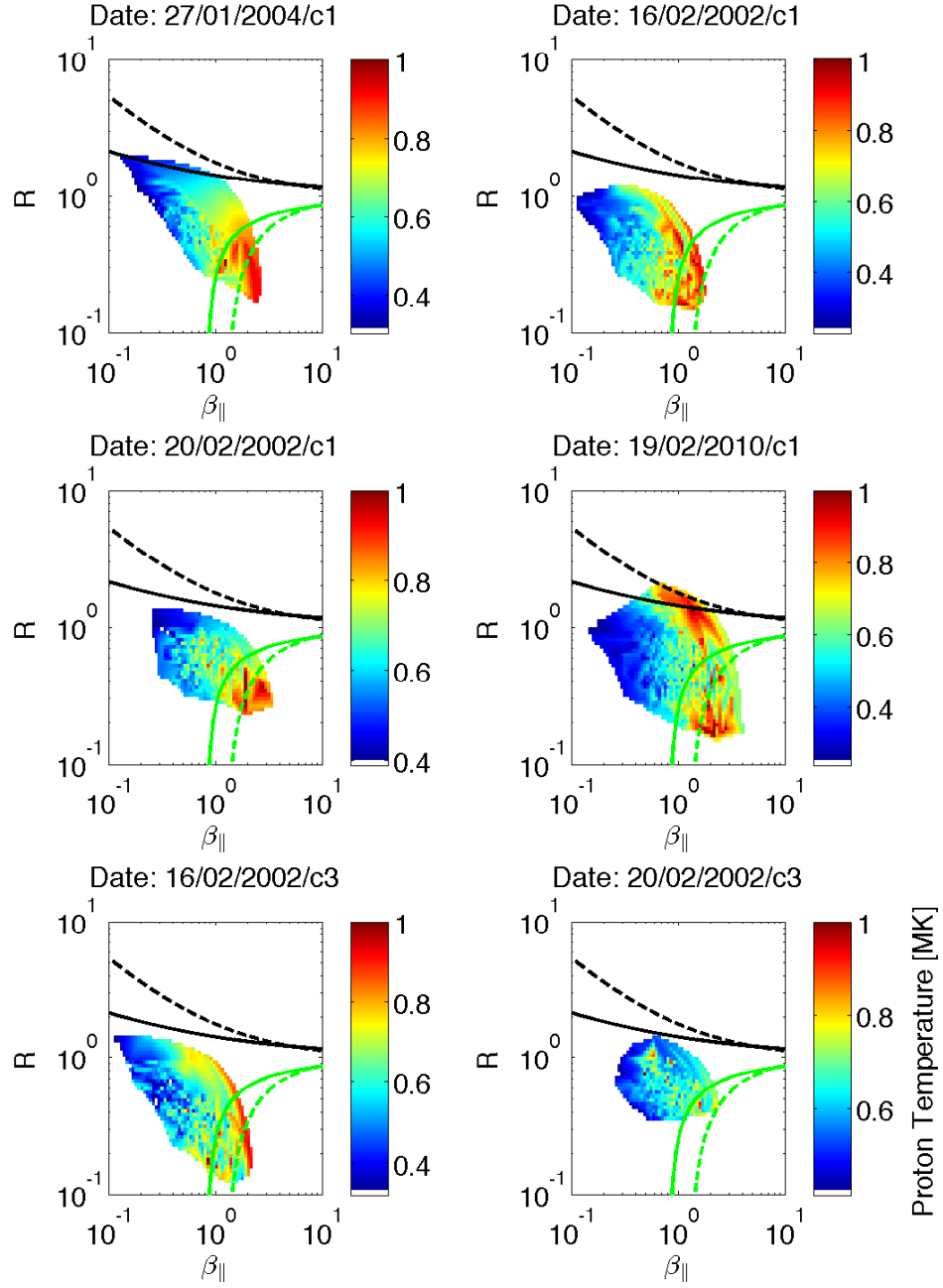


Figure 4.12: Anisotropy plots for the intrinsically right-hand polarised intervals for both Cluster 1 and Cluster 3. The curves show the maximum growth rates for the proton cyclotron instability (solid black curve), mirror instability (dashed black curve), oblique fire hose instability (green dashed curve) and the parallel fire hose instability (solid green curve). The growth rates were plotted for  $\gamma_{max}=10^{-3}\omega_{ci}$ . The colour was assigned using the Cluster HIA ion temperature data.

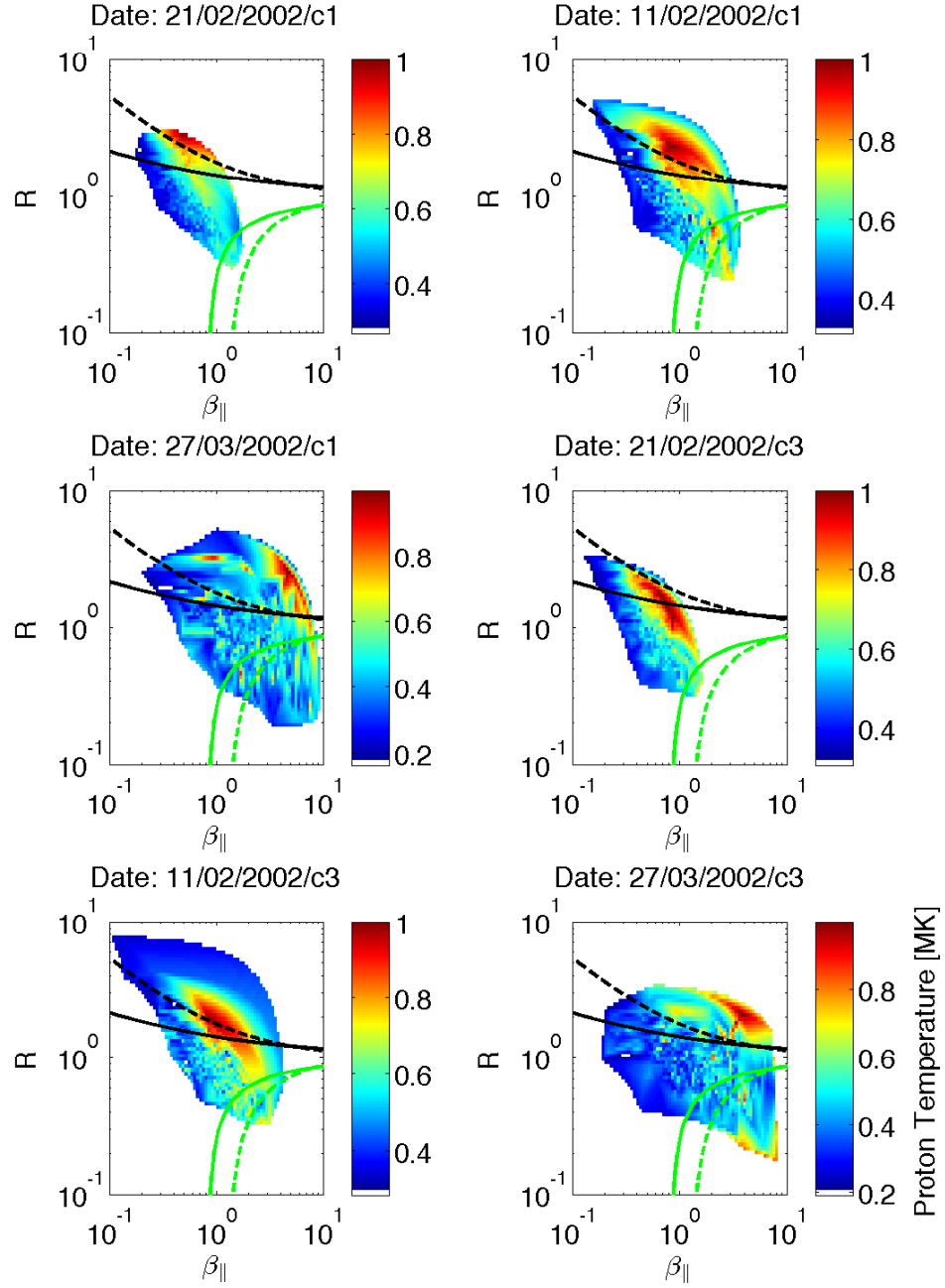


Figure 4.13: Anisotropy plots for the intrinsically left-hand polarised intervals for both Cluster 1 and Cluster 3. The curves show the maximum growth rates for the proton cyclotron instability (solid black curve), mirror instability (dashed black curve), oblique fire hose instability (green dashed curve) and the parallel fire hose instability (solid green curve). The growth rates were plotted for  $\gamma_{max}=10^{-3}\omega_{ci}$ . The colour was assigned using the Cluster HIA ion temperature data.

likely is that the C3 satellite passed through the wave region at a later time due to a larger Cluster formation at this date. Interval 19/02/2010 also shows some heating along the PC and mirror instability thresholds. This could be due to the existence of some secondary left-handed ULF waves occurring at the same time.

The left-hand intervals show similar elevated temperatures near the PC / mirror instability thresholds. While the differences between the proton cyclotron and the mirror mode instability threshold are small for  $\beta_{\parallel} > 1$ , the mirror mode is linearly polarised and thus can be excluded from our consideration. A problem arises by carrying out analysis in this fashion. The low count rate in the individual plots do not individually provide a statistically significant result. However by combining the individual plots into an ensemble plot for each polarisation we were able to build a statistically significant result, see figure 4.14.

Figure 4.14, panels (a,b) shows distributions of counts for the left- and right hand wave intervals, respectively. The ensemble averaged distribution of temperatures, based on core ion distributions for intervals of specific polarisation are shown in panels (c,d) of Figure 4.14. Only temperature in the bins with more than 3 counts was considered for these plots. We highlight that the axis of these plots are related via their common dependence on the parallel temperature. Note that for the IL intervals, the count distribution has its maximum nearer to the isotropy line and the outliers stretch from PC to fire hose marginal stability lines. This, and a smaller number of data points contributing to the plot for the left-hand polarised waves makes the interpretation difficult.

Elevated temperatures around the marginal thresholds of the kinetic instabilities do not imply net heating of plasma. Indeed, available energy may simply be transferred between perpendicular and parallel particle motions. In addition, similar correlations between ion temperature and the anisotropy have been previously reported for the ambient solar wind [Bale et al., 2009, Osman et al., 2012]. Thus it was crucial to verify that the upstream solar wind conditions were not fully responsible for these observations. Such a test requires a contemporaneous observation of upstream and foreshock plasmas. We have identified one interval (interval 19/02/2010 of Table 4.2) where Wind and Cluster spacecraft magnetic fields correlated well after a forward time shift of 3200 seconds, applied to Wind data.

Panel (a) of Figure 4.15 shows Wind (black diamonds) and Cluster (red circles) measured temperature anisotropy, with Wind data shifted forward in time by 3200 seconds. Blue solid line corresponds to the integrated wavelet power for the ULF frequencies in the range 0.02 – 0.06 Hz. While the upstream solar wind conditions broadly modulate foreshock conditions, it was clear that the temperature

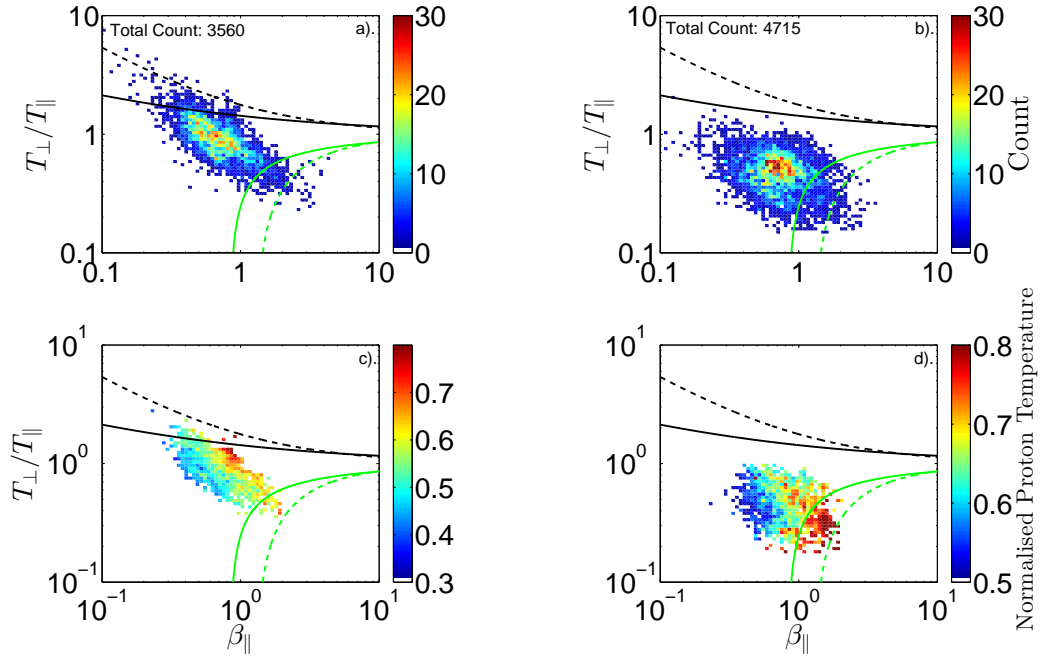


Figure 4.14: (a) Ensemble averaged distribution of counts for all intervals with left-hand polarisation. (b) Same as (a) for the ensemble of right-hand polarisation. (c) Pixelised plot of the ensemble averaged, normalised proton temperature at  $(\beta_{\parallel}, R)$  for the left-handed intervals. Only bins with counts larger than 3 are considered. (d) same as (c) for the right-hand intervals. The curves show the maximum growth rates for proton cyclotron instability (solid black curve), mirror instability (dashed black curve), oblique fire hose instability (green dashed curve) and the parallel fire hose instability (solid green curve). The growth rates were plotted for  $\gamma_{max}=10^{-3}\omega_{ci}$ , from [Selzer et al., 2014].

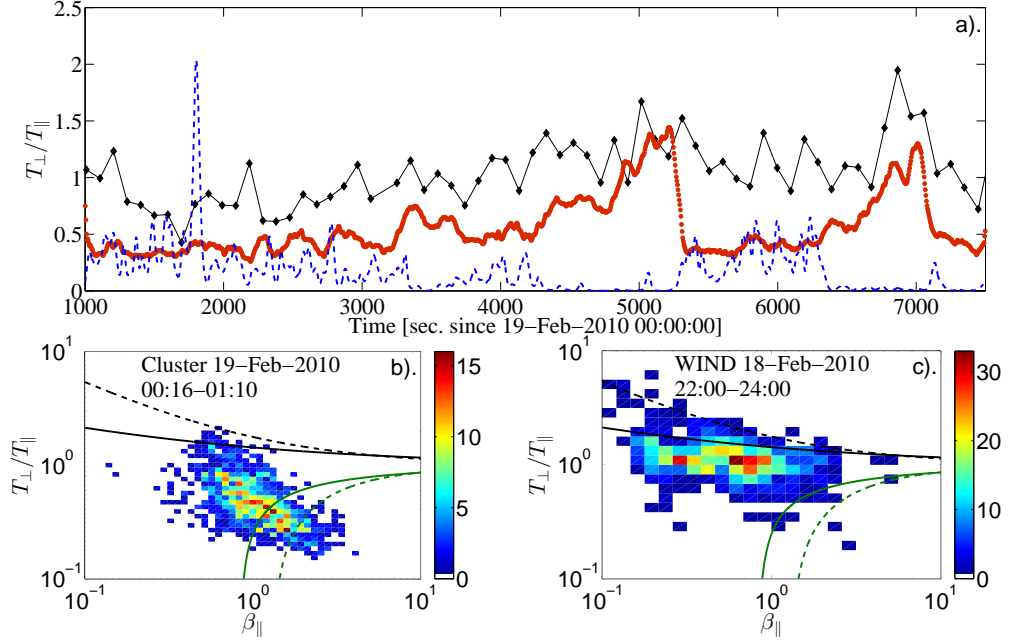


Figure 4.15: (a) A Comparison of the upstream solar wind anisotropy, as seen by Wind spacecraft (black solid line) with that observed by Cluster spacecraft (red solid line) is presented. The dashed blue curve shows the integrated wavelet coefficient power in the ULF frequencies of 0.02 – 0.06 Hz. (b, c) Distribution of counts for Cluster and Wind spacecraft, from [Selzer et al., 2014].

anisotropy in the foreshock was much lower when compared to Wind. We find a sharp increase in the mean (and median) parallel temperature from 27 eV (0.31 MK) to about 76 eV (0.88 MK), a factor of  $\approx 3$  increase between the upstream and the foreshock plasma. The perpendicular temperature exhibits only a small increase (within the error bar). Interestingly, the power in the ULF waves appear to correlate well with the observed anisotropy where the ULF wave activity exhibit sharp decrease, the anisotropy rises and reaches values observed by Wind in the ambient solar wind.

We have also examined intervals 1 – 4, listed in Table 4.2, for times when Cluster’s orbit appeared to be in the ambient solar wind. While this is not equivalent to the upstream-foreshock analysis, we have identified similar behaviour in the interval 3, with the parallel temperature increase by factor of  $\sim 2$  between the solar wind and the foreshock part of the Cluster trajectory.

### 4.6.3 Time Evolution

We next examined the temporal dynamics of the measurements, presented in Figure 4.14(b), on the  $(\beta_{\parallel}, R)$  plane. The aim was two-fold: to establish if points contributing to the temperature peak come from a single time interval within the time series and to check if changes in anisotropy are always associated with changes in the magnetic field strength. In order to facilitate such a test, we examined an observed correlation between temperature and the anisotropy,  $R$ , for time intervals where  $\beta_{\parallel}$  is not varying significantly. We also considered the relation between anisotropy and the macroscopic versions of adiabatic invariants discussed in section 1.2.3.

Figure 4.16 shows quantity of interest for each data point of the interval 27/01/2004 between times 04:05-04:25. Panel (a) shows the magnetic field magnitude down-sampled to 4 seconds resolution of the plasma data as well as proton density perturbations. It is clear that the density is well correlated with magnetic field strength perturbations, already established in section 4.3.2. Panel (b) shows temperature for this time period and panel (c) shows the temperature anisotropy,  $R$ . Solid filled circles in panel (c) represent temporal positions of 30 highest temperature measurements. Panels (d) and (e) show temporal traces of first ( $\mu = p_{\perp}/2B$ ) and second (approximated by  $J = p_{\parallel}B^2$ ) adiabatic invariants (section 1.2.3) normalised to their maximum values, respectively. In the fluid description these adiabatic invariants should be constant, but we observe significant fluctuations on small time-scales, which are of order  $\approx 21\%$  for  $\mu$  and  $\approx 46\%$  for  $J$ .

It is clear that the points close to the fire hose marginal stability line ( $R \leq 0.5$ ) do not originate from a single set of data. We observe an intermittent behaviour where the temperature anisotropy varies considerably and does not follow periodic oscillations of the magnetic field components. The highest temperatures coincide with points of minimum anisotropy and these are also evenly distributed throughout this interval. We note that between times  $t_0 = 900$  s and  $t_1 = 1150$  s, the magnetic field magnitude and the anisotropy both decrease, but this does not coincide with a significant increase of concentration for temperature enhancements. Close examination of traces in Figure 4.16 shows that sharp drops in the anisotropy trace do not show direct correlation with magnetic field strength, that is they do not coincide with magnetic field strength maxima or minima, exclusively. In the same time, however, the times of elevated temperatures coincide with large deviations in the second adiabatic invariant, suggestive of parallel heating via wave particle interactions.



## 4.7 Discussion

Results presented above indicate a correlation between higher plasma temperature, the presence of the right-hand polarised waves and the plasma proximity to the fire hose marginal stability threshold in the parametric space. Similar correlation was observed for the left-hand polarised waves, close to the marginal stability line of the PC instability. Correlations are not synonymous with causality and, given the complexity of plasma dynamics in the foreshock region, the interpretations of these results are non-trivial.

The proximity of core plasma distribution to the fire hose marginal stability line does not imply that the instability itself must necessarily control the dynamics of the plasma. By monitoring the upstream conditions, using Wind spacecraft, we have demonstrated that the temperature anisotropy was modified in the foreshock in such way that  $T_{\perp} \ll T_{\parallel}$ . The enhancement in the total temperature correlates well with the factor 2 – 3 increase in  $T_{\parallel}$  observed in two intervals. The results suggest that the power in ULF waves was also strongly correlated with the observed temperature anisotropy in the foreshock, at least for the right-hand polarised waves.

One possible interpretation of these results was to suggest that the “secondary” fire hose instability was indirectly driven by the right-hand polarised ULF waves. Aided with observations presented in figure 4.16, we consider two distinct mechanisms which can modify plasma temperature anisotropy in the presence of large magnetic field fluctuations. If the first adiabatic invariant was conserved, any decrease in the magnetic field strength would lead to an equivalent decrease in the perpendicular pressure,  $p_{\perp}$ , pushing the bulk plasma fluctuations towards the fire hose unstable region. Our results, however, show that the anisotropy changes are not exclusively associated with such magnetic field decreases. This suggests the second mechanism in a form of Landau damping of oblique fast magnetosonic ULF waves and it has been often discussed in the context of cosmic ray acceleration [see e.g. Schlickeiser and Miller, 1998, and references therein]. The wave energy was transferred into the parallel particle motion in the presence of a compressive magnetic field component. Compressibility is essential for the viability of this proposed heating mechanism and it is clearly visible from the panel (a) of Figure 4.16 that these right-hand polarised wave do perturb the magnetic field magnitude. For large amplitude waves, particles with super-Alfvénic velocities will experience a large mirror force  $F_m = -(mv_{\perp}^2/2B)\nabla_{\parallel}B$  and will be accelerated if they experience a head-on reflection. The net heating is a result of the difference between the occurrence of wave-particle interactions for particles moving with (lower occurrence) and against

(higher occurrence) the wave.

In summary, the results presented here pertain directly to a correlation between elevated temperatures and temperature anisotropy in the terrestrial foreshock. However, these could also be relevant to studies of the solar wind plasma, where similar correlations have also been observed. For example, given a small number of points, which populate regions close to marginal stability thresholds in the solar wind studies [Bale et al., 2009, Kasper et al., 2002], it is reasonable to suggest that these signatures may arise from wave activity near relatively small number of coherent structures, such as shocks [Wilson et al., 2009]. The Landau damping of ULF waves, identified as a possible driving mechanism for the fire hose instability, may also be important in solar wind turbulence, where oblique fast magneto-acoustic waves of low frequency are believed to be present, for example, in the foreshocks of quasi-parallel CME shocks [Gonzalez-Esparza et al., 1996, Tu et al., 1989].

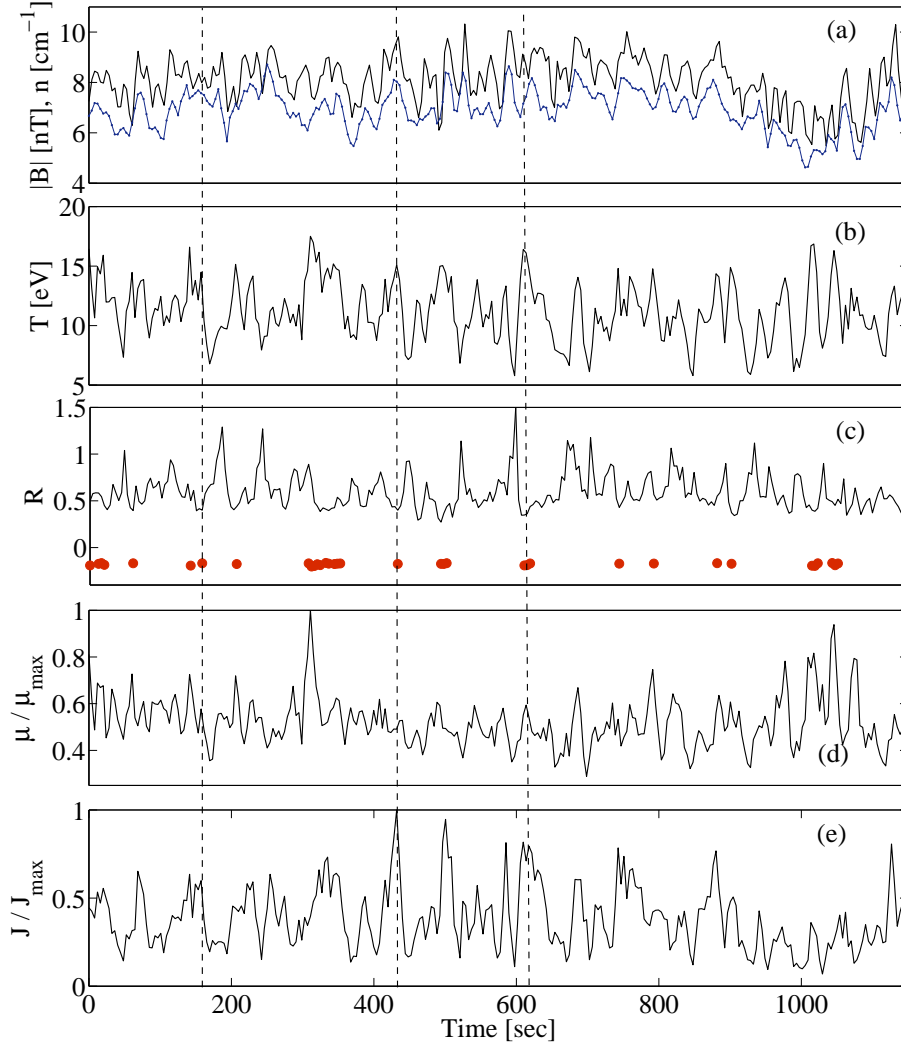


Figure 4.16: Magnetic field strength down-sampled to 4 sec. resolution (black line) and HIA proton density (blue line) (a), ion temperature (b), temperature anisotropy ratio  $R$  (c), normalised first adiabatic invariant (d) and normalised second adiabatic invariant (e) for the interval: 27/01/2004 4:07-04:26. Solid symbols (circles) in panel (c) indicate temporal position of 30 highest temperature measurements. Dashed vertical lines indicate examples of drops in the anisotropy trace, which are not coinciding with a significant magnetic field strength change, from [Selzer et al., 2014].

## Chapter 5

# Zebra Patterns I: Simulation and Analytics

### 5.1 Introduction

In this chapter we have followed on from section 2.5.4 and delved into the relationship between MHD fluctuations and the double plasma resonance (DPR, see section 2.5.4) emission mechanism for zebra patterns (ZP). We implemented analytical and numerical techniques to arrive at theoretical predictions for the behaviour of ZP in the presence of MHD waves affected by plasma structuring. There are some observational indicators that there is indeed a link as shown in [Yu, Nakariakov, Selzer, Tan, and Yan, 2013] which we will discuss in further detail in chapter 6.

Initially a broad assessment was carried out into the current state of research into solar radio bursts. [Chernov, 2006] was used as a skeleton to provide what is generally accepted in the radio physics community. [Chernov, 2006] describes the growing field of type IV radio bursts and events involving stripes in emission and absorption against the continuum background. Traditionally observed in the meter, decimeter and more recently centimetre wavebands, fine structure elements of type IV events are divided into two types, zebra patterns (ZP) and fibre bursts (FB). It is now commonly thought that the two phenomena are produced by the same mechanism under different conditions.

In recent years a new page has opened on ZP in the microwave range, mainly due to the new observations from the Chinese spectrometer at a finer spectral and time resolution (10 - 20 MHz and 5 ms). New data on zebra pattern structures at centimetre wavelengths show that they are similar to the corresponding structures at meter wavelengths. Hence we aim to align our analytical and numerical results

with the new data. We began with an attempt at analytically deriving the spatial structure of ZP in coronal loops.

## 5.2 Analytical Description of Zebra Pattern Fine Structure.

This work calls upon simulation and analytical techniques to derive ZP emission from first principles to underpin our current understanding of DPR emission mechanism.

### 5.2.1 Deriving the Density Field

The investigation began with the work of [Cooper et al., 2003], a study into the propagation of short period fast magnetoacoustic waves (see section 1.7.3) in a coronal loop (section 2.4.4). The same assumptions were taken and the derivation follows from there. A magnetic slab geometry was chosen to model the coronal loop. It consists of a *smooth* density profile across the magnetic field, given by the function:

$$\rho_0 = \rho_{\max} \text{sech}^2 \left( \frac{x}{\delta} \right) + \rho_{\infty}, \quad (5.1)$$

where  $\rho_0$ ,  $\rho_{\max}$  and  $\delta$  are all constants. Here the parameter  $\rho_{\max}$  is the density at the centre of the loop and  $\rho_{\infty}$  is the density at  $x = \infty$ . The constant  $\delta$  governs the width of the inhomogeneity. This profile is known as the *symmetric Epstein profile*, see figure 5.1, [Adams, 1981, Nakariakov and Roberts, 1995]. With a uniform background magnetic field,  $\mathbf{B}_0 = B_0 \hat{z}$  the model satisfies a total pressure balance at equilibrium under the zero- $\beta$  limit.

According to [Nakariakov and Roberts, 1995], linear perturbations of the transverse plasma velocity:

$$V_x = U(x) \exp i(\omega t - kz), \quad (5.2)$$

are described by the equation:

$$\frac{d^2 U(x)}{dx^2} + \left[ \frac{\omega^2}{v_{A\infty}^2} - k^2 \frac{\omega^2}{v_{Amax}^2} \text{sech}^2 \left( \frac{x}{\delta} \right) \right] U(x) = 0, \quad (5.3)$$

where  $v_{A\infty}$  is the Alfvén speed at  $x = \infty$  and  $v_{Amax}$  is the Alfvén speed based upon the difference in density between that at  $x = 0$  and that as  $x \rightarrow \infty$ . As the corresponding profile of the Alfvén speed maintains a minima at the center of the slab,

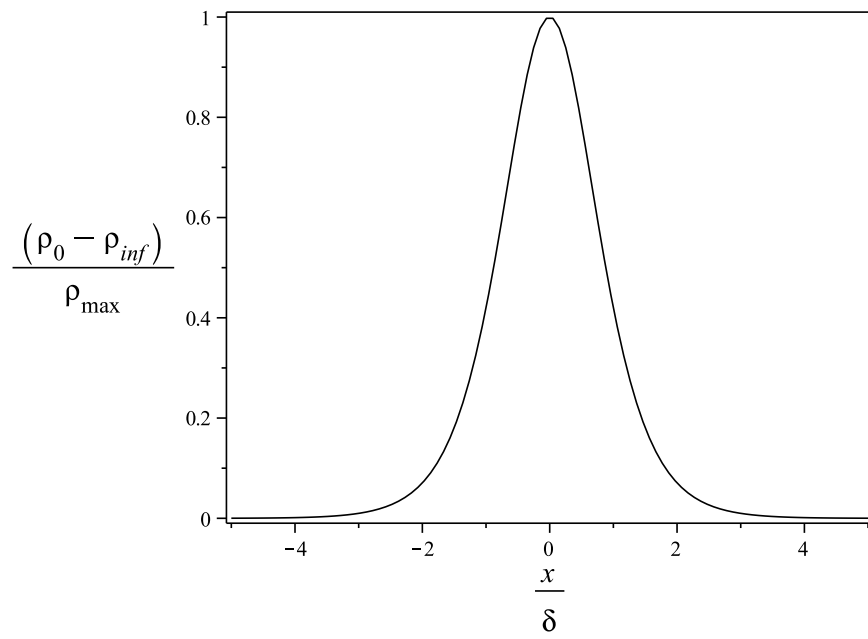


Figure 5.1: The symmetric Epstein profile representing the plasma density across a coronal loop, normalised to the width paramter  $\delta$  and the maximum density,  $\rho_{max}$  (see [[Adams, 1981](#), [Nakariakov and Roberts, 1995](#)]).

the slab can be considered as a refractive waveguide for the fast magnetoacoustic waves (see [Edwin and Roberts, 1988] for discussion).

Equation 5.3 states an eigenvalue problem which can be solved analytically if supplemented by the boundary condition  $U(x \rightarrow \pm \infty) \rightarrow 0$ , [Adams, 1981]. The eigen function describing the sausage mode is given by:

$$U = \frac{\sinh(x/\delta)}{\cosh^\lambda(x/\delta)}, \quad (5.4)$$

with  $\lambda$  given by:

$$\lambda = \frac{|k|\delta}{v_{A\infty}^2} \sqrt{v_{A\infty}^2 - a^2} + 1. \quad (5.5)$$

Here  $a$  was defined as the wave phase speed where  $a = \omega/k$ . The phase speed was then prescribed by the dispersion relation:

$$\frac{|k|\delta}{v_{A0}^2} (a^2 - v_{A0}^2) - 2 \frac{1}{|k|\delta} = \frac{3}{v_{A\infty}} \sqrt{v_{A\infty}^2 - a^2}, \quad (5.6)$$

for the sausage mode. We define  $v_{A0} = v_{A\infty} v_{Amax} / (v_{A\infty}^2 + v_{Amax}^2)^{\frac{1}{2}}$  as the Alfvén speed at the center of the Epstein profile,  $x = 0$ .

To understand the effect of sausage perturbations on the zebra pattern, equations 5.4 to 5.6 need to be solved analytically for the density and absolute magnetic field profiles,  $\rho = \rho(x, z, t)$  and  $\mathbf{B} = \mathbf{B}(x, z, t)$ . First it was necessary to define a set of normalised units:

$$\begin{aligned} k' &= |k|\delta \\ v_{A\infty} &= 1, \\ x' &= x/\delta, \\ z' &= \frac{2\pi}{L}z, \\ t' &= \omega t, \end{aligned} \quad (5.7)$$

where  $L$  is the length of the loop. The dispersion relation, equation 5.6, could then be reduced to the explicit form  $a = a(k)$  with only one parameter  $v_{A0}$ . The primes were dropped for convenience, hence the normalised dispersion relation:

$$\frac{k}{v_{A0}^2} (a^2 - v_{A0}^2) - \frac{2}{k} = 3 \sqrt{1 - a^2}. \quad (5.8)$$

This was solved as a bi-quadratic with 4 roots, two roots do not obey the condition that  $v_{A\infty}^2 - a^2 > 0$  reducing the solution to two symmetric roots for waves travelling in opposing directions. Picking the positive solution:

$$a = \frac{v_{A0} \sqrt{8 + 4k^2 - 18v_{A0}^2 + 6\sqrt{4k^2 - 4k^2v_{A0}^2 - 8v_{A0}^2 + 9v_{A0}^4}}}{2k}. \quad (5.9)$$

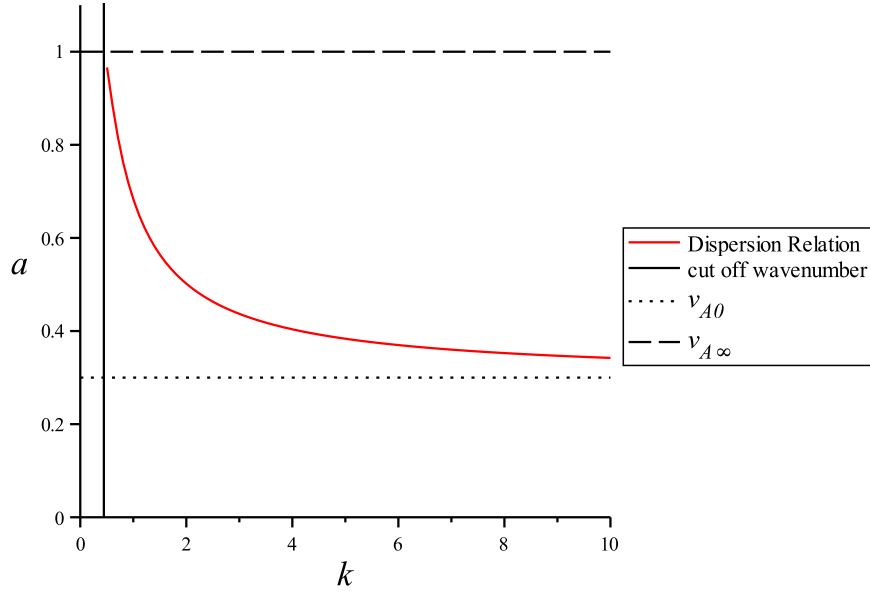


Figure 5.2: The dispersion relation plotted for equation 5.9. The solution is confined between the region of  $v_{A0} < a < v_{A\infty}$  in phase speed ( $v_{A0}$  is chosen at 0.3). A cutoff wavelength  $k_c$  also prescribes the domain in  $k$  space to insure a real phase speed defined as  $k_c$ .

This dispersion relation was plotted in figure 5.2, the solution is confined between the region of  $v_{A0} \leq a < v_{A\infty}$  in phase speed ( $v_{A0}$  is arbitrarily set to 0.3). A cutoff wavelength  $k_c$  also prescribes the domain in the  $k$  space to insure a real phase speed, defined as:

$$k_c = \sqrt{\frac{2v_{A0}^2}{1 - v_{A0}^2}}. \quad (5.10)$$

This solution was then passed to the normalised solution for the  $\lambda$  exponent:

$$\lambda = k\sqrt{1 - a^2} + 1, \quad (5.11)$$

substitution into equation 5.4 resulted in the full normalised transverse plasma velocity in the fast sausage mode:



$$U(k, x) = \frac{\sinh(x)}{\cosh^{|k|\sqrt{1-a^2}+1}(x)}. \quad (5.12)$$

The result was plotted in figure 5.3 for various values of  $k$ .

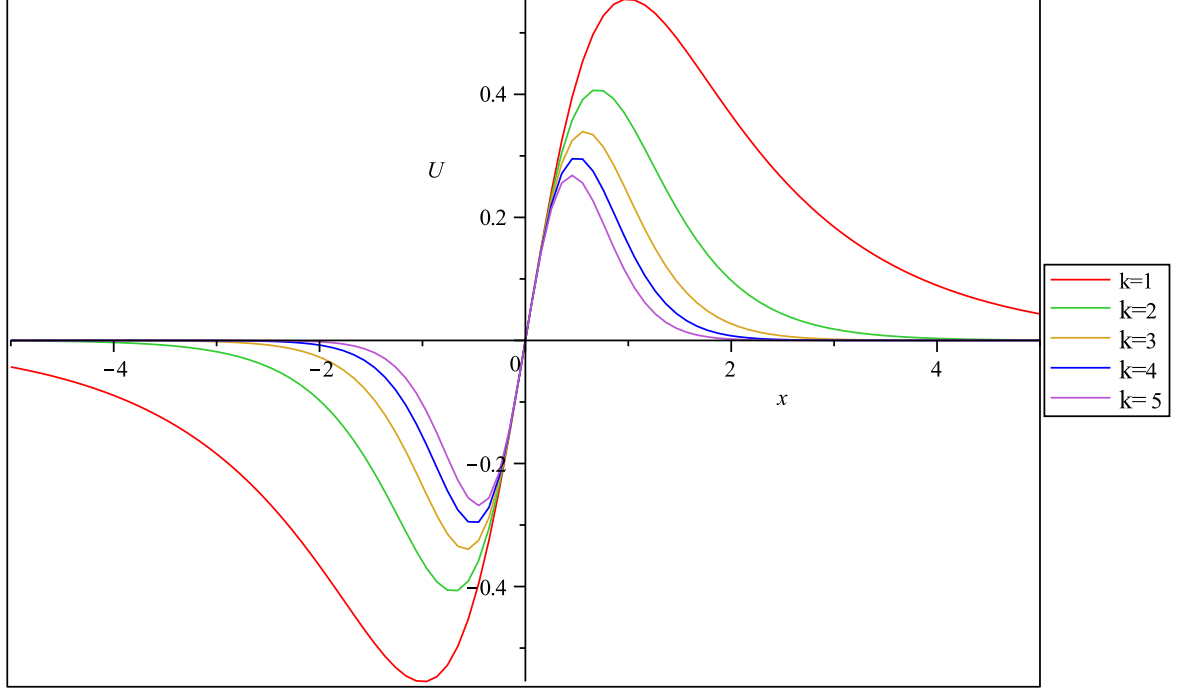


Figure 5.3: The normalised transverse profile of plasma velocity perturbations in a sausage mode was plotted for various values of normalised longitudinal wave number  $k$  as a function of the transverse spatial variable  $x$ .

Only small perturbations were considered such that  $\rho = \rho_0 + \tilde{\rho}$  where  $\tilde{\rho}$  was assigned by a small perturbation in the plasma velocity field  $V_x$ . Hence from the continuity equation:

$$\tilde{\rho} = - \int \frac{\partial(\rho_0 V_x)}{\partial x} dt, \quad (5.13)$$

substituting equation 5.12 into this:

$$\tilde{\rho} = - \int \frac{\partial}{\partial x} \left[ \frac{(\rho_{\max} \text{sech}^2(x) + 1) \sinh(x) \cos(t) \sin(z)}{(\cosh(x))^{k\sqrt{1-a^2}}} \right] dt, \quad (5.14)$$

returns:

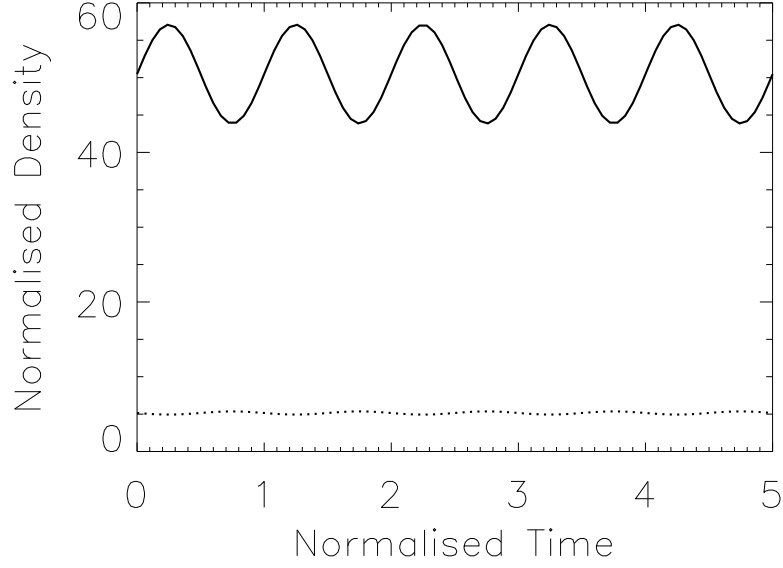


Figure 5.4: The normalised density perturbations were plotted for the loop apex ( $x = 0$ ) (solid line) and the loop edge ( $x = \delta$ ) (dotted line). A clear regular oscillation was seen in both regions with the greatest amplitude shown in the loop apex.

$$\begin{aligned}
\tilde{\rho}(x, z, t, k) &= 2 \frac{\rho_{\max} \text{sech}^2(x) \tanh(x) \sinh(x) \sin(t) \sin(z)}{(\cosh(x))^{k\sqrt{1-a^2}}} \\
&- \frac{(\rho_{\max} \text{sech}^2(x) + 1) \cosh(x) \sin(t) \sin(z)}{(\cosh(x))^{k\sqrt{1-a^2}}} \\
&+ \frac{(\rho_{\max} \text{sech}^2(x) + 1) \sinh^2(x) \sin(t) \sin(z) k\sqrt{1-a^2}}{(\cosh(x))^{k\sqrt{1-a^2}} \cosh(x)}.
\end{aligned} \tag{5.15}$$

The perturbation was then added to the background density, the Epstein profile such that  $\rho(x, z, t, k)$  can be expressed in its full form, shown in figure 5.4:

$$\begin{aligned}
\rho(x, z, t, k) &= \rho_{\max} \text{sech}^2(x) + 1 \\
&+ 2 \frac{\rho_{\max} \text{sech}^2(x) \tanh(x) \sinh(x) \sin(t) \sin(z)}{(\cosh(x))^{k\sqrt{1-a^2}}} \\
&- \frac{(\rho_{\max} \text{sech}^2(x) + 1) \cosh(x) \sin(t) \sin(z)}{(\cosh(x))^{k\sqrt{1-a^2}}} \\
&+ \frac{(\rho_{\max} \text{sech}^2(x) + 1) \sinh^2(x) \sin(t) \sin(z) k\sqrt{1-a^2}}{(\cosh(x))^{k\sqrt{1-a^2}} \cosh(x)} \\
&+ \rho_{\infty}.
\end{aligned} \tag{5.16}$$

### 5.2.2 Deriving the Magnetic Field Perturbations

An analytical description of the magnetic field perturbation,  $\tilde{\mathbf{B}}$  was needed to reconstruct the ZP fine structure using the DPR mechanism. The magnetic field perturbation is induced due to small oscillations in the plasma velocity field,  $\tilde{\mathbf{v}}$  such that the overall magnetic field becomes  $\mathbf{B} = \mathbf{B}_0 + \tilde{\mathbf{B}}$  where  $\tilde{\mathbf{B}} \ll \mathbf{B}_0$ . The linear MHD equations (1.69) were used as the starting point to derive  $\tilde{\mathbf{B}}$ , in particular the Euler equation in the zero- $\beta$  approximation:

$$\rho_0 \frac{\partial \tilde{\mathbf{v}}}{\partial t} = \frac{1}{\mu_0} (\mathbf{B}_0 \wedge \nabla \wedge \tilde{\mathbf{B}}), \quad (5.17)$$

and the induction equation:

$$\frac{\partial \tilde{\mathbf{B}}}{\partial t} = \nabla \wedge \tilde{\mathbf{v}} \wedge \mathbf{B}_0, \quad (5.18)$$

where  $\tilde{\mathbf{B}}$  and  $\tilde{\mathbf{v}}$  are the perturbations of the magnetic field and plasma velocity, respectively. They are defined by:

$$\begin{aligned} \tilde{\mathbf{B}} &= B_x \hat{\mathbf{x}} + B_z \hat{\mathbf{z}}, \\ \tilde{\mathbf{v}} &= V_x \hat{\mathbf{x}} + V_z \hat{\mathbf{z}}, \end{aligned} \quad (5.19)$$

where  $V_x$  is given by (5.2) while  $B_x, B_z, V_z$  are to be derived. To begin (5.17) was projected onto the coordinate axis such that in the  $z$  direction:

$$\rho_0 \frac{\partial V_z}{\partial t} = 0 \quad (5.20)$$

If we assume  $V_z$  to be harmonic like  $V_x$  then  $i\rho_0\omega V_z = 0$  or  $V_z = 0$ , thus the only velocity perturbation component lies in the  $x$  direction. Equation (5.18) allows the derivation of the magnetic field perturbation components using  $V_x$ :

$$\frac{\partial B_x}{\partial t} = -B_0 \frac{\partial V_x}{\partial z}, \quad (5.21)$$

and:

$$\frac{\partial B_z}{\partial t} = B_0 \frac{\partial V_x}{\partial x}, \quad (5.22)$$

which yields:

$$\begin{aligned} \frac{B_x}{B_0} &= -\frac{V_x}{a}, \\ \frac{B_z}{B_0} &= -\frac{i}{\omega} \frac{\partial V_x}{\partial x}, \end{aligned} \quad (5.23)$$

which produces:

$$\frac{B_x}{B_0} = -\frac{1}{a} \frac{\sinh(x)}{\cosh^{1+k\sqrt{1-a^2}}(x)} \cos(t-z), \quad (5.24)$$

and:

$$\frac{B_z}{B_0} = \frac{1}{a} \left( \frac{(1+k\sqrt{1-a^2}) \sinh^2(x)}{\cosh^{2+k\sqrt{1-a^2}}(x)} - \frac{\cosh(x)}{k \cosh^{1+k\sqrt{1-a^2}}(x)} \right) \sin(t-z). \quad (5.25)$$

### 5.2.3 Zebra Pattern Formation

The next stage of the study was to assess whether it was possible to analytically derive the results found in [Yu et al., 2013], discussed in detail in chapter 6. In the paper we observe periodic oscillations in both stripe frequency and stripe separation known as ‘wiggles’. The perturbations in the ZP are hypothesised to be induced by a fast mode propagating through the zebra pattern emission region. We aimed to simulate a standing or propagating sausage mode in the emitting loop and observe the disturbance induced in the simulated ZP, as an attempt to support this interpretation theoretically. To begin with the double plasma resonance model’s (see [Kuznetsov and Tsap, 2007, Zheleznyakov and Zlotnik, 1975]) conditions (section 2.5.4) needed to be satisfied by the density function given in equation 5.16 and the magnetic field perturbations given by equations 5.24 and 5.25. ZP stripe locations and frequencies in radio emission were given by the regions where the DPR condition is fulfilled, see section 2.5.4. These regions amplify plasma fluctuations excited by an electron beam passing through the background non-uniform plasma with a non-uniform magnetic field, through the DPR mechanism. The new larger amplitude fluctuations then coalesce and induce radio emission processes, for the sketch of this mechanism see figure 2.19. The DPR condition is given by:

$$s\omega_{ce} = \sqrt{\omega_{ce}^2 + \omega_{pe}^2} = \omega_{uh}, \quad (5.26)$$

where  $f_{ce}$  is the electron cyclotron frequency (equation 1.2),  $f_{pe}$  is the plasma frequency and  $s$  is the harmonic number which can hold any positive integer value.

The radio emission is produced at the frequency  $f_{uh}$  or the double harmonics of  $f_{uh}$  as a consequence of coalescence of two plasma waves generated by kinetic instabilities. These instabilities are greatly enhanced under the DPR condition. Equation 5.26 can be rewritten with  $\omega_{pe}^2$  substituted by  $\rho$  and  $\omega_{ce}^2$  substituted by  $B^2$  as:

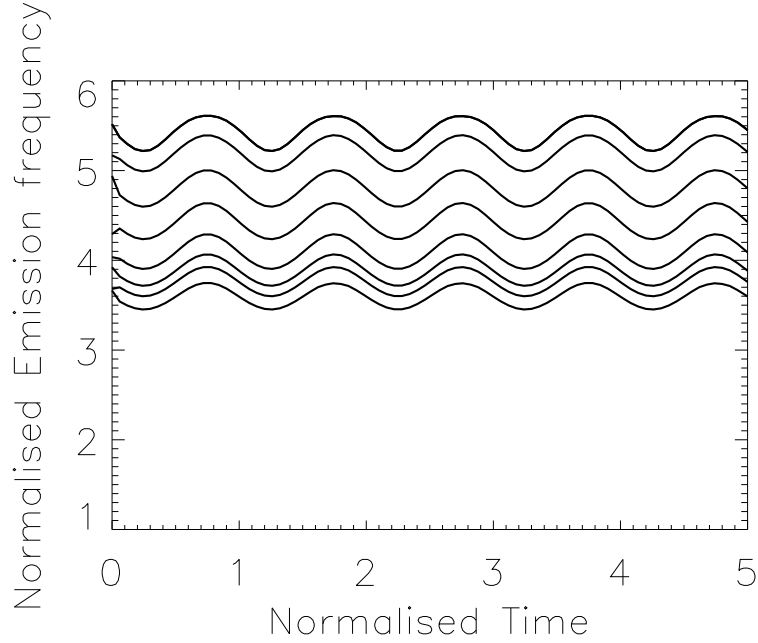


Figure 5.5: The analytically derived zebra pattern in radio emission is recreated. The zebra pattern clearly exhibits the ‘wiggle’ result shown in [Yu et al., 2013, figure 1, section 1].

$$\frac{\rho}{|\mathbf{B}|^2} = s^2 - 1, \quad (5.27)$$

due to the definitions of  $f_{pe}$  and  $f_{ce}$ . Using equations (5.24, 5.25) and (5.16) it was possible to find the spacial location of the DPR for different integer values of  $s$  at different instances of time. Using the  $(x, z)$  co-ordinates the local density fields was converted to frequency and values that satisfied the DPR mechanism were plotted as a function of time resulting in the dynamic spectra, figure 5.5. The wiggle period as derived analytically was observed at  $P_A = 1$  s in figure 5.5, as simulation time was normalised to the fast mode period which is typically 1 s in coronal loops.

### 5.3 Numerical Simulations

Having derived the ZP using analytical techniques it was beneficial to use simulations to confirm that these results do in fact agree with the experimental results outlined by [Yu et al., 2013]. Key results from section 5.2 will be compared to those produced by the simulations to underpin the location of the DPR resonances.

### 5.3.1 Static Simulations

The starting point of ZP simulation was a snapshot of the sausage at a fixed instant in time. Time dynamics were neglected to allow us to understand what the background ZP should look like and how to effectively simulate it. Once established it will be possible to perturb these simulations using the different phases of the MHD oscillation.

#### 1D

An investigation was undertaken to assess if the simulation of ZPs was a viable concept. We began with a simple 1D toy model accounting for the variation of the density along the field only. The intent was to understand the spacial scales involved in the ZP emission region. We implemented the work of [Dulk and McLean, 1978] as an attempt to reproduce the results shown in [Chernov, 2006] on a one dimensional zebra pattern. We consider a stratified plane atmosphere with the density depending on the height,  $h$  measured along the field only such that:

$$\rho(h) = \rho_0 \exp \left[ \frac{-(h - h_0)}{10^4 T} \right], \quad (5.28)$$

where  $\rho_0$  is the equilibrium density at the base of the chromosphere,  $T$  is the constant coronal temperature and  $h_0$  is the base of the chromosphere. The introduction of a constant temperature from photosphere to the outer corona is a huge oversimplification. As described in chapter 2 the chromosphere and corona have a complicated temperature structure, but as we have already stated this is the most simple model to start our investigation and thus its results should only be used as a starting point. In particular any resonances found in the chromosphere region are unlikely to be physically relevant due to the error in temperature values at these lower altitudes.

It proved to be easier to convert this into a relationship for electron plasma frequency via (1.1). This meant that the model was scaled by an average coronal electron plasma frequency  $f_{pe0}$  rather than trying to estimate the height of the photosphere-chromosphere boundary:

$$f_{pe}(h) = f_{pe0} \exp \left[ \frac{-h}{10^4 T} \right]. \quad (5.29)$$

The 1D approach violates the  $\nabla \cdot \mathbf{B} = 0$  condition, but we restrict our attention to the emission from the central axis of the emitting loop only. The magnetic field profile was taken as:

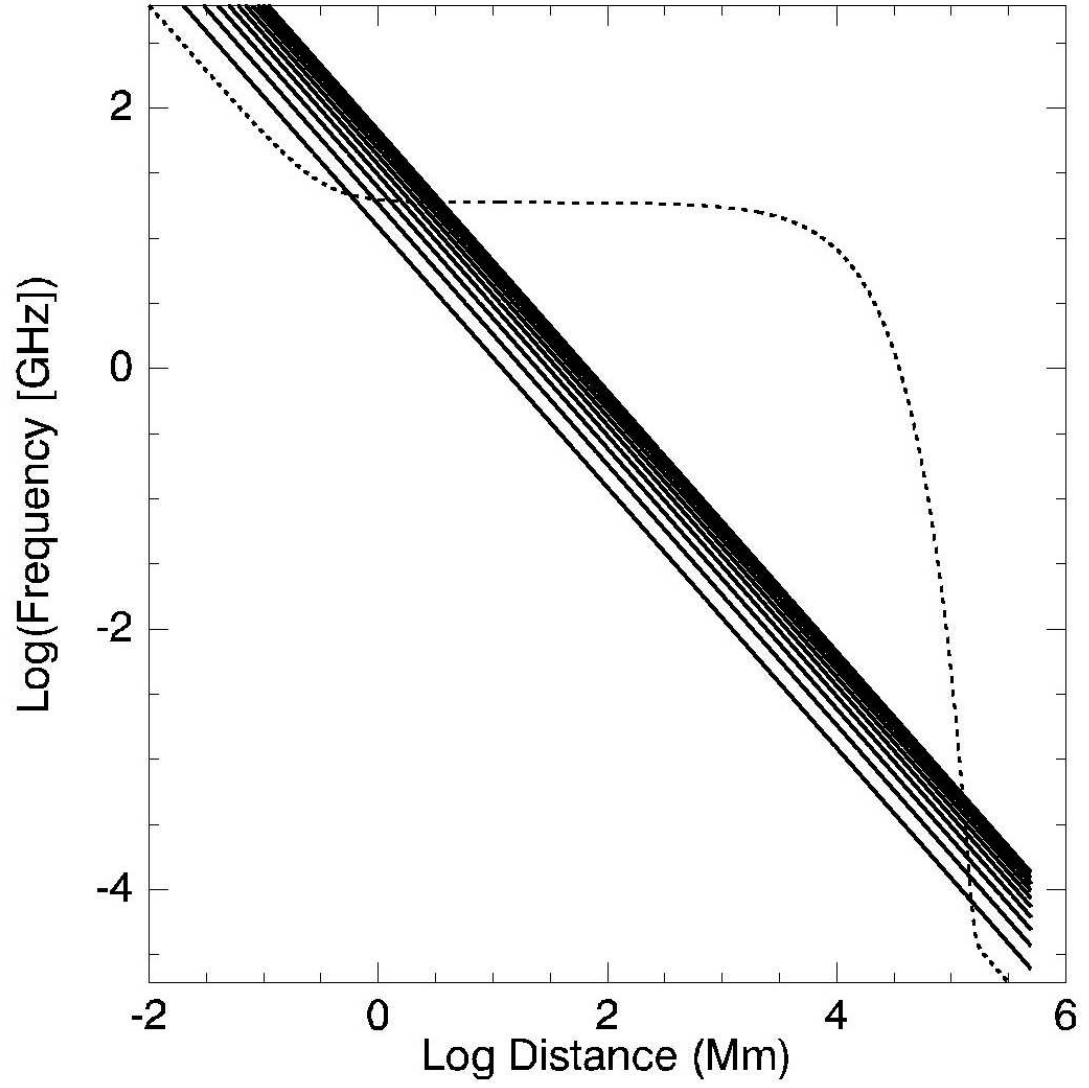


Figure 5.6: The  $s$  harmonics of  $f_{ce}$  are plotted (solid black) against  $f_{uh}$  (dashed). Intersections are where the DPR condition was satisfied.

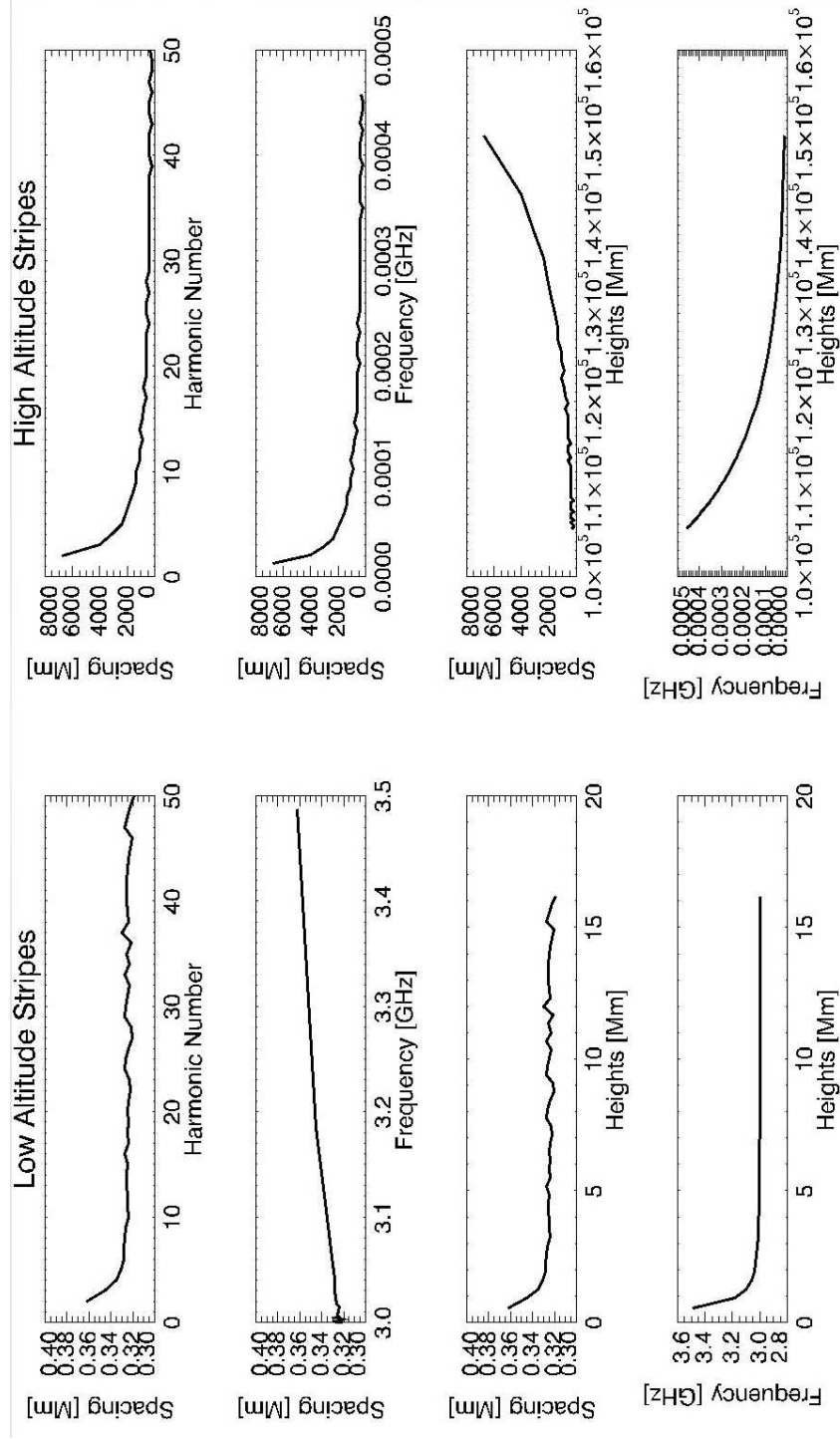


Figure 5.7: The following are plotted for the one dimensional zebra pattern emission system for both high and low altitude solutions: The stripe spacing is plotted against the double resonance harmonic number; the stripe spacing is plotted against stripe frequency; the stripe spacing is plotted against stripe emission height and finally the frequency is plotted against stripe emission height.



Harmonic Number - $s$	Height [Mm]	Frequency [GHz]
2	0.54	3.49
3	0.91	3.18
4	1.25	3.10
5	1.58	3.06
6	1.91	3.04
7	2.24	3.03
8	2.57	3.02
9	2.90	3.02
10	3.22	3.01

Table 5.1: Results for the 1D static ZP model. A value of 1.2 MK was taken for the coronal temperature while the coronal magnetic field was assumed to take a value of 1 mT (10 gauss). The coronal plasma frequency was estimated at 3 GHz.

$$B = \frac{B_0}{2} \left( \frac{z}{R_\odot} \right)^{-a}, \quad (5.30)$$

where  $R_\odot$  is the solar radius and  $B_0$  the magnetic field at the base of the chromosphere;  $a$  is a scaling parameter which was chosen to be from 1 – 1.5, [Dulk and McLean, 1978]. The magnetic field was then transformed into the electron cyclotron frequency via (1.2). The  $f_{pe}$  and  $f_{ce}$  values were subsequently used to find what heights and frequency values the DPR condition,  $f_{uh} = \sqrt{f_{ce}^2 + f_{pe}^2} = s f_{ce}$  (equation 2.3) were fulfilled for each harmonic. The results are shown in table 5.1.

These values align with recent observations made in the GHz range, see section 2.5.4. Figure 5.6 shows  $s f_{ce}$  for 10 values of  $s$  plotted against  $f_{uh}$ . Intersections are where the DPR condition is satisfied. As shown in table 5.1 there are crossings up to a heights of 3 Mm. We also found DPR fulfilment at far larger altitudes and therefore lower frequencies i.e. in the MHz range.

The difference between the lower and higher altitude stripe emission was further explored by looking at several parameters as shown in figure 5.7. The most interesting observation was the stripe separation, or ‘frequency spacing’ versus frequency. The two regions seem to exhibit the opposing behaviour. While these observations are interesting it is important to remember that this is an oversimplified toy model. Several assumptions have been made which would not hold in the vastly structured solar atmosphere. Even so the study showed that it was possible to reproduce an extended source region for ZPs. Further to that we were able to retrieve realistic frequency and height information for a 1D system. The ZP emission heights were greatly underestimated when in comparison with [Chen et al., 2011] who predicted heights of 60 – 80 Mm, a factor of 20 larger.

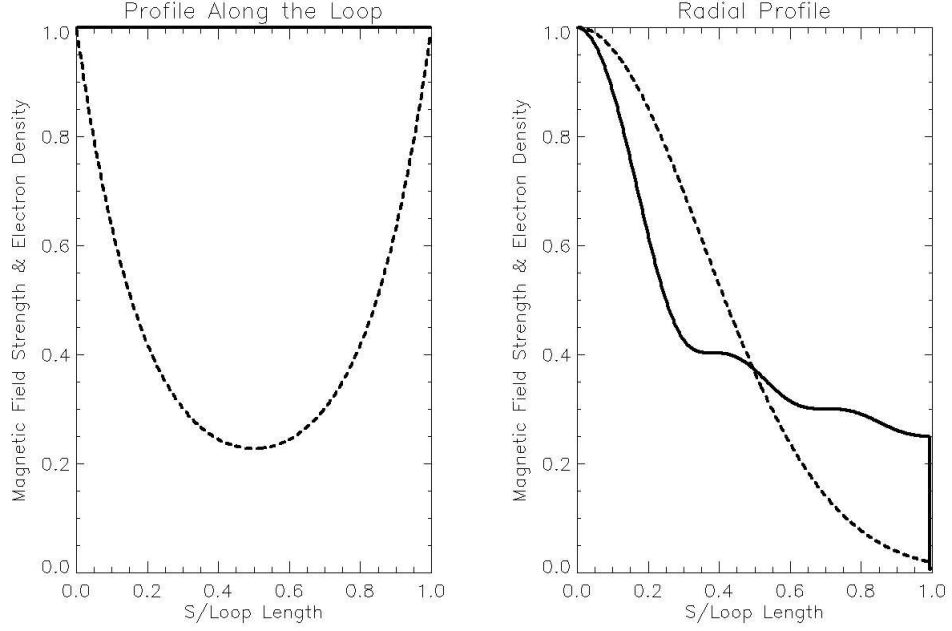


Figure 5.8: Normalised transverse and longitudinal electron density (dashed) and absolute magnetic field (solid) profiles for the static 2D loop model. The loop’s density structure was used to solve for the magnetic field under equilibrium conditions according to [van Hoven et al., 1977].

## 2D

The main motivation to progress into two dimensional modelling is the possibility that different harmonics of DPR can be situated not only at the non-uniformity along the field, as considered above, but also across the field. Following on from section 5.3.1 we move into a two dimensional snapshot model. In 2D we began to build a naive loop structure to resemble that of a coronal loop. The coordinate system is aligned along the loop axis,  $z$  and hence the magnetic field, with the radial coordinate  $r$ . As the system is now 2D we need to ensure the pressure field retains the magnetostatic equilibrium across the loop. A pressure field was constructed by combining a pressure profile along the loop with a pressure field across the loop. We were then able to substitute pressure for density as they maintain a local relation via (1.23).

The radial pressure profile,  $p_r(r)$  was taken as the Epstein profile (5.1), used in section 5.2. The longitudinal profile,  $p_l(z)$  was taken as the [Dulk and McLean, 1978] model from section 5.3.1 which assumed a stratified atmosphere. The profiles were then normalised and multiplied together to evaluate the pressure as a function of  $r$  and  $z$ ,  $p(r, z) = p_r(r)p_l(z)$ .

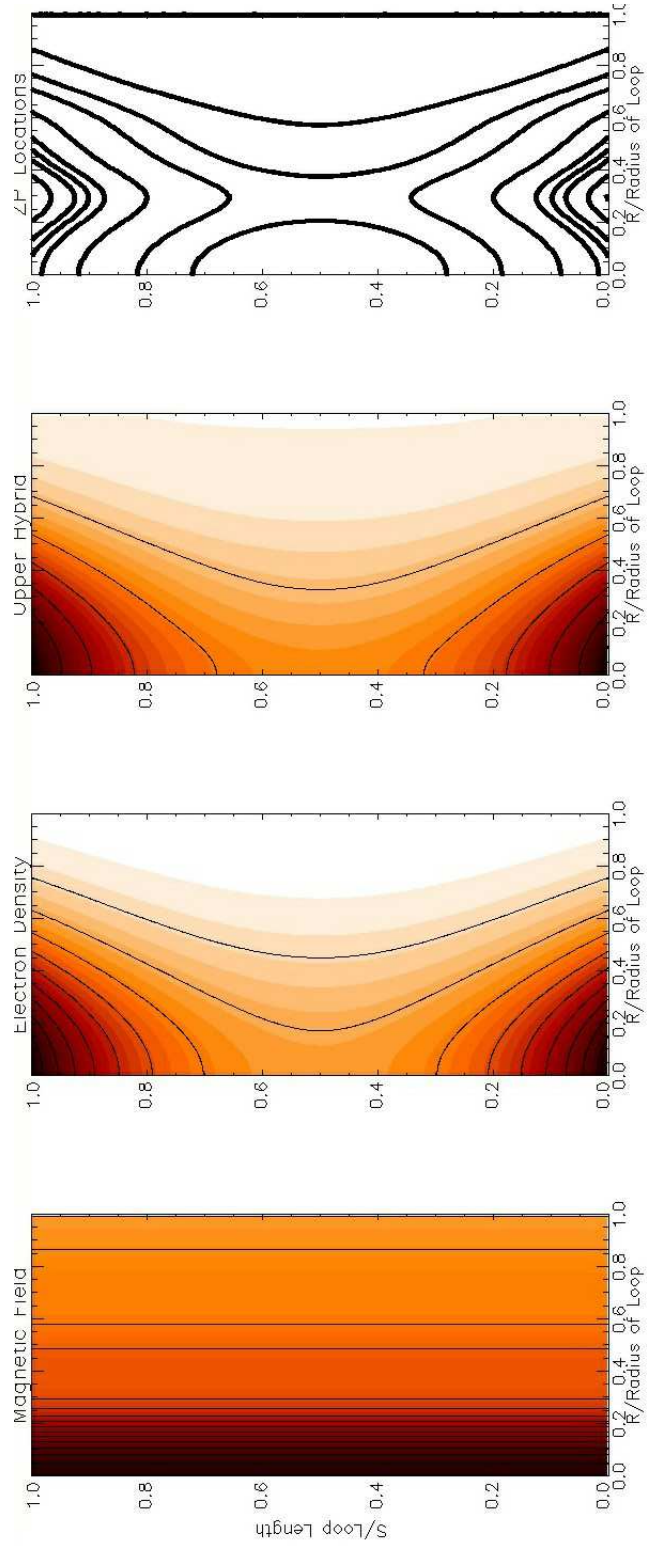


Figure 5.9: The 2D static loop model for ZP emission using the DPR mechanism. Magnetic field, electron density, upperhybird frequency and ZP locations are plotted onto the 2D loop.

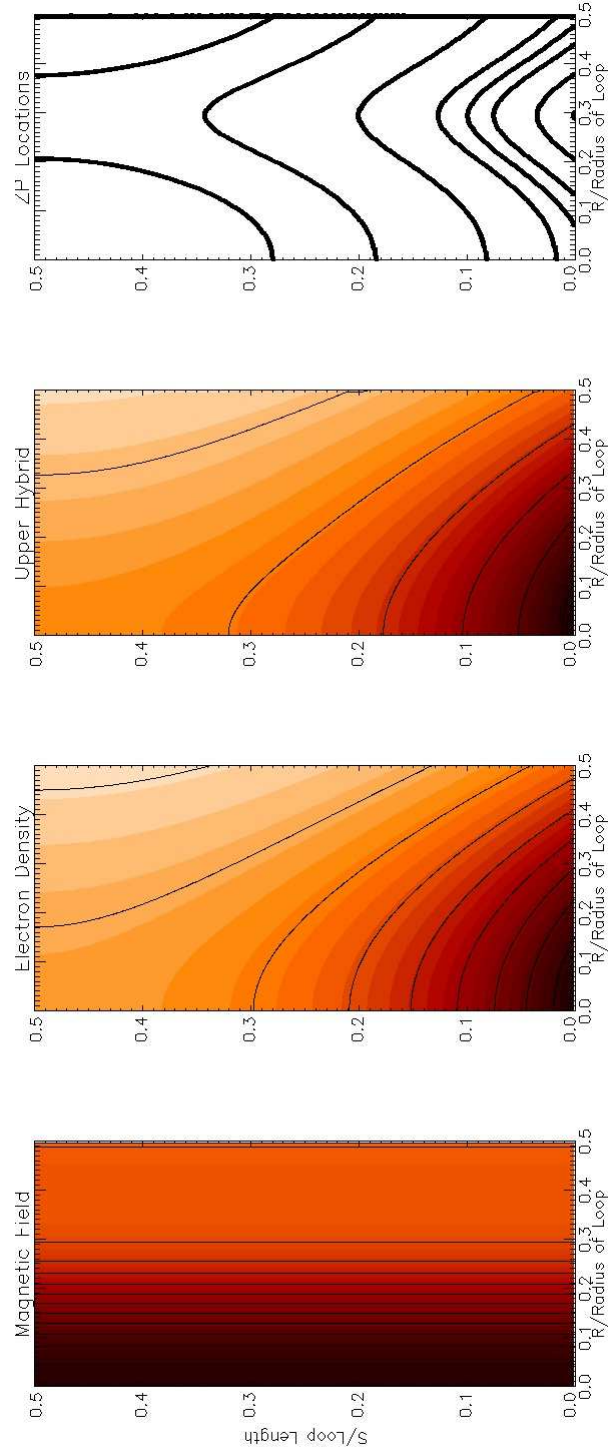


Figure 5.10: A 2D static loop model for ZP emission using the DPR mechanism zoomed in the vicinity of one of the footpoints. Magnetic field, electron density, upperhybird frequency and ZP locations are plotted onto the 2D loop.

The equilibrium magnetic field was found by following the derivation in [van Hoven et al., 1977]. The derivation uses small-scale pressure gradients to specify the locally non-force-free field which is embedded in a global force free configuration. The assumption is that in the loop, pressure forces become important thus dropping the low- $\beta$  limit in these small regions. The paper demonstrates that the configuration can be stable given certain parameter choices. In this chapter we merely use it as a starting point for 2D modelling as a proof of concept. They began by using the static momentum-transfer equation, (1.31) in a static regime ( $\partial_t \rightarrow 0$  and  $\mathbf{v} = 0$ ) in order to incorporate the pressure gradients, with  $\mathbf{E} = 0$ :

$$0 = -\nabla p + \mathbf{j} \wedge \mathbf{B}. \quad (5.31)$$

Separating the current density  $\mathbf{j}$  into the parallel and perpendicular components to  $\mathbf{B}$ , we see that only  $\mathbf{j}_\perp$  enters the force balance equation hence we needed another relation for  $\mathbf{j}_\parallel$ . Since  $\mathbf{j}_\parallel$  can always be written as  $\mathbf{j}_\parallel = \alpha(\mathbf{r}, t)\mathbf{B}$ , we only need to specify the dependence of  $\alpha$  on  $\mathbf{r}$  and  $t$ . In this simplistic model we selected the linear case where  $\alpha$  is constant and uniform. Then using Ampere's Law (1.7) we have:

$$\begin{aligned} \nabla \wedge \mathbf{B} &= \mu_0(\mathbf{j}_\parallel + \mathbf{j}_\perp) \\ &\approx \alpha \mathbf{B}(r) + \frac{\mu_0 \mathbf{B} \wedge \nabla p}{B^2}. \end{aligned} \quad (5.32)$$

Following [van Hoven et al., 1977], this was solved analytically using the Bessel-function solution of the force free equation. In cylindrical coordinates where  $\mathbf{B} = (B_r, B_\theta, B_z)$ :

$$B_r = 0, \quad (5.33)$$

to conserve  $\nabla \cdot \mathbf{B} = 0$ , while:

$$B_z(r) = B_0(r)J_0(\alpha r), \quad (5.34)$$

and

$$B_\theta(r) = B_0(r)J_1(\alpha r), \quad (5.35)$$

where  $J_0$  and  $J_1$  are the Bessel functions of the first kind.  $B_0$  is the common field amplitude given by, [van Hoven et al., 1977]:

$$\frac{d}{dr}(B_0^2) = -\frac{2\mu_0}{J_0^2(\alpha r) + J_1^2(\alpha r)} \frac{dp}{dr}. \quad (5.36)$$

The magnetic field strength profile  $B(r)$  was reconstructed from the the magnitude of its components:

$$B(r) = |\mathbf{B}| = \sqrt{B_z^2 + B_\theta^2}. \quad (5.37)$$

The solution requires solving for the equilibrium magnetic field,  $B_0$  using (5.36). A differential finite element analysis was carried out to solve for  $B_0$  at each point on the grid using the input pressure field  $p(r, z)$ . The result was fed through the system of equations above to produce the overall magnetic field strength  $B(r)$ . The two normalised functions,  $p(r, z)$  and  $B(r)$  shown in figure 5.8, were then converted to  $f_{pe}$  and  $f_{ce}$  respectively using average coronal parameters. The process carried out in section 5.3.1 was then repeated to find the location and emission frequencies of regions where the DPR condition was satisfied. The results are shown in figures 5.9 and 5.10. The frequency values found range from 0.8 – 1.9 GHz which again aligns with observational values seen in table 2.5.3.

This simple model predicted the location of the zebra patterns to be extended from the foot points to the apex of the coronal loop with the higher harmonics isolated to an outer shell running the length of the loop. This is in agreement with [Chen et al., 2011] who constrain the ZP emission region to an area at a height of 60 – 80 Mm above the foot points, shown in figure 5.11. However [Chen et al., 2011] do not observe ZP emission in the loop foot points. There may be secondary absorption mechanisms which prevent ZP radio emission from the foot points however they are beyond the scope of this model. Moreover, [Chen et al., 2011] did not manage to see the DPR layers at the transverse slopes of the loop. This discrepancy with our theoretical results could be caused by the localisation of the non-thermal electron beam near the central axis of the loop cylinder. In this scenario the DPR layers at the transverse slopes are not excited because of the lack of non-thermal electrons there.

### 5.3.2 2D Dynamic Coronal Loop Model

Through sections 5.2 - 5.3.1 we have begun to understand the spatial structure and frequency range of ZP using numerical simulations. In this section we progress the numerical analysis by modelling a dynamic coronal loop which we have perturbed with MHD oscillations in an attempt to observe their impact on the ZPs. Numerical simulations were executed using *Lare2D* numerical MHD code, [Arber et al., 2001].

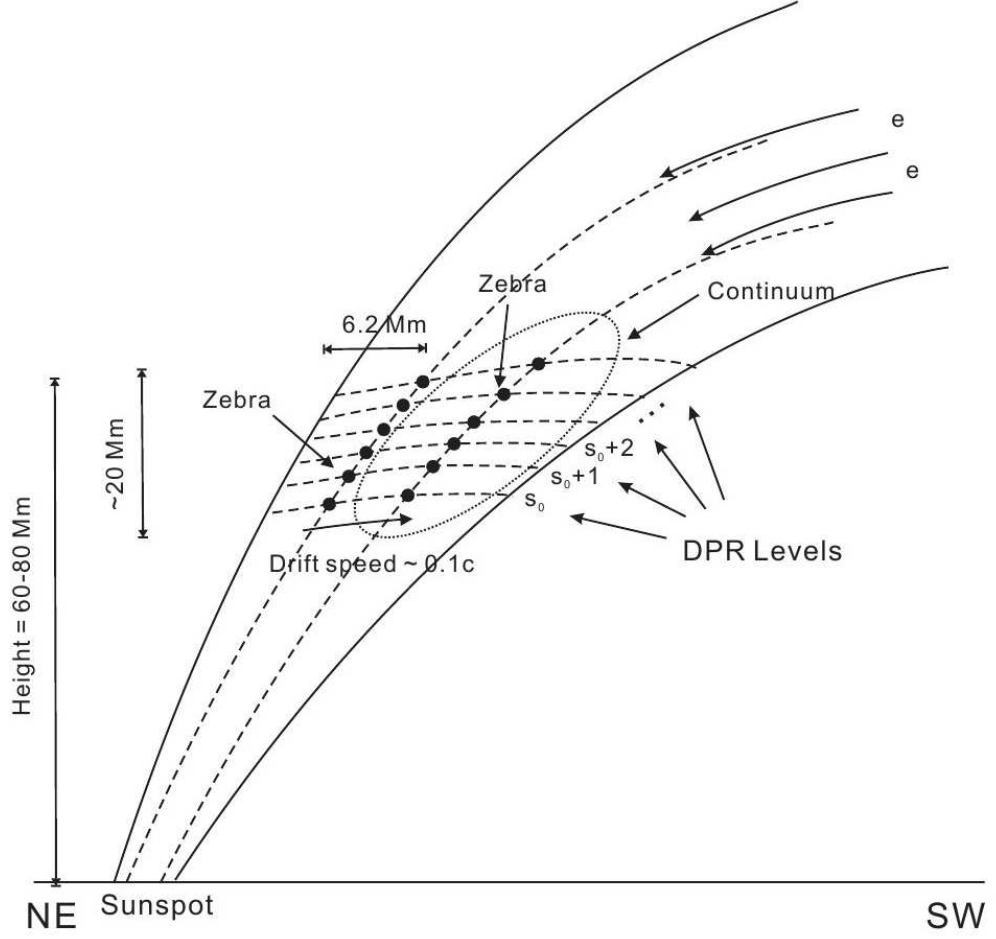


Figure 5.11: Schematic diagram outlining the observations of [Chen et al., 2011]. The ZP sources are located at a height of 60–80 Mm in a post flare/post-CME loop system. The ZP source region was observed to be extended across a height range of  $\approx 20$  Mm. Within the zebra source, individual stripes correspond to emissions near the local plasma frequencies at the DPR levels (horizontal dashed lines, of which the lowest one corresponds to the  $s = f_{pe}/f_{ce} = 8$  layer).

## Lare2D

Lare2D is a shock capturing Lagrangian remap code that solves the resistive MHD equations in a Cartesian geometry. These were reduced to ideal MHD by setting resistivity to zero. The following ideal MHD equations (taken from section 1.3.2) were used for the simulations:

$$\frac{\partial \rho}{\partial t} = -\nabla \cdot (\rho \mathbf{v}), \quad (5.38)$$

$$\left( \frac{\partial}{\partial t} + \mathbf{v} \cdot \nabla \right) \mathbf{v} = \frac{1}{\rho} (\nabla \times \mathbf{B}) \times \mathbf{B} - \frac{1}{\rho} \nabla P, \quad (5.39)$$

$$\left( \frac{\partial}{\partial t} + \mathbf{v} \cdot \nabla \right) \mathbf{B} = (\mathbf{B} \cdot \nabla) \mathbf{v} - \mathbf{B} (\nabla \cdot \mathbf{v}), \quad (5.40)$$

$$\left( \frac{\partial}{\partial t} + \mathbf{v} \cdot \nabla \right) \epsilon = -\frac{P}{\rho} \nabla \cdot \mathbf{v}, \quad (5.41)$$

$$\nabla \cdot \mathbf{B} = 0, \quad (5.42)$$

where  $\rho$  is the mass density,  $\mathbf{v}$  is the velocity,  $\mathbf{B}$  is the magnetic field,  $\epsilon$  is the internal energy,  $P = \rho\epsilon(\gamma - 1)$  is the thermal pressure and  $\gamma = 5/3$  is the ratio of specific heats. The effects of gravity on the evolution of the loop are neglected in the equations above. This holds under the assumption that the flow induced by the gravitational forces are much slower than the fast waves we are studying. A simple acceleration calculation for the free fall time from the typical 10 Mm loop height used, under the acceleration of gravity on the Sun,  $274 \text{ ms}^{-2}$ , yields a time scale of  $\approx 100 \text{ s}$ . Therefore the relaxation process due to these forces would be expected to modify profiles over the simulation time scales chosen but much slower than compared to most of the wave periods of interest (1–5 s), thus the qualitative dynamics would not be affected.

The software is second order accurate in space and time and each computational time step is split into two. First, the Lagrangian step during which the MHD equations are advanced in time on a mesh that moves with the solution. Next the solutions are remapped onto the fixed Eulerian grid. The numerical grid is staggered to prevent the development of the checker-board numerical instability and is shown in figure 5.12. Velocities are defined at the cell vertices, scalar quantities and the ignorable magnetic field component are defined at cell centres and the remaining magnetic field components are defined at the cell edges. The code solves the normalised form of the MHD equations and the dimensionless forms of the length scale,



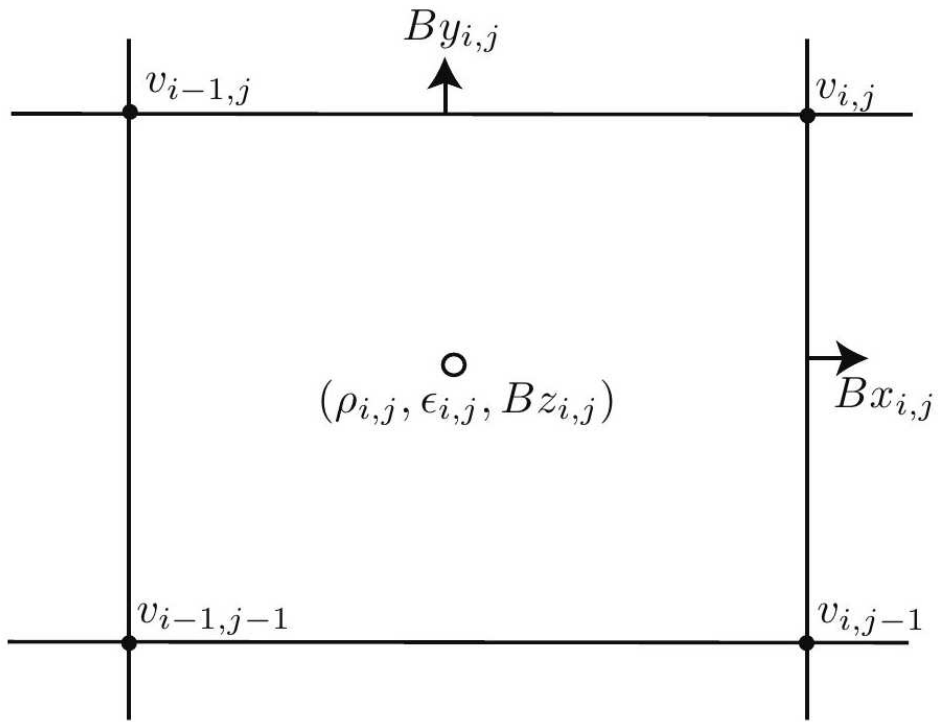


Figure 5.12: The numerical grid used in the Lare2D numerical software.

magnetic field and density are defined as:

$$\begin{aligned} x &= L_0 \hat{x}, \\ \mathbf{B} &= B_0 \hat{\mathbf{B}}, \\ \rho &= \rho_0 \hat{\rho}, \end{aligned} \tag{5.43}$$

where  $L_0, B_0$  and  $\rho_0$  are user defined normalisation parameters for length, magnetic field and density respectively. These are then used to define the normalisation of other quantities such as the velocity, pressure and time:

$$\begin{aligned} v_0 &= \frac{B_0}{\sqrt{\mu_0 \rho_0}}, \\ p_0 &= \frac{B_0^2}{\mu_0}, \\ t_0 &= \frac{L_0}{v_0}. \end{aligned} \tag{5.44}$$

## A 2D Dynamic Coronal Loop

A semi-circular coronal loop was modelled as a simple magnetic slab [Edwin and Roberts, 1982] of enhanced density, with a uniform constant initial magnetic field  $\mathbf{B}_0 = B_0 \hat{\mathbf{z}}$  along the coronal loop (See figure 5.13). The density distribution in the transverse direction is given by the slab step function of width  $2\delta$ . All the simulations were carried out in a domain of  $(-L/2, L/2) \times (-L/2, L/2)$ , covered by  $1000 \times 1000$  grid points. In the  $z$ -direction the density distribution is governed by the gravitational force:

$$\rho(x, s(z)) = \begin{cases} \rho_0 \exp(-\frac{s}{H}), & |x| < \delta, \\ \rho_e \exp(-\frac{s}{H}), & |x| > \delta, \end{cases} \tag{5.45}$$

where  $\rho_0$  and  $\rho_e$  are the internal and external density at  $y = 0$  (the loop apex),  $s = \frac{L}{\pi} \cos(\frac{L}{\pi} z)$  is the loop length coordinate (starting at the loop apex),  $L$  is the loop length and  $H = \frac{L}{2}$  is the scale height of density along the loop. The magnetic field and density at  $z = 0$  were chosen such that the Alfvén speed, (1.72) inside and outside the loop,  $v_{A0}$  and  $v_{Ae}$  respectively, are  $0.7 \text{ Mm s}^{-1}$  and  $1.2 \text{ Mm s}^{-1}$ , which is typical for the solar corona.

In all simulations the length of the loop  $L$  is chosen to be 10 Mm, the magnetic field  $B_0$  was 0.5 mT (50 gauss) and the density contrast was  $\rho_0/\rho_e = 10$ . The boundary conditions fixed the magnetic field direction  $z$  at  $z = -L/2, L/2$ , corresponding to the photospheric boundary conditions at the coronal base. In the

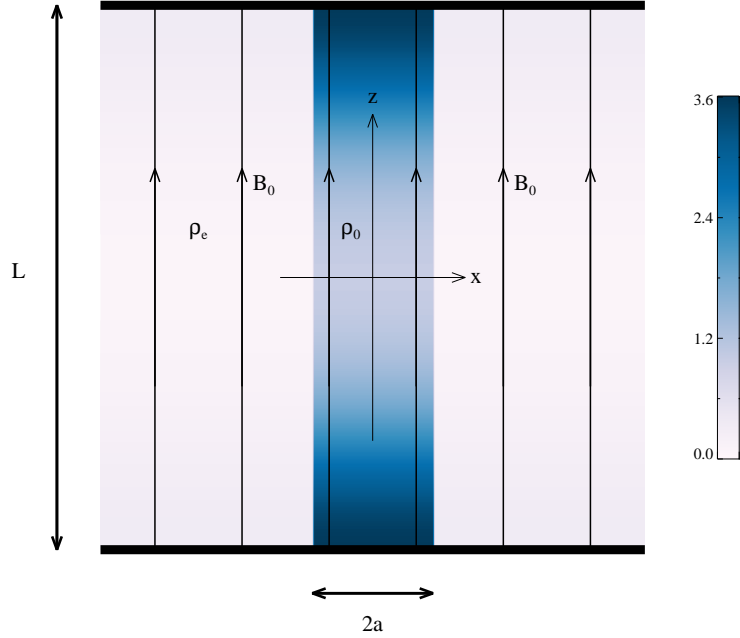


Figure 5.13: Illustration of the straight slab geometry.  $L$  is the loop length with  $2a$  representing the cross-sectional width. A uniform magnetic field is shown as  $B_0$  with internal and external density values given by  $\rho_0$  and  $\rho_e$  respectively. The colour denotes the scaling of the density structure.

transverse direction, open boundary conditions were applied. The plasma  $\beta$  was chosen to be 0.1 internally and externally.

We hypothesised that magnetoacoustic waves should interact with the ZP as they perturb both density and magnetic field as shown in section 1.6.1, key quantities in the DPR mechanism. The most prevalent of these oscillations situated in coronal loops are the sausage mode disturbances predicted by wave mode analysis of a plasma cylinder, section 1.6.2. The fast magnetoacoustic sausage mode was the wave that most closely matched the 1 s periodicity observed in [Yu et al., 2013, Section 3].

The standing and propagating fast waves in a coronal loop periodically modify the magnetic field and density in phase, see section 1.6.1. Which, in consideration

with the work carried out in section 5.2 looked like a promising avenue of research. So we began by introducing these magnetoacoustic oscillations to the system by triggering a propagating fast wave of the sausage symmetry [Nakariakov et al., 2004]. Propagating waves were excited by a velocity pulse situated at the loop apex was induced:

$$V_x = A_0 x \exp \left[ - \left( \frac{x}{\lambda_x} \right)^2 \right] \exp \left[ - \left( \frac{z}{\lambda_z} \right)^2 \right], \quad (5.46)$$

where  $A_0$ ,  $\lambda_x$ ,  $\lambda_y$  are the pulse amplitude and widths in the transverse and longitudinal directions, respectively. The pulse width was set to the half loop width with  $\lambda_x = \lambda_y = \delta$ . A transverse velocity pulse was induced at the loop apex to trigger a standing fast wave:

$$V_x = A_0 U(x) \cos(kz), \quad (5.47)$$

where the transverse velocity  $U(x)$  is prescribed by equation 5.4. In all simulations the pulse amplitude  $A_0$  was chosen to be 0.1 to prevent the appearance of non-linear effects.

A cut across the loop was taken to observe the transverse velocity profile for comparison to figure 5.3 obtained analytically. As shown by figure 5.14 the form of the velocity field closely matches that found analytically in figure 5.3. This provides further evidence that the simulated perturbations are similar in nature to the solutions found for equation 5.3.

### 5.3.3 Zebra Pattern Simulation

As in section 5.2, the ZP showed a strong response to the induced magnetoacoustic structures (section 5.3.2). The density field was converted to  $f_{pe}$  via (1.1), while the magnetic field to  $f_{ce}$  via (1.2). The two fields were then cross-referenced for regions which satisfied the DPR mechanism outlined by equations 5.26 & 5.27. The emission frequency for each location was then determined at each time interval. This process was repeated for each  $s$  harmonic and thus the dynamic spectra of the induced radio emission were constructed. The stripe width was produced using an artificial Gaussian profile in frequency space for each value produced by the simulation. The results for a propagating and standing fast modes are shown in figures 5.15e and 5.15j.

Another proxy for the correlation between simulation and analytics was the wiggle period of the dynamic spectra. Both simulated and derived dynamic spectra

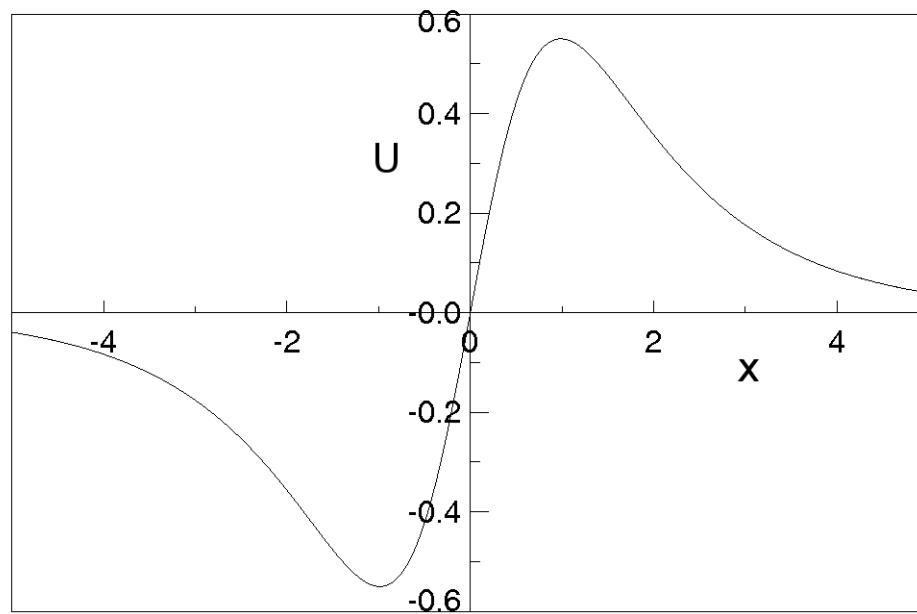


Figure 5.14: The transverse velocity is measured across the loop performing a sausage oscillation and plotted. It shows identical form as that demonstrated in figure 5.3 produced from an analytical investigation.

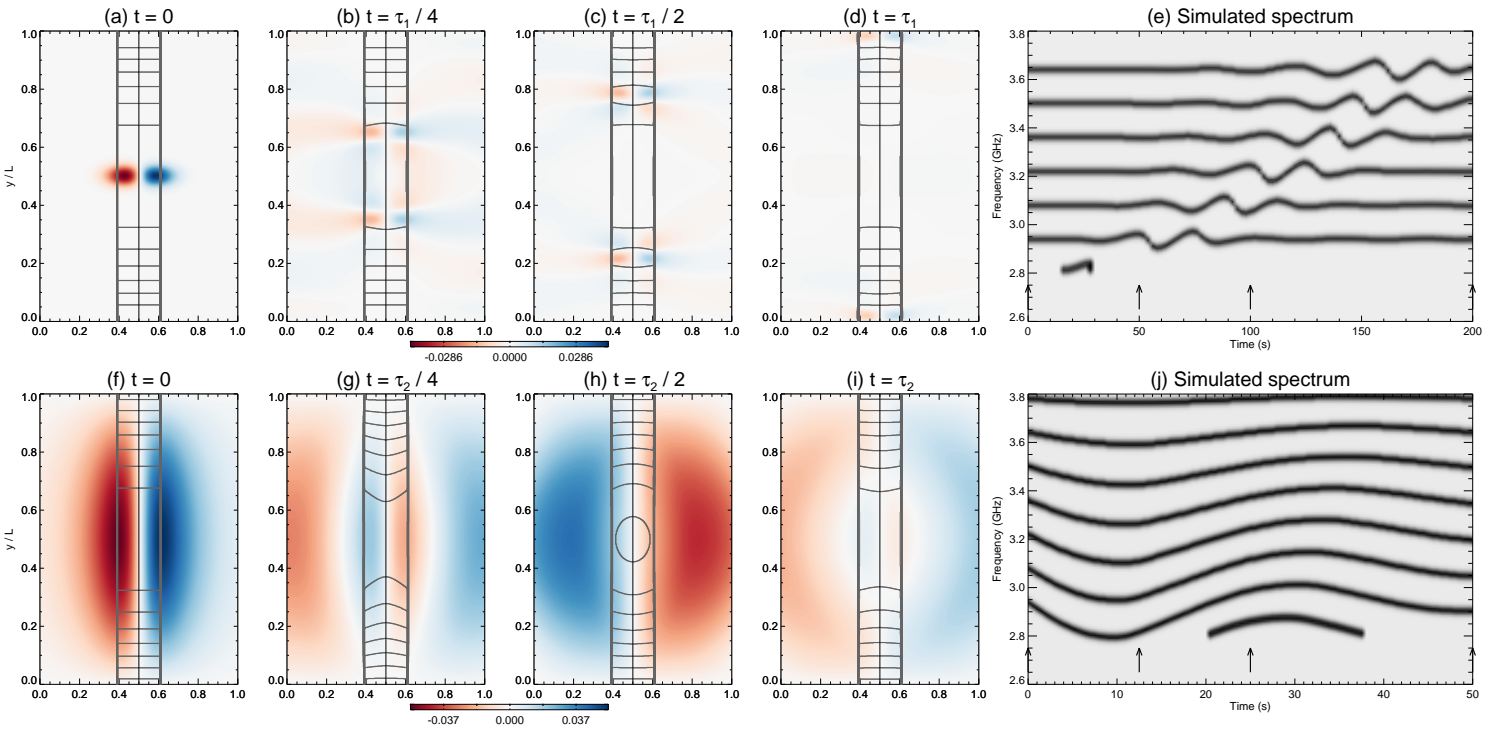


Figure 5.15: Snapshots of the evolutions of the pulses in the slab and the simulated spectrum with ZP structures of the fast-propagating mode (first row) and the fast-standing mode (second row). The  $x$ -component of velocity  $V_x$  is shown at times of  $0, \frac{1}{4}, \frac{1}{2}, 1$  of the simulation runtimes. The simulation runtimes  $\tau_1$  and  $\tau_2$  for each wave were 20 s and 5 s respectively. The grey contours in the snapshots show the position of the resonance levels.

Model	Section	ZP Emission Heights (normalised)	Frequency Range [GHz]
1D Static	5.3.1	0.01 – 0.05	3.0 – 3.5
2D Static	5.3.1	0.00 – 1.00	0.9 – 1.3
2D Dynamic	5.3.2	0.00 – 1.00	2.8 – 3.8
Analytical	5.2	0.00 – 1.00	0.0 – 1.7
[Chen et al., 2011]	n/a	0.80 – 1.07	1.0 – 1.5
[Yu et al., 2013]	n/a	(not known)	2.6 – 3.8

Table 5.2: A comparison of frequency and height results from the reproduction of ZPs using several techniques. All heights are normalised to the height of the loop apex of 75 Mm which corresponds to a loop of length 235 Mm, [Chen et al., 2011]. All simulations were carried out for the  $s = 1 - 50$  harmonics.

demonstrate a wiggle in the zebra pattern radio structure. The analytically derived dynamic spectra shown in figure 5.5 exhibits a normalised wiggle period of  $P_A = 1$ . The time domain is normalised to the period of the propagating velocity disturbance in (5.7). Based on [Roberts et al., 1984] a period of 1 s was chosen as the driving fast sausage mode wave period.

This results in the wiggle period,  $P_A$ , being  $P_A = 1$  s for the analytically derived zebra pattern. This one to one relation indicates that the fast wave acts as a direct driver of the ZP wiggles. Periodicity analysis of the simulated zebra pattern (figure 5.5) reveals that the wiggle periodicity for the simulations,  $P_N$ , are approximately  $P_N = 0.3$  s for both propagating and standing fast wave disturbances. This is the same order of magnitude as that found analytically with  $P_A \approx 3P_N$ . These periods also correspond to the periods observed experimentally for the ZP wiggles in [Yu et al., 2013, Section 3], which observed a period of 1 s in their periodicity analysis.

## 5.4 Conclusion

Using [Yu et al., 2013] as the motivation we investigated the link between ZP ‘wiggles’ (chapter 6) and propagating and standing fast modes in a coronal loop using analytical and numerical techniques. The results presented in this chapter clearly indicate that ZPs are strongly affected by the presence of magnetoacoustic waves, in particular the fast sausage mode. This link was first shown in the analytically derived ZP shown in section 5.2 where we derived the perturbed density and magnetic field for a fast mode in the loop context.

The ZP was constructed using the DPR mechanism and the analytically derived density and magnetic field perturbations. Figure 5.5 clearly shows the periodic

modification of the simulated zebra pattern in the presence of fast magnetoacoustic waves. This was an indication of the manifestation of the fast mode in the ZP emission region.

With this clear result we decided to underpin the result by carrying out the same investigation using numerical techniques. We approached the problem systematically by starting with a 1D static toy model (section 5.3.1). This proved useful as we were able to recreate the 1D results for the DPR emission mechanism presented in [Chernov, 2006]. An extended source region was observed for DPR emission, thus we have shown that numerical analysis could reproduce observational results with a relatively simple model. Moreover, we demonstrated that high frequency ZP may have a low-frequency counterpart that should be looked for in the data, e.g. obtained with LOFAR or spaceborne radiospectrometers.

A 2D study was the logical next step, which came with a higher degree of complexity in balancing magnetic and thermal pressures under magnetostatic equilibrium. We were successfully able to reconstruct a magnetic field which would maintain equilibrium from an input pressure distribution. The pressure distribution was converted to  $f_{pe}$  via (1.1), while the magnetic field was used to create the spacial structure of  $f_{ce}$  field via (1.2) for each  $s$  harmonic. The two spatial distributions were then cross-referenced for regions which satisfied the DPR conditions outlined by equations 5.26 and 5.27. The results showed an extended source region along the loop. ZP emission was found to be produced in the foot points and along the transverse slopes of the loop which was not observed by [Chen et al., 2011]. We speculate that radio emission from low altitude regions of the coronal loop may be reabsorbed before reaching an optically thin region. The frequency and spatial ranges of obtained simulated ZPs have been compared to [Chen et al., 2011] and [Yu et al., 2013] in table 5.2. The simple 1D static model seems to underestimate the maximum height of the ZP emission which implies that a 1D magnetic topology is not sufficient to capture the full extent of the ZP. ZP emission is seen along the entire length in all the 2D loop models. This implies the maximum emission height is limited by the loop length. If we take the loop value of 235 Mm from [Chen et al., 2011] we arrive at the same upper bound on heights where ZPs are created. The emission frequencies are scaled by electron density that has a fairly large range of values in coronal loops. We used an average value of  $10^{11} \text{ cm}^{-3}$  for our simulations, [Aschwanden, 2006], however this does leave some uncertainty in the frequency ranges.

Having successfully reproduced ZP emission regions and frequencies in a time independent system we moved to follow its evolution in the presence of magnetoa-



coustic fluctuations using a dynamic model. Section 5.3.2 successfully implements the use of Lare2D numerical MHD code to produce a stable 2D loop. A frame by frame approach allowed for the methodology from the section 5.3.1 to be used. A dynamic ZP spectrum was produced from the emission frequencies found using the DPR mechanism at each instant of time for both standing and propagating fast waves.

The resultant ZP by a visual inspection closely matched the observed wiggles in [Yu et al., 2013]. The standing mode produced a more closely matching spectra than propagating.

As a secondary check we compared analytical and numerical transverse velocity profiles, figures 5.3 and 5.14. They were in strong agreement concluding that both analytical and numerical studies yielded the manipulation of ZPs in the presence MHD disturbances such as the fast wave.

Finally we compared the oscillation periods of the reproduced ZP wiggles. We found that periodicity analysis of the simulated zebra pattern (figure 5.5) revealed that the wiggle period for the simulations was approximately  $P_N = 0.3$  s for both propagating and standing fast wave disturbances. This was the same order of magnitude as that found analytically in the previous chapter with  $P_A \approx 3P_N$  where  $P_A$  is the analytical period. These periods also correspond to the 1 s experimentally observed period for the ZP wiggles, [Yu et al., 2013].

So to conclude this chapter, we have successfully shown that a standing sausage magnetoacoustic oscillation in a coronal loop is most likely responsible for the wiggles found in ZP emission in [Yu et al., 2013]. We have confirmed this both numerically and analytically. However it is important to highlight that all the results presented in this chapter are model dependent, particularly the results outline in table 5.2. Many approximations have been made to the simulations due to the complex nature of coronal loop modelling. This was manifest by the variety of magnetic field and density profiles used. We have also not accounted for the change in plasma parameters seen in the chromosphere, instead only focusing on coronal values. Thus results pertaining to this region are not physically founded. The variety in the assumptions made in these models could provide an explanation for the diversity of model predictions shown in table 5.2. Which in turn is an indication that the modelling used in this thesis has not fully captured the complexity of a coronal loop. However, with new experimental techniques becoming available, a future avenue of work would be to reconcile these coronal and chromospheric models with newly available experimental data to gain a better understanding of loop geometry and ZP themselves.

Importantly, we have shown that both loop geometry and wave propagation have an equal part to play in ZP evolution. We can consider these results as a good starting point to explore more detailed and realistic simulations in the future which can then be compared to new experimental observations.

## Chapter 6

# Zebra Patterns II: Observational Work

### 6.1 Introduction

Quasi-periodic pulsations (QPP) discussed in section 2.5.2 are a common feature of solar flares (section 2.5). QPP are observed in a vast energy range from radio to hard X-ray and gamma-ray bands (see [Nakariakov and Melnikov, 2009a, Nakariakov et al., 2010, Tan et al., 2010] for recent reviews). Typically, QPP appear as a pronounced oscillatory patterns in the intensity of the radiation, with the typical periods ranging from a fraction of a second to several minutes, see figure 2.14. QPP have been found as oscillations of the Doppler shift of the emission lines associated with the hot plasma in flaring sites [Mariska, 2006] or its density [Kim et al., 2012].

QPP events are often found to contain zebra pattern (ZP) structures as those discussed in Chapter 5. Analysis of ZPs indicated the occasional presence of periodic variation within the ZP itself. In particular, [Chernov et al., 2005] found that the intensity of ZP stripes observed on 21/04/2002 pulsated quasi-periodically. The ZP stripes consisted of separate short-duration pulses with the period of about 30 ms. Pulsations of the intensity in the adjacent stripes were found to be similar. The detected periodicity was associated with the oscillatory non-linear interaction of whistlers with ion-sound and Langmuir waves.

In this Chapter we focus on another, less studied type of ZP modulation: the quasi-coherent oscillating drift of spectral stripes known as ‘wiggles’. We have already discussed its possible generation mechanism in depth in Chapter 5 using analytical and numerical techniques. We will present the results published in [Yu, Nakariakov, Selzer, Tan, and Yan, 2013] which were carried out as a collaboration

work into the observation of ZP wiggles.

Generally, the periods detected in ZP wiggles coincide, by the order of magnitude, with the transverse fast magnetoacoustic (or Alfvén) crossing time in a typical loop of a coronal active region [De Moortel and Nakariakov, 2012] as discussed in Chapter 5. Thus, it is natural to expect that the periodicity may be associated with either an impulsively-generated fast magnetoacoustic wave train [Roberts et al., 1984, Nakariakov et al., 2004] or with a standing sausage mode of a fast magnetoacoustic resonator [Kopylova et al., 2007, Zaitsev and Stepanov, 2008, Nakariakov et al., 2012], or result from a passage of a perpendicular fast wave through a randomly-structured coronal plasma [Nakariakov et al., 2005]. An improved understanding of these events will provide us with unique information about fine, sub-resolution structuring of coronal plasmas. It is difficult for these studies to be carried out at other wavelengths due to a insufficient time resolution in observational instruments.

## 6.2 Radio Data

Our data consisted of dynamic radio spectrograms observed and calibrated by the ground-based Chinese Solar Broadband Radio Spectrometer, Huairou (detailed in section 3.4.1). The data has already been processed to remove any instrument noise or Earth based artefacts by the instrumental team.

We focused on a flare that occurred on 03/12/2006. A typical two-ribbon flare in the NOAA active region 10930 located on the disk (S05W33), [Isobe et al., 2007, Yan et al., 2007]. This flare was also observed by the Nobeyama Radioheliograph. Thirteen ZPs were observed by SBRS/Huairou at 2.6 – 3.8 GHz during the flaring process in this event [Yu et al., 2012].

We focused on the time interval 02:40-03:05 UT after the soft X-ray maximum. Two long lasting zebra pattern structures were obtained at 02:43:00-02:43:20 UT (ZP1) and 03:03:00-03:03:20 UT (ZP2), respectively, which were considered to be associated with quasi-periodic oscillations.

We cross-referenced the ZP radio signal with both SOHO and NoRH (see Chapter 3 for details on the instrumentation) in an attempt to confirm the signal was solar in origin. The left panel in Figure 6.1 shows the full disk EUV image at 195 Å obtained by Extreme-ultraviolet Imaging Telescope [Delaboudinière et al., 1995, EIT] onboard *SOHO* during the decay phase, with inset of the *TRACE* [Handy et al., 1999] image at 195 Å showing the post-flare loop arcade with explosive features at the time of ZP2. The right panel shows the NoRH 17 GHz full disk intensity image,

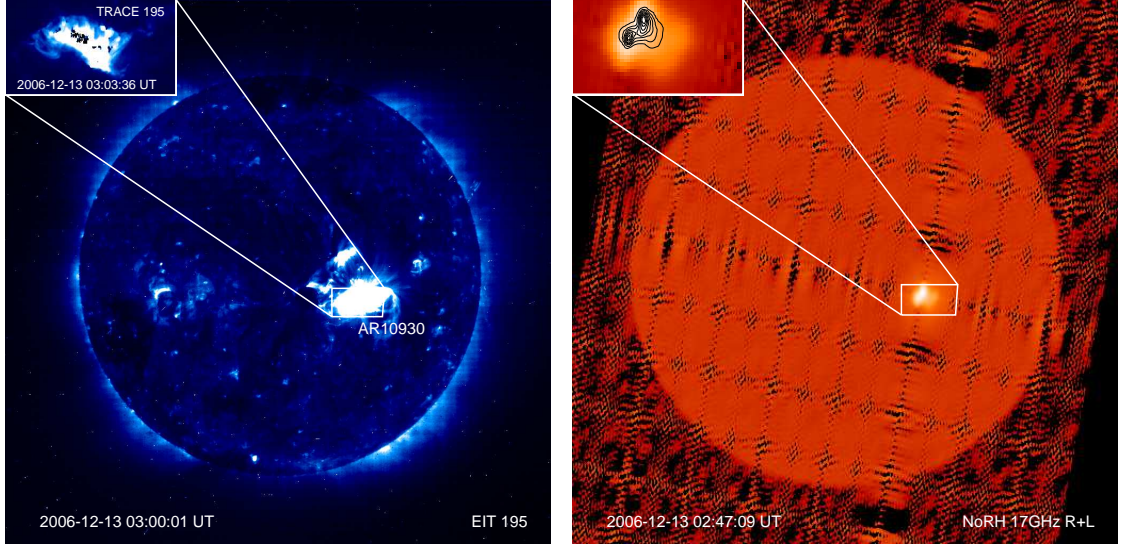


Figure 6.1: Full disk *SOHO/EIT* 195 Å at 03:00:01 UT and NoRH 17 GHz intensity images at 02:47:09 UT on 13/12/2006. Insets show the *TRACE* 195 Å image and the enlarged NoRH 17 GHz image of AR 10930, from [Yu et al., 2013].

and inset of the enlarged 17 GHz image superposed with 34 GHz image. The source region of radio emission at 17 GHz has approximately the same position as the EUV arcade structure in flare region during the decay phase, with the maximum situated in the northeast of the arcade, between the opposite footpoints of 34 GHz radio sources. The spatial separation of the footpoints is about 50 arcsec. The NoRH 17 GHz full disk image shows the AR 10930 is the unique strong radio emission source on the solar disk in this flare event, confirming that the radiation of the ZPs comes from the flare core region.

### 6.3 Zebra Pattern Wiggles

The extended duration ( $t > 15$  s) of the two ZP structures ZP1 and ZP2 made it possible to study the long-term QPP in the solar corona. To analyse the QPP oscillations in ZP structures, we extracted the ZP stripes from background emission in the raw microwave spectrogram, with the intent to study frequency variation of individual stripes  $f_N$ , where  $N = 1, 2, 3, 4, \dots$ , note here  $N$  is not the ZP harmonic number  $s$  discussed in section 2.5.4 but  $N = s + \alpha$ , where  $\alpha$  is some integer value corresponding to  $s$  at the first observable harmonic of the ZP. The microwave dynamic spectrograms of ZP1 and ZP2 in left-handed circular polarization (LHCP) are shown in figures 6.3(a, b). The right-handed circular polarization (RHCP) compo-

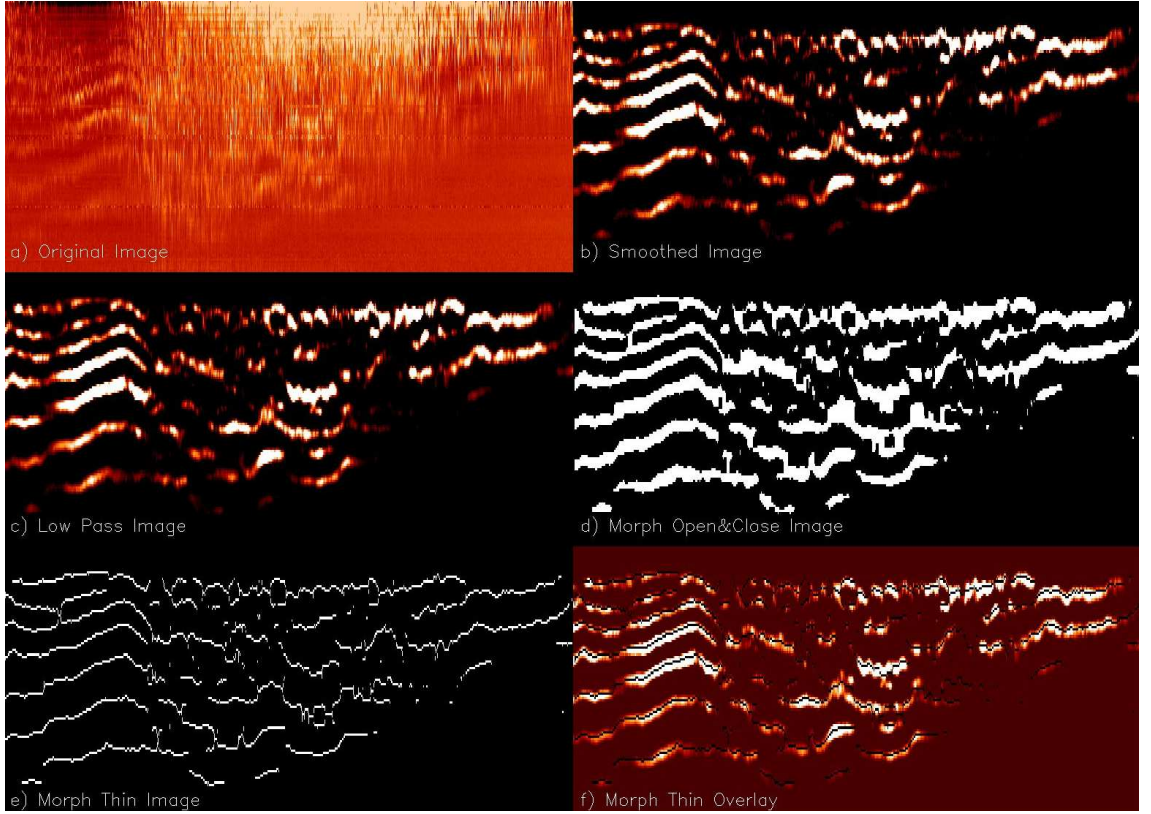


Figure 6.2: The various image processing techniques used in the extraction of ZP stripe data. In image: a) the original image is displayed; b) the trend has been removed; c) a low pass filter was applied; d) a threshold filter was applied; e) the image was thinned to stripes and f) the final stripe locations are plotted over b).

nents are not used for data processing here due to large saturation in low frequency range ( $< 2.9$  GHz).

### 6.3.1 ZP Image Processing

The extraction of individual ZP stripes from the dynamic spectra required several image processing techniques. The end goal was to obtain the variation of a ZP stripe as a function of frequency and time. This enabled us to carry out periodicity analysis to study ZP wiggles directly.

### 6.3.2 Large Scale Trend Removal

The raw dynamic spectrograms are noisy and prove difficult when extracting ZP stripes, such as our example ZP, figure 6.2(a). Therefore the images required several layers of filtering to purify the data. The first of these was an overall trend removal.



The ZP emission is observed with a background continuum emission superimposed. This varies with time as discussed in section 2.5.4. The first step was to remove these trends from our ZPs.

The trend removal process takes place on a slice by slice basis, i.e. the dynamic spectrogram is divided into the static spectra which were originally used to construct the image. Each spectra or slice is a function of intensity against frequency. The slices are then smoothed over a large window of the data usually a fifth of the overall number of frequencies. This smoothed trend was then subtracted from the original data to emphasise small scale variations such as ZP frequency modulation. The result is shown in figure 6.2(b). After this procedure the stripes appear more pronounced and defined, which greatly reduced errors in the stripe extraction process.

### 6.3.3 Low Pass Filter

Figure 6.2(b) still presented some trouble with high frequency noise. To reduce this the image was convoluted using a low pass filter kernel:

$$K = \begin{bmatrix} 0.11 & 0.11 & 0.11 \\ 0.11 & 0.11 & 0.11 \\ 0.11 & 0.11 & 0.11 \end{bmatrix}. \quad (6.1)$$

Convolution is a general process that can be used for various types of smoothing, signal processing, shifting, differentiation, edge detection, etc. [Scargle, 1982]. The kernel is multiplied to each element of the ZP image, 6.2(b). The intent of this process was to smooth small scale structuring so that the essential stripe skeleton could be isolated. The results are shown in figure 6.2(c).

### 6.3.4 Threshold Filter

A threshold filter was applied to make data processing easier as a binary image made stripe detection analysis more efficient. An optimum threshold value was decided, following this every data element below the threshold was set to zero while every data element equal to or above was set to one. The output was a binary version of the ZP spectra shown in figure 6.2(d).

The binary image was then passed to a ‘Morph Thin’ filter. The Morph Thin function performs a thinning operation on binary images. The thinning operator is implemented by first applying a hit or miss operator to the original image with a pair of structuring elements, and then subtracting the result from the original image.

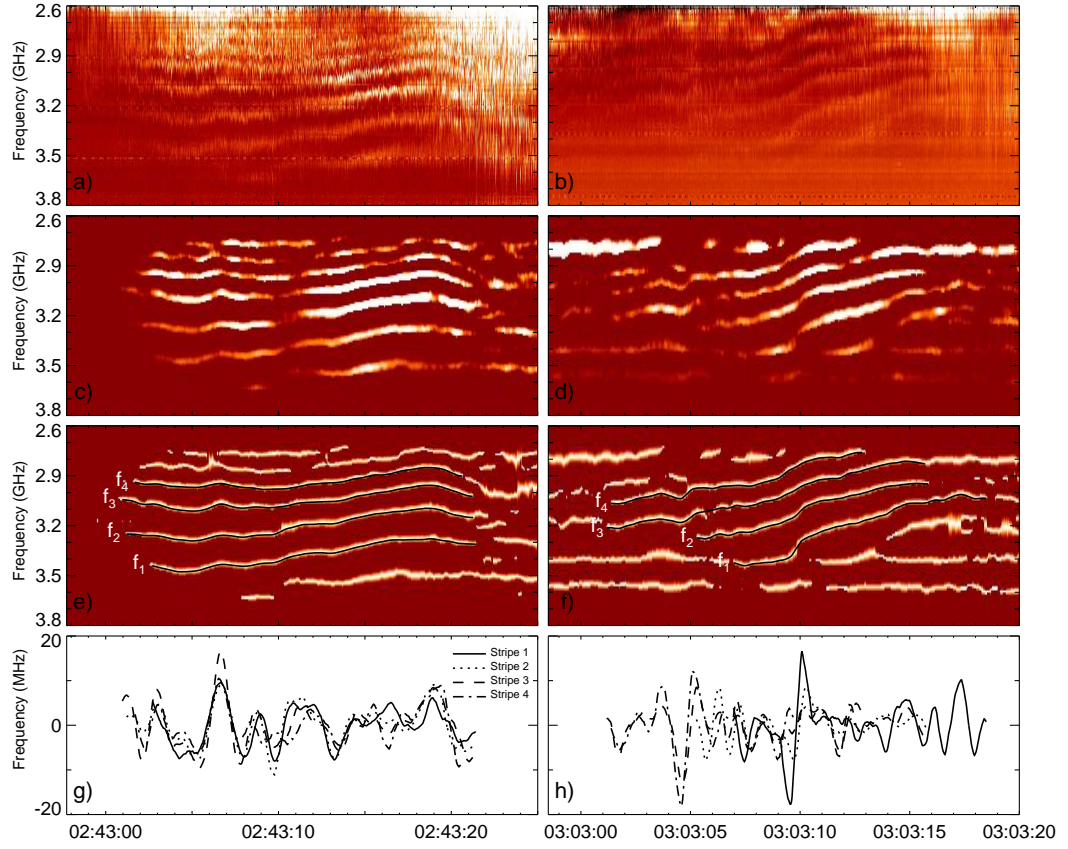


Figure 6.3: Zebra pattern structures on 13 December 2006 02:43:00-02:43:25 UT and 03:03:00-03:03:20 UT observed by *SBR/Suairou* at 2.6-3.8 GHz, and the illustration of the processes of extracting the zebra pattern stripes. a,b) The raw spectrograms at 2.6-3.8GHz on LHCP; c,d) high contrast images; e,f) the rescaled images with the extracted stripes superimposed; (g, h) the de-trended stripes frequency  $f_N$ , from [Yu et al., 2013].

Its purpose was to transform the binary image to a series of candidate-stripes which can be extracted for analysis. The result of this process is shown in 6.2(e).

## 6.4 Data Series Extraction

The aim of this investigation was to test the frequency modulation of ZP stripes, to do this we required a time series  $f_N = f_N(\nu, t)$  where  $\nu$  is the channel frequency, for each stripe  $N$ . Image processing was carried out on ZP1 and ZP2 after a successful cleaning algorithm had been established in section 6.3.1. Each ZP underwent the same analysis to extract the candidate-stripes. We began by fitting a Gaussian to the frequency profile of each candidate-stripe and then normalised the Gaussians



to their amplitudes, so that the brightness of stripes was uniform. This procedure removed the information about the amplitude modulation of the signal, however it emphasised the frequency modulation. The centres of the Gaussian peaks gave us the instant radio-frequency  $\nu$  of the stripes.

We then progressed to manually identify and track the frequency data of several of the longest stripes. The variation of the centres of the best-fitted Gaussians in time allowed us to obtain the ‘skeletons’,  $f_N(t)$  of the frequency modulation for the individual spectral stripes in the analysed ZPs. Note that here  $N$  denotes the  $N$ -th extracted stripe enumerated from the highest to lowest observed frequency in the spectrogram. Also, we were able to study the time variation of the stripe difference by  $\Delta f_N = f_{N+1} - f_N$  between the neighbouring stripes. Figures 6.3(e-f) show the rescaled Gaussian image superimposed with the spectral skeletons of the four stripes of highest frequencies. Note that as the third extracted stripe in ZP2 was seen to be gapped in the raw spectrogram 6.3(b) and the high contrast image 6.3(d) at 03:03:05 - 03:03:06 UT, so we connected the two segments with a straight line to produce a continuous stripe.

## 6.5 Periodicity Analysis

In the sections above we successfully obtained a data set of stripes for both ZP1 and ZP2 with the stripe data  $f_N(\nu, t)$  extracted for ( $N = 1, 2, 3, 4$ ) as shown in figures 6.3(g,h). We progressed the analysis by deploying periodicity analysis techniques, some of which were previously used in section 4.3.

### 6.5.1 Auto-Correlation

The time profiles of  $f_N$  were first smoothed by 30 points (0.24s) to remove high-frequency noise, and then de-trended by subtracting  $f_N$  smoothed with a 100 points (0.8s) using the boxcar technique. The  $f_N$  stripes were then autocorrelated to shown any regular periodicity. The four auto-correlation functions shown in figure 6.4(b) and figure 6.5(b) displayed very clear in-phase periodic behaviour over several periods. There were two well-pronounced periodicities observed, ( $P_1 \sim 1.43$ s and  $P_2 \sim 0.83$ s).  $P_1$  was apparent in all stripes, while  $P_2$  was only present in  $f_3$  and  $f_4$ .

The auto-correlation functions of the de-trended  $\Delta f_N$  in figure 6.4(d) and 6.5(d) show pronounced periodic oscillatory patterns. Frequency modulation in both stripe position  $f_N$  and separation  $\Delta f_N$  in conjunction with the DPR mechanism infers oscillations in both magnetic field and electron density. This in turn indicates the presence of MHD fluctuations.

### 6.5.2 Periodogram

We implemented the periodogram procedure to confirm the appearance of the observed periodicities in the autocorrelation while simultaneously insuring that the periodicities are not artificial due to smoothing.

#### Lomb-Scargle Periodogram

The Lomb-Scargle periodogram is a widely used tool in period searches and frequency analysis of time series, [Scargle, 1982]. It fits the data with a harmonic oscillation in the form:

$$y = a \cos \omega t + b \sin \omega t + c, \quad (6.2)$$

where  $a, b$  and  $c$  are fitting parameters. Standard fitting procedures require the solution of a set of linear equations for each sample frequency. The Lomb-Scargle periodogram, for a time series  $(t_i, y_i)$  with a zero mean ( $\bar{y} = 0$ ) in its simplest form is given by:

$$\hat{p}(\omega) = \frac{1}{\sum_i y_i^2} \left\{ \frac{[\sum_i y_i \cos \omega(t_i - \hat{\tau})]^2}{\sum_i y_i \cos^2 \omega(t_i - \hat{\tau})} + \frac{[\sum_i y_i \sin \omega(t_i - \hat{\tau})]^2}{\sum_i y_i \sin^2 \omega(t_i - \hat{\tau})} \right\}, \quad (6.3)$$

where the  $\hat{\tau}$  parameter is calculated via:

$$\tan 2\omega\hat{\tau} = \frac{\sum_i \sin 2\omega t_i}{\sum_i \cos 2\omega t_i}. \quad (6.4)$$

There are shortcomings to the Lomb-Scargle periodogram as it does not take measurement errors into account. This was solved by introducing weighted sums by [Gilliland and Baliunas, 1987] and [Irwin et al., 1989] equivalent to the generalisation to a  $\chi^2$  fit.

### Results

The presence of structured, periodic components in the two ZP structures was confirmed by periodogram and autocorrelation analyses of time profiles  $f_N$  and  $\Delta f_N$  of the extracted stripes ( $N = 1, 2, 3, 4$ ), which are shown in Figures 6.4-6.5.

Figure 6.4(a) presents the periodograms of the time profiles of  $f_N$  of four extracted stripes in ZP1 with large-scale trend removed. There are two well-pronounced spectral peaks in the vicinities of 0.70 and 1.20 Hz ( $P_1 \sim 1.43$  s and  $P_2 \sim 0.83$  s) which are seen in all four stripes. Figure 6.4(c) presents the periodograms of time

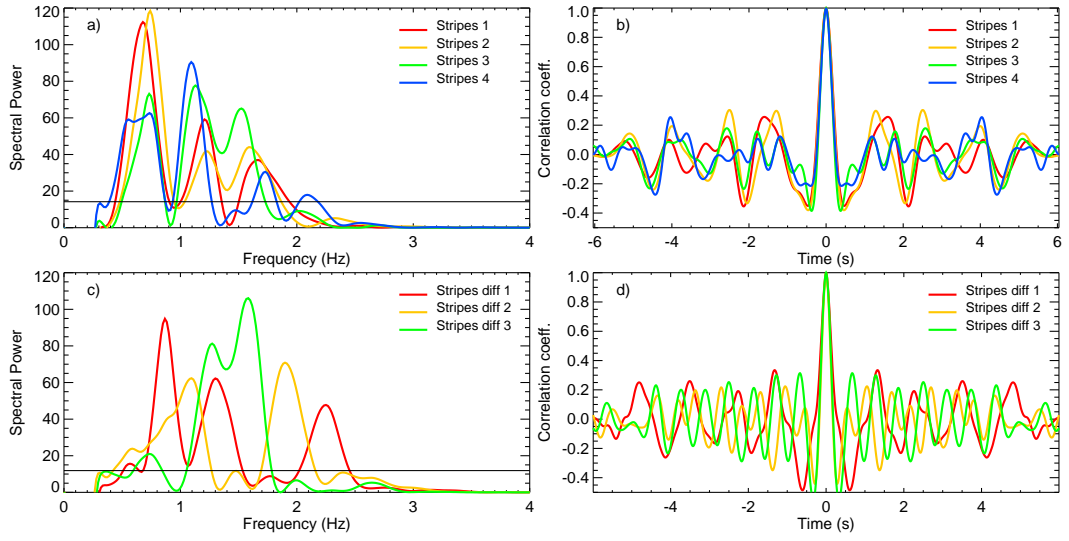


Figure 6.4: Periodograms and auto-correlation functions of QPP components of a,b) stripe frequency  $f_N$  and c,d) frequency separation  $\Delta f_N$  in the ZP structure (ZP1) recorded on 13 December 2006, 02:43:00-02:43:25 UT: red line for  $f_1$ , yellow line for  $f_2$ , green line for  $f_3$ , blue line for  $f_4$ . The horizontal line in periodograms indicates the 99.99% confidence level for the highest spectral peak, calculated using the Fisher randomisation test detailed in section 6.5.2. The confidence levels for each trace were tightly packed in the power range therefore a representative level was plotted. Figure taken from [Yu et al., 2013].

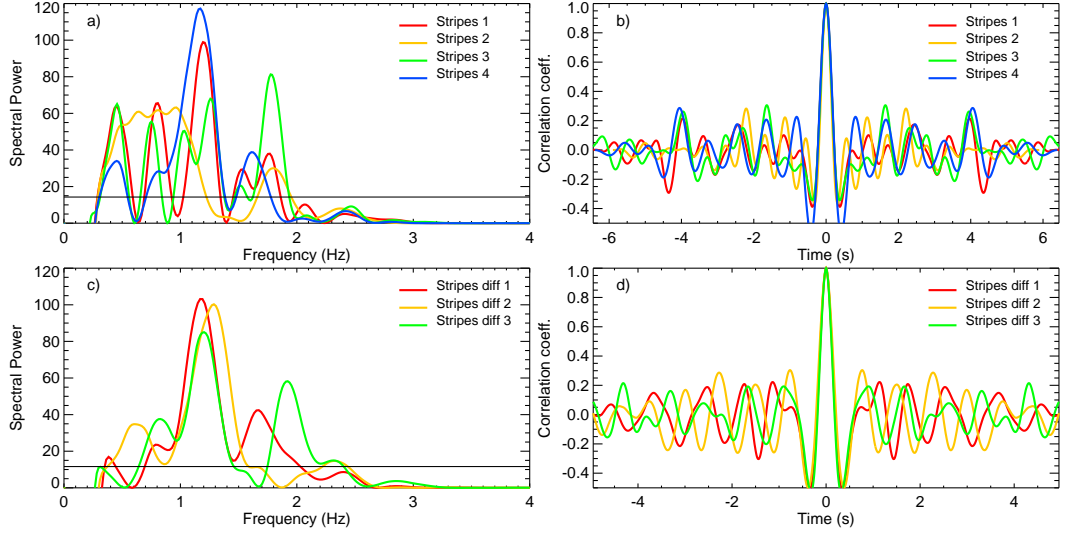


Figure 6.5: Periodograms and auto-correlation functions of QPP components of a,b) stripe frequency  $f_N$  and c,d) frequency separation  $\Delta f_N$  in the ZP structure (ZP2) recorded on 13 December 2006, 03:03:00-03:03:20 UT: red line for  $f_1$ , yellow line for  $f_2$ , green line for  $f_3$ , blue line for  $f_4$ . The horizontal line in periodograms indicates the 99.99% confidence level calculated using the Fisher randomisation test detailed in section 6.5.2. Figure taken from [Yu et al., 2013].

profiles of de-trended  $\Delta f_N$ . The three profiles of  $\Delta f_N$  show different periodicity behaviours with three dominant peaks in the vicinities of 0.86, 1.58 and 1.90 Hz (1.16, 0.63 and 0.53 s) separately.

Figure 6.5(a) shows the periodograms of the de-trended time profiles of  $f_N$  of the four extracted stripes in ZP2. Two pronounced common peaks are seen in the vicinities of 1.20 and 1.70 Hz ( $P_2 \sim 0.83$  s and  $P_3 \sim 0.59$  s). The periodicity of  $P_2$  is not detected in the de-trended time profile of  $f_2$ . The auto-correlation functions of the de-trended time profiles of  $f_N$  all have pronounced oscillatory patterns over several periods (figure 6.5(b)). Periods  $P_2$  and  $P_3$  are both found to be present in the auto-correlation function of  $f_1$ ,  $f_3$  and  $f_4$ . Figure 6.5(c) presents the periodograms of time profiles of de-trended  $\Delta f_N$ , showing a obvious peak at 1.20 Hz ( $P_2 \sim 0.83$  s). The auto-correlation functions in Figure 6.5(d) present a similar periodicity for all the three  $\Delta f_N$ .

We calculated the periodograms of the time profiles of  $f_N$  corresponding to a set of noise-removing boxcars (10, 20, 30 points) and trend-removing boxcars (60, 70, 80, 100 points). The positions of the pronounced spectral peaks do not show any dependence on the smoothing width, implying that these spectral peaks are real and have not resulted from smoothing. The periods corresponding to the highest peaks

of each curve revealed in Figures 6.4-6.5 are strongly significant in the periodograms as they are all above the 99.99% confidence level from Fisher randomisation analysis, section 6.5.2.

### Fisher Randomisation Test

The observed wiggles only last for 5-7 periods, hence it is important to test the validity of the spectral properties observed in the periodogram technique. We implemented the Fisher randomization analysis outlined in [Linnell Nemec and Nemec, 1985]. The basic principle involves multiple random rearrangements of the time series in the time domain. The assumption is that in a non-periodic time signal the measured values are independent of the observation time. A maximum spectral peak of a periodic fluctuation will vanish under the reordering while a non-periodic signal will be invariant. A series of  $n!$  permutations of the original data set are constructed as the number of occurrences,  $l$  of the the spectral peak in question are recorded. The ratio of  $l/n!$  gives the probability that no periodic component is present. Hence the probability of a spectral peak corresponds to a true periodicity in the periodogram is given by:

$$P = 1 - \frac{l}{n!}, \quad (6.5)$$

where  $P$  is the Fisher randomisation periodic signal probability. In practice, the  $P$  is only calculated for a random sample of  $m$  permutations out of  $n!$ , due to the large value of  $n!$ . Here we calculate the peak power for 200 iterations and it turns out that all wiggle spectral peaks give probabilities  $> 99.99\%$  which result in confidence that the stripes exhibit truly oscillatory behaviour.

## 6.6 Discussion

ZP1 and ZP2 spectrogram images were successfully cleaned using image processing techniques outlined in section 6.3.1. The stripes were subsequently extracted using the techniques outlined in section 6.4 to provide a data set of  $f_N(\nu, t)$  and  $\Delta f_N(\nu, t)$  displayed in figures 6.3(g,h).

Periodicity analysis carried out on  $f_N$  and  $\Delta f_N$  (section 6.5) of the fine spectral structure of individual stripes in two microwave ZP observed with SBRS/Huairou revealed that radio frequencies of the stripes performed quasi-periodic oscillations (wiggling) with a periodicity ranging from 0.5 s to 1.5 s. Simultaneously, the oscillations were found to have two to three significant periodicities. Similar periodicities

were detected in the spectral difference of neighbouring ZP stripes,  $\Delta f_N$ . The frequency variation amplitude was approximately 20 MHz, giving a relative amplitude of 0.7 %. The wiggling periods and amplitudes observed were consistent with the previous investigations into this effect, [Chernov et al., 1998, Ning et al., 2000, Chernov et al., 2001]. The wiggling of neighbouring stripes were found to be almost in phase. The detected periods were of the order of the fast magnetoacoustic (section 1.6.1) transverse time in a typical active region loop (for typical spatial scale of 1 Mm and Alfvén speed of 1 Mms<sup>-1</sup>).

These values of periodicity correspond closely with the numerical and analytical results found in Chapter 5 table 5.2. However if the oscillations were in fact caused by a propagating magnetoacoustic wave as discussed in Chapter 5, neighbouring ZP stripes, separated by several Mm, would be positioned at different phases of the perturbation. Hence, neighbouring ZP stripes would wiggle with a significant phase difference, this was not found in our analysis. As a result, we rule out the interpretation of the ZP wiggling in terms of propagating waves. Instead, we considered a global standing mode in which the coronal loop oscillates in phase. In a non-uniform, field aligned plasma structure the transverse size determines the periodicity of the global sausage mode, [Kopylova et al., 2007, Nakariakov et al., 2012]. As the periods of the detected oscillations were on the order of 1 s, we obtain that the required spatial size of the waveguiding plasma non-uniformity with the estimated value of the Alfvén speed is about 1 Mm. This value is a typical minor radius of an active region loop. Consequently, the systematic lack of a significant phase shift between oscillations of different stripes, coming from several different spatial locations in the DPR mechanism, indicates that the MHD oscillation is most likely to be standing.

All of the above suggests that the detected ZP wiggles were caused by a standing sausage oscillation. This conclusion is supported by the finding that both instant frequencies of individual stripes and their spectral separation oscillate with the same periods. Thus it is consistent with a sausage oscillation that perturb both the plasma density and magnetic field [Nakariakov et al., 2012]. These results are further underpinned by the results derived in Chapter 5 in which a standing sausage mode was shown to analytically and numerically produce a wiggle periodicity of approximately 1 s.

## Chapter 7

# Summary and Discussion

In this thesis two vastly different space plasmas were investigated, the terrestrial foreshock and the solar corona. We began with an introduction into plasma theory, instrumentation and plasma environments which spanned chapters 1 to 3, providing a grounding for the following research chapters. In chapter 4 an observational study was carried out into the interaction between the solar wind and the Earth's magnetic field and bow shock. The nature of the chapters 5 and 6 shifted to analysis of radio fine structure emitted from the solar corona. In chapter 5 zebra pattern emission was investigated using simulations and analytical techniques while in chapter 6 we proceeded to explore observational evidence for the results derived in the previous chapter. These studies were motivated by growing interest in the respective fields accompanied by newly available data. Here we summarise each study by chapter and describe its contribution to plasma physics.

In Chapter 4 we implemented the theoretical constructs outlined in Chapter 1 in an observational study of seven intervals of Cluster solar wind data. These intervals were selected as periods when the Cluster satellite group was directly observing the terrestrial foreshock. Wave modes in the frequency range (0.03-0.06 Hz) were successfully identified in each interval using a variety of data analysis procedures. The observed fluctuations agreed with previous results in the identification of ULF waves in the terrestrial foreshock. We identified individual circularly polarised waves using the hodogram technique. A difficulty arose in distinguishing between spacecraft polarisation and intrinsic wave polarisation. The supersonic nature of the solar wind caused the observed waves to undergo an apparent polarisation reversal. The solution was to implement multi-spacecraft delay analysis to estimate wave direction. This, in conjunction with the hodogram technique allowed us to successfully identify the intrinsic polarisation of the ULF wave intervals. The waves

were subsequently labelled left- and right-handed depending on the intrinsic wave polarisation.

A technique to investigate the compressibility directly from magnetic field measurements was developed and implemented. Increased compressibility above background turbulence levels was observed in the presence of the ULF waves. This provided further evidence for the magnetoacoustic nature of ULF waves as observed in other publications. The novel step was to investigate the contrasting effect of different polarisations on the solar wind anisotropy using quasilinear plasma theory. Specific attention was paid to the instability mechanisms engaged by the ULF waves. The  $(\beta_{\parallel}, T_{\parallel}/T_{\perp})$  parametric space was used to investigate subtle changes in plasma stability conditions between the two polarisations. A clear divide was observed between left- and right-handed polarisation intervals. The results indicated a correlation between higher plasma temperatures in the presence of right handed waves while the plasma was in proximity to the firehose marginal stability threshold on the  $(\beta_{\parallel}, T_{\parallel}/T_{\perp})$  plane. In turn, higher plasma temperatures were demonstrated by the left handed waves close to the proton cyclotron instability threshold. Correlations are not synonymous with causality and, given the complexity of plasma dynamics in the foreshock region, the interpretations of these results are difficult. Using the WIND spacecraft data to monitor the upstream conditions it was possible to demonstrate that the temperature anisotropy was not modified until reaching the foreshock region. The enhancement in the total temperature correlates well with the factor 2 – 3 increase in  $T_{\parallel}$  observed in LH and RH intervals. The results suggest that the power in ULF waves also strongly correlated with the observed anisotropy in the foreshock, at least for the right-hand polarised waves.

The results obtained in Chapter 4 relate directly to a correlation between elevated temperatures and temperature anisotropy in the terrestrial foreshock. The impact of these results could also relate to studies of the solar wind plasma, where similar correlations have also been observed. The Landau damping of ULF waves, identified as a possible driving mechanism for the fire hose instability, may also be important in solar wind turbulence, where oblique fast magneto-acoustic waves of low frequency are believed to be present such as the quasi parallel shocks observed in CMEs.

In Chapter 5 we change tack and move to investigate the interaction of MHD waves in flaring coronal loops however still following the overarching concept of plasma modification due to collective plasma behaviours. The motivation arose due new results presented in the field of zebra pattern (ZP), in particular the interaction between the DPR mechanism and MHD waves. We investigated the link between



ZP ‘wiggles’ and fast magnetoacoustic modes in a coronal loop using analytical and numerical techniques.

Initially we used analytical techniques to derive the presence of a ZP in a static 1D system. The ZP was reconstructed using the DPR mechanism in conjunction with the analytically derived density stratification. After successfully constructing the ZP structure using a 1D theoretical model we perturbed the system to induce magnetoacoustic oscillations. The dynamic radio spectrum was artificially reconstructed using the frequencies predicted by the model. As a result we were able to successfully reproduce observations of ZP wiggling using a purely analytical approach. This underpinned the hypothesis that fast magnetoacoustic waves do affect the ZP emission structure through modification of the DPR levels.

After this clear result, we progressed to strengthen the hypothesis by carrying out the same investigation but instead using numerical techniques. We approached the problem systematically by starting with a 1D static toy model. This proved useful as we were able to reproduce previous 1D analytical results for the observed frequencies. However, the simple 1D static model seemed to underestimate the maximum height of the spatial localisation of ZP emission, implying that a 1D model was not sufficient to capture the full spatial extent of the ZP.

Thus we extended to a 2D static study which came with a higher degree of complexity in balancing magnetic and thermal pressures under magnetostatic equilibrium. We were successfully able to reconstruct the magnetic field from an input pressure structure. The results showed an extended source region which stretched along the loop. This implies the maximum emission height is limited by the loop length. In particular if we take the loop value of 235 Mm we arrive at the same upper bound on spatial heights as found in literature. The emission frequencies are scaled by electron density which has a fairly large range of values in coronal loops. ZP emission was also found to be produced in the footpoints of the loop which was not observed in literature. We speculate that radio emission from the footpoints may be reabsorbed before reaching an optically thin region. Alternatively there is a secondary process inhibiting the plasma from engaging the DPR mechanism.

The reproduction of ZP emission regions and frequencies in a static system provided the starting point for a time dependent model which could follow the ZP evolution in the presence of MHD fluctuations. The Lare2D numerical MHD code was implemented to produce a stable 2D loop. Standing and propagating fast waves were triggered by inducing MHD pulses at the loop apex. The dynamic radio spectrum was reproduced using a frame by frame approach to visualise the emission frequencies found accounting for the DPR mechanism, as a result the synthesised

ZP were found to closely match the observed wiggles.

Finally we compared the oscillation periods of the reproduced ZP wiggles. We found that the periodicity analysis of the simulated zebra pattern revealed that the wiggle period for the simulations was approximately  $P_N = 0.3$  s for both propagating and standing fast wave disturbances. This was the same order of magnitude as that found analytically,  $P_A$ , with  $P_A \approx 3P_N$ . These periods also correspond to the 1 s experimentally observed period for the ZP wiggles.

In Chapter 6 we present the collaboration work carried out into the observation of ZP wiggles using the Chinese Solar Broadband Radio Spectrometer (SBRS/Huairou). Two ZP found in a QPP flare event were identified to contain ZP wiggles, labelled ZP1 and ZP2 respectively. ZP1 and ZP2 spectrogram images were successfully cleaned by sequentially using several image processing techniques. The stripes were subsequently extracted from the images to provide a data set of the central stripe frequency as a function of time.

Analysis on well-pronounced fine spectral structure of individual stripes in both ZP1 and ZP2 revealed strong periodicity. Studies showed that the ZP stripes performed quasi-periodic oscillations (wiggling) with a periodicity ranging from 0.5 s to 1.5 s in the frequency domain. Similar periodicities were detected in the spectral difference of neighbouring ZP stripes. The frequency variation amplitude was approximately 20 MHz, giving a relative amplitude of 0.7 %. The wiggling periods and amplitudes observed were consistent with the previous investigations into this effect. Wiggling of neighbouring stripes were found to be almost in phase. The detected periods were of the order of the fast magnetoacoustic transverse time in a typical active region loop (for typical spatial scale of 1 Mm and Alfvén speed of  $1 \text{ Mms}^{-1}$ ).

The periodicity observed in the data closely matches that found in both numerical and analytical studies described in Chapter 5. If the oscillations were instead caused by a propagating magnetoacoustic wave as discussed in Chapter 5, neighbouring ZP stripes, separated by several Mm, would present a different phase of the perturbation than their neighbouring stripes. This was not observed in the periodicity analysis. Hence, we ruled out the interpretation of the ZP wiggling in terms of propagating waves. Instead, we considered a global standing mode in which the whole coronal loop oscillates in phase. In a non-uniform, field aligned plasma structure the transverse size determines the periodicity of the global sausage mode. As the periods of the detected oscillations were on the order of 1 s, we obtained that the required spatial size of the wave guiding plasma non-uniformity with the estimated value of the Alfvén speed is about 1 Mm. This value is a typical minor

radius of an active region loop. Consequently, the distinct lack of a significant phase shift between oscillations of different stripes, coming from several different spatial locations in the DPR mechanism, indicates that the MHD oscillation is most likely to be standing.

Overall this thesis has successfully employed various signal analysis techniques to extract observational results. Theoretical techniques in both kinetic plasma physics and MHD were used in parallel to explain and reproduce experimental results. The collective behaviours of space plasmas such as the terrestrial foreshock and solar corona have made it possible to use analytical tools to probe into the dynamics of the highly non-linear medium of space plasmas. The result is an improved understanding in the effect of waves on kinetic processes in the terrestrial foreshock and new insights into the impact of MHD waves in the kinetic process of coronal loop ZP emission. We have repeatedly demonstrated the benefit of using kinetic and MHD techniques together to gain a deeper understand of events that span large time and spatial ranges.

# Bibliography

- M. Abramowitz and I. A. Stegun. *Handbook of Mathematical Functions*. Dover, New York, 1967.
- J. Adams. *An Introduction to Optical Waveguides*. Wiley-Interscience Publication. John Wiley & Sons, 1981. ISBN 9780471279693.
- J. Anderson. *Fundamentals of Aerodynamics*. Anderson series. McGraw-Hill Education, 2010. ISBN 9780073398105.
- T. D. Arber, A. W. Longbottom, C. L. Gerrard, and A. M. Milne. A staggered grid, lagrangian-eulerian remap code for 3d mhd simulations. *Journal of Computational Physics*, 171(1):151 – 181, 2001. ISSN 0021-9991.
- M. Aschwanden. *Physics of the Solar Corona: An Introduction with Problems and Solutions*. Springer Praxis Books / Astronomy and Planetary Sciences. Praxis Publishing Limited, Chichester, UK, 2006. ISBN 9783540307655.
- M.J. Aschwanden. Theory of radio pulsations in coronal loops. *Solar Physics*, 111(1):113–136, 1987. ISSN 0038-0938.
- S. D. Bale, J. C. Kasper, G. G. Howes, E. Quataert, C. Salem, and D. Sundkvist. Magnetic Fluctuation Power Near Proton Temperature Anisotropy Instability Thresholds in the Solar Wind. *Physical Review Letters*, 103(21):211101, November 2009.
- A. Balogh, C. M. Carr, M. H. Acuña, M. W. Dunlop, T. J. Beek, P. Brown, K.-H. Fornacon, E. Georgescu, K.-H. Glassmeier, J. Harris, G. Musmann, T. Oddy, and K. Schwingenschuh. The Cluster Magnetic Field Investigation: overview of in-flight performance and initial results. *Annales Geophysicae*, 19:1207–1217, October 2001.
- A. Barnes. Theory of generation of bow-shock-associated hydromagnetic waves in the upstream interplanetary medium. *Cosmic Electrodynamics*, 1:90–114, 1970.

- W. Baumjohann and R.A. Treumann. *Basic Space Plasma Physics*. Imperial College Press, 2012. ISBN 9781848168947.
- A. O. Benz. Flare observations. *Living Reviews in Solar Physics*, 5(1), 2008.
- J.A. Bittencourt. *Fundamentals of Plasma Physics*. Springer New York, 2013. ISBN 9781475740301.
- J. M. Borrero and K. Ichimoto. Magnetic structure of sunspots. *Living Reviews in Solar Physics*, 8(4), 2011.
- D. Burgess. What do we really know about upstream waves? *Advances in Space Research*, 20:673–682, September 1997.
- H. Carmichael. A Process for Flares. *NASA Special Publication*, 50:451, 1964.
- I. V. Chashei, A. I. Efimov, L. N. Samoznaev, D. Plettemeier, and M. K. Bird. Two-velocity structure observed in the inner solar wind. *Advances in Space Research*, 35:2195–2198, 2005.
- B. Chen, T. S. Bastian, D. E. Gary, and J. Jing. Spatially and Spectrally Resolved Observations of a Zebra Pattern in a Solar Decimetric Radio Burst. *ApJ*, 736:64, July 2011.
- F.F. Chen. *Introduction to Plasma Physics and Controlled Fusion: Plasma physics*. Plenum Press, 1984. ISBN 9780306413322.
- G. P. Chernov. Solar Radio Bursts with Drifting Stripes in Emission and Absorption. *Space Sci. Rev.*, 127:195–326, December 2006.
- G. P. Chernov, A. K. Markeev, M. Poquerusse, J. L. Bougeret, K.-L. Klein, G. Mann, H. Aurass, and M. J. Aschwanden. New features in type IV solar radio emission: combined effects of plasma wave resonances and MHD waves. *A&A*, 334:314–324, June 1998.
- G. P. Chernov, L. V. Yasnov, Y.-H. Yan, and Q.-J. Fu. On the Zebra Structure in the Frequency Range near 3 GHz. *Chinese J. Astron. Astrophys.*, 1:525, December 2001.
- G. P. Chernov, Y. H. Yan, Q. J. Fu, and C. M. Tan. Recent data on zebra patterns. *A&A*, 437:1047–1054, July 2005.

- G. F. Chew, M. L. Goldberger, and F. E. Low. The boltzmann equation and the one-fluid hydromagnetic equations in the absence of particle collisions. *Proceedings of the Royal Society of London. Series A. Mathematical and Physical Sciences*, 236 (1204):112–118, 1956.
- P.C. Clemmow and J.P. Dougherty. *Electrodynamics of particles and plasmas*. Addison-Wesley series in advanced physics. Addison-Wesley Pub. Co., 1969.
- CLWeb. Cluster spin distribution products, 2014. URL [www.clweb.cesr.fr](http://www.clweb.cesr.fr).
- J. W. Cooley and J. W. Tukey. An algorithm for the machine calculation of complex Fourier series. *Math. Comput.*, 19:297–301, 1965.
- F. C. Cooper, V. M. Nakariakov, and D. R. Williams. Short period fast waves in solar coronal loops. *A&A*, 409:325–330, October 2003.
- I. Dandouras and A Barthe. User guide to the cis measurements in the cluster active archive (caa). *CIS Team*, 2012.
- O. Darrigol. *Electrodynamics from Ampère to Einstein*. Clarendon Press, 2000. ISBN 9780198505945.
- P.A. Davidson. *An Introduction to Magnetohydrodynamics*. Cambridge Texts in Applied Mathematics. Cambridge University Press, 2001. ISBN 9780521794879.
- K. Davies and Institution of Electrical Engineers. *Ionospheric Radio*. IEE electromagnetic waves series. Peregrinus, 1990. ISBN 9780863411861.
- I. De Moortel and V. M. Nakariakov. Magnetohydrodynamic waves and coronal seismology: an overview of recent results. *Royal Society of London Philosophical Transactions Series A*, 370:3193–3216, July 2012.
- J.-P. Delaboudinière, G. E. Artzner, J. Brunaud, A. H. Gabriel, J. F. Hochedez, F. Millier, X. Y. Song, B. Au, K. P. Dere, R. A. Howard, R. Kreplin, D. J. Michels, J. D. Moses, J. M. Defise, C. Jamar, P. Rochus, J. P. Chauvineau, J. P. Marioge, R. C. Catura, J. R. Lemen, L. Shing, R. A. Stern, J. B. Gurman, W. M. Neupert, A. Maucherat, F. Clette, P. Cugnon, and E. L. van Dessel. EIT: Extreme-Ultraviolet Imaging Telescope for the SOHO Mission. *Sol. Phys.*, 162: 291–312, December 1995.
- G. A. Dulk and D. J. McLean. Coronal magnetic fields. *Sol. Phys.*, 57:279–295, April 1978.

- J. P. Eastwood, A. Balogh, E. A. Lucek, C. Mazelle, and I. Dandouras. On the existence of Alfvén waves in the terrestrial foreshock. *Annales Geophysicae*, 21: 1457–1465, July 2003.
- J. P. Eastwood, E. A. Lucek, C. Mazelle, K. Meziane, Y. Narita, J. Pickett, and R. A. Treumann. The Foreshock. *Space Sci. Rev.*, 118:41–94, June 2005.
- P. M. Edwin and B. Roberts. Wave propagation in a magnetically structured atmosphere. III - The slab in a magnetic environment. *Sol. Phys.*, 76:239–259, March 1982.
- P. M. Edwin and B. Roberts. Wave propagation in a magnetic cylinder. *Sol. Phys.*, 88:179–191, October 1983.
- P. M. Edwin and B. Roberts. Employing analogies for ducted MHD waves in dense coronal structures. *A&A*, 192:343–347, March 1988.
- ESA. Cluster active archive, 2014a. URL [caa.estec.esa.int/caa/home.xml](http://caa.estec.esa.int/caa/home.xml). Accessed: 2014-05-29.
- ESA. Image of cluster satellite group, 2014b. URL <http://sci.esa.int/cluster/>. Accessed: 2014-05-29.
- C. Escoubet and M. Goldstein. The Cluster Mission. *AGU Fall Meeting Abstracts*, page D1, December 2001.
- D. H. Fairfield. Bow shock associated waves observed in the far upstream interplanetary medium. *J. Geophys. Res.*, 74:3541, 1969.
- J. B. J. Fourier. *Théorie analytique de la chaleur*. Chez Firmin Didot, père et fils, 1822.
- J.P. Freidberg. *Ideal magnetohydrodynamics*. Modern Perspectives in Energy Series. Plenum Publishing Company Limited, 1987. ISBN 9780306425127.
- Q. Fu, Z. Qin, H. Ji, and L. Pei. A Broadband Spectrometer for Decimeter and Microwave Radio Bursts. *Sol. Phys.*, 160:97–103, August 1995.
- A. A. Galeev, V. I. Karpman, and R. Z. Sagdeev. Multiparticle aspects of turbulent-plasma theory. *Nuclear Fusion*, 5(1):20, 1965.
- S. P. Gary. *Theory of Space Plasma Microinstabilities*. September 1993.

- S. P. Gary, H. Li, S. O'Rourke, and D. Winske. Proton resonant firehose instability: Temperature anisotropy and fluctuating field constraints. *J. Geophys. Res.*, 103:14567–14574, July 1998.
- R. L. Gilliland and S. L. Baliunas. Objective characterization of stellar activity cycles. I - Methods and solar cycle analyses. *ApJ*, 314:766–781, March 1987. doi: 10.1086/165103.
- V. L. Ginzburg and V. V. Zhelezniakov. On the Possible Mechanisms of Sporadic Solar Radio Emission (Radiation in an Isotropic Plasma). *AZh*, 35:694, 1958.
- L. Gizon and A. C. Birch. Local helioseismology. *Living Reviews in Solar Physics*, 2(6), 2005.
- L. Golub and J.M. Pasachoff. *The Solar Corona*. The Solar Corona. Cambridge University Press, 2010. ISBN 9780521882019.
- J. A. Gonzalez-Esparza, E. J. Smith, A. Balogh, and J. L. Phillips. The quasi-parallel shock wave detected by ULYSSES on day 92:109. *A&A*, 316:323–332, December 1996.
- D.J. Griffiths. *Introduction to electrodynamics*. Prentice Hall, 1999. ISBN 9780138053260.
- B. N. Handy, L. W. Acton, C. C. Kankelborg, C. J. Wolfson, D. J. Akin, M. E. Bruner, R. Carvalho, R. C. Catura, R. Chevalier, D. W. Duncan, C. G. Edwards, C. N. Feinstein, S. L. Freeland, F. M. Friedlaender, C. H. Hoffmann, N. E. Hurlburt, B. K. Jurcevich, N. L. Katz, G. A. Kelly, J. R. Lemen, M. Levay, R. W. Lindgren, D. P. Mathur, S. B. Meyer, S. J. Morrison, M. D. Morrison, R. W. Nightingale, T. P. Pope, R. A. Rehse, C. J. Schrijver, R. A. Shine, L. Shing, K. T. Strong, T. D. Tarbell, A. M. Title, D. D. Torgerson, L. Golub, J. A. Bookbinder, D. Caldwell, P. N. Cheimets, W. N. Davis, E. E. Deluca, R. A. McMullen, H. P. Warren, D. Amato, R. Fisher, H. Maldonado, and C. Parkinson. The transition region and coronal explorer. *Sol. Phys.*, 187:229–260, July 1999.
- P. Hellinger, P. Travnicek, J. C. Kasper, and A. J. Lazarus. Proton Temperature Anisotropy in the Solar Wind: Linear Theory, Observations and Simulations. *AGU Fall Meeting Abstracts*, page A404, December 2006.
- J. P. Heppner, M. Sugiura, T. L. Skillman, B. G. Ledley, and M. Campbell. OGO-A Magnetic Field Observations. *J. Geophys. Res.*, 72:5417, November 1967.



- T. Hirayama. Theoretical Model of Flares and Prominences. I: Evaporating Flare Model. *Sol. Phys.*, 34:323–338, February 1974.
- J. V. Hollweg. Kinetic Alfvén wave revisited. *J. Geophys. Res.*, 104:14811–14820, July 1999.
- G. G. Howes, K. G. Klein, and J. M. TenBarge. Validity of the Taylor Hypothesis for Linear Kinetic Waves in the Weakly Collisional Solar Wind. *ApJ*, 789:106, July 2014.
- S. Ichimaru. *Statistical Plasma Physics, Volume I: Basic Principles*. Frontiers in Physics Series. Westview Press, 2008. ISBN 9780786740987.
- Infactcollaborative. Solar structure, 2014. URL <http://infactcollaborative.com>. Accessed: 2014-05-29.
- A. R. Inglis, V. M. Nakariakov, and V. F. Melnikov. Multi-wavelength spatially resolved analysis of quasi-periodic pulsations in a solar flare. *A&A*, 487:1147–1153, September 2008.
- IPS. Solar radio burst classifications, 2014. URL [www.ips.gov.au](http://www.ips.gov.au).
- A. W. Irwin, B. Campbell, C. L. Morbey, G. A. H. Walker, and S. Yang. Long-period radial-velocity variations of Arcturus. *PASP*, 101:147–159, February 1989. doi: 10.1086/132415.
- H. Isobe, M. Kubo, T. Minoshima, K. Ichimoto, Y. Katsukawa, T. D. Tarbell, S. Tsuneta, T. E. Berger, B. Lites, S. Nagata, T. Shimizu, R. A. Shine, Y. Sue-matsu, and A. M. Title. Flare Ribbons Observed with G-band and FeI 6302Å, Filters of the Solar Optical Telescope on Board Hinode. *PASJ*, 59:807, November 2007.
- H. Karimabadi, V. Roytershteyn, H. X. Vu, Y. A. Omelchenko, J. Scudder, W. Daughton, A. Dimmock, K. Nykyri, M. Wan, D. Sibeck, M. Tatineni, A. Majumdar, B. Loring, and B. Geveci. The link between shocks, turbulence, and magnetic reconnection in collisionless plasmas. *Physics of Plasmas (1994-present)*, 21(6):062308, 2014.
- J. C. Kasper, A. J. Lazarus, and S. P. Gary. Wind/SWE observations of firehose constraint on solar wind proton temperature anisotropy. *Geophys. Res. Lett.*, 29:1839, September 2002.

- C. F. Kennel and F. Engelmann. Velocity Space Diffusion from Weak Plasma Turbulence in a Magnetic Field. *Physics of Fluids*, 9:2377–2388, November 1966.
- S. Kim, V. M. Nakariakov, and K. Shibasaki. Slow Magnetoacoustic Oscillations in the Microwave Emission of Solar Flares. *ApJ*, 756:L36, September 2012.
- R. A. Kopp and G. W. Pneuman. Magnetic reconnection in the corona and the loop prominence phenomenon. *Sol. Phys.*, 50:85–98, October 1976.
- Y. G. Kopylova, A. V. Melnikov, A. V. Stepanov, Y. T. Tsap, and T. B. Goldvarg. Oscillations of coronal loops and second pulsations of solar radio emission. *Astronomy Letters*, 33:706–713, October 2007.
- N.A. Krall and A.W. Trivelpiece. *Principles of Plasma Physics*. International series in pure and applied physics. San Francisco Press, 1986. ISBN 9780911302585.
- J. Kuijpers. Theory of type IV DM bursts. In M. R. Kundu and T. E. Gergely, editors, *Radio Physics of the Sun*, volume 86 of *IAU Symposium*, pages 341–360, 1980.
- E.G. Kupriyanova, V.F. Melnikov, V.M. Nakariakov, and K. Shibasaki. Types of microwave quasi-periodic pulsations in single flaring loops. *Solar Physics*, 267(2): 329–342, 2010. ISSN 0038-0938.
- A. A. Kuznetsov and Y. T. Tsap. Loss-Cone Instability and Formation of Zebra Patterns in Type IV Solar Radio Bursts. *Sol. Phys.*, 241:127–143, March 2007.
- L. D. Landau and E. M. Lifshitz. Fluid mechanics. 2nd english edition. pergamon press, 1987. 539 pp. (paperback). *Journal of Fluid Mechanics*, 205:593–594, 8 1989. ISSN 1469-7645.
- A. J. Lazarus, J. C. Kasper, and K. W. Ogilvie. A Faraday-Cup Solar Wind Experiment for Solar Orbiter. In *ESA Special Publication*, volume 641 of *ESA Special Publication*, January 2007.
- A. F. Linnell Nemec and J. M. Nemec. A test of significance for periods derived using phase-dispersion-minimization techniques. *AJ*, 90:2317–2320, November 1985.
- F. Mandl. *Statistical Physics*. Manchester Physics Series. Wiley, 2013. ISBN 9781118723432.
- J. T. Mariska. Characteristics of Solar Flare Doppler-Shift Oscillations Observed with the Bragg Crystal Spectrometer on Yohkoh. *ApJ*, 639:484–494, March 2006.

- E. Marsch. Kinetic physics of the solar corona and solar wind. *Living Reviews in Solar Physics*, 3(1), 2006.
- E. Marsch, X.-Z. Ao, and C.-Y. Tu. On the temperature anisotropy of the core part of the proton velocity distribution function in the solar wind. *Journal of Geophysical Research (Space Physics)*, 109:A04102, April 2004.
- L. Matteini, S. Landi, M. Velli, and W. H. Matthaeus. Proton temperature anisotropy and current sheet stability: 2-D hybrid simulations. In G. P. Zank, J. Borovsky, R. Bruno, J. Cirtain, S. Cranmer, H. Elliott, J. Giacalone, W. Gonzalez, G. Li, E. Marsch, E. Moebius, N. Pogorelov, J. Spann, and O. Verkhoglyadova, editors, *American Institute of Physics Conference Series*, volume 1539 of *American Institute of Physics Conference Series*, pages 247–250, June 2013.
- J. Clerk Maxwell. A dynamical theory of the electromagnetic field. *Philosophical Transactions of the Royal Society of London*, 155:459–512, 1865.
- N. Meyer-Vernet. *Basics of the Solar Wind*. Cambridge Atmospheric and Space Science Series. Cambridge University Press, 2007. ISBN 9780521814201.
- D.C. Montgomery and D.A. Tidman. *Plasma Kinetic Theory*. McGraw-Hill advanced physics monograph series. McGraw-Hill, 1964.
- M. D. Montgomery, S. P. Gary, W. C. Feldman, and D. W. Forslund. Electromagnetic instabilities driven by unequal proton beams in the solar wind. *J. Geophys. Res.*, 81:2743–2749, June 1976. doi: 10.1029/JA081i016p02743.
- M.J. Moran and H.N. Shapiro. *Fundamentals of Engineering Thermodynamics*. Wiley, 2006. ISBN 9780470032091.
- D. J. Mullan and C. W. Smith. Solar Wind Statistics at 1 AU: Alfvén Speed and Plasma Beta. *Sol. Phys.*, 234:325–338, April 2006.
- H. Nakajima, M. Nishio, S. Enome, K. Shibasaki, T. Takano, Y. Hanaoka, C. Torii, H. Sekiguchi, T. Bushimata, S. Kawashima, N. Shinohara, Y. Irimajiri, H. Koshiishi, T. Kosugi, Y. Shiomi, M. Sawa, and K. Kai. The Nobeyama radioheliograph. *IEEE Proceedings*, 82:705–713, May 1994.
- V. M. Nakariakov and V. F. Melnikov. Quasi-Periodic Pulsations in Solar Flares. *Space Sci. Rev.*, 149:119–151, December 2009a.
- V. M. Nakariakov and B. Roberts. On Fast Magnetosonic Coronal Pulsations. *Sol. Phys.*, 159:399–402, July 1995.

- V. M. Nakariakov, T. D. Arber, C. E. Ault, A. C. Katsiyannis, D. R. Williams, and F. P. Keenan. Time signatures of impulsively generated coronal fast wave trains. *MNRAS*, 349:705–709, April 2004.
- V. M. Nakariakov, D. J. Pascoe, and T. D. Arber. Short Quasi-Periodic MHD Waves in Coronal Structures. *Space Sci. Rev.*, 121:115–125, November 2005.
- V. M. Nakariakov, A. R. Inglis, I. V. Zimovets, C. Foullon, E. Verwichte, R. Sych, and I. N. Myagkova. Oscillatory processes in solar flares. *Plasma Physics and Controlled Fusion*, 52(12):124009, December 2010.
- V. M. Nakariakov, C. Hornsey, and V. F. Melnikov. Sausage Oscillations of Coronal Plasma Structures. *ApJ*, 761:134, December 2012.
- V.M. Nakariakov and V.F. Melnikov. Quasi-periodic pulsations in solar flares. *Space Science Reviews*, 149(1-4):119–151, 2009b. ISSN 0038-6308.
- Y. Narita, K. Glassmeier, S. Schäfer, U. Motschmann, M. Fränz, I. Dandouras, K. Fornaçon, E. Georgescu, A. Korth, H. Rème, and I. Richter. Alfvén waves in the foreshock propagating upstream in the plasma rest frame: statistics from Cluster observations. *Annales Geophysicae*, 22:2315–2323, July 2004.
- NASA. Nasa image, solar wind speed., 2014a. URL <http://solarscience.msfc.nasa.gov>. Accessed: 2014-05-29.
- NASA. Nasa image, coronal phenomena overview., 2014b. URL <http://spaceplace.nasa.gov>. Accessed: 2014-05-29.
- NASA. Wind satellite, 2014c. URL <http://pwg.gsfc.nasa.gov/istp/gifs/wind.gif>. Accessed: 2014-05-29.
- NASA. Wind satellite orbit, 2014d. URL <http://cdaweb.gsfc.nasa.gov>. Accessed: 2014-05-29.
- NASA. Solar dynamics observatory, the corona, 2014e. URL <http://sdo.gsfc.nasa.gov/gallery/main/item/410>. Accessed: 2014-05-29.
- NASA. Nasa image, bow shock example., 2014f. URL <http://www.hq.nasa.gov>. Accessed: 2014-05-29.
- NASA. Nasa image, x-15 model in supersonic tunnel., 2014g. URL <http://dayton.hq.nasa.gov>. Accessed: 2014-05-29.

- Z. Ning, Q. Fu, and Q. Lu. Special fine structures of solar radio bursts on April 15 1998. *A&A*, 364:853–858, December 2000.
- NOAJ. Photograph of nobeyama radioheliograph, 2014. URL <http://solar.nro.nao.ac.jp>. Accessed: 2014-05-29.
- A.V. Oppenheim and R.W. Schaffer. *Discrete-time Signal Processing*. Prentice-Hall signal processing series. Prentice Hall, 1989. ISBN 9780132162920.
- A.V. Oppenheim and R.W. Schaffer. *Discrete-time signal processing*. Prentice-Hall signal processing series. Prentice Hall, 2010. ISBN 9780131988422.
- K. T. Osman, W. H. Matthaeus, B. Hnat, and S. C. Chapman. Kinetic Signatures and Intermittent Turbulence in the Solar Wind Plasma. *Physical Review Letters*, 108(26):261103, June 2012.
- S. Parenti. Solar prominences: Observations. *Living Reviews in Solar Physics*, 11(1), 2014.
- E. N. Parker. Dynamics of the Interplanetary Gas and Magnetic Fields. *ApJ*, 128: 664, November 1958.
- G. Paschmann and P.W. Daly. *Analysis Methods for Multi-spacecraft Data*. ISSI scientific report. International Space Science Institute, 1998.
- K. B. Quest and V. D. Shapiro. Evolution of the fire-hose instability: Linear theory and wave-wave coupling. *J. Geophys. Res.*, 101:24457–24470, November 1996.
- F. Reale. Coronal loops: Observations and modeling of confined plasma. *Living Reviews in Solar Physics*, 7(5), 2010.
- P. H. Reiff. The sun-earth connection, 1999. URL <http://space.rice.edu>.
- H. Rème, C. Aoustin, J. M. Bosqued, I. Dandouras, B. Lavraud, J. A. Sauvaud, A. Barthe, J. Bouyssou, T. Camus, O. Coeur-Joly, A. Cros, J. Cuvilo, F. Ducay, Y. Garbarowitz, J. L. Medale, E. Penou, H. Perrier, D. Romefort, J. Rouzaud, C. Vallat, D. Alcaydé, C. Jacquey, C. Mazelle, C. D’Uston, E. Möbius, L. M. Kistler, K. Crocker, M. Granoff, C. Mouikis, M. Popecki, M. Vosbury, B. Klecker, D. Hovestadt, H. Kucharek, E. Kuenneth, G. Paschmann, M. Scholer, N. Sckopke, E. Seidenschwang, C. W. Carlson, D. W. Curtis, C. Ingraham, R. P. Lin, J. P. McFadden, G. K. Parks, T. Phan, V. Formisano, E. Amata, M. B. Bavassano-Cattaneo, P. Baldetti, R. Bruno, G. Chionchio, A. di Lellis, M. F. Marcucci,

- G. Pallochia, A. Korth, P. W. Daly, B. Graeve, H. Rosenbauer, V. Vasyliunas, M. McCarthy, M. Wilber, L. Eliasson, R. Lundin, S. Olsen, E. G. Shelley, S. Fuselier, A. G. Ghielmetti, W. Lennartsson, C. P. Escoubet, H. Balsiger, R. Friedel, J.-B. Cao, R. A. Kovrazhkin, I. Papamastorakis, R. Pellat, J. Scudder, and B. Sonnerup. First multispacecraft ion measurements in and near the Earth's magnetosphere with the identical Cluster ion spectrometry (CIS) experiment. *Annales Geophysicae*, 19:1303–1354, October 2001.
- B. Roberts, P. M. Edwin, and A. O. Benz. On coronal oscillations. *ApJ*, 279: 857–865, April 1984.
- M. S. Rosin, A. A. Schekochihin, F. Rincon, and S. C. Cowley. A non-linear theory of the parallel firehose and gyrothermal instabilities in a weakly collisional plasma. *MNRAS*, 413:7–38, May 2011.
- C. T. Russell, D. D. Childers, and P. J. Coleman, Jr. Ogo 5 observations of upstream waves in the interplanetary medium: Discrete wave packets. *J. Geophys. Res.*, 76:845, 1971.
- J. D. Scargle. Studies in astronomical time series analysis. II - Statistical aspects of spectral analysis of unevenly spaced data. *ApJ*, 263:835–853, December 1982.
- R. Schlickeiser and J. A. Miller. Quasi-linear Theory of Cosmic-Ray Transport and Acceleration: The Role of Oblique Magnetohydrodynamic Waves and Transit-Time Damping. *ApJ*, 492:352–378, January 1998.
- M. Scholer, I. Shinohara, and S. Matsukiyo. Quasi-perpendicular shocks: Length scale of the cross-shock potential, shock reformation, and implication for shock surfing. *Journal of Geophysical Research (Space Physics)*, 108:1014, January 2003.
- L. A. Selzer, B. Hnat, K. T. Osman, V. M. Nakariakov, J. P. Eastwood, and D. Burgess. Temperature Anisotropy in the Presence of Ultra Low Frequency Waves in the Terrestrial Foreshock. *ApJ*, 788:L5, June 2014.
- D. D. Sentman, J. P. Edmiston, and L. A. Frank. Instabilities of low frequency, parallel propagating electromagnetic waves in the earth's foreshock region. *J. Geophys. Res.*, 86:7487–7497, September 1981.
- K. Shibata and T. Magara. Solar flares: Magnetohydrodynamic processes. *Living Reviews in Solar Physics*, 8(6), 2011.
- C. Slottje. Zebra patterns in solar type IV radio bursts. 2:88, 1971.

- C. Slottje. Fast fine structure in solar microwave flares. 86:195–203, 1980.
- B.V. Somov. *Plasma Astrophysics, Part II: Reconnection and Flares*. Astrophysics and Space Science Library. Springer London, Limited, 2007. ISBN 9780387688947.
- T. H. Stix. *Waves in plasmas*. 1992.
- T.H. Stix. *Waves in Plasmas*. American Inst. of Physics, 1992. ISBN 9780883188590.
- P. A. Sturrock. Model of the High-Energy Phase of Solar Flares. *Nature*, 211: 695–697, August 1966.
- P.A. Sturrock. *Plasma Physics: An Introduction to the Theory of Astrophysical, Geophysical and Laboratory Plasmas*. Stanford-Cambridge Program. Cambridge University Press, 1994. ISBN 9780521448109.
- D.G. Swanson. *Plasma Waves, 2nd Edition*. Series in Plasma Physics. Taylor & Francis, 2003. ISBN 9780750309271.
- D.G. Swanson. *Plasma waves*. Elsevier Science, 2012. ISBN 9780323141635.
- B. Tan, Y. Zhang, C. Tan, and Y. Liu. Microwave Quasi-Periodic Pulsations in Multi-timescales Associated with a Solar Flare/CME Event. *ApJ*, 723:25–39, November 2010.
- G. I. Taylor. The spectrum of turbulence. *Proceedings of the Royal Society of London. Series A - Mathematical and Physical Sciences*, 164(919):476–490, 1938.
- Tesla. Plasma wave schematic, 2013. URL <http://tesla.desy.de>. Accessed: 2014-05-29.
- R.A. Treumann and W. Baumjohann. *Advanced Space Plasma Physics*. London : Imperial College Press, 1997. ISBN 9781860940262.
- C.-Y. Tu, E. Marsch, and K. M. Thieme. Basic properties of solar wind MHD turbulence near 0.3 AU analyzed by means of Elsasser variables. *J. Geophys. Res.*, 94:11739–11759, September 1989.
- G. van Hoven, C. Chiuderi, and R. Giachetti. A model for a stable coronal loop. *ApJ*, 213:869–873, May 1977.
- D. Verscharen and B. D. G. Chandran. The Dispersion Relations and Instability Thresholds of Oblique Plasma Modes in the Presence of an Ion Beam. *ApJ*, 764: 88, February 2013.

- A.A. Vlasov. *Many-particle theory and its application to plasma*. Russian monographs and texts on advanced mathematics and physics. Gordon and Breach, 1961.
- J. Wesson and D.J. Campbell. *Tokamaks*. Oxford engineering science series. Clarendon Press, 1997. ISBN 9780198562931.
- L. B. Wilson, III, C. A. Cattell, P. J. Kellogg, K. Goetz, K. Kersten, J. C. Kasper, A. Szabo, and K. Meziane. Low-frequency whistler waves and shocklets observed at quasi-perpendicular interplanetary shocks. *Journal of Geophysical Research (Space Physics)*, 114(A13):A10106, October 2009.
- R. M. Winglee and G. A. Dulk. The electron-cyclotron maser instability as a source of plasma radiation. *ApJ*, 307:808–819, August 1986.
- Y. Yan, J. Huang, B. Chen, and T. Sakurai. Diagnostics of Radio Fine Structures around 3 GHz with Hinode Data in the Impulsive Phase of an X3.4/4B Flare Event on 2006 December 13. *PASJ*, 59:815, November 2007.
- S. H. Yang, J. Zhang, C. L. Jin, L. P. Li, and H. Y. Duan. Response of the solar atmosphere to magnetic field evolution in a coronal hole region. *A&A*, 501:745–753, July 2009.
- S. Yu, Y. Yan, and B. Tan. Relaxation of Magnetic Field Relative to Plasma Density Revealed from Microwave Zebra Patterns Associated with Solar Flares. *ApJ*, 761:136, December 2012.
- S. Yu, V. M. Nakariakov, L. A. Selzer, B. Tan, and Y. Yan. Quasi-periodic Wiggles of Microwave Zebra Structures in a Solar Flare. *ApJ*, 777:159, November 2013.
- V. V. Zaitsev and A. V. Stepanov. On the Origin of the Hard X-Ray Pulsations during Solar Flares. *Soviet Astronomy Letters*, 8:132–134, April 1982.
- V. V. Zaitsev and A. V. Stepanov. Reviews of Topical Problems: Coronal Magnetic Loops. *Physics Uspekhi*, 51:1123–1160, November 2008.
- V. V. Zheleznyakov and E. Y. Zlotnik. Cyclotron wave instability in the corona and origin of solar radio emission with fine structure. III. Origin of zebra-pattern. *Sol. Phys.*, 44:461–470, October 1975.